

UNIVERSITAT DE BARCELONA

# Nonlinear and spatial dynamics for multicellular organisms

Josep Mercadal Melià



Aquesta tesi doctoral està subjecta a la llicència ***Reconeixement 4.0. Espanya de Creative Commons***.

Esta tesis doctoral está sujeta a la licencia ***Reconocimiento 4.0. España de Creative Commons***.

This doctoral thesis is licensed under the ***Creative Commons Attribution 4.0. Spain License***.

Tesi doctoral

# Nonlinear and spatial dynamics for multicellular organisms

Josep Mercadal Melià



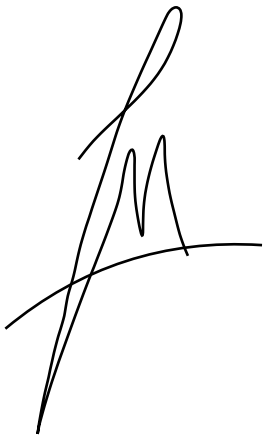

UNIVERSITAT DE BARCELONA

# Nonlinear and spatial dynamics for multicellular organisms

Universitat de Barcelona

Programa de Doctorat en Física

Autor:
Josep Mercadal Melià



Directors:
Marta Ibañes
José María Sancho

Tutor:
Giancarlo Franzese

Departament de Física de la Matèria Condensada
Facultat de Física




UNIVERSITAT DE BARCELONA

Josep Mercadal Melià
Departament de Física de la Matèria Condensada
Facultat de Física
Universitat de Barcelona
Barcelona, E-08028 (Spain)
josepmercadal@ub.edu
josep.mercadal@fmc.ub.edu

**Nonlinear and spatial dynamics for multicellular organisms**
Ph.D. Thesis
Barcelona, Febrer 2022

I acknowledge financial support from BES-2016-078218 funded by Ministerio de Ciencia e Innovación (MCIN)/Agencia Estatal de Investigación (AEI)/10.13039/501100011033 and Fondo Social Europeo (FSE) "El FSE invierte en tu futuro". The results of this thesis are part of grants PGC2018-101896-B-I00 and FIS2015-66503-C3-3-P funded by MCIN/AEI/10.13039/501100011033/ FEDER "Una manera de hacer Europa". We also acknowledge support by the Generalitat de Catalunya through Grup de Recerca Consolidat 2014 SGR 878 and 2017 SGR 1061.

A sa família

About thirty years ago there was much talk that geologists ought only to observe and not theorize; and I well remember someone saying that at this rate a man might as well go into a gravel-pit and count the pebbles and describe the colours. How odd it is that anyone should not see that all observation must be for or against some view if it is to be of any service!

Charles Darwin,
*in a letter to Henry Fawcett (1861)*

# ACKNOWLEDGEMENTS

Aquesta tesi no hauria estat possible sense el suport i la inspiració que he rebut durants tots aquests anys per part de moltes persones, les contribucions—directes o indirectes—de les quals em sent obligat a professar.

Estic profundament en deute amb na Marta Ibañes, que m'ha fet de guia durant tots aquests anys, fent que aquesta tesi sigui possible. El seu ànim constant, combinat amb un bon judici en qüestions teòriques i pràctiques, m'han donat l'espai per créixer com a científic. Fora d'aquest àmbit, però, on destaca és en seu caràcter amable i compassiu, valors que, lamentablement, són difícils de trobar en un món acadèmic cada cop més competitiu, però totalment necessari si l'objectiu és construir una comunitat de recerca sana. Gràcies, Marta!

Gracias a Jose Maria Sancho, por omitir los detalles y ver el *big picture*, un ejercicio difícil cuando uno está abrumado con fórmulas y simulaciones.

He tingut la sort d'haver format part d'una estreta col·laboració amb el laboratori de l'Ana I. Caño-Delgado al CRAG (Bellaterra). Els lab meetings setmanals i les abundants discussions sobre plantes i modelització han estat una gran font d'inspiració. Muchas gracias a Nadja, Isa y Ainoa, por las colaboraciones, y a Mar, por las que nos esperan.

Estic especialment en deute amb en Jordi Garcia-Ojalvo, amb qui vaig donar els meus primers passos en el fascinant món de la biologia. Passar gairebé un any al seu grup de recerca va ser una experiència que serà difícil d'oblidar. Vull donar les gràcies a tota la gent del laboratori d'en Jordi durant la meva breu estada, per crear un ambient tan fantàstic. Gràcies sobretot a n'Elena, en Carlos, na Rosa, en Marçal i na Letícia.

Als memebres del departament de Física de Matèria Condensada, per fer-me sentir com a casa. En especial, als companys amb els quals he tingut el plaer de compartir despatx i planta, dinars, sopars, i sobretot, cerveses: Helena, Andreu 1, Andreu 2, Adrià, Josep 2, Mattia, Sergio, Irina, Joan, Carla, Carol, Antonio, Eric, Gaspard, Pam, Zaida. Moltes gràcies!

Als companys de carrera, amb qui vaig fer els primers passos en el món de la Física: Marc, Albert, Joana, Juanpe, Blasco, Eudald, Roger, Víctor, Joseda i Pablo.

Amigues i amics de Mercadal, es de sempre, que no us mencionaré a tots però ja sabeu qui sou, per totes ses coses que ham viscut junts durant aquests 30 anys. Mos veim prest!

A nes membres de Black Pearl i Estruendo. És un gust compartir escenari amb voltros. Moltes gràcies i rock&roll!

Als ornitorrincs de Canet, per les barbacoes, pujades a la Creu, escape-rooms i tot el que hem compartit durant aquests anys. Espero seguir fent-ho molts anys més!

A la que ha sigut la meva segona família durant els últims set anys: Sonia, Xavi, Oriol, i també a la Mari i en Julio.

A sa Family: alorencs, fornellers i es de s'Estància, a l'avi, s'àvia i sa tia. Gràcies a tots per ser com sou. Us estim família!

A tu, Helena, per compartir amb jo tots aquests anys; per ser companya d'aventures, de viatges, de penes i d'alegries. Per fer-me veure ses coses amb altres ulls. Gràcies també per donar-me espai aquests últims mesos; esper poder compensar-t'ho. T'estim molt!

A en Biel i en Lau, germans, millors amics i confidents, amb qui he tingut es privilegi de conviure sa majoria d'aquests anys. A voltros us dec gran part de lo que sóc avui. Sincerament, sa meva vida sense voltros hauria estat molt avorrida. Gràcies!

Finalment, i més important, a na Rita i en Biel, sa mamà i es papà, principals responsables de tot açò. Un agraïment a una tesi no fa justícia a tot lo que m'hau donat. Sou es millors pares que un fill pot tenir. Aquesta tesi és per voltros. Us estim!

*Disclaimer*: my contributions to the research presented in this thesis have been mostly theoretical and computational. While I have proposed, assessed, and in some cases, modestly helped with most of the experiments described, the bulk of the experimental work has been performed by our collaborating group, led by Ana I. Caño-Delgado's at Centre for Research in Agricultural Genomics (CRAG). Experiments have been done by Isabel Betegón-Putze, Nadja Bosch, Ainoa Planas-Riverola, Mar Marquès-Bueno and Mar Ferreira-Guerra. Nevertheless, in some cases, I helped with the analysis of experimental data. Some of the experiments in [Betegón-Putze et al., 2021] (part of which is included in Chapter 4 of this thesis) have been performed in the labs of Yvonne Stahl, Rosangela Sozzani, Ana Conesa and Salomé Prat. Therefore, I will explicitly reiterate, when needed, my contributions as opposed to those from our collaborators.

# SUMMARY AND STRUCTURE

This thesis covers several aspects of nonlinear and spatiotemporal processes occurring in multicellular organisms in the context of developmental biology. Our approach relies on mathematical and computational modelling of such processes, borrowing techniques from nonlinear dynamical systems. Using this framework and by analysing different biological scenarios, we disclose mechanisms involved in specifying patterns formed by distinct cell types. While the theoretical and numerical methodologies we used can be generally applied without regard to any specific organism, our attention has been mainly focused on plants. Our deep bias towards organisms that look and behave like us has traditionally tilted the scales towards animal research and has made us partly oblivious of the crucial role plants have in the stability of ecosystems and our everyday lives. The truth, however, is that plants constitute an exceptional substrate for studying biological processes and will undoubtedly become paramount in our quest to fight inequality, world hunger, and climate change. Luckily, the trend is shifting, and plant biology is gaining strength not only on the experimental side but as a source for understanding the general principles that define living systems, of which hopefully the work of this thesis is testimony.

The thesis is structured in four parts. Part I aims to introduce and motivate the contents of the thesis. The results and main body of work are presented across Part II and Part III. Finally, Part IV outlines the most significant conclusions of the thesis, as well as future perspectives. Some chapters are complemented with an appendix providing additional information to the topics discussed in the main part.

Within Part I, in Chapter 1 we recount, in a casual tone, a brief history of the development of genetics through the study of plants, an account which lies at the heart of biological research, and whose main characters include figures of such stature as Aristotle, Gregor Mendel or Charles Darwin. This opening sets the stage to introduce, in Chapter 2, the plant systems we have focused on the most: the model plant *Arabidopsis thaliana*, easily the most well-studied organism in plant genetics; and its evolutionarily distant cousin, the liverwort *Marchantia polymorpha*. This section is followed by a generic account of pattern formation in

plants and animals, with special emphasis on patterns in developmental biology. Next, we comment on pattern-generating mechanisms, permeated with excerpts of historical relevance. Finally, in Chapter 3, the last chapter of this part, we present the technical methods we will recurrently use throughout the thesis, including how to construct models of gene regulation in time and space and how these can be analyzed mathematically.

Part II is concerned with the regulation of cell division in specific cells of the *Arabidopsis* root meristem. At the tip of the primary root, a small group of cells called the stem cell niche (SCN) have the ability to both renew themselves and produce daughter cells, which are fated to develop into the differentiated tissues of the plant. In this SCN, a group of rarely dividing cells called the quiescent center (QC) helps preserve the stemness of those cells. We specifically focus on the regulations between two transcription factors, BRAVO and WOX5, known for their role as repressors of QC division. In Chapter 4 we establish, using empirical evidence from our collaborators and mathematical modelling, the precise regulatory and molecular interactions between BRAVO and WOX5, finding that their mutual regulations involve their physical interaction, presumably by binding into a complex. Owing to the convergence of the two transcription factors at the QC, we propose a simple mechanism for regulating cell division and find that the formation of the BRAVO-WOX5 complex can be relevant. In Chapter 5 the mathematical model of the interactions between BRAVO and WOX5 is extended to include spatial effects. Through a minimal reaction-diffusion model, we show that the formation of the BRAVO-WOX5 complex, together with the diffusion of WOX5, can qualitatively explain the expression patterns observed experimentally in wild-type roots and those where these transcription factors have lost their function. We show that BRAVO, through the attenuation of its diffusible activator WOX5, confines its expression domain to the stem cell niche. We explore several ways this attenuation can occur, of which complex formation between BRAVO and WOX5 is but one instance. We extend these simple models to realistic root layouts by numerically solving the equations in a segmented root, where diffusion can occur both within and between cells. The expression patterns of BRAVO and WOX5 obtained with this realistic approach are in excellent agreement with their experimental counterparts, highlighting the predictive strengths of this framework.

In Part III, the first chapter (Chapter 6) deals with the formation and maintenance of rhizoids in the liverwort *Marchantia polymorpha*. Rhizoid precursors in the gemma epidermis of *Marchantia* are specified from a field of initially equivalent epidermal cells, a process that takes place during the first day after germination. While genetic factors controlling rhizoid precursor specification have been identified, the mechanisms underlying the patterning of rhizoids in the epidermis remain unknown. Building on recent experiments, we propose that rhizoid patterns emerge from the interactions between the microRNA FRH1 and the rhizoid-promoting transcription factor RSL1. Our approach is based on coupled

differential equations on a lattice of hexagonal cells mimicking the *Marchantia* epidermis, with the assumption that FHR1 is mobile. We show that the model can quantitatively predict all the experimental results—from the literature and our collaborators—with high accuracy, both in wild-type conditions and in loss of function and overexpressor mutants. This study constitutes another instance where mathematical and computational modelling sheds light on the mechanistic interactions behind cellular decision-making and pattern formation, a theme increasingly common in plant biology.

In Chapter 7, the second chapter of Part III, we mathematically explore a model based on the mixed feedback loop, a genetic circuit overrepresented in statistical analyses of gene and protein interaction databases. It consists of the transcriptional regulation of a gene by another, plus the formation of a complex between the proteins coded by the two genes. Mathematical analyses have shown that this circuit can display oscillations for transcriptional activation and bistability for transcriptional repression but with complex formation irreversibility as a constraint. We show that for transcriptional repression, lifting the requirement of irreversibility and allowing the complex to disassociate confers the circuit the ability to display both bistability and oscillations without changing the nature of transcriptional regulations. By introducing spatial coupling through the diffusion of the complex, we show that initially stable spatially homogeneous or oscillatory states can lose stability and form periodic patterns. Moreover, new spatiotemporal behaviours such as chimeras—states where oscillating regions coexist with regions where patterns are stable—, or circular patterns induced by intrinsic noise can also be observed. This work provides a novel mechanism for generating fine-grained periodic patterns and demonstrates the unintuitive effect of diffusion already anticipated by Turing, namely its role as a destabilizing agent of a preceding spatially homogeneous state, resulting in stable periodic structures. It also embodies an increasingly common theme in developmental and evolutionary systems biology: the importance of small circuits capable of performing multiple, qualitatively different functions, which arise from the circuit's topology but depend on the specific external context of which the circuit is embedded.

We conclude with a final part (Part IV) summarizing the main findings of each chapter, indicating the novel contributions they have provided, and commenting on the prospects we envisage for future research.

# Contents

SUMMARY AND STRUCTURE ix

I General introduction and methods 1

1 An incomplete and biased introduction to plants 3

2 General introduction 15
2.1 Rooting systems in *A. thaliana* and *M. polymorpha* . . . . . 15
2.1.1 Root development in *A. thaliana* . . . . . 20
2.1.2 Rhizoid formation in *M. polymorpha* . . . . . 21
2.2 Patterns in biology . . . . . 23

3 Mathematical models and methods 31
3.1 Models of gene expression in space and time . . . . . 31
3.1.1 Regulation of gene expression in time . . . . . 32
3.1.2 Gene regulation in space . . . . . 41
3.2 Mathematical tools . . . . . 45
3.2.1 Linear stability analysis and bifurcations . . . . . 45
3.2.2 Linear instabilities in spatially extended systems . . . . . 50
3.2.3 Noise and the chemical Langevin equation . . . . . 55

II BRAVO and WOX5 in the stem cell niche 57

4 Regulatory control at the *Arabidopsis* root stem cell niche 59
4.1 Introduction . . . . . 60
4.2 Experimental data and its interpretation . . . . . 61
4.3 Two possible circuits for the regulations between BRAVO and WOX5 . . . . . 66
4.3.1 Modelling mutants and overexpressors . . . . . 69
4.4 BRAVO and WOX5 directly interact to form a heterodimeric complex . . . . . 76
4.4.1 The effect of additional sequestrators . . . . . 82

4.5 The BRAVO-WOX5 complex is sufficient for the control of QC divisions . . . 84
4.6 Discussion . . . 89

**Appendix** **93**
4.A Error propagation for QC division contributions . . . 93
4.B Numerical methods . . . 93
4.C Supplementary Figures . . . 95

**5 BRAVO restricts its own expression in the stem cell niche** **103**
5.1 Introduction . . . 104
5.2 Modelling BRAVO self-confinement in the root SCN . . . 106
5.2.1 Confinement through immobilization of WOX5 . . . 106
5.2.2 Confinement through inactivation of WOX5 . . . 114
5.2.3 Confinement through the repression of a mobile activator 118
5.3 Modelling BRAVO self-confinement in a realistic root layout . . 122
5.4 Discussion . . . 129

**Appendix** **135**
5.A Numerical solution of steady state expression profiles of the one-dimensional models . . . 135
5.B Construction of realistic root layouts . . . 135
5.C Numerical implementation of heterogeneous reaction-diffusion equations in the realistic root layout . . . 136
5.D Supplementary Figures . . . 137

**III Lateral inhibition by diffusion** **143**

**6 Formation of rhizoids in *Marchantia polymorpha*** **145**
6.1 Introduction . . . 146
6.2 A null model: cell-autonomous random decisions for rhizoid precursor patterns . . . 150
6.3 A model with self-activation and lateral inhibition through diffusion 156
6.3.1 Model formulation . . . 156
6.3.2 The model recapitulates rhizoid patterns in WT and mutants . . . 160
6.4 A balance between randomness and lateral-inhibition by diffusion 163
6.4.1 Model predictions . . . 163
6.4.2 Experiments support the model predictions . . . 168
6.5 Discussion . . . 172

**Appendix** **177**
6.A Analytical expressions for $f_k$, $n_k$, $F_r^k$ and $g_l^k$ in the null model . 177

**7 Diffusion induced lateral inhibition patterns** **181**
7.1 Introduction . . . . . 182
7.2 The reversible mixed feedback loop . . . . . 185
7.2.1 Dynamics and stability of fixed points . . . . . 186
7.2.2 The RMFL with intrinsic noise . . . . . 194
7.3 The diffusively coupled mixed feedback loop . . . . . 195
7.3.1 Two-cell system . . . . . 197
7.3.2 The RMFL in cellular lattices . . . . . 199
7.3.3 Noise-induced phenomena . . . . . 206
7.4 Discussion . . . . . 208

**IV Conclusions** **213**

**8 Conclusions and perspectives** **217**

**Resum en català** **225**

**List of figures** **229**

**List of tables** **233**

**Contributions and publications** **235**

**Bibliography** **237**

# Part I

# General introduction and methods

# Chapter 1

# An incomplete and biased introduction to plants

Plants are truly remarkable organisms. They harness the energy from the sun, virtually the only source available to our planet, and through photosynthesis they transform raw materials such as carbon dioxide and water into sugars—an ability shared with all photoautotrophs, including algae and cyanobacteria. As a waste product, photosynthesis releases oxygen, making this process responsible for producing and maintaining most of the oxygen content in the Earth's atmosphere, and accounts for most of the energy necessary for life. But the appeal of plants not only lies at the molecular scale. From the millimeter-wide duckweed to the colossal giant sequoias of California's Sierra Nevada Mountains, plant sizes span almost five orders of magnitude. Yet, any single tree dwarfs—both in size and in age—against what can be achieved by some clonal plant colonies. For example, in central Utah, a single colony of quaking aspen (*Populus tremuloides*) connected by a subterranean root system—which for the untrained eye looks like a typical forest of individual trees—is thought to be the most massive living organism on the planet, with an estimated weight of 6 million kilograms and an approximate age of 14.000 years [Ding et al., 2017]. On the other side of the Atlantic, in the cozy waters of the Mediterranean, a single patch of the endemic *Posidonia oceanica* located in the narrow strait separating Eivissa from the smaller island of Formentera, is thought to be the oldest living organism on the planet, with an estimated age that ranges between 80.000 and 200.000 years [Arnaud-Haond et al., 2012], although these figures might well be an overestimate[2].

Plants also dominate ecosystems in terms of mass. Current estimates of biomass distribution on Earth place plants at the top tier, with a staggering figure of 450 gigatons of carbon (Gt C), constituting roughly 80% of the total

[2]During the last ice-age (∼115.000–11.000 ya), sea levels in the Mediterranean were about 100m above their current values, placing the habitat of *Posidonia* among the landmass, making its survival unlikely [Arnaud-Haond et al., 2012].



**Figure 1.1: Quaking aspens from Utah, posidonia from Menorca and duckweeds from the Lake of Banyoles. Top:** Part of the Pando quaking aspen (*Populus tremuloides*) colony of central Utah, presumably the most massive living organism on the planet (photo from https://pixabay.com). **Bottom left:** Patches of posidonia (*Posidonia oceanica*) in the southern coast of Menorca (original picture). **Bottom right:** Duckweed of the species *Lemna minor*, in the rims of the Lake of Banyoles, Girona (original picture).

biomass in the planet's biosphere [Bar-On et al., 2018]. Just to have a reference, and to grasp the magnitude of this number, consider the second largest group, bacteria, with an admirable 70 Gt C (≈ 13% of the total), or fungi, ranking third with 12 Gt C (≈ 2%). Animals constitute only 2 Gt C (≈ 0.4%), most of them either arthropods (1 Gt C) or fish (0.7 Gt C). Humans—always ready to brag about our presumed topmost position in a fabricated ladder of progress—make up an insignificant 0.06 Gt C (≈ 0.01%). While it is true that biomass need not be a direct measure of importance—whatever that means outside an anthropocentric perspective—it does give an idea about how organic resources are distributed across the planet, thus exposing who holds the best cards in the game of life.

The role of plants as crucial elements in the biosphere is difficult to overstate. The diet of most animal species depends either directly on plants by eating them or indirectly by eating herbivores. Most fungi and plants engage in mutualistic relationships known as mycorrhizae, where the plant provides fungi with carbohydrates, and in exchange, fungi help the plant to get water and nutrients from the soil. Many bacteria also form symbioses with plants, such as those of the genus *Rhizobium*, which colonize cells of many legume species and fix nitrogen

for these plants to use, while plants provide them sugars. Viruses such as the tobacco mosaic virus use plants as their hosts to reproduce. Even some protists need plants for their survival, such as the infamous *Phytophthora infestans*, an agent causing the potato blight, a disease which makes tubers shrink and rot, and one of the main reasons behind the Great Irish Famine, a period of mass starvation and disease that lasted from 1845 to 1852 and took the lives of over a million people [Laxton, 1998]. Humans are no exception in using plants to their benefit. Our relationship with them goes back to the very origin of our species, not merely as a food source but as a fundamental part of our culture.

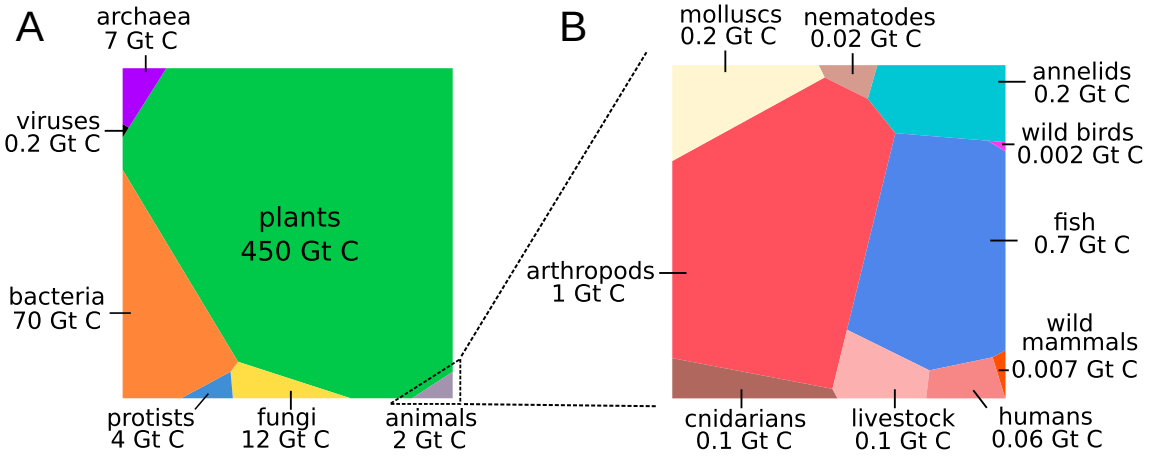



**Figure 1.2: The biomass distribution on Earth.** Plants constitute the largest category of organisms in terms of biomass, followed by bacteria and fungi. In animals, most biomass is distirbuted among arthropods and fish, while humans comprise only a tiny fraction. Image adapted from [Bar-On et al., 2018].

The evolutionary history of our species is inextricably linked with the use of plants. They are one of our main sources of food; they provide materials for building shelter and tools; they store energy in the form of wood[1] which can be easily released to warm us up; they are used for aesthetic purposes and are the lifeblood of many medicinal and recreational drugs [Shaal, 2019]. Plants have been objects of worship, such as Yggdrasil in Norse mythology, the ash tree around which all else exists, of which Midgard, the world of humans, is but one branch; the tree of the knowledge of good and evil, from which Eve, deceived by the serpent, eats the forbidden fruit and costs her and Adam their expulsion from the garden of Eden. Some plants hold spiritual value, such as the lotus flower, sacred in both Hinduism and Buddhism, representing the path to spiritual awakening and enlightenment; they embody human qualities and connect

[1] And when decayed, buried, and put under heat and pressure over millions of years, they may become coal, as it happened to Earth's tropical forests in the Carboniferous (359–299 mya). We are nowadays in the aftermath of such event, inexorably burning energy from long-gone forests, seemingly oblivious of the fact that the carbon we release into the atmosphere is the very same carbon those trees captured to build themselves.

us with the gods, as the bay tree or laurel (also called *daphne*), which symbolized triumph and high status in ancient Greece, in reference to the god Apollo and his affair with the nymph Daphne. Plants have shaped us biologically and culturally, and we have changed them in return. Given such an intimate relationship, it is no surprise that over millennia humans—with our characteristically strong urge to comprehend the many foibles of the world—went on the accumulate, compile and classify information about the inner workings of many plants. In this regard, the study of plants is arguably one of the oldest branches of science. Plant science, often referred to as botany or phytology—this last term having its etymological roots in the Greek words φυτόν ('plant') and λόγος ('reason', 'discourse', or in more modern interpretations, 'science'), which would be a term homologous to zoology, the study of animals—evolved from the need of early humans to identify—and later domesticate and cultivate—edible, medicinal and poisonous plants.

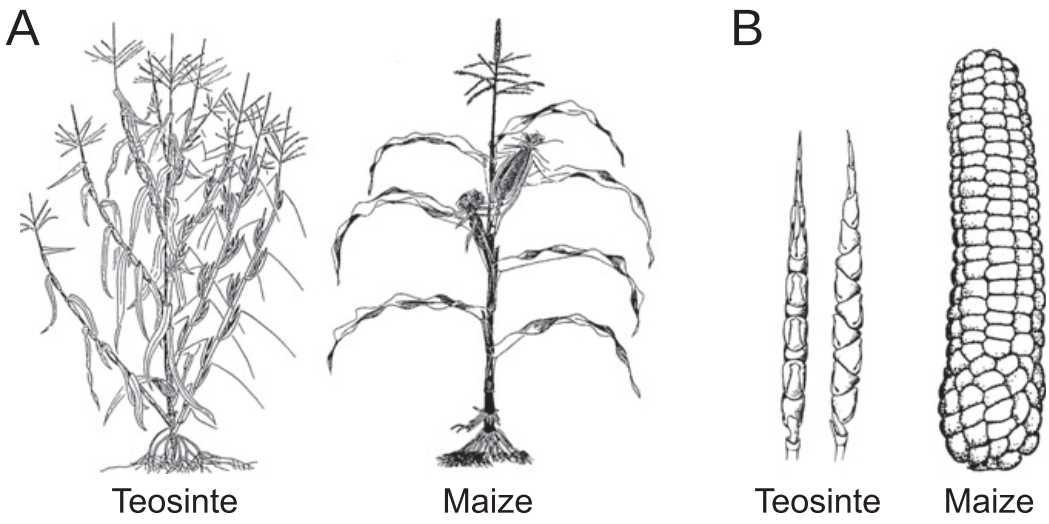



**Figure 1.3: Morphological differences between teosinte and maize.** *Zea mays*, commonly known as corn or maize, was domesticated from the grass family known as teosintes. **A)** While teosintes produce many branches with multiple ears—the grain-bearing parts of cereal plants—on each branch, maize has fewer branches with a single ear on each branch. **B)** Selection for larger fruits has led maize to produce ears with exposed cases and many grains, contrasting with the enclosed cases and few grains in teosintes. Image adapted from [Yang et al., 2019].

Domestication of previously wild plants has arguably been one of the most significant technological developments in the history of our species [Flannery, 1973]. Dating back at least 12.000 years, such an innovation occurred almost simultaneously in diverse regions across the world [Zeder, 2008]. At around 9.500 BC, the Middle East saw the birth of crops such as wheat, barley, peas, or lentils [Zeder, 2011]; in China, rice may have been domesticated as early as 11.500 BC [Molina et al., 2011], while by 8.000 BC, potatoes were probably being cultivated in Mesoamerica [Spooner et al., 2005]. Cultivating these plants

close to settlements paved the way to a significant societal shift, the echoes of which have reverberated up to this day. The population grew around villages where food was readily available, leading to a division of labour and setting the stage for most of the social structures we know today. Out of agriculture, civilizations thrived. This new societal configuration facilitated by the rise of agriculture created a niche for specialized people, who were fortunate enough to spend their time, not in the field but the coziness of their homes musing about the cosmos, nature, or society. Among those were the first economic and political thinkers, the first philosophers, and the first scientists. Plants, being such a cornerstone for survival, were undoubtedly in the minds of those early humans.

Documented accounts on plant classification appear as early as 1.500 BC in a collection of Vedic Sanskrit hymns known as the Rigveda, where plants are classified into trees, herbs with some utility to humans and creeper plants, with additional subclasses in each of them [Morton, 1981]. The ancient Greeks were among the first who left exhaustive documented reports on the idiosyncrasies of the natural world, and on plants in particular. In the 4th century BC, among Aristotle's (384 – 322 BC) writings on biology—the first in the history of science—were accounts on the systematics of plants, but none of them has made it to this day [Day, 2013]. The first surviving works on plant studies come from one of Aristotle's students, Theophrastus (371 – 287 BC)—called the "father of botany"—published under the name of *Historia Plantarum* (Enquiry into Plants) and *De causis plantarum* (On the Causes of Plants). In those books, Theophrastus described over 500 plant species, and classified them according to their usage, their localities, how they reproduced or their physical structure. While this classification was far from formal, but based on folk knowledge, they constituted the most important sources of botanical science, including plant anatomy, physiology, morphology and ecology, during antiquity [Morton, 1981]. Like many other ancient Greek works, Theophrastus' botany fell into oblivion during the early Middle Ages, and was only recovered in the 15th century when Greek manuscripts in the Vatican were translated into Latin by Theodorus Gaza (1398 – 1475 AD), a Byzantine Greek refugee, during the fall of the Byzantine Empire to the Ottomans [Schmitt, 1971]. Meanwhile, Islamic culture and science was thriving in the east, a renaissance reflected through the botanical works by figures such as Abu Hanifa Dinawari (828 – 896 AD), a Persian polymath known as the founder of Arabic botany, or Ibn Sina (980 – 1037 AD), one of the most renowned thinkers of the Islamic Golden Age [Fahd, 1996, Morton, 1981].

During the Renaissance, the rise of European powers such as the Portuguese or the Spanish empires fostered sea voyages of exploration and the creation of global trade networks which renewed interest in plants. Ships returned from newly discovered lands with exotic specimens unknown to the Old World. Plants such as tobacco and cocoa became highly coveted goods, together with spices,



**Figure 1.4: Plant illustrations by Joseph D. Hooker.** Illustrations of some of the plants described by Hooker in his voyages, included in the book *Flora Antarctica*, formally *The botany of the Antarctic voyage of H.M. discovery ships Erebus and Terror in the Years 1839-1843, under the Command of Captain Sir James Clark Ross*, published in parts between 1844 and 1859. **Left:** *Ranunculus insignis*. **Middle:** *Metrosideros robusta*. **Right:** *Africa sapida*. Images from the Biodiversity Heritage Library (https://www.flickr.com/photos/biodivlibrary/sets/72157679138207300/).

drugs and decorative species. The creation of botanical gardens with exotic and strange plants was a reflection of the empire's power, and fostered full-scale projects on plant systematics. Aristocrats, fascinated by the stories of those explorers, craved for a share of those commodities, and financed the voyages of botanical explorers and plant hunters [Reed, 1942]. It was at this age where the study of plants was beginning to establish itself as a bona fide profession, although only for the most resourceful. The British explorer Joseph Banks (1743 – 1820 AD), known as the chief botanist in the famous expedition of captain James Cook to the south Pacific Ocean from 1768 to 1771, belonged to this privileged lot [Gascoigne, 2011]. Among his achievements as a botanist, he is believed to have brought home over 30,000 plant specimens, of which around 1,400 were discovered by him [Gooley, 2012]. Banks corresponded with perhaps the most well-known naturalist of this period, Carl Linnaeus (1707 – 1778 AD), botanist, zoologist and taxonomist, who also wrote extensively on plant classification. His works include the books *Systema Naturae* (1735), *Genera Plantarum* (1737), *Philosophia Botanica* (1751) and *Species Plantarum* (1753), this last being the first to consistently use the binomial nomenclature which would later become the standard method for naming any living organism [Morton, 1981].

Well into the 19th century, another important figure who paved the way for transforming the status of botany as a respectable profession was Joseph Dalton Hooker (1817 – 1911 AD), famous for becoming one of Charles Darwin's (1809 –

1882 AD) closest friends, with whom he corresponded frequently and advised in the long process of the publication of the *Origin of Species* (finally published in 1859) [Strager, 2016]. Hooker took part in the Ross expedition of the Antarctic between 1839 to 1843, collecting and studying plants who would become the object of his massive treatise on Antarctic findings, the *Flora Antarctica* (Figure 1.4), published in parts between 1844 and 1859, and one of the first endorsements of Darwin's theory of natural selection, at a time when those ideas were still unknown to the plubic [van Wyhe, 2007]. After the voyage, Hooker struggled for years in search for a paid position who would allow him pursue his passion for botany. Through minor works with several private collectors—the role of which is often ignored in the development of Victorian natural history—he slowly established himself as a respected, professional botanist [Endersby, 2001]. Hooker grew from a young creationist to a fierce defender of Darwin's theory, to the point of partaking, together with Thomas H. Huxley (1825 – 1895 AD), on Darwin's side in the infamous 1860 Oxford evolution debate, against the bishop Samuel Wilberforce (1805 – 1873 AD), which opposed to Darwin's theory in favour of a creationist view of life on Earth [McCalman, 2009]. As the story goes, Hooker's close friendship with Darwin let to giving him a copy of *Flora Antarctica*. In a letter in November 1845, Darwin wrote to Hooker that the geographical distribution of organisms would be "the key which will unlock the mystery of species" [1] As is well-known, Darwin eventually published the *Origin of Species* in 1859, after working extensively on coral reefs and barnacles, and continually gathering evidence likely in fear of the uproar his ideas could cause. After the *Origin*, the tone of Darwin's books became filled with evolutionary ideas. Among those, many were about plants, including his 1862 *Fertilisation of Orchids*, in which he explored the intricate interactions between the plant and pollinator insects, demonstrating the power of natural selection to explain complex ecological relationships; his 1875 *Insectivorous Plants*, in which the remarkable adaptations of carnivorous plants were studied; or *The Power of Movement in Plants* (1880), were he explored how plants responded to external stimuli with the aspiration of disclosing universal principles underlying their growth and motion [Desmond and Moore, 1992] (Figure 1.5).

In 1865, unbeknownst to Darwin, a monk in Brno (then belonging to the Margraviate of Moravia, one of the Lands of the Bohemian Crown) by the name of Gregor Mendel (1822 – 1884 AD) was laying down the foundations of what would become modern genetics. With his inheritance experiments with peas, Mendel proposed an alternative to blending inheritance, which was the prevailing theory at the time. Mendel's work, save a few favourable reports in local newspapers, received little attention from the scientific community and fell into oblivion for almost forty years [Henig, 2001]. It was not until the early

[1] Letter from C. R. Darwin to J. D. Hooker [5 or 12 November 1845] (MS DAR 114: 45), University of Cambridge Digital Library (http://cudl.lib.cam.ac.uk/view/MS-DAR-00114-00045/1).

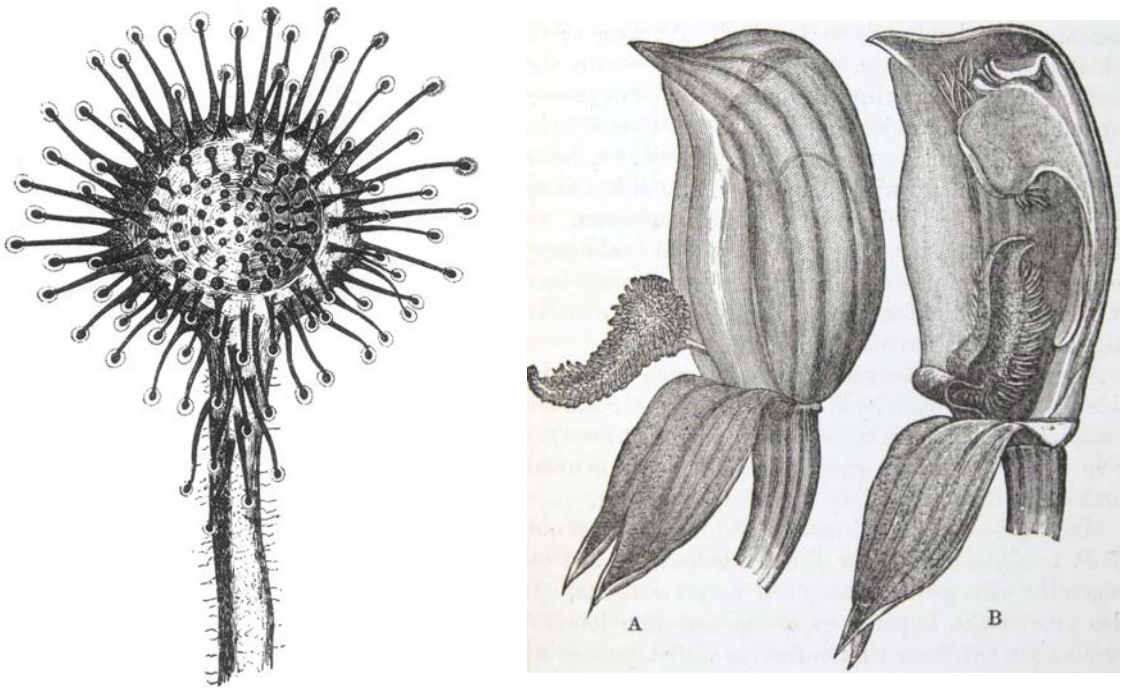



**Figure 1.5: Illustrations from Charles Darwin's books on plants. Left:** Drawing of the carnivorous plant *Drosera rotundifolia*, the common sundew, belonging to *Insectivorous Plants* (1875). Insects are attracted and get stuck to the mucilage covered leaves, from which the plant can then feed upon. **Right:** Drawing of the orchid *Pterostylis longifolia*, the common leafy greenhood, from the book *Fertilisation of Orchids* (1862). Panel A shows the flower in its natural state, while in panel B the lateral petal is removed, displaying the flower's interior.

20th century that Mendel's work was rediscovered independently by Hugo de Vries, Carl Correns and Erich von Tschermak, an occurrence that set in motion a series of seminal works on population genetics by giants like Ronald Fisher and J.B.S. Haldane, which wed the ideas of Darwin with the newly salvaged inheritance rules of Mendel [Gayon, 2016].

The early 20th century saw the rebirth of genetics, which put the new science on quantitative grounds. Again, plants had a big role to play in this unfolding. In the first half of the 20th century, Barbara McClintock (1902 – 1992 AD) studied the dynamics of chromosomes during reproduction in maize, and together with Harriet Creighton (1909 – 2004 AD), put forward the notion of genetic recombination by crossing-over during cell division. In the 40s and 50s, again using maize as a preferred organism, she uncovered the existence of transposable elements, segments of DNA that are able to change their position within the genome, and used them to demonstrate that genes were indeed the elements determining physical traits [Keller and McClintock, 1983].

During the first half of the 20th century, plants were also involved in one of the darkest chapters in the history of genetics, a period where sound science was eclipsed by radical ideology, leading to the death of millions. Under Stalin's

regime, the USSR saw the collapse of virtually all scientific disciplines, of which genetics was particularly had hit. In the 20s and 30s, many Soviet scientists who embraced the newly born science of genetics—which highlighted the fixity of physical traits, encoded by genes—were publicly denounced as enemies of the state, being dismissed, imprisoned, or directly executed in a campaign to silence scientific ideas that clashed with the government's ideals [Soyfer, 2001]. Among the prosecuted was Nikolai Vavilov (1887 – 1943 AD), botanist, agronomist, president of the Soviet Agriculture Academy and founder of the Leningrad seed bank—by then the world's largest collection of plant seeds—who worked extensively on the biogeography and evolutionary history of crop plants, and who devoted most part of his life to improve crop yields such as maize or wheat in a ambitious crusade to feed a rapidly increasing world population [Cohen, 1991]. This campaign against "bourgeois science" was led by Trofim Lysenko (1898 – 1976 AD), also a botanist and agronomist by training, who had once been encouraged by Vavilov to perform his experiments on the effects of temperature in wheat [Joravsky, 1986]. Lysenko, under Stalin's protection, rejected natural selection and Mendelian genetics, in favour of an approach more sympathetic to the Marxist premises that neither nature nor society were fixed, but changeable [Joravsky, 1986]. With this Lamarckian stance, Lysenko claimed he could create new wheat varieties and increase crop yields by changing environmental conditions, most notably through vernalization—the change in the plant's flowering time via the prolonged exposure to cold [Leone, 1952]. Lysenko's ideas—which were largely based on falsified data—came at a time when drought and famine was hitting most of the USSR regions. Out of despair, and seeing an opportunity to push their political agenda, the Soviet government rapidly adopted Lysenko's program, a decision which led to a widespread loss of crop yields and the dying of millions[1] [Soyfer, 2001].

But political matters aside, the 20th century has also been an exceptionally fruitful period for plant science. Thanks to the development of molecular biology, we have seen the discovery of plant hormones, including auxins, gibberellins, cytokinins and ethylene [Thimann, 1974], as well as the more recently discovered brassinosteroids or jasmonates [Weyers and Paterson, 2001]; we improved our understanding of molecular nature of photosynthesis [Hohmann-Marriott and Blankenship, 2011], the processes involved in gravitropism [Swarup et al., 2005] or the mechanisms underlying flowering morphogenesis [Haughn and

[1] As a disclaimer, remark that this account is heavily Eurocentric, as most historical accounts are. As such, this does not mean that botany was absent in major nations such as China. On the contrary, traditional Chinese medicine, for instance, relied heavily on a good understanding of plants. Nevertheless, Chinese botany as a proper science did not kickstart since the beginning of the 20th century, with people such as Hu Xiansu (1898 – 1976 AD), considered the founding father of plant taxonomy in China. As an amusing side-note, Hu was a strong critic of the agricultural practices of Lysenko, a position which led to the banning of his works, as well as preventing his entering in the Chinese Academy of Sciences [Hu and Ma, 2021].

Somerville, 1988].

Today, plant science constitutes a tool to fight two of the most critical problems of our time: unequal food availabiliy and climate change. As of 2019, it is estimated that $\sim$ 8.9% of the world's population (roughly 690 million people) are underfed [FAO et al., 2020], a figure which varies disproportionately across countries. Moreover, over two billion people ($\sim$ 25.9% of the world's population) do not have regular access to food. In 2015, over 406,000 people died from causes related to nutritional deficiencies [Mortality and of Death Collaborators, 2016]. Crop improvements driven by conceptual and technological advances in plant breeding might help to ameliorate such challenges, specially in light of the rapidly increasing global population [Gupta et al., 2020]. Breeding crops that produce higher yields and are resistant to increasingly extreme climate conditions will surely help in the quest to end world hunger [Hickey et al., 2019]. However, the problem will not be solved by science alone. At most, it can mitigate an issue which is political at its root. Severe decisions must be made that threaten the very foundations of a capitalist world, a system which feeds on human inequality and thrives because of it.

On this line, climate change is probably the most imminent threat our species has had to face upon. The levels of $CO_2$ we pour into the atmosphere keep rising, despite the alleged changes in policies to reduce our environmental impact. Rising $CO_2$ concentrations lead to increasing temperatures which in turn cause increasing concentrations of carbon dioxide, in a positive feedback loop which can lead to sharp, irreversible transitions [Solomon et al., 2009, Scheffer et al., 2009]. The evidence strongly suggests that we are approaching one of such transitions, as revealed by early warning signs such as critical slowing down, which translates in a reduction of recovering time after perturbations, or noise amplification, reflected in increasingly abundant extreme meteorological phenomena [Barnosky et al., 2012, Lenton, 2011]. Most of the energy from fossil fuels we release into the atmosphere come from the carbon plants—specially trees—captured millions of years ago to build themselves. Today's forests, and in particular large tropical rainforests such as those in the Amazon and Congo basins, and those covering most of Indonesia, are the major carbon sinks of our planet [Pan et al., 2011]. As we are well aware, deforestation of these regions has led not only to the loss of carbon sinks, but to a dramatic decrease in biodiversity as well [Giam, 2017, Barlow et al., 2016]. Reforestation and plant-based carbon capture strategies have been proposed as solutions to these problems, that would help to slow down the increasingly higher levels of $CO_2$ as well as to mitigate the already irreversible damages caused by ecosystem destruction [Griscom et al., 2017], although some of these ideas have been recently called into question [Popkin, 2019]. Switching to a plant-based diet may also help fighting the climate crisis [Stehfest et al., 2009]. The impact of animal products, including meat, fish, eggs and dairy, largely exceed those of their plant-based counterparts, contributing to $\sim$ 83% of land use, $\sim$ 58% of green-

house gas emissions, yet only providing $\sim 37\%$ of our protein and $\sim 18\%$ of our calories [Poore and Nemecek, 2018]. Reducing the consumption of animal-based products in favour of those plant-based would not only reduce our environmental footprint, but also the economic costs of maintaining the suboptimal system that is the meat industry; it would help in the advocacy of animal welfare and contribute in preventing health problems associated with diets with excess consumption of animal products [Godfray et al., 2018].

But again, these are only partial solutions to a problem which has to be solved through political action, through a change in the very structure of the economy which must include penalties to the misuse of fossil fuels, fostering and cheapen the cost of renewable energies, but specially by taking away the power of private multinationals, which as we know are the main contributors of such a crisis. Only a global social change will permit tackling this problems effectively.

Whatever happens in this uncertain future, plants will surely be fine; they will keep dominating most Earth ecosystems, in close connection with bacteria, animals and fungi, providing shelter to some, food to others, and constantly reinforcing their mutual relations in the delicate harmony of the biosphere. The world is a plant world.

# Chapter 2

# General introduction

## Contents


**2.1 Rooting systems in *A. thaliana* and *M. polymorpha* . 15**
2.1.1 Root development in *A. thaliana* . . . . . 20
2.1.2 Rhizoid formation in *M. polymorpha* . . . . . 21
**2.2 Patterns in biology . . . . . 23**


This chapter aims to present the main topics discussed in this thesis. We begin with a casual opening about the evolution of rooting systems, which acts as the anchor to introduce the two model plants *Arabidopsis thaliana*, easily the most well-studied organism in plant genetics and the main topic of Part II (Chapter 4 and Chapter 5), and its evolutionarily distant cousin *Marchantia polymorpha*, a more modestly studied model organism whose epidermal cellular patterns form the basis of study of the first chapter of Part III (Chapter 6). We next shift to a more general introduction about pattern formation, commenting on its historical relevance on developmental biology, its generative mechanisms and its uses throughout this thesis. This last section serves as a conceptual framework for Part III, where we study rhizoid patterns in the *Marchantia* epidermis (Chapter 6), and a simple, multi-functional circuit which is capable of displaying a diverse repertoire of spatiotemporal behaviours, including oscillations, pattern formation and their coexistence (Chapter 7).

## 2.1 Rooting systems in *A. thaliana* and *M. polymorpha*

The Cambrian period (∼541–485 mya) witnessed one of the most critical evolutionary transitions in the history of the Earth. It owes its popularity to the sudden rise of multicellular life after almost three billion years of unicellular supremacy [Gould, 1994]. While the animal kingdom probably appeared earlier—the oldest known fossils date back to 635 million years, right at the

boundary between the Cryogenian (∼720–635 mya) and the Ediacaran (∼635–541 mya) [Maloof et al., 2010]—it was not until the Cambrian when most of the animal body plans we see today appeared, giving rise to an unprecedented diversity of which the fossil record, many of which unearthed in the exceptional deposits of the Burgess Shale[1], in the rims of British Columbia Rocky Mountains, is testimony [Gould, 1989]. Archetypical depictions of this "Cambrian explosion" feature, among other creatures, the famous trilobites, who reigned the Cambrian seas and left an extensive fossil record due to their hard exoskeleton; the shrimp-like arthropod *Anomalocaris* (literally "abnormal shrimp"), whose long mouth appendages and a body extending up to half a meter placed it at the very top of the Cambrian food chain; the *Pikaia*, a flat writhing creature whose possession of a notochord would eventually make it a far relative to our own species; or the bizarre *Hallucigenia*, a small spiny monster who crawled the sea bed in search for easy food, scavenging for dead bodies of lesser organisms, perhaps a leftover prey of a satiated *Anomalocaris* (Figure 2.1).

But of all the awe that might inspire the remains of a long lost world, a common theme emerges in most popular depictions of Cambrian life, one that is conspicuous by its absence: the lack of plants and algae. While this might be a bit unfair for algae—as multicellular algae were already thriving much earlier[2]—the fact is that land plants did not appear until the middle Cambrian and Early Ordovician (485–444 mya) [Morris et al., 2018], where the oldest known fossils have been found [Wellman et al., 2003]. This epoch saw a group of plants leaving warm and cozy waters and venturing into the unknown, initially hostile environments of land [Kenrick and Crane, 1997, Fürst-Jansen et al., 2020]. These first dwellers were probably descendants of streptophyte algae, who lived in fresh, shallow waters, and who were at least partially accustomed to the otherwise detrimental effects of temperature variation, high levels of ultra-violet radiation and seasonal dehydration [Becker and Marin, 2009] (Figure 2.2). This lead to a progressive adaptation from freshwater, to moist terrains, to the eventual colonization of dry land, which demanded a complete reliance on rainwater [de Vries and Archibald, 2018].

Early evolution of plants on land involved a myriad of innovations so as to cope with the unexplored conditions of terrestrial environments. One of the most decisive of these evolutionary novelties was the appearance of rooting sys-

[1]Other less known but equally important Cambrian deposits include the Emu Bay Shale in South Australia or the Maotianshan Shales in the Yunnan province of China. The Burgess Shale gained fame after the success of Stephen J. Gould's 1989 book *Wonderful Life: The Burgess Shale and the Nature of History* [Gould, 1989], who made it to the top of the US bestseller lists. Quite a feat, to be sure, for a popular science book.

[2]Multicellular algae trace back its origins several million years before the Cambrian. The earliest known evidence for the presence of green algae comes from one-billion year old fossilized remains of an organism hernceforth christened as *Proterocladus antiquus* [Tang et al., 2020]. The lineage of red algae is much older, going back to 1.6 billion years ago, after the recent discovery of *Rafatazmia chitrakootensis* fossils [Bengtson et al., 2017].

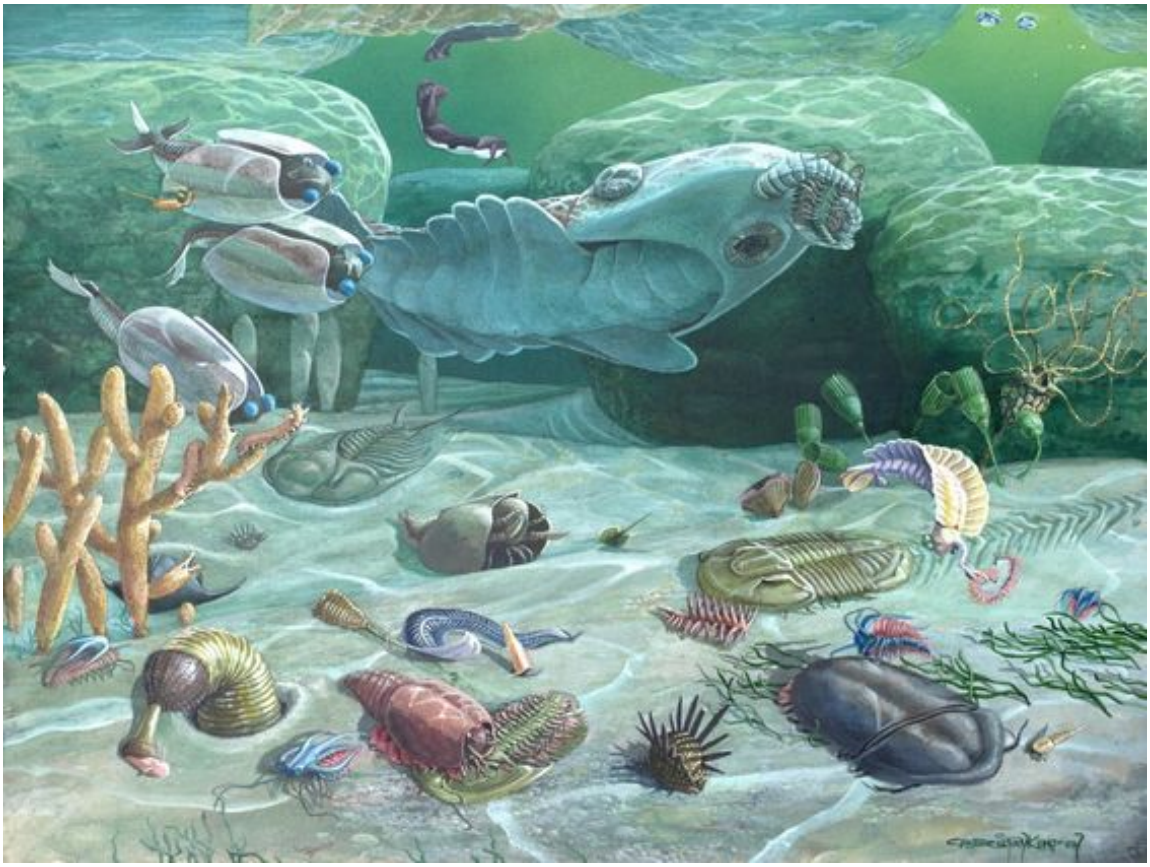


**Figure 2.1: Fauna of the Cambrian.** Illustration of some of the organisms found in the Cambrian deposits of the Burgess Shale. Notice that only few algae appear, a common practice in most artistic depictions of Cambrian life. Artwork: Burgess Shale Fauna (1989) by Carel Pieter Brest van Kempen (http://www.cpbrestvankempen.com/)

tems, which involved dramatic structural changes for plants to maintain proper anchorage to the soil, optimal water uptake and nutrient acquisition [Bateman et al., 1992, Kenrick and Crane, 1997]. At the interface between the plant main body and the substrate to which it is attached, some cells protruded from epidermal tissues forming long, thin outgrowths extending distally from the main plant body and into the soil, effectively increasing the total surface area for water and nutrient absorption. These first rooting systems consisted of simple filamentous structures called rhizoids, and were probably inherited from earlier adaptations from land plants' algal ancestors [Kenrick and Strullu-Derrien, 2014] (Figure 2.3). Rhizoid-like structures have been found among the Rhynie chert fossils—fossil deposits from the Lower Devonian with exceptionally preserved plants—and seem to have been present in early vascular plants [Hetherington and Dolan, 2018a].

These rhizoids can be seen today in most bryophytes, which emerge from single cells in hornworts and liverworts but can consist of multicellular composites in mosses [Frangedakis et al., 2021]. The fossil evidence strongly suggests that rhizoid-based rooting systems preceded true roots, the earliest evidence of which

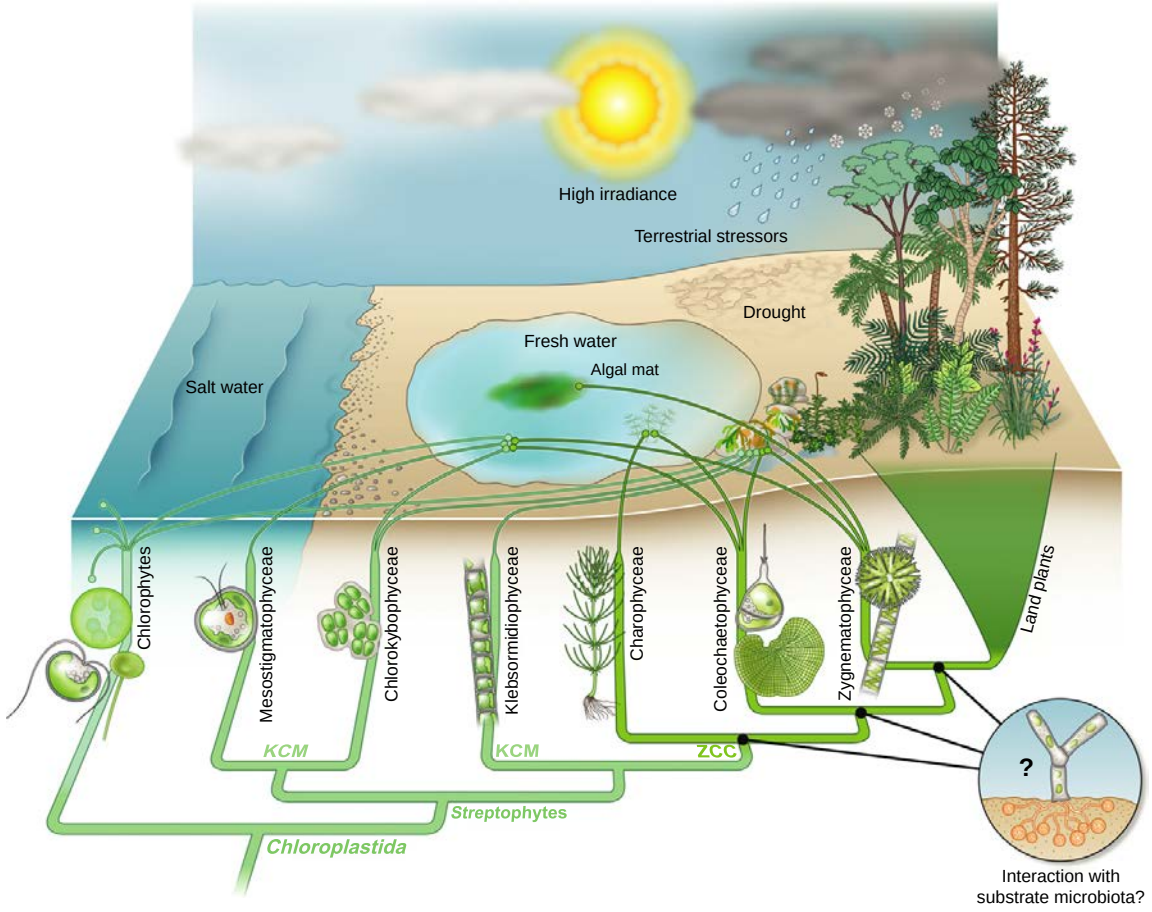



**Figure 2.2: Early evolution of land plants.** The first land plants descended from streptophyte algae, who split from Chloroplastida about 1 billion years ago, and they lived in fresh waters or in moist habitats, such as wet soils and rocks. The transition from water to land was progressive, and involved a plethora of physiological changes so as to endure the stresses brought by the terrestrial environment, such as large temperature fluctuations, drought or high irradiance from the sun. Image adapted from [de Vries and Archibald, 2018].

points to their appearence at $\sim$ 407 Mya, also among Rhynie chert fossils [Hetherington and Dolan, 2018b]. Contrary to rhizoid-based rooting systems, roots consist of larger multicellular protuberances characterized by distinctive trademarks such as gravitropic responses, which allows the plant to grow downwards into the soil; endogenous branching, to increase its effective surface for proper anchorage and nutrient and water acquisition; root hairs, unicellular protrusions which extend perpendicularly to the root and contribute in the anchoring functions; and a root cap which protects the sensitive tissue of the root tip and is also involved in gravity perception [Kenrick and Strullu-Derrien, 2014]. Roots are a hallmark of vascular plants, allowing them to grow taller than their bryophyte cousins, which usually remain small and close to the surface. Moreover, the emergence of roots had major impacts on ecosystems, specially by stabilizing soils and preventing their erosion, and as critical elements in plant-fungi and

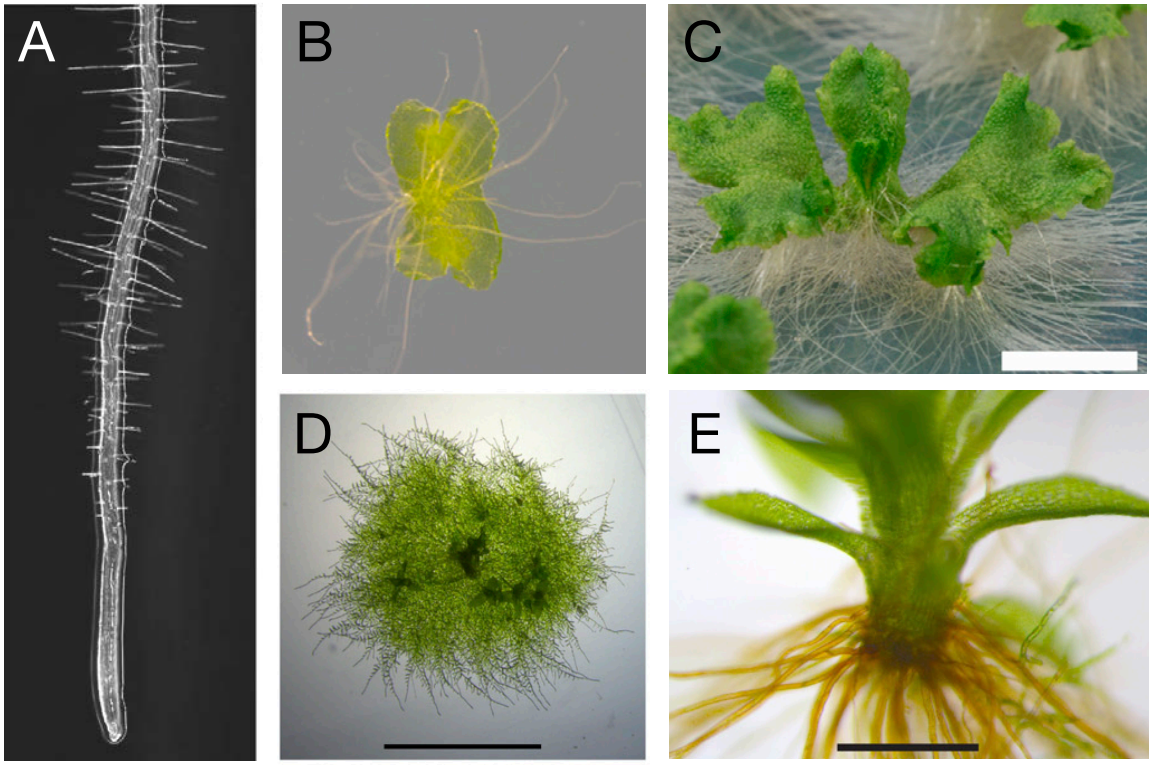



**Figure 2.3: Roots, root hairs and rhizoids.** **A)** Root with root hairs in *Arabidopsis thaliana* (adapted from [Shibata and Sugimoto, 2019]). **B,C)** Rhizoids in the liverwort *Marchantia polymorpha* in two developmental stages (adapted from [Proust et al., 2016]). **D,E)** Rhizoids in the moss *Physcomitrella patens* in two distinct developmental stages (adapted from [Tam et al., 2015]).

plant-bacteria symbioses [Kenrick and Strullu-Derrien, 2014].

Proper development of roots (in vascular plants) and rhizoids (in bryophytes) is crucial for the survival of the plant. Knowing which factors are involved in their formation and maintenance, as well as the specific interactions between them, is therefore of uppermost importance to understand their role as crucial organs of the plant. Roots have been extensively studied mainly in *Arabidopsis*, owing to its status as quintessential model organism in the plant community [Grierson et al., 2014]. The study of rhizoids, for its part, has traditionally remained in the background. Only recently, with the renewed interest in understanding the evolution of plants on land [Kenrick, 2017], and the subsequent sequencing of new model organisms such as *Marchantia polymorpha* or *Physcomitrella patens* [Jones and Dolan, 2012, Cao et al., 2014, Bowman, 2017, Sakakibara et al., 2003, Jang et al., 2011], has the interest in rhizoids increased. In this thesis we are concerned with processes involved in root development in *Arabidopsis* and in rhizoid formation in *Marchantia*. In the following sections we outline the major goals of this work and its underlying motivations.

### 2.1.1 Root development in *A. thaliana*

Advances in root development have progressed considerably through their study in *Arabidopsis*, thanks to its relatively simple cellular organization—exhibiting a stereotypical radial pattern—and easy manipulation and visualization, which allows to robustly track and control the different cell types [Dolan et al., 1993, Petricka et al., 2012]. After germination, the *Arabidopsis* embryo undergoes a series of cellular divisions and rearrangements which establish the apical-basal polarity, with the emergence of what will become the shoot apical meristem at the top and the root apical meristem at the bottom (Figure 2.4A). During embryogenesis, these meristems supply the growing root and shoot with new cells that will eventually form all surrounding tissues [Perilli et al., 2012]. In the seedling, at the tip of the root a small group of pluripotent, rarely dividing cells called the quiescent center (QC) keeps its surrounding stem cells from differentiating through short-range signals, ensuring that after each division only one of the daughter cells becomes disattached from the QC and differentiates [van den Berg et al., 1997, Liu et al., 2017]. The QC, together with the surrounding stem cells form the so called stem cell niche (SCN). The cells of the SCN will be the precursors of all root tissues.

Extending shootwards and laterally, these cells will belong to the vasculature, endodermis, cortex, epidermis and lateral root cap, whereas those facing rootwards will become columella cells (Figure 2.4). The identity of these different cell types is mediated by a myriad of signals, including plant hormones, transcription factors, small peptides, microRNAs and reactive oxygen species. Specifically, positional information conferred by auxin signalling is thought to play a major role in establishing the precise location of the SCN [van den Berg et al., 1995, Kidner et al., 2000]. This positioning further involves several overlapping transcription factors, including SCARECROW (SCR) and SHORTROOT (SHR), as well as PLETHORA (PLT) activated by a peak in auxin levels at the SCN [Shimotohno et al., 2018]. It is argued that this positional signalling confers the necessary plasticity to establish a new niche when it has been destroyed or damaged, by virtue of a continual supply and renewal of stem cells at the very same location [Sena et al., 2009]. Knowing the origin and function of these signals, and how they interact in complex gene regulatory networks to control cellular identities is therefore essential to understand the role of stem cells in the processes underlying organism development and sustenance.

In Part II of this thesis (Chapter 4 and Chapter 5), we specifically focus on two factors controlling the division of QC cells. As already stated, QC cells divide infrequently, but the specific molecular mechanisms by which quiescence is controlled still remain elusive. While many factors are known to affect the frequency of QC division, our focus is on two stem cell-specific transcription factors, BRAVO and WOX5, which independently have been shown to promote QC quiescence. In Chapter 4, through our mathematical approaches and exper-

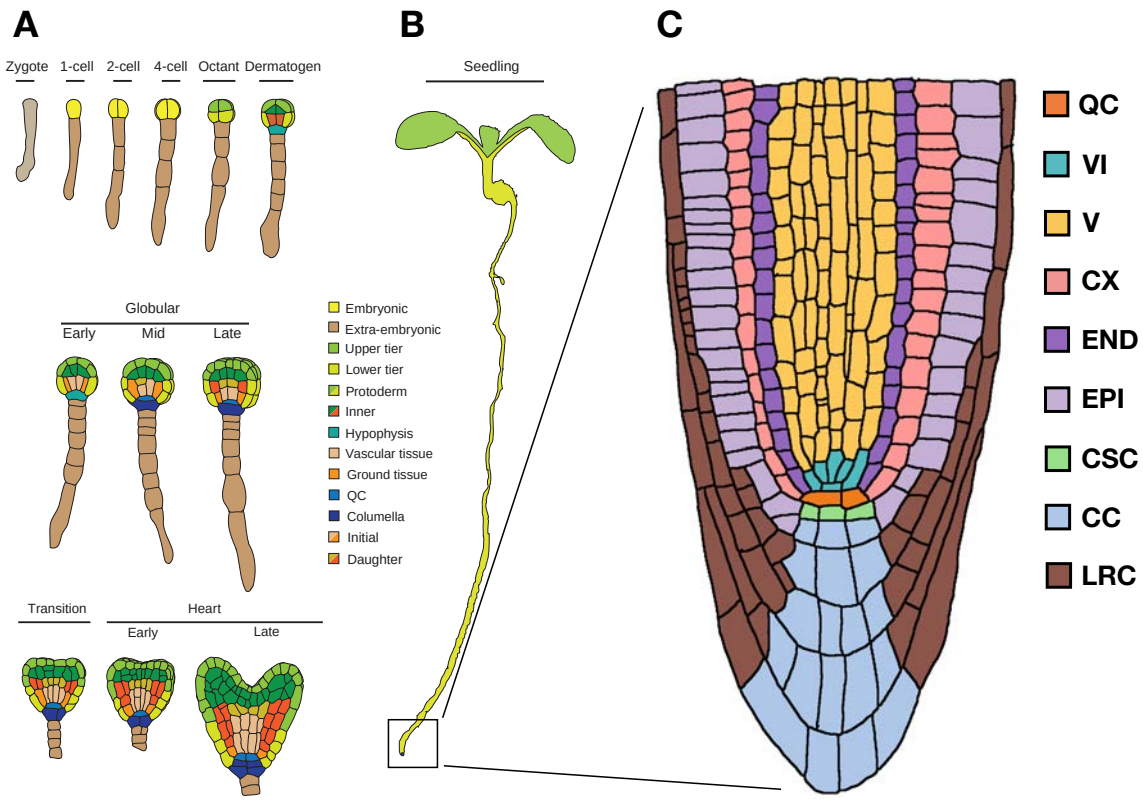



**Figure 2.4: Initial stages of *Arabidopsis* development and root structure. A)** From an initial zygote, embryonic development in *Arabidopsis* involves a series of assymetric cell division which define the apical-basal axes, from which the shoot and the primary root emerge. **B)** Seedling, with the shoot apical meristem at the top, and the root apical mersitem at the tip of the root. **C)** The organization of cell-types in the root apical meristem includes the quiescent center (QC), vascular initials (V), vascular cells (V), cortex (CX), endodermis (END), epidermis (EPI), columella stem cells (CSC), columella cells (CC), lateral root cap (LRC). Panels **A)** and **B)** adapted from [ten Hove et al., 2015].

imental data from our collaborators, we study in detail the molecular interactions between the two, revealing a regulatory circuit which is able to recapitulate promoter activities in both WT and mutant backgrounds. The structure of the BRAVO-WOX5 circuit further allows us to propose a specific way for the two factors to control QC division. Still, this chapter does not address the fact that their regulations are embedded in space, where the cellular structure of the root may play an important role. To tackle this problem, in Chapter 5 we extend the models of Chapter 4 to include spatial effects, where we include the movement of some of the regulating factors and show how it constitutes a key ingredient for explaining the expression patterns of BRAVO in the root.

### 2.1.2 Rhizoid formation in *M. polymorpha*

The thalloid liverwort *Marchantia polymopha* has recently emerged as an exceptional model organism to study the adaptations that made the transition of

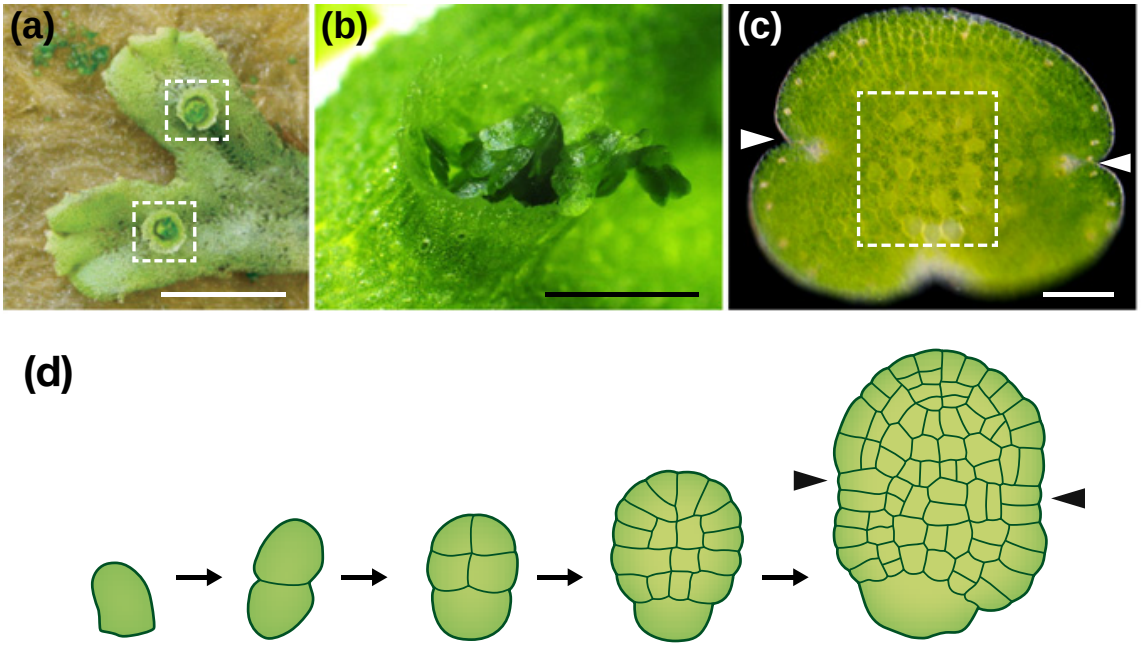



**Figure 2.5: Gemma development in *Marchantia*.** **(a)** Gemma cups in the thallus. **(b)** Gemma cup showing the emergence of a new gemma. **(c)** Mature gemma on the first day after germination, showing rhizoid precursors (pale cells) beginning to differentiate from a field of epidermal cells. Arrows indicate the two notches, where the apical meristems reside. **(d)** The development of a gemma from a single cell. Arrows indicate where the future notches, and subsequently the apical meristems, will appear. Figure adapted from [Kato et al., 2020].

plants from water to land possible [Bowman, 2017], a status owed by its small genome, relatively short life cycle, as well as its easy-to-cross nature [Ishizaki et al., 2016]. The development of *Marchantia* consists of a diploid phase and a multicellular haploid sporophyte phase, a feature common in all land plants which was crucial for the transition from water to land. The multicellular phase, also called the thallus, grows from an unicellular spore that germinates and forms an initial short filamentous structure called protonema, together with attached rhizoids. As cells in the protonema divide, apical meristems are formed through a series of bifurcations, until reaching the form of a full-grown thallus. As the thallus further develops, cup-shaped organs named gemma cups harbour small clonal propagules called gemmae (Figure 2.5), which can then be dispersed for new thalli to develop [Kato et al., 2020, Chang et al., 2016].

Cells in the gemma epidermis are specified the first day after germination. Most of these will become epidermal cells, while some will differentiate into rhizoid precursor cells. These rhizoid precursors are specified from a field of initially equivalent epidermal cells, and eventually producing tip-growing projections that penetrate the growth substrate and carry out rooting function [Cao et al., 2014]. Some genetic factors controlling rhizoid precursor specification have been identified, and shown to be conserved in many land plants [Menand et al., 2007, Tam et al., 2015, Proust et al., 2016, Honkanen et al., 2016]. How-

ever, the mechanisms underlying the patterning of rhizoids in the epidermis remain unknown.

Recent experiments have shed some light on how the spatial distribution of rhizoids is regulated, with the action of the microRNA FRH1 on the rhizoid-promoting factor RSL1 being a crucial ingredient [Proust et al., 2016, Thamm et al., 2020]. In particular, these experiments have shown that before elongation, rhizoid precursors form distinctive patterns, appearing either as isolated cells surrounded by epidermal cells or forming small, filamentous clusters. A detailed analysis of these patterns has revealed that lateral inhibition—where signals from particular cells inhibit the very same signals in their adjacent neighbours—may be at play [Thamm et al., 2020]. How this lateral inhibition is mediated is still unknown, but the same authors propose that it can happen through the movement of the microRNA MpFRH1 [Thamm et al., 2020].

However, how the interactions between MpRSL1 and MpFRH1 lead to the specific distributions of rhizoids observed in the experiments remains unknown. Building on these experiments, and together with data from our collaborators, in the first chapter of Part III (Chapter 6) we propose a simple mathematical model for explaining the patterning of rhizoid precursors. The model has the form of an activator-inhibitor system, where the rhizoid-promoting factor RSL1 induces the synthesis of the microRNA FRH1, which in turn moves from cell to cell to non-cell-autonomously inhibit RSL1. Therefore, our approach provides a mechanistic interpretation for how lateral inhibition is implicated in specifying rhizoid precursor patterns.

Lateral inhibition interactions are known for its ability to generate periodic patterns in both plants and animals, a topic we will explore in the next section and that will serve as a bedrock for the topics explored in Part III. Since many of the mechanisms involved in the generation of patterns are quite general, this next section will present them in a very broad manner, emphasizing its range of applicability in both the developmental biology of plants, animals, as well other contexts such as microbiology or ecology.

## 2.2 Patterns in biology

Humans crave order; when we can not find it, we create it. With order in time, we predict the future; with order in space we see pattern and structure. That is how we make sense of the complexity of the world. We delight in the majesty of the perfectly built Giza pyramids, but ignore a pile of rocks randomly scattered across the desert. The second law of thermodynamics does not help in such a relentless quest. But beyond these banal human desires, biology has found a way to dodge the otherwise ill nature of the second law: being far from equilibrium. Through the continual interchange of energy and matter with the environment, biological systems can create order out of chaos, a self-organization without the need of any external guidance. Biological systems

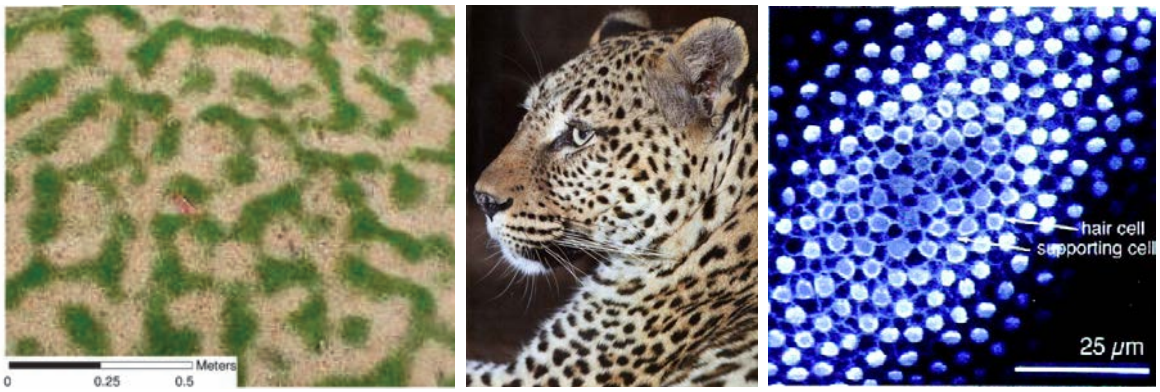



**Figure 2.6: Patterns in biology across scales. Left:** Vegetation patterns showing labyrinth-like patches of grass (adapted from [Rietkerk et al., 2004]). **Middle:** The spots of leopard skins (and of animal coats in general) are one of the archetypal pattern-displaying systems in biology (from [Murray, 1988]). **Right:** Salt-and-pepper patterns of Notch activity in the chick basilar papilla (from [Eddison et al., 2000]).

are not impaired by the second law; they thrive because of it. Animal coat patterns such as zebra stripes or leopard spots are archetypical examples of how far from equilibrium processes lead to the formation of ordered structures [Murray, 1988] (Figure 2.6). Patterns also appear at larger scales, such as in the spatial distribution of grass in semiarid ecosystems [Rietkerk et al., 2004], and at smaller scales, such as in the formation of vertebrate body segments [Hubaud and Pourquié, 2014, Pourquié, 2001] or in the emergence of digits in the developing limb, to name a few [Raspopovic et al., 2014]. The existence of these ordered patterns in natural phenomena has long intrigued biologists, and explaining their origin one of the outstanding questions in biology. Of particular interest has been pattern formation in the context of organismal development—our main interest in this thesis—a topic which across history caught the attention of many well-known scholars, including the very same Theophrastus, which noted the regularities in the position of leaves in plant stems; Leonardo da Vinci and Johannes Kepler, who identified the presence of the Fibonacci sequence in the arrangement of leaves from many plants; or Ernst Haeckel, who studied the symmetries of radiolarians and diatoms, and whose drawings still serve as an inspiration for today's naturalists and scientific illustrators [Livio, 2003].

Be that as it may, the formation of patterns in development was not put on formal grounds until the beginning of the 20th century, with works such as D'Arcy Thompson's massive *Of Growth and Form* [Thompson, 1992], where he went on to explain the shapes and structures of animals and plants not by invoking mystical forces, but through physical principles, making the book one of the pioneering works of mathematical biology [Ball, 2009, Ball, 2013]. By the mid 20th century, a young English mathematician was bound to revolutionize how we think about the self-organization of matter. In 1952, Alan

Turing published *The chemical basis of morphogenesis* [Turing, 1952], a pioneering paper that laid the ground for what would be one of the great revolutions of theoretical biology. It transformed the way we think about morphogenesis, or how shapes and patterns can spontaneously emerge from purely physical or chemical processes. Turing's original idea was that differential diffusion of two chemical species (what he called *morphogens*) could lead to an instability of a spatially homogeneous state, leading to the emergence of periodic patterns (Figure 2.7). In a more biological context, such morphogens would be the informational guides for initially identical cells to become different types within a tissue, their specific characteristics determining whether a cell becomes, say, a neuron or a skin cell. Before Turing's insight, diffusion was seen as an homogenizing force, a macroscopic phenomenon arising from the random motion of particles and molecules. Diffusion, it was thought, acted as a steadying mechanism, making nearby regions in space to blend towards equilibrium, as happens with the diffusion of air molecules in a room when flows with different temperatures mix. Initially, Turing's ideas would be largely ignored among biologists, for another infamous paper came to light just a year later, leaving Turing in the shade: *Molecular structure of nucleic acids: a structure for deoxyribose nucleic acid* by James Watson and Francis Crick [Watson and Crick, 1953], owing to the experimental work of Rosalind Franklin and Maurice Wilkins. The uproar caused by the discovery of the structure of DNA led many biologists to engage in the quest to disclose the mysteries of the genetic code, and to decipher the various mechanisms involved in gene regulation. In the upcoming years after Turing's publication, pattern formation was largely neglected, displaced by the fancy methods of the now well-established science of molecular biology [Nanjundiah, 2003]. But there were exceptions to the rule: one of the few people who got interested in Turing's ideas was, incidentally, a botanist. C. W. Wardlow was a professor based on Manchester—the same university Turing was professor—and was, at that time, interested in plant morphogenesis, with particular preference to understand phyllotaxis. Turing's work was saved from being forgotten in part thanks to Wardlow's *Organization and Evolution in Plants* (1965) and the work of one of the most prominent biologists of the 20th century, Conrad H. Waddington, who discussed Turing's ideas in his 1963 *New Patterns in Genetics and Development* [Saunders, 1993].

As the computational power of computers increased in the late 60s and early 70s, simulations of Turing systems began to shed light on particular molecular mechanisms by which patterns could emerge. In 1972, Gierer and Meinhardt identified a subset of systems which were able to generate patterns *à la* Turing, which involved a short range activator and a long range inhibitor [Meinhardt and Gierer, 1972]. Activator-inhibitor systems have since then become the archetypical pattern generating systems [Meinhardt and Gierer, 2000], being the basis for understanding the distribution of feathers in birds [Harris et al., 2005], the spacing of hair follicles in mice [Sick et al., 2006] or pigmentation

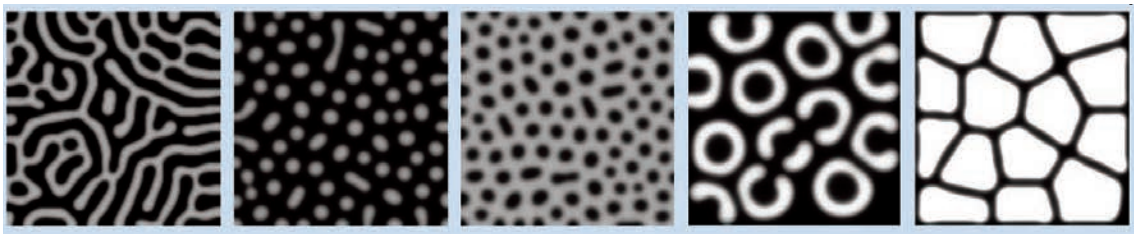


**Figure 2.7: Reaction-diffusion Turing patterns.** Archetypical patterns generated by the same reaction-diffusion equations Turing used in his original paper. These include labyrinthic stripes, spots, rings or cells, each arising in different regions of parameter space. Image adapted from Figure 2B in [Kondo and Miura, 2010].

patterns in flowers [Ding et al., 2020]. However, activator-inhibitor systems do not hold exclusive privilege for pattern generating ability. Others include activator-depletion systems—also advanced by Gierer and Meinhardt—, where in the place of an inhibitor there is a substrate which can be depleted [Meinhardt and Gierer, 1972], or mass-conserving systems, where patterns emerge due to a spatial redistribution of conserved quantities [Halatek et al., 2018]. These have been proposed as better models for explaining, for example, intercellular pattern formation, such as in the oscillatory Min system in *E. coli* [Meinhardt and de Boer, 2001, Loose et al., 2008].

While Turing patterns provided a neat and simple way to explain some of the patterns seen in biological forms (such as animal coat patterns), his model only allowed for periodic patterns such as spots or stripes, and could not explain a highly precise, non-periodic structure such as the arm, the formation of which would surely demand the action of much more complex molecular processes. Apparently, Turing himself was not completely convinced about the power of his model for explaining morphogenesis. While adressing the capacity of reaction-diffusion systems to explain the stripes of a zebra, he famously uttered: "Well the stripes are easy, but what about the horse part?" [Hogeweg, 2011].

This was to be approached, in 1969, by Lewis Wolpert, who proposed a mechanism by which cells could in some sense know their position in space by interpreting diffusive molecules along gradients of activity [Wolpert, 1969]. This introduced the notion of *positional information*, spatial cues mediated by signals present during development processes, the combination of which is interpreted by cells to become distinct cell types [Wolpert, 1971] (Figure 2.8). The virtually infinite combinations of distinct morphogens, coupled to the diverse shapes and sizes of organs would provide the necessary ingredients to explain Turing's "horse part".

Reaction-diffusion Turing systems and positional information have contributed much needed theoretical frameworks for bridging the scales between molecular mechanisms and the specific, macroscopic traits of organisms. They are build with sufficient generality so as their methodologies can be applied to a plethora of systems, yet they are sufficiently simple to be amenable to analysis

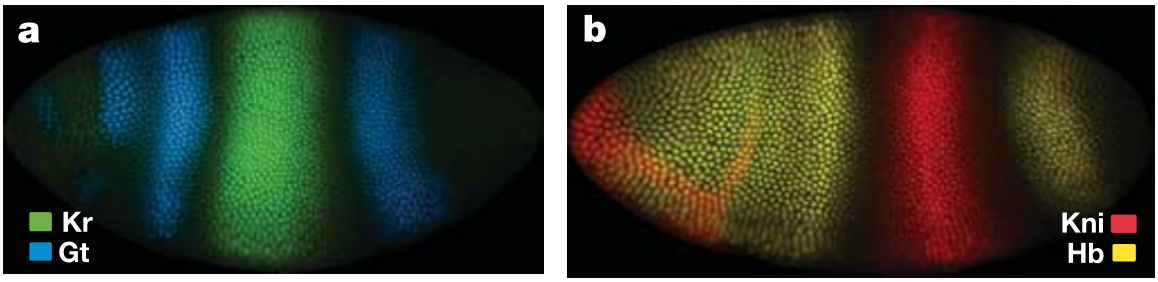



**Figure 2.8: Pattern formation through positional information.** In the *Drosophila* embryo, body segments form by the interpretation of morphogen gradients by distinct genes. In this case, the gap genes *Krüppel* (Kr, green), *giant* (Gt, blue), *knirps* (Kni, red) and *hunchback* (Hb, yellow) are arranged in specific domains which determine distinct cellular identities. Image adapted from [Jaeger et al., 2004].

through mathematical and computational means. Today we know that both Turing patterns and positional information may act together to control developmental processes, as it happens, for instance, in the formation of vertebrate digits [Raspopovic et al., 2014, Green and Sharpe, 2015].

The molecular mechanisms involved in pattern formation often rely on cell-to-cell communication. Of particular interest is *juxtacrine signalling*, where communication is mediated not through classical diffusion as in Turing systems, but by direct cell-to-cell contact [Fagotto and Gumbiner, 1996]. Proteins in the cell membrane—typically ligands and receptors—physically interact and induce a cascade of molecular events leading to particular activation or repression of other factors. A paradigmatic example of juxtacrine signalling can be found in animals with the Notch receptor, whose interaction with a diverse repertoire of ligands at the membrane of adjacent cells is responsible for coordinating cellular decision making in many developmental processes [Bray, 2016]. A particular instance of juxtacrine signalling is lateral inhibition, where the signalling cascade induced by the receptor-ligand binding leads to the repression of the very same ligand, in a feedback mechanism of lateral cell regulation. These mutually repressive interactions can make neighbouring cells to adopt different identities, and when operating in cellular tissues they can generate fine-grained patterns (or salt-and-pepper patterns) [Collier et al., 1996], as it happens with the Notch receptor and its Delta ligand in the chick inner ear [Eddison et al., 2000, Petrovic et al., 2014] (right panel in Figure 2.6) or in the specification of *Drosophila* sensory organ precursor cells [Corson et al., 2017].

Contrasting with juxtacrine signalling is *paracrine signalling*, where instead of cell-to-cell contact, signals between neighbouring cells are mediated by the intercellular movement of molecules [Singh and Harris, 2005]. Paracrine signalling might be mediated either by passive diffusion, where molecules or proteins can simply pass through cellular membranes or pores, or by active transport, where they move from cell to cell through the action of intermediary factors. For instance, the diffusible molecules in Turing patterns and the positional infor-

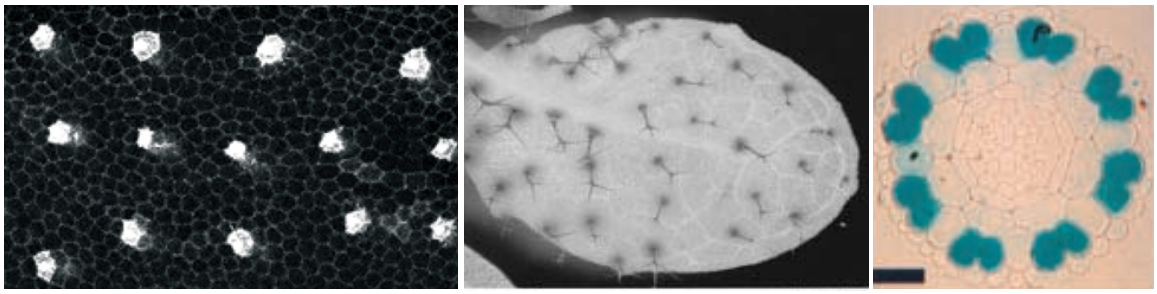


**Figure 2.9: Pattern formation through lateral inhibition. Left:** Bristle patterning in the *Drosophila* notum, here visualized through the Neu-GFP reporter, is mediated by Notch and Delta (adapted from [Cohen, 1991]). **Middle:** Interactions between the two transcription factors TRIPTYCHON and CAPRICE mediate trichome patterning in *Arabidopsis* leaves (adapted from [Schellmann et al., 2002]). **Right:** In the *Arabidopsis* root epidermis, activity of the gene GLABRA2 (in blue) is high in cells which will become epidermal cells, in contrast with hair cells, where the activity of GLABRA2 is absent (adapted from [Lee and Schiefelbein, 2002]).

mation conferred by morphogen gradients in cellular tissues can be mediated by factors acting in a paracrine way. Despite its diffusive nature, in some cases paracrine signalling has been seen to act similarly to juxtacrine signalling, specifying cellular identities in ways akin to lateral inhibition and forming periodic patterns. Lateral inhibition though paracrine signalling has been observed in plants, particularly in *Arabidopsis*, in the specification of root epidermal cells [Lee and Schiefelbein, 2002], trichome formation [Schellmann et al., 2002] and stomatal patterning [Digiuni et al., 2008, Horst et al., 2015] (Figure 2.9), most of them involving the transport of transcription factor complexes through plasmodesmata [Torii, 2012].

The problems tackled in Part III of this thesis are related to this type of paracrine signalling. In Chapter 6 we propose that the rhizoid patterns observed in the *Marchantia* epidermis involve lateral inhibition interactions mediated by the microRNA FRH1, which is able to move from cell to cell and prevent its own production through the inhibition of its activator RSL1. Thus, the interactions between RSL1 and FRH1 constitute a particular instance of an activator-inhibitor system. In Chapter 7 we study a genetic circuit which can exhibit fine-grained patterns such as the ones observed for Notch and Delta, not in a juxtacrine way, but though the diffusion of one of the circuit's components.

Biological processes are complex, and the formation of patterns through lateral inhibition—whether by juxtacrine or paracrine signalling—might also be coupled with positional signals, which might in turn be coupled with activator-inhibitor systems. Moreover, tissues are constantly subject to mechanical stresses, where cells constantly divide, move and die. While physical changes in the cellular structure of tissues are indeed important to understand many developmental processes, more often than not the time-scales at which these occur are much larger than those involved in the molecular processes of gene expression. In this

thesis we do not consider such physical effects, and focus on the dynamics of pattern formation at a molecular level. Therefore the cellular lattices we consider will be static, and without considering cellular division nor cell death. In the next section we provide a way to tackle many problems in gene regulation and its role in the formation of patterns, namely, mathematical modelling, an approach that allows us to asses and quantify the (usually unintuitive) dynamic behaviours these systems commonly exhibit, a task that would be challenging to undertake otherwise.

# Chapter 3

# Mathematical models and methods

## Contents


**3.1 Models of gene expression in space and time . . . . . 31**
3.1.1 Regulation of gene expression in time . . . . . 32
3.1.2 Gene regulation in space . . . . . 41
**3.2 Mathematical tools . . . . . 45**
3.2.1 Linear stability analysis and bifurcations . . . . . 45
3.2.2 Linear instabilities in spatially extended systems . . . . 50
3.2.3 Noise and the chemical Langevin equation . . . . . 55


In this chapter we provide the basic biological and mathematical methods we will recurrently use throughout the thesis. We begin by introducing a common framework for modelling gene expression, namely differential equations, first only in time, and later both in time and in space. We begin with very simplified models of transcription and translation and gradually add more layers of complexity. Then we provide the basic tools to mathematically analyse the biological models described previously, including linear stability analysis and basic bifurcation theory. We end this section with a brief note on how to introduce stochastic effects in these models.

## 3.1 Models of gene expression in space and time

In most sections of this thesis we will be interested in the behaviour (either in time or in the steady state) of the activity of one or several genes and their interaction with other genes through their protein products or with signalling molecules such as hormones or micro RNAs. The inherently non-linear nature of these interactions makes their study only attainable through mathematical and computational modelling, whose methods and tools allow us to assess the

specific details and many of the non-trivial behaviours usually present in such systems. We will first describe how to model gene expression through ordinary differential equations, a modelling strategy we will use in the first chapter of Part II. We then take a similar procedure to include spatial coupling via diffusion, a framework that will allow the study of spatial effects in the second chapter of Part II and pattern formation in the two chapters of Part III.

In an admittedly idealized scenario, we can model the activity of a gene via the production of its corresponding protein through the intermediary messenger RNA, much in the spirit of the famous dictum "DNA makes RNA makes protein", which has often been used as a maxim for the *central dogma of molecular biology* [Crick, 1958, Crick, 1970]—which in its original form, as devised by Francis Crick, deals with the flow of genetic information, not with the molecular chain of events leading from DNA to protein[1].

### 3.1.1 Regulation of gene expression in time

We will consider that from a certain gene $G$ its mRNA is produced at a constant rate $\alpha_m$, and this mRNA linearly degrades with rate $d_m$. This mRNA in turn is translated into protein with rate $\alpha_p$, and the protein is degraded with rate $d_p$. If $m$ and $p$ are the concentrations of mRNA and protein, respectively, then this two-step process can be cast in differential form as the system:

$$\frac{dm}{dt} = \alpha_m - d_m m \tag{3.1a}$$

$$\frac{dp}{dt} = \alpha_p m - d_p p \tag{3.1b}$$

Notice that, while mRNAs are created constantly—for instance, we can assume that there is an infinite pool of aminoacids for the mRNA to be assembled—the synthesis of proteins depends on mRNA, therefore the term $\alpha_p m$. Owing to its linear nature, this simple system can be solved analytically, with the solution of the form $m(t) = a_1 + b_1 e^{-c_1 t}$ and $p(t) = a_2 + b_2 e^{-c_2 t}$, where the constants depend on the parameters of the model and the initial mRNA and protein concentrations $m_0 = m(t = 0)$, $p_0 = p(t = 0)$. Since most of the times analytical solutions cannot be found for more complicated systems, we will often be interested in the steady state, defined as the values of $m$ and $p$ as $t \to \infty$. From the previous equations it is easy to see that, in the steady state, $m_s \equiv m(t \to \infty) = \frac{\alpha_m}{d_m}$ and $p_s \equiv p(t \to \infty) = \frac{\alpha_m \alpha_p}{d_m d_p}$. In fact, to compute the solution of dynamical systems in the steady state we do not even need to

[1] For our intended purposes, the causal implications of "DNA makes RNA makes protein" provide a good starting point to construct mathematical models of gene expression, but it is good to bear in mind that the coining of the phrase (by Jean Brachet) partially stemmed from a misinterpretation of Crick's original goal (see [Cobb, 2017]).

compute the whole time-evolution of the system. If the system has at least one stable fixed-point, that is, a stable state to which dynamical trajectories converge, then the steady state can be thought of as the point at which the solution does not further change in time. Therefore, the steady state solution can be computed by simply setting to zero the time derivatives and solving the resulting algebraic equations. In our case, the two remaining equations, $0 = \alpha_m - d_m m$ and $0 = \alpha_p m - d_p p$, are easily solvable, leading to the solution $m_s = \frac{\alpha_m}{d_m}$, $p_s = \frac{\alpha_m \alpha_p}{d_m d_p}$ , which coincides, as it should, with the result obtained by computing the full, time-dependent solution.

While this simplified model can provide some insight on how the concentrations of mRNA and protein change in time, and what are the contributions of each biochemical parameter in determining the solutions, it falls short on key aspects of gene expression, some of which we are going to discuss along the following lines.

In any living organism, the number of different RNAs and proteins encoded by the genome is far larger than those produced at any given moment [Milo and Phillips, 2016]. At each different developmental stage and cell-type, from the thousands of protein-encoding genes present in the DNA, only a portion are actively synthesizing protein, the others being quiet and inactive. This remarkable feat can be achieved by means of a tightly coordinated regulation of gene expression, highly dynamic in nature and that depends on both internal signals and external environmental cues. For example, the rate of transcription of a gene ($\alpha_m$ in our simplified model) depends on a multitude of regulatory processes, including RNA polymerase binding at the gene's promoter, the unzipping of the double-stranded DNA for its subsequent transcription into RNA or the splicing of precursor RNA into mature mRNA, where the non-coding regions of the sequence, called introns, are removed and the coding regions, called exons, are joined together [Alberts et al., 2014] (Figure 3.1).

In the simplified model, the fact that all these processes are clumped together into the single, constant parameter $\alpha_m$ may raise some suspicion, as it's hard to imagine how the final result of merging so large a number of complicated processes results into a constant rate of transcription. The truth is that all these processes are in some way or another regulated, either by other RNAs, proteins or by the epigenetic state of DNA. To make amends with this apparent inconsistency—and indeed to make sense of the complicated behaviour of real genes—our first approach will consist of modifying the rate of transcription $\alpha_m$, relinquish of its fixedness and instead let it depend on other factors. In many cases the activity of RNA polymerases depends on the binding of proteins to specific sequences of DNA. These proteins are generally known as *transcription factors* and can be broadly classified into two functional groups depending on their action on transcription: activators, which promote the recruitment RNA polymerase to activate transcription, and repressors, which directly or indirectly block transcription [Phillips et al., 2012, Alberts et al., 2014].

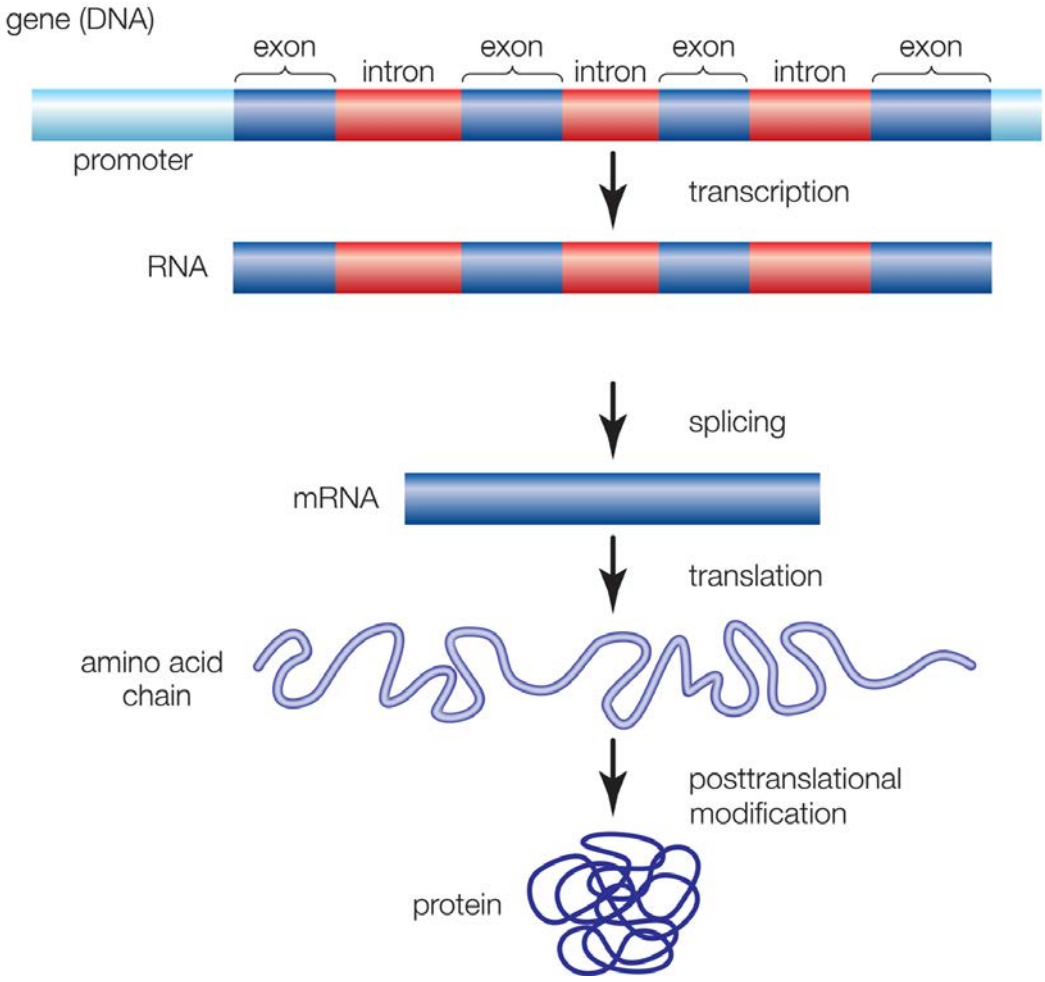



**Figure 3.1: Gene regulation from mRNA to protein.** The process of gene regulation from DNA into protein involves a complex set of steps, the unzipping of the double-stranded DNA for its subsequent transcription into precursor RNA, the splicing of precursor RNA into mature messenger RNA, where the introns—non-coding regions of the sequence—are removed from the exons—the coding regions—which are then joined together. For our intended purposes, many of these intermediary processes are ignored in the name of simplicity. Image from [Britannica, 2019].

The existence of transcription factors makes the process of gene expression inevitably circular: transcription factors are coded by genes, so their production will ultimately be subject to regulation by other transcription factors. These *gene networks* generated by such interwoven regulations can be rather complex, with transcription factors regulating other transcription factors in a constantly flowing cascade of molecules and proteins, which act on other proteins and molecules to keep the network operating as a whole. Such networks are able to generate a remarkably rich spectrum of dynamical behaviours, even in the most simple cases [Jiménez et al., 2017, Jaeger and Monk, 2021a].

In the above simplified model, in the interest of keeping the mathematics to a bare minimum while including some of these complexities, we will con-

sider a scenario in which the very protein translated from the mRNA acts as a transcription factor of its own promoter, a situation which has been observed experimentally both in bacteria and eukaryotes [Rosenfeld et al., 2002,Freeman, 2000] and implemented synthetically [Becskei et al., 2001]. We thus consider $\alpha_m$ to be not constant but a function of the protein itself, which feeds back on its own rate of production. The updated model can be written as:

$$\frac{dm}{dt} = \alpha_m(p) - d_m m \tag{3.2a}$$

$$\frac{dp}{dt} = \alpha_p m - d_p p \tag{3.2b}$$

The specific functional form of $\alpha_m(p)$ depends on the nature of the regulations. In most cases involving transcription factors, the dependence of $\alpha_m(p)$ on the protein can be derived from a simple model of binding kinetics, in which the proteins are able to bind and unbind the promoter with certain rates, thus modifying the rate of transcription depending on their presence or absence. If mRNAs $M$ are produced at rate $\alpha$ when proteins $P$ are not bound and with rate $\varepsilon\alpha$ when they are bound to the promoter $G$, we can write the following processes [Guantes and Poyatos, 2006]:

$$G \xrightarrow{\alpha} G + M \tag{3.3a}$$

$$P + G \underset{k_{off}}{\overset{k_{on}}{\rightleftharpoons}} G_b \xrightarrow{\varepsilon\alpha} G_b + M \tag{3.3b}$$

$$M \xrightarrow{d_m} \emptyset \tag{3.3c}$$

$$P \xrightarrow{d_p} \emptyset \tag{3.3d}$$

where $G_b$ represents the bound promoter. The newly introduced parameters $k_{on}$ and $k_{off}$ set the rates of protein binding and unbinding to the promoter, respectively. Following mass-action kinetics, the rates of the reactions are directly proportional to the product of the concentrations of the reactants, so we can translate the previous system to the following system of ODEs for the concentrations of each species. If we denote the concentrations of mRNA, $G$,

$G_b$ and $P$ as $m$, $g$, $g_b$ and $p$, respectively, we can write:

$$\frac{dg}{dt} = k_{off} g_b - k_{on} p g \tag{3.4a}$$
$$\frac{dg_b}{dt} = k_{on} p g - k_{off} g_b \tag{3.4b}$$
$$\frac{dm}{dt} = \alpha g + \varepsilon \alpha g_b - d_m m \tag{3.4c}$$
$$\frac{dp}{dt} = \alpha_p m - d_p p + k_{off} g_b - k_{on} p g \tag{3.4d}$$

In most situations, a good approximation takes into consideration that the binding/unbinding dynamics are very fast compared to the other reactions. This means that we can let $\frac{dg}{dt} = \frac{dg_b}{dt} = 0$, and obtain the equilibrium solution for the binding of proteins to the promoter, $k_{off} g_b = k_{on} p g$. Moreover, since equations (3.4) imply that the concentration of the promoter is fixed, we have the condition $g_T = g + g_b = g + \frac{k_{on}}{k_{off}} p g = constant$, with $K \equiv k_{on}/k_{off}$, expressing the fact that the promoter can only be in two configurations, either bound or unbound. This expression can be rearranged to give $g = g_T \frac{1}{1+Kp}$, which in turn implies $g_b = g_T \frac{Kp}{1+Kp}$. When substituted into the remaining equations of (3.4), we obtain:

$$\frac{dm}{dt} = \alpha g_T \left( \frac{1 + \varepsilon K p}{1 + K p} \right) - d_m m \tag{3.5a}$$
$$\frac{dp}{dt} = \alpha_p m - d_p p \tag{3.5b}$$

Thus, our transcriptional regulatory function $\alpha_m(p)$ behaves as a constant ($\alpha g_T$) for small values of $p$, but rapidly increases as $p$ approaches $K$, until it reaches a saturating value $\alpha g_T \varepsilon$. The parameter $\varepsilon$, defined as the fold-change in transcription rate when the protein is bound to the promoter, determines whether the protein acts as a transcriptional activation ($\varepsilon > 1$) or as a transcriptional repressor ($\varepsilon < 1$), as shown in Figure 3.2.

An additional feature commonly found in transcriptional regulatory circuits is that of *cooperativity*, i.e. binding of a protein to the promoter stimulates the binding of yet more proteins, in a regulation which becomes self-enhancing. A similar effect can be obtained when proteins can only bind to the promoter when joined together as an oligomer. As a simple case, imagine that proteins $P$ can bind each other forming dimers, and that both the monomeric and dimeric forms are able to bind to the promoter. One must modify the equations given

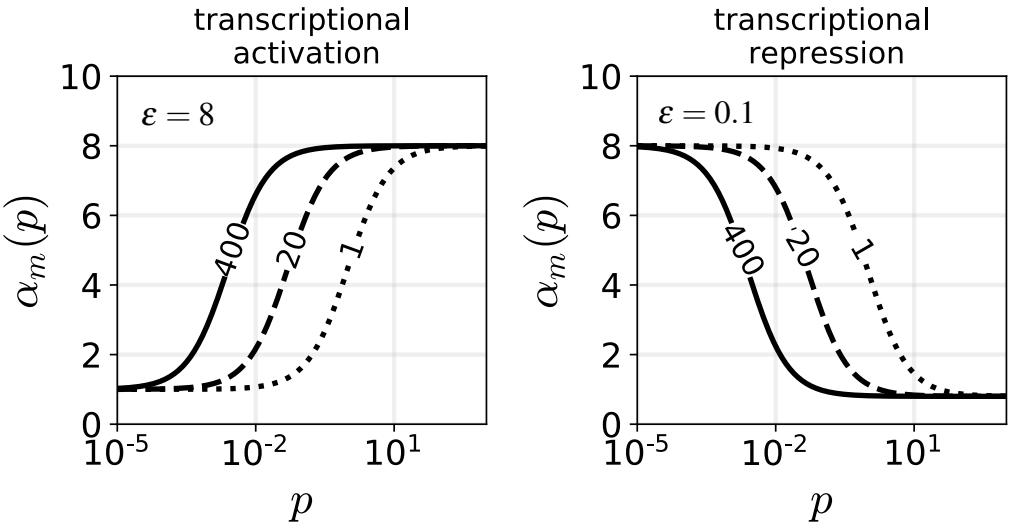



**Figure 3.2: Transcriptional activation and repression for distinct dissociation constants. Left:** In transcriptional activation ($\varepsilon > 1$), the rate of mRNA production is small for low concentrations of protein, $\alpha_m \simeq \alpha g_T$, but rapidly increases as $p$ approaches $K$, up to a saturation value $\alpha_m \simeq \varepsilon \alpha g_T > \alpha g_T$. The parameters used are $\alpha = 1$, $g_T = 1$, $\varepsilon = 8$. **Right:** In transcriptional repression ($\varepsilon < 1$), the rate of mRNA production is large for low concentrations of protein, $\alpha_m \simeq \alpha g_T$, but rapidly decreases as $p$ approaches $K$, up to the constant value $\alpha_m \simeq \varepsilon \alpha g_T < \alpha g_T$. The parameters used in this case are $\alpha = 1$, $g_T = 8$, $\varepsilon = 0.1$. Different curves correspond to different values of $K$.

by system Equation 3.4 to include such features:

$$\frac{dg}{dt} = k_{off} g_b - k_{on} p g + k^d_{off} g_{2b} - k^d_{on} p_2 g \tag{3.6a}$$

$$\frac{dg_b}{dt} = k_{on} p g - k_{off} g_b \tag{3.6b}$$

$$\frac{dg_{2b}}{dt} = k^d_{on} p_2 g - k^d_{off} g_{2b} \tag{3.6c}$$

$$\frac{dm}{dt} = \alpha g + \varepsilon_m \alpha g_b + \varepsilon_d \alpha g_{2b} - d_m m \tag{3.6d}$$

$$\frac{dp}{dt} = \alpha_p m - d_p p + 2k_u p_2 - 2k_d p^2 \tag{3.6e}$$

$$\frac{dp_2}{dt} = -k_u p_2 + k_d p^2 + k^d_{off} g_{2b} - k^d_{on} p_2 g \tag{3.6f}$$

where we have defined the new parameters $k^d_{on}$ and $k^d_{off}$, the binding and unbinding rates of the dimers to the promoter, respectively, $k_d$ and $k_u$, the rates of dimerization and unbinding of $P$, respectively, and $\varepsilon_m$ and $\varepsilon_d$ the relative strengths of transcription when the monomer and the dimer, respectively, are bound to the promoter. Notice that an implicit assumption in this model is that the dimer does not degrade, but only unbinds into its constituent monomers.

It may well be that in some biological systems the degradation of $P$ occurs in both monomers and dimers, as can even be regulated, for example through proteases whose activity depends on the multimeric form of the protein. In any case, in the simple model with no dimer degradation we can assume, as in the previous case, that binding/unbinding reactions are much faster that all other reactions, and we can thus approximate them in the steady state (3.6), implying $k_{on}pg = k_{off}g_b$, $k^d_{on}p_2g = k^d_{off}g_{2b}$ and $k_up_2 = k_dp^2$. Then, in a similar way than before, we can write $g_T = g + Kpg + K_dp_2g = g(1 + Kp + K_dp^2)$, where $K \equiv k_{on}/k_{off}$ and $K_d \equiv \frac{k_{on}k_d}{k_{off}k_u}$. Upon substitution of these expression on Equation 3.6, we obtain:

$$\frac{dm}{dt} = \alpha g_T\left(\frac{1 + \varepsilon_m Kp + \varepsilon_d K_d p^2}{1 + Kp + K_d p^2}\right) - d_m m \tag{3.7a}$$

$$\frac{dp}{dt} = \alpha_p m - d_p p \tag{3.7b}$$

With the very same procedure one can generalize this result to an arbitrary number of multimeric forms of the protein, obtaining a transcription rate $\alpha_m(p)$ of the form:

$$\alpha_m(p) = \alpha g_T\left(\frac{1 + \sum_{n=1}^{N} K_n\varepsilon_n p^n}{1 + \sum_{n=1}^{N} K_n p^n}\right) \tag{3.8}$$

where $n$ runs from 1, the monomeric form of the protein, to $N$, the value of the largest possible oligomer. Each contribution is accompanied by its corresponding dissociation constant $k_n$ and its relative transcriptional strength $\varepsilon_n$. In many cases, only one of the many forms of the protein will be dominant, in which case one can simplify the previous expression to:

$$\alpha_m(p) = \alpha g_T\left(\frac{1 + \varepsilon_n K_n p^n}{1 + K_n p^n}\right) \tag{3.9}$$

This is one of the forms of the celebrated *Hill function*, widely used in systems biology as a phenomenological model for sigmoidal input-output functions with cooperativity [Alon, 2019]. Even though with this definition the cooperativity exponent $n$ is an integer, the phenomenological nature of the Hill equation allows $n$ to take real values as well. The limiting case $n = 1$ is just the Michaelis-Menten equation, while for exponents larger than 1, the function has a sigmoid form with threshold $1/\sqrt[n]{K_d}$, to which changes in the input $p$ lead to increasingly abrupt changes in output, a phenomena sometimes dubbed, when $n$ is very large, as *ultrasensitivity* [Ferrell and Ha, 2014]. Sometimes, Equation 3.9 is written in

the slightly different form depending on the nature of $\varepsilon_n$:

$$\alpha_m(p) = \beta_0 + \beta \frac{p^n}{p^n + k^n} \quad \text{for transcriptional activation} \tag{3.10a}$$

$$\alpha_m(p) = \beta_0 + \beta \frac{k^n}{p^n + k^n} \quad \text{for transcriptional repression} \tag{3.10b}$$

Where the parameters $\alpha$, $g_T$ and $\varepsilon_n$ from Equation 3.9 have been rescaled. We use regulatory functions of the type Equation 3.9 and Equation 3.10 in Chapter 4, when we study the mutual regulatory interactions between BRAVO and WOX5, two transcription factors involved in the regulation of stem cell quiescence in the root of the model plant *Arabidopsis thaliana*.

Typically, gene regulation does not only involve a single gene, but whole gene regulatory networks, where multiple molecules interplay in a complex web of activating and repressing interactions. Within these networks one usually finds small subunits called *network motifs*, recurrent circuits that are present more frequently that one would expect were the networks randomly assembled [Milo et al., 2002b, Alon, 2007]. Due to their relatively simple nature, these network motifs allow a mathematical treatment which becomes impossible for larger networks. As the final part of this section on gene regulation, we exemplify the interaction between two genes with one of these network motifs, which in turn is a common feedback circuit operating in developmental contexts: the genetic toggle-switch [Gardner et al., 2000, Jaeger and Monk, 2021b]. The system consists of two genes whose products are able to mutually repress each other's expression, so that the activity of one is inversely proportional to the activity of the other (Figure 3.3).

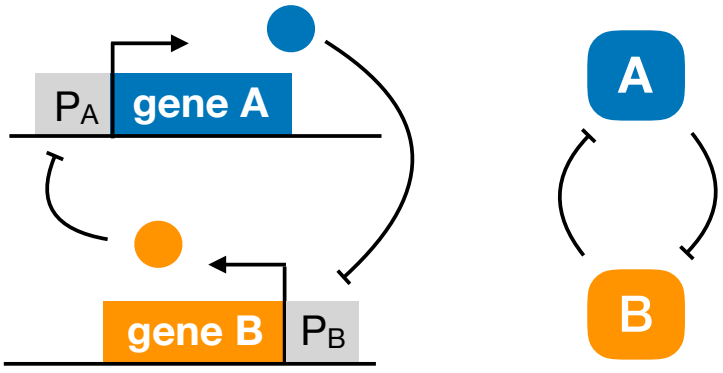



**Figure 3.3: The genetic toggle-switch. Left:** Two genes $A$ and $B$ interact through the production of their proteins that act as repressors of the opposite gene, by binding to its promoters $P_B$ and $P_A$, respectively. **Right:** Simplified circuit topology of the toggle-switch, evidencing the mutually repressive nature of the interactions. Blunt arrows denote repressive interactions.

If the concentrations of each protein are $a$ and $b$, we can write the dynamics of the toggle switch as the following system (recall (3.10)):

$$\frac{da}{dt} = \alpha_0 + \alpha \frac{k_a^n}{k_a^n + b^n} - d_a a \tag{3.11a}$$

$$\frac{db}{dt} = \beta_0 + \beta \frac{k_b^m}{k_b^m + a^m} - d_b b \tag{3.11b}$$

The parameters $\alpha_0$ and $\beta_0$ represent constitutive production rates of the proteins. $\alpha$ and $\beta$ are, respectively, the maximum values the regulated production rate of $A$ and $B$ can take; $k_a$ and $k_b$ set the repression threshold of $a$ and $b$, and $m, n$ measure the cooperativity of each species when binding to their corresponding promoter. Notice that in the previous equations mRNA molecules do not appear. This is because have introduced another simplification, namely that the dynamics of the mRNA are very fast compared to the dynamics of proteins. This time-scale separation allows us to treat the dynamics of the mRNA to be approximately in the steady state, so our system can be written in terms of proteins alone. The rationale behind such simplification is the following: half-lifes of mRNAs typically range from a few minutes in bacteria and yeast to hours in mammals, while those of proteins are generally longer [Milo and Phillips, 2016, Schwanhäusser et al., 2013], with extreme cases such as nuclear pore proteins in rat brains, which have been shown to last more than a year [Savas et al., 2012].

System (3.11) displays the basic feature and main function of the toggle-switch: opposite activities of $a$ and $b$. These activities can be swapped if some control parameter is changed, and depending on the specific values of the parameters, an intermediary bistable region may appear. In this region, states with high $a$ and low $b$ coexist with opposite states, with low $a$ and high $b$. In this bistable region, the particular state the system ends up in will depend on the initial concentrations of $a$ and $b$. This can be easily understood as follows: when the activity of one of the genes (say $A$) is large, high repression will prevent the activity of $B$ to grow, thus maintaining the system in a $A$-high, $B$-low state. As some parameter lowering the activity of $A$ changes (for example, degradation of $A$ grows), the repression on $B$ will diminish, up to the point of the activity of $B$ becoming large enough compared to the activity of $A$ to induce a large repression, sharply swapping the system to a $B$-high, $A$-low state (Figure 3.4). Depending on the cooperativity exponents $n, m$, the system can exhibit a sharp transition that might include an intermediate region at which the two states $A$-high, $B$-low and $B$-high, $A$-low coexist, the selection of which will be determined by the initial conditions of equations (Figure 3.4). The toggle-switch constitutes one of the prototypical circuits displaying bistability via a saddle-node bifurcation. We will treat bifurcations in more detail in

section Section 3.2.

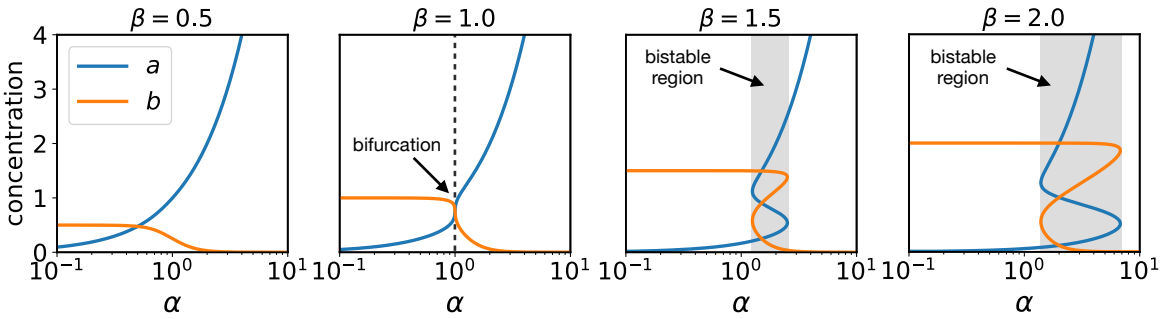



**Figure 3.4: Bifurcation diagram of the toggle-switch.** Depending on the parameters of the toggle-switch system, protein concentrations $a$ and $b$ can display distinct steady state regimes, namely monostability (with low $a$ and high $b$ for small values of $\alpha$, or high $a$ and low $b$ for large values of $\alpha$) or bistability, where low $a$, high $b$ and high $a$, low $b$ states coexist. The rest of the parameters are $k_a = k_b = 1$, $d_a = d_b = 1$, $n = m = 4$.

These examples set the stage for most of the mathematical problems we will face along this thesis. While we have specifically focused on transcriptional regulation, it is important to bear in mind that all steps of gene expression are regulated. For example, the rates of degradation and translation of the mRNA can be affected by the presence of microRNAs (miRNAs), non-coding RNAs which are not translated into protein but instead prevent mRNAs to become translated, either by cleaving the mRNA into two pieces or by directly affecting the translation efficiency [Fabian et al., 2010, Bartel, 2009]. The rate of protein degradation can also be enhanced by the presence of proteases, enzymes that catalyse the breakdown of proteins into smaller polypeptides or single amino acids. Moreover, other post-translational modifications such as the ubiquitylation of a protein may target them for degradation by the proteasome. The activity of these proteases and the epigenetic state of proteins can in turn be regulated by other proteins, thus generating a convoluted web of interlinked post-translational interactions, adding a further layer to the already acknowledged complexity of gene regulation [Phillips et al., 2012]. In the absence of feedbacks, however, all these regulations can be absorbed in the parameters of the models, making their analysis more amenable.

### 3.1.2 Gene regulation in space

While models based on ordinary differential equations can provide very useful information about the dynamic behaviour of proteins—whether they oscillate, have multiple states or they do not change at all—they fall short on one key aspect, namely that genes and mRNAs and proteins do not lie on a single point as the ODE model implies, but are embedded in space. In analysing equations of the type (3.11), we implicitly assumed that neither mRNA nor proteins are able to move, of if they do they do it in such a way to maintain the same concentra-

tion at every point in space (we say the system is "well-mixed"). This appears to be a gross oversimplification, as we know of the dynamic nature of small molecules and their potential roles in locations far from their source of origin. Furthermore, if we want to study gene expression not in a single cell—where one could arguably make a case about treating each cellular unit as a point, thus ignoring spatial dependences in their interior—but on tissues or cellular arrays, where cells are by definition located at different places, the inclusion of spatial dependences becomes unavoidable. To overcome this issue, one of the simplest, most common strategies is to introduce the spatial component via the diffusion of one or more species, which turns the original ODEs into partial differential equations (PDEs). In general, full solutions of PDEs can rarely be found analytically, and one needs to recur to approximation methods or to study the system in the steady state, which turns the PDE into an ODE. Numerical methods for solving PDEs, on the other hand, while harder to implement than in ODEs, become of utter importance in the analysis of spatially dependent systems. Of course, this approach still lacks the specific details present in the actual random motion of the molecules, and instead treats movement as averages over certain regions of space, which in turn makes its analysis far more accessible. In the archetypical example of explicitly space-dependent gene regulation, the dynamics of a set of molecular variables $\mathbf{u}$ include, besides the conventional terms corresponding to production and degradation (i.e., the reactions), an additional diffusive term, of the form:

$$\frac{\partial \mathbf{u}(\mathbf{x})}{\partial t} = \mathbf{F}[\mathbf{u}(\mathbf{x})] - d_{\mathbf{u}}\mathbf{u}(\mathbf{x}) + D\nabla^2\mathbf{u}(\mathbf{x}) \tag{3.12}$$

Here $\mathbf{u}(\mathbf{x}) = (u_1, u_2, \ldots, u_N)$ is a vector of the different molecular species involved, $\mathbf{x}$ denote the spatial degrees of freedom (for example $\mathbf{x} = (x, y)$ in $\mathbb{R}^2$), and $\mathbf{F}$ is a vector of functions denoting the production terms of each species. Notice that in the reaction terms we assume, as before, that production, but not degradation, can be regulated. Moreover, we also assume that, in the case where $\mathbf{u}$ are proteins, mRNA dynamics are very fast compared to protein dynamics. The $\nabla^2$ operator is the Laplacian, defined in two-dimensions as $\nabla^2 = \frac{\partial^2}{\partial x^2} + \frac{\partial^2}{\partial y^2}$. The vector $D = (D_1, D_2, \ldots, D_2)$ dictates the diffusion strength of each species. Introducing space in this way involves the transition from ODEs to PDEs, which incidentally turns the system infinite dimensional. In order to have a well-defined equation, (3.12) must be supplemented with an initial condition of the form $\mathbf{u}(\mathbf{x}, t = 0) = \mathbf{g}(\mathbf{x})$, i.e. an initial distribution from which the dynamical process can be applied. In Chapter 5 we use these kind of equations to model the spatiotemporal behaviour of BRAVO and WOX5 in the stem cell niche of *Arabidopsis*.

When writing Equation 3.12 we implicitly assume that the diffusion coefficient of each species is constant across the domain where the equation applies. In some cases this may not be the case, and the diffusion matrix instead de-

pends on the spatial position, $D = D(\mathbf{x})$. In these situations of *heterogeneous diffusion*, Equation 3.12 takes the form:

$$\frac{\partial \mathbf{u}(\mathbf{x})}{\partial t} = \mathbf{F}[\mathbf{u}(\mathbf{x})] - d_{\mathbf{u}}\mathbf{u}(\mathbf{x}) + \nabla(D(\mathbf{x})\nabla\mathbf{u}) \tag{3.13}$$

When expanded, the new diffusion term gives $\nabla D\nabla\mathbf{u} + D\nabla^2\mathbf{u}$, i.e. a term with classical diffusion $D\nabla^2\mathbf{u}$ plus an additional term $\nabla D\nabla\mathbf{u}$ which takes into account the spatial variation of the diffusion coefficient. In Chapter 5 we use this approach to model the dynamics of BRAVO and WOX5 in a realistic root layout, where the diffusion coefficient is different inside the cells' cytoplasm and in cell walls.

Theoretical modelling with spatially continuous systems has indeed been very fruitful for developmental biology, constituting a large field whose mathematical methods are well-established [Cross and Hohenberg, 2010, Cross and Greenside, 2009]. However, many systems of interest—such as cellular arrays with juxtacrine or paracrine signalling, or systems where not all molecules are able to diffuse from cell to cell—can be understood by considering cells as discrete entities, located in a lattice and where coupling happens between nearest neighbours. A classic example of such discrete modelling has been the Delta-Notch lateral inhibition system [Collier et al., 1996], where pattern formation happens at the level of single cells via juxtacrine, nearest-neighbour interactions, a phenomenon that cannot be modelled in continuous space. In this framework, instead of dealing with infinite dimensional dynamical systems as happens with PDEs, we will have molecules assigned to different cells acting as different *variables*, where space is implemented implicitly through interactions between them. To model such systems, we first consider a vector of molecular species $\mathbf{u}_{ij}$, where the subscripts $i, j$ denote the discrete spatial positions, i.e. they act as indices of the spatial lattice, and span a range equal to the number of lattice points in the domain. As we will apply these techniques to study the dynamics of biological proteins/molecules in cellular tissues, we will refer to each spatial point in the discrete lattice as a *cell*. Then, an equivalent of Equation 3.12 in this cellular lattice can be written as:

$$\frac{d\mathbf{u}_{ij}}{dt} = \mathbf{F}[\mathbf{u}_{ij}] - d_{\mathbf{u}}\mathbf{u}_{ij} + D\nabla^2\mathbf{u}_{ij} \tag{3.14}$$

Here the specific form of the Laplacian $\nabla^2$ will depend on the characteristics of the lattice. For a regular, 2 dimensional square lattice (Figure 3.5), this is just:

$$\nabla^2\mathbf{u}_{ij} \equiv \frac{1}{\Delta x^2}(\mathbf{u}_{i+1,j} + \mathbf{u}_{i-1,j} + \mathbf{u}_{i,j+1} + \mathbf{u}_{i,j-1} - 4\mathbf{u}_{i,j}) \tag{3.15}$$

where $\Delta x$ is the distance between cells. Notice that in this discrete version of the reaction-diffusion system the spatial coupling is introduced through finite

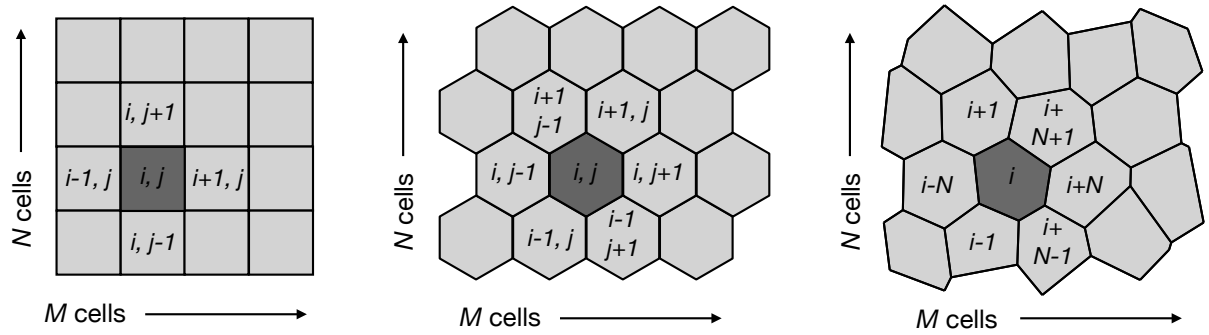



**Figure 3.5: Labelling schemes for the square, regular hexagonal, and irregular lattices.**

differences, not through derivatives. In a way, this makes the analysis more complicated, as the set of techniques we would use to study continuous spatially dependent systems is of no use here. However, as we will see, the fact that the spatial coupling happens only through cells which are nearest neighbours will greatly simplify our study. In Chapter 7 we use this discrete approach with a square lattice to model the spatiotemporal dynamics of a small, multi-functional regulatory circuit. In reality, however, cellular tissues are usually not square arrays. Cells usually pack into tissues forming more or less hexagonal arrays, a situation often connected to mechanical constraints such as energy minization [Classen et al., 2005, Farhadifar et al., 2007]. For a perfectly hexagonal lattice labelled as in Figure 3.5, the Laplacian is given by:

$$\nabla^2 \mathbf{u}_{ij} \equiv \frac{1}{\Delta x^2}(\mathbf{u}_{i+1,j-1} + \mathbf{u}_{i+1,j} + \mathbf{u}_{i,j-1} + \mathbf{u}_{i,j+1} + \mathbf{u}_{i-1,j} + \mathbf{u}_{i-1,j+1} - 6\mathbf{u}_{ij}) \quad (3.16)$$

This framework has been used to model the formation of rhizoid patterns in *Marchantia polymorpha* of Chapter 6.

For completeness, and even though their use throughout this thesis has been minor (in the last section of Chapter 7), we also consider irregular tissue layouts generated using Voronoi tesselations.

To do this we start with a two-dimensional points arranged in a perfect triangular lattice, the positions of which can be labelled as $(x, y) = (i + j/2, \frac{\sqrt{3}}{2} j)$, where $i, j$ are integers, and randomly displace each point a certain distance from its original location, such that the new lattice looks like $(\hat{x}, \hat{y}) = (i + j/2 + v\xi_x, \frac{\sqrt{3}}{2} j + v\xi_y)$, where $(\xi_x, \xi_y)$ are random numbers taken from a uniform distribution between 0 and 1, and $v$ sets the variability from the perfect hexagonal layout. If $v$ takes a small value, the lattice will be more or less hexagonal, with mostly six-sided cells, while for large values, four and three-sided cells can appear (Figure 3.6). To model diffusion in this general setting we must take into account the fact that the number of contact area and neighbours may differ from cell to cell. In its most general form, this can be implemented through the

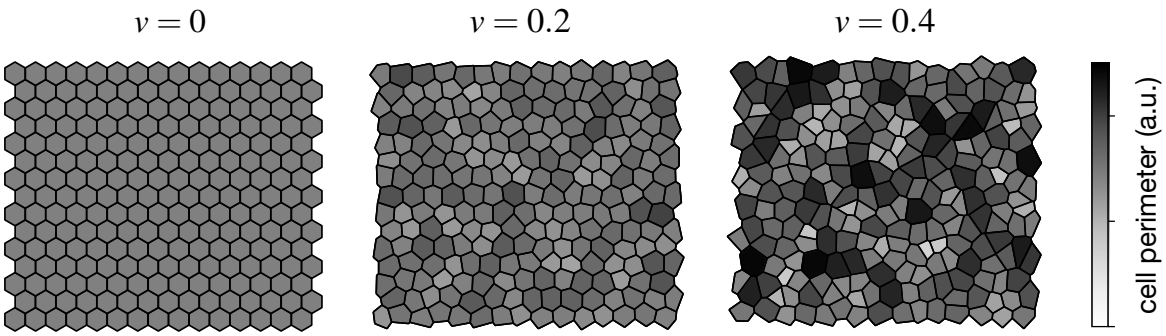



**Figure 3.6: The effect of variability in irregular lattices.** As the variability coefficient $v$ increases, the deviation from the hexagonal lattice increases, generating cells with different shapes, areas and perimeters.

Laplacian:

$$\nabla^2 \mathbf{u}_i \equiv \frac{1}{A_i} \sum_{j=nn_i} \frac{L_{ij}}{L_0} (\mathbf{u}_j - \mathbf{u}_i) \tag{3.17}$$

where the sum runs from the $j$ nearest neighbours $nn_j$ of cell $i$. $L_{ij}$ represents the contact length between cells $i$ and $j$, and $A_i$ is the area of cell $i$. $L_0$ is a characteristic length. Notice that for regular lattices the areas and contact lengths will be fixed, i.e., $A_i = A$, $L_{ij} = L$.

## 3.2 Mathematical tools

In this section we provide the basic mathematical methods we will use to analyse the models we encounter throughout this thesis. These mainly involve linear stability analysis of dynamical systems, which allows us to find the stability of fixed points and whether any bifurcation occurs, and whether instabilities happen in spatially extended systems.

### 3.2.1 Linear stability analysis and bifurcations

For generic dynamical systems, the study of time-evolution and steady states is hard. The full, time-dependent solution we have found for the generic model of gene expression Equation 3.1 has been a lucky—and deliberate—exception, and has been possible to obtain due to two main reasons: linearity of interactions and absence of feedback. The cool thing about linear things is that they have a tendency to spawn more linear things; take a very complicated, highly dimensional and coupled dynamical system, consisting only of linear interactions, and rest assured that the dynamics of each one of the variables will be exponential, as for Equation 3.1. This includes the possibility that the exponent is a complex number, in which case the system will oscillate with a constant frequency.

Exponentials we know how to solve. The downside is that exponential dynamics are dull and boring, as no other interesting behaviours are able to emerge from them. For its part, a dynamical system's lack of feedback indicates that it is *uncoupled*, that is, we can study each equation separately without worrying about the effect it has on the other. In the case of Equation 3.1, it is easy to see that the equation for the mRNAs can be solved analytically without knowledge of the equation for the proteins, i.e. they are uncoupled. Something happens, however, when $p$ feeds back on the equation for $m$, promoting its transcription, as happens in Equation 3.7: now the system has become both nonlinear and coupled. Trying to find the explicit time-evolution would be a hopeless exercise, as there is no way to directly integrate the equations as we did in Equation 3.1. However, we can find solutions in the long time limit by letting the time derivatives go to zero, and solving the corresponding algebraic equations. The solutions of such equations are called the *fixed points* of the system. The classical problems in dynamical systems theory are to know the nature of these fixed points—e.g. if they are stable under perturbations—and whether the number and nature of the fixed points changes as the parameters of the system change. A powerful tool to study the stability of fixed points is *linear stability analysis* (LSA) [Strogatz, 2014], which tells us how the fixed points of the system behave as we perturb them in a certain way. Roughly speaking, if these perturbations decay and the system rapidly relaxes to the fixed point, then we say it is stable; conversely, if a perturbation grows then the fixed point can be considered unstable. There is a third situation where the stability of the fixed point will depend on *how* the perturbation is performed, that is, it can be stable for perturbations along a certain direction but unstable for perturbations along another direction. These are called saddle-points, and can be understood by visualizing the rolling of a ball along the two orthogonal directions of a saddle: if a ball sits exactly on the saddle point, a perturbation along one direction will inevitably cause to ball to roll down-hill, while a perturbation along the orthogonal direction will oscillate back into the saddle point. There are some situations—which we will not encounter here—that a perturbation around a fixed point won't return back nor it won't go away from where it started without limit. These fixed points are called marginally (or neutrally) stable (Figure 3.7).

All this can be formalized mathematically as follows. Let's consider a generic dynamical system given by:

$$\frac{d}{dt}\mathbf{x} = \mathbf{F}(\mathbf{x}) \tag{3.18}$$

where $\mathbf{x} = (x_1, x_2, \ldots, x_N)$ represents the variables of the system (for example, different molecular species) and $\mathbf{F} = (F_1, F_2, \ldots, F_N)$ are functions dictating how these species interact with each other. Let's assume $\mathbf{x}_p$ is a fixed point of the system. In order to know how a perturbation around this fixed point be-

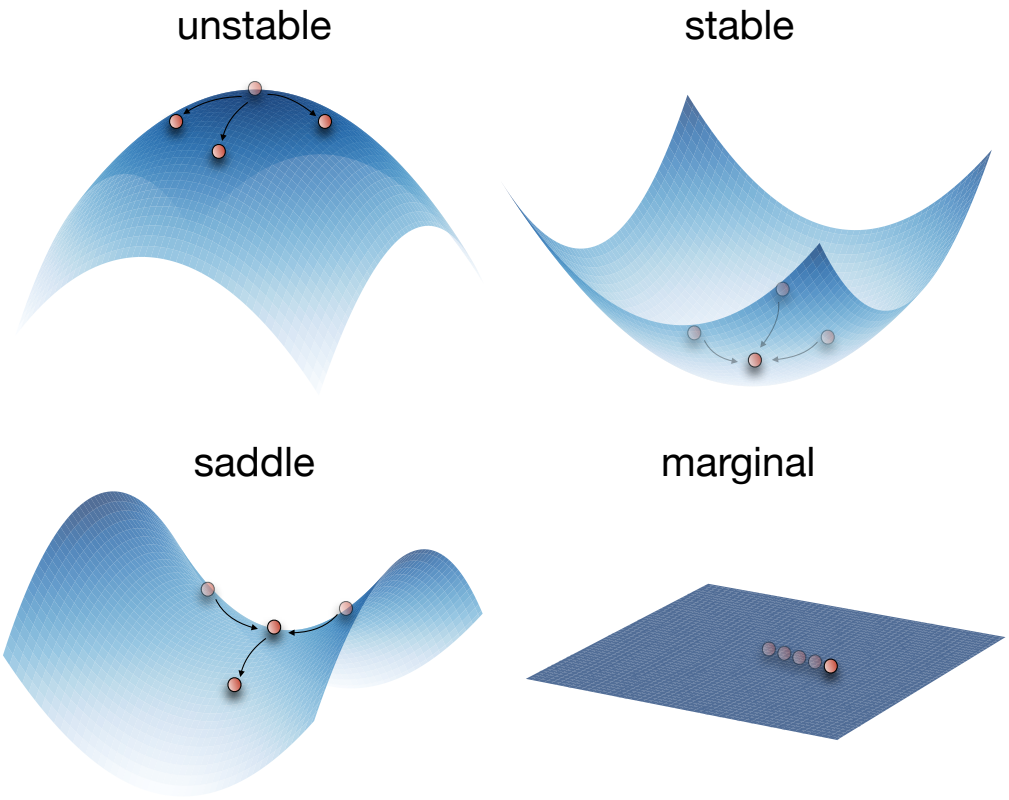



**Figure 3.7: Types of stability of a fixed point**. When the fixed point is unstable, small perturbations grow, causing the trajectories to move away from the fixed point. If the fixed point is stable, small perturbations decay and trajectories converge to the fixed point. In a saddle point, perturbations grow or decay depending on the direction of the perturbation. If a point is marginally stable, a perturbation from the fixed point can take the system to a new state that might depend on the strength of the perturbation.

haves, let's construct a new variable $\delta\mathbf{x} = \mathbf{x} - \mathbf{x}_p$, denoting a small offset from the fixed point, i.e. the perturbation. We can try to find how this variable evolves in time:

$$\frac{d}{dt}\delta\mathbf{x} = \frac{d}{dt}(\mathbf{x} - \mathbf{x}_p) = \frac{d\mathbf{x}}{dt} = \mathbf{F}(\mathbf{x}) \tag{3.19}$$

Here the second to last equality holds because $\mathbf{x}_p$ is the fixed point and does not change in time. Thus this tells us that the function $\mathbf{F}(\mathbf{x})$ dictates how the perturbation grows or decays in time. Notice that, by writing $\mathbf{x} = \mathbf{x}_p + \delta\mathbf{x}$, we see that $\mathbf{F}(\mathbf{x}) = \mathbf{F}(\mathbf{x}_p + \delta\mathbf{x})$. Since the perturbation is assumed to be very small, we can Taylor-expand the previous expression for small $\delta\mathbf{x}$, obtaining, at first order:

$$\mathbf{F}(\mathbf{x}_p + \delta\mathbf{x}) = \mathbf{F}(\mathbf{x}_p) + \mathbf{F}'(\mathbf{x}_p)\delta\mathbf{x} + \mathcal{O}(\delta\mathbf{x}^2) \tag{3.20}$$

where the function $\mathbf{F}'(\mathbf{x}_p)$ is just a matrix whose entries are partial derivatives

of $\mathbf{F}(\mathbf{x})$ with respect to the different combinations of $\mathbf{x} = (x_1, x_2, \ldots, x_N)$, i.e.

$$\mathbf{F}'(\mathbf{x}_p) = \begin{pmatrix} \frac{\partial F_1}{\partial x_1}\Big|_{\mathbf{x}_p} & \frac{\partial F_1}{\partial x_2}\Big|_{\mathbf{x}_p} & \cdots & \frac{\partial F_1}{\partial x_N}\Big|_{\mathbf{x}_p} \\ \frac{\partial F_2}{\partial x_1}\Big|_{\mathbf{x}_p} & \frac{\partial F_2}{\partial x_2}\Big|_{\mathbf{x}_p} & \cdots & \frac{\partial F_2}{\partial x_N}\Big|_{\mathbf{x}_p} \\ \vdots & \vdots & \ddots & \vdots \\ \frac{\partial F_N}{\partial x_1}\Big|_{\mathbf{x}_p} & \frac{\partial F_1}{\partial x_2}\Big|_{\mathbf{x}_p} & \cdots & \frac{\partial F_N}{\partial x_N}\Big|_{\mathbf{x}_p} \end{pmatrix} \tag{3.21}$$

This matrix is called the *Jacobian*, and is evaluated at the fixed point $\mathbf{x}_p$. From now on we will write it as $J = \mathbf{F}'(\mathbf{x}_p)$ to follow standard nomenclature [Strogatz, 2014, Alon, 2019]. Since by the very definition of fixed point we have $\mathbf{F}(\mathbf{x}_p) = 0$, we end up with the following expression for the dynamics of a small perturbation around $\mathbf{x}_p$:

$$\frac{d}{dt}\delta\mathbf{x} = J\delta\mathbf{x} \tag{3.22}$$

Let's take a moment to understand the power of this equation. In order to know how trajectories around the fixed point will behave when perturbed, we only need to solve a system of *linear* equations for the perturbation variable $\delta\mathbf{x}$! The proportionality constants of this linear system are given by the entries of the Jacobian $J$, which are just numbers. Now the specific nature of these numbers will tell us whether the fixed point will be stable (perturbations decay), unstable (perturbations grow), a saddle-point (perturbations grow or decay depending on how they are applied), or marginally stable (perturbations do not grow nor decay). Due to its linearity, the system $\frac{d}{dt}\delta\mathbf{x} = J\delta\mathbf{x}$ can be solved as a linear combination of exponentials:

$$\delta\mathbf{x} = \sum_{k=1}^{N} \mathbf{v}_k e^{\lambda_k t} \tag{3.23}$$

where the coefficients $\lambda_k$ and the vectors $\mathbf{v}_k$ are still to be determined. $\mathbf{v}_k$ and $\lambda_k$ satisfy:

$$\frac{d}{dt}(\mathbf{v}_k e^{\lambda_k t}) = J\mathbf{v}_k e^{\lambda_k t} \tag{3.24}$$

and since $\frac{d}{dt}(\mathbf{v}_k e^{\lambda_k t}) = \lambda_k \mathbf{v}_k e^{\lambda_k t}$, we end up with the following equation

$$(J - \lambda_k \mathbb{1})\mathbf{v}_k = 0 \tag{3.25}$$

The last equation tells us that the $\lambda_k$ and $\mathbf{v}_k$ are, respectively, the eigenvalues and eigenvectors of the Jacobian matrix $J$. This means that we have reduced a dynamical problem to a simple exercise of finding the eigenvalues of a matrix. From basic algebra, this can be done by solving the characteristic equation $\det(J - \lambda_k \mathbb{1}) = 0$. Notice from Equation 3.23 that each eigenvalue can be interpreted as the *growth rate* of its corresponding eigenvector, in such a way

that for $\lambda_k < 0$, the term corresponding to $\mathbf{v}_k$ will decay to zero, while for $\lambda_k > 0$ it will grow. This very fact gives us the conditions for the stability of fixed points when they are slightly perturbed: if the real parts of all of the eigenvalues are negative $\mathrm{Re}(\lambda_k) < 0$ (as eigenvalues can be complex numbers) then the fixed point will be stable, because all terms in Equation 3.23 will decay as $t \to \infty$; if at least one of the $\lambda_k$ has a positive real part, $\mathrm{Re}(\lambda_k) > 0$, then the corresponding term will grow, making the fixed point unstable on that direction. A saddle point would be an unstable fixed point of this type, while a point where all eigenvalues have positive real part would be completely unstable in all directions. If it so happens that an eigenvalue has $\mathrm{Re}(\lambda_k) = 0$, then the direction of the corresponding eigenvector will be marginally stable, as a perturbation will neither grow nor decay.

We have discussed all these situations without regarding the nature of the imaginary part of the eigenvalues. If eigenvalues have an imaginary part exactly zero $\mathrm{Im}(\lambda_k) = 0$, then the return or escape of the perturbed trajectory will follow a monotonic path towards or away from the fixed point, respectively. If instead $\mathrm{Im}(\lambda_k) \neq 0$, by virtue of Euler's formula $e^{i\theta} = \cos\theta + i\sin\theta$, the exponential becomes oscillatory. This means that if a fixed point has, for example, $\mathrm{Im}(\lambda_k) \neq 0$ and $\mathrm{Re}(\lambda_k) < 0$, a perturbation will tend to converge to the fixed point by spiralling in, while in the same situation but with $\mathrm{Re}(\lambda_k) > 0$, the trajectory will spiral out of the fixed point, with oscillations of increasing amplitude. The situation where $\mathrm{Im}(\lambda_k) \neq 0$ and $\mathrm{Re}(\lambda_k) = 0$ is called a center, and is an example of a marginally stable, oscillatory state, where the effect of perturbations is to modify the amplitude of the oscillation. In the case of an unstable fixed point with $\mathrm{Im}(\lambda_k) \neq 0$ and $\mathrm{Re}(\lambda_k) > 0$, the trajectory will often end up in a *limit cycle*, an isolated periodic orbit in phase space, the existence of which can be assessed via the Poincaré–Bendixson theorem [Strogatz, 2014]. The study of the stability of limit cycles is a bit more sophisticated than linear stability analysis of fixed points, and since all limit cycles we are going to encounter in this thesis are stable, we are not going to describe it here.

In practice, dynamical system of dimensions larger than 3 are hardly ever analysed analytically, as the polynomials involved to find the eigenvalues cannot be solved without aid from numerical algorithms. In the models studied in this thesis the dimensions will always be 2 o 3, so at least some analytical work can be done. While in 2 dimensions the roots of the characteristic polynomial are usually easy to find, involving only quadratic formulas, for 3 dimensions the expression involved are much more complicated, and so other criteria for stability might be needed. Luckily, the *Routh-Hurwitz criterion* gives the necessary and sufficient conditions for the stability of fixed points in more complicated systems [Murray, 2002]. For a 3-dimensional dynamical system with characteristic polynomial $P(\lambda) = \lambda^3 + a_2\lambda^2 + a_1\lambda + a_0 = 0$, the conditions for stability of a fixed point (that is, all $\mathrm{Re}(\lambda) < 0$) are:

$$a_2 > 0, \quad a_0 > 0, \quad a_2 a_1 - a_0 > 0 \tag{3.26}$$

while similar—albeit more complicated—conditions can be found for more than three dimensions, the $3d$ case will suffice for our purposes.

Knowing which are the conditions for the stability of fixed points, one now may ask whether the nature of these fixed points can change as we let the parameters of the system vary. Indeed, when a fixed point appears or disappears, or changes its stability—for example from unstable to stable—we say that a *bifurcation* has occurred. The stability of fixed points is reflected in the nature of the eigenvalues, which may change, for instance, from $\mathrm{Re}(\lambda) < 0$ to $\mathrm{Re}(\lambda) > 0$, where the bifurcation happens when $\mathrm{Re}(\lambda) = 0$. It might also happen that as a parameter changes, not only the nature of the fixed point changes, but the very *number* of fixed points as well. This is the case when the number of solutions of the system (3.18) in the steady state also changes. Bifurcations can be classified as *local*, when the stability of a fixed point changes as a parameter varies, or *global*, when not only the local structure of the fixed point changes, but the topology of the whole phase space [Strogatz, 2014]. We are mostly interested in local bifurcations, which are the ones we will encounter in Chapter 7. Among these, particular examples are the *saddle-node* bifurcation, in which two fixed points—one stable and one unstable—collide and annihilate each other, and the *Hopf* bifurcation, where a fixed point switches its stability and becomes a periodic solution in a limit cycle. This happens when a pair of complex conjugate eigenvalues $\lambda_\pm$ associated with the fixed point cross the line $\mathrm{Re}(\lambda_\pm) = 0$. The saddle-node bifurcation is the one appearing in the toggle-switch example (3.3), where for particular values of the parameters $\alpha$ and $\beta$, the system passes from a single steady state to a region of bistability, where two steady states, separated by an unstable one, coexist (Figure 3.4). The Hopf bifurcation will appear in Chapter 7, where oscillations emerge out of a previously stable fixed point.

### 3.2.2 Linear instabilities in spatially extended systems

The main goal of performing linear stability analysis on a dynamical system is to find the nature of fixed points, and which are the conditions at which they may lose or gain stability. When space enters the game, much richer behaviours are possible, as the interactions between variables no longer need to be local, but can reach all space. Linear stability analysis can be extended to spatially extended systems, but in this case one must specify how perturbations depend on space. Since in this thesis we mostly study discrete systems in a regular square lattice, we begin with a reaction-diffusion system of the type described by (3.12):

$$\frac{d\mathbf{u}_{ij}}{dt} = \mathbf{F}[\mathbf{u}_{ij}] + D\nabla^2 \mathbf{u}_{ij} \tag{3.27}$$

where $i = 1, 2, \ldots, N$, $j = 1, 2, \ldots, M$ represent the explicit spatial dependence of $\mathbf{u}$, and the operator $\nabla^2$ is the Laplacian for a rectangular lattice, as previously defined in subsection 3.1.2. Let's assume that our system has a spatially homogeneous steady state (i.e. all cells with the same state), which would be the spatial equivalent of the stable fixed point in the spatially uncoupled (i.e., with $D = 0$) system. Upon the introduction of a perturbation, two related questions follow: what are the conditions for this homogeneous state to lose stability, and how does the previously uniform spatial structure change after the instability? A simple, but uninteresting, case would be an instability where the homogeneous state transitions to another homogeneous state. While the spatial structure of the transients could be interesting (for example, via the formation of travelling waves), we are not going to study such cases. Instead, we will focus on situations where the homogeneous state, with its spatially uniform structure, loses stability due to diffusion, and another spatially inhomogeneous (where cells end up in different states) pattern appears.

Let's consider, as in the non-spatial case, a perturbation around the homogeneous state $\mathbf{u}_h$, given by $\delta\mathbf{u}_{ij} = \mathbf{u}_{ij} - \mathbf{u}^h$, where in this case the perturbation does not affect the homogeneous state uniformly, but can depend on the spatial position $(i, j)$. The perturbation can change in time according to:

$$\frac{d}{dt}\delta\mathbf{u}_{ij} = \frac{d\mathbf{u}_{ij}}{dt} - \frac{d\mathbf{u}^h}{dt} = \frac{d\mathbf{u}_{ij}}{dt} \equiv \mathbf{F}[\mathbf{u}_{ij}] + D\nabla^2\mathbf{u}_{ij}(\mathbf{x}) \tag{3.28}$$

where the last but one equality holds because $\frac{d\mathbf{u}^h}{dt} = 0$. Since $\mathbf{u}_{ij} = \delta\mathbf{u}_{ij} + \mathbf{u}^h$, we can Taylor-expand the function $\mathbf{F}$ for small perturbations, $\mathbf{F}[\delta\mathbf{u}_{ij} + \mathbf{u}^h] \simeq \mathbf{F}[\mathbf{u}^h] + \mathbf{F}'[\mathbf{u}^h]\delta\mathbf{u}_{ij}$, where $\mathbf{F}'[\mathbf{u}^h]$ denotes the gradient of $\mathbf{F}$ evaluated at the homogeneous state $\mathbf{u}^h$, i.e. the Jacobian $J$. Since by definition $\mathbf{F}[\mathbf{u}^h] = 0$, and $\nabla^2\mathbf{u}^h = 0$ we are left with the following equation for the time-evolution of the perturbation $\delta\mathbf{u}_{ij}$:

$$\frac{d}{dt}\delta\mathbf{u}_{ij} = J\delta\mathbf{u}_{ij} + D\nabla^2\delta\mathbf{u}_{ij} = \hat{L}\delta\mathbf{u}_{ij} \tag{3.29}$$

where we wrote $J \equiv \mathbf{F}'[\mathbf{u}^h]$ and defined the matrix operator $\hat{L} \equiv J + D\nabla^2$. While the first term merely consists of a multiplying factor, the role of the second term is to transform any quantity at position $i, j$ to its corresponding set of neighbours, in this case the four adjacent cells given by the labelling scheme of the square lattice.

The solution of the previous equations does not follow immediately as in the non-spatial case, where a linear combination of exponentials came as a direct solution to the linear differential equation. In the spatial case, due to the linear nature of the operator $\hat{L}$, we can try to solve the problem in a similar manner, by assuming that the solution also has the form of a linear combination of exponentials, but in this case both in time and space. Thus, we consider the following *ansatz* for the perturbation around the homogeneous state:

$$\delta \mathbf{u}_{jk} = \sum_{r,s}^{N,M} \mathbf{A}_{rs} e^{2\pi i(\frac{jr}{N}+\frac{ks}{M})} e^{\sigma_{rs} t} \tag{3.30}$$

where we switched notation from the dummy indices $i, j$ to $j, k$ to avoid any confusion with the imaginary unit $i = \sqrt{-1}$. Let's try to digest what writing the perturbation in such a way really expresses. First, notice that the sum consists of a linear superposition of the terms, or modes $r, s$, each associated with an amplitude $\mathbf{A}_{rs}$ and a phase $e^{2\pi i(\frac{jr}{N}+\frac{ks}{M})} e^{\sigma_{rs} t}$. These amplitudes are just numbers, and set the strength or weight of each mode, while the phase encodes both the spatial and temporal dependencies. Since the spatial parts are complex exponentials, we can think of them as dictating which combinations of sines and cosines are going to be present in the spatial structure of each mode, with terms such as $\cos(6\pi ij/N + 10\pi ik/M)$ (for the mode $(r, s) = (3, 5)$), each modulated by its corresponding amplitude. Indeed, written in this way, the perturbation can be thought of as being decomposed in its Fourier components, with an inverse transform given by:

$$\mathbf{A}_{rs} = \frac{1}{NM} \sum_{j,k}^{N,M} \delta \mathbf{u}_{jk} e^{-2\pi i(\frac{jr}{N}+\frac{ks}{M})} e^{-\sigma_{rs} t} \tag{3.31}$$

Finally, the term $e^{\sigma_{rs} t}$ is the one selecting which mode of the perturbation will grow, decay or oscillate in time, depending on the structure of the complex growth rate $\sigma_{rs} = \mathrm{Re}(\sigma_{rs}) + i\mathrm{Im}(\sigma_{rs})$. If for a mode $r, s$ we have $\mathrm{Re}(\sigma_{rs}) < 0$, then the mode will decay in time, as the corresponding term will go to zero as $t \to \infty$. If instead a mode $r, s$ has $\mathrm{Re}(\sigma_{rs}) > 0$, then depending on $\mathrm{Im}(\sigma_{rs})$ two things can happen: for $\mathrm{Im}(\sigma_{rs}) > 0$ the mode will oscillate in time, leading to a periodic, possibly inhomogeneous behaviour that will depend on the amplitude of each mode. If $\mathrm{Im}(\sigma_{rs}) \leq 0$ oscillations decay and instead a spatially inhomogeneous structure can emerge, modulated by the specific values of $r, s$ and the amplitude $\mathbf{A}_{rs}$.

To make things less abstract, let's apply this to our reaction diffusion model in a $2d$ square lattice. Substituting Equation 3.30 into Equation 3.29, we obtain the following expression:

$$\sum_{r,s}^{N,M} \sigma_{rs} \mathbf{A}_{rs} e^{2\pi i(\frac{jr}{N}+\frac{ks}{M})} e^{\sigma_{rs} t} = J\delta \mathbf{u}_{jk} - 4D\delta \mathbf{u}_{jk} + D\Omega_{rs} \delta \mathbf{u}_{jk} \tag{3.32}$$

where $\Omega_{rs}$ is defined as

$$\Omega_{rs} \equiv 2\cos\left(\frac{2\pi r}{N}\right) + 2\cos\left(\frac{2\pi s}{M}\right) \tag{3.33}$$

This factor appears due to the residual exponential terms which can come out of the sum and be expressed in trigonometric form in light of Euler's for-

mula for the cosine, i.e. $2\cos(x) = e^{ix} + e^{-ix}$. The specific form of this function will depend on the neighbour structure of the lattice. In this case, $\Omega_{rs}$ corresponds to a square lattice with the classic von Neumann neighbourhood. For an hexagonal lattice with the labelling shown in Figure 3.5, for example, a similar form can be obtained[1]. Notice that we can write the right hand side of the previous equation as $(J - 4D + D\Omega_{rs})\delta\mathbf{u}_{jk} \equiv \mathbb{J}\delta\mathbf{u}_{jk}$, where the new Jacobian $\mathbb{J}$ has been defined. Thus, our original Jacobian $J$ as defined in the non-spatial case has now been modified by the addition of a new term $J_D \equiv -4D + D\Omega_{rs}$, representing the spatial coupling through diffusive interactions. Homogeneous patterns correspond to $\Omega_{rs} = 4$ (corresponding to the modes $(r, s) = (0, 0)$ or $(r, s) = (N, M)$), while periodic structures such as the salt-and-pepper (or chessboard) pattern (with modes $(r, s) = (N/2, M/2)$) have $\Omega_{rs} = 0$. We now make use of the orthonormality of the Fourier series to obtain a closed-form solutions for the growth rate. Recall that in a discrete Fourier decomposition, the terms $e_r \equiv \frac{1}{\sqrt{N}} e^{2\pi i r n/N}$ form an orthonormal basis over the set of $N$-dimensional complex vectors, i.e. they have an inner product of the form $\langle e_r, e_p \rangle = \frac{1}{N}\sum_{n=1}^{N} e^{\frac{2\pi i n}{N}(r-p)} = \delta_{rp}$. In two dimensions, as is our case, these eigenfunctions have the form $e_{rp} \equiv \frac{1}{\sqrt{NM}} e^{\frac{2\pi i r n}{N} + \frac{2\pi i p m}{M}}$, with a similar inner product $\langle e_{rs}, e_{pq} \rangle = \frac{1}{NM}\sum_{n,m}^{N,M} e^{\frac{2\pi i n}{N}(r-p)} e^{\frac{2\pi i m}{M}(s-q)} = \delta_{sq}^{rp}$, where $\delta_{sq}^{rp}$ is a four-dimensional Kronecker delta, being 1 for $r = p$ and $s = q$ and 0 otherwise. Due to this condition, there is a one-to-one correspondence between the terms on the left hand side of Equation 3.32 and the terms on the right hand side. This can be formally seen by noticing that the perturbation can be written as:

$$\delta\mathbf{u}_{jk} = \sum_{r,s}^{N,M} \mathbf{A}_{rs} e^{\sigma_{rs} t} e_{rs} \tag{3.34}$$

where $e_{rs}$ is a basis function as defined previously. Then, by projecting another orthogonal eigenfunction $e_{pq}$, corresponding to the mode $(p, q)$, to Equation 3.32, and taking the inner product, one obtains:

$$\sum_{r,s}^{N,M} \sigma_{rs}\mathbf{A}_{rs}\langle e_{rs}, e_{pq}\rangle e^{\sigma_{rs}t} = \mathbb{J}\sum_{r,s}^{N,M} \mathbf{A}_{rs}\langle e_{rs}, e_{pq}\rangle e^{\sigma_{rs}t} \tag{3.35}$$

Using the properties of the Kronecker delta, the only terms different than zero will be the ones corresponding to $r = p$ and $s = q$. By factoring out the common term $e^{\sigma_{pq}t}$, we finally arrive to an equation for the amplitude of each mode:

$$\sigma_{pq}\mathbf{A}_{pq} = \mathbb{J}\mathbf{A}_{pq}, \quad \text{or} \quad (\mathbb{J} - \mathbb{I}\sigma_{pq})\mathbf{A}_{pq} = 0 \tag{3.36}$$

where $\mathbb{I}$ is the identity matrix. Thus, all this tedious process eventually boils

[1] In particular, $\Omega_{rs} \equiv 2\cos\left(\frac{2\pi r}{N} - \frac{2\pi s}{M}\right) + 2\cos\left(\frac{2\pi r}{N}\right) + 2\cos\left(\frac{2\pi s}{M}\right)$

down to, once again, finding the eigenvalues of a Jacobian $\mathbb{J}$, which are just the possible values of the growth rate $\sigma_{pq}$. As already mentioned, the signs of the real and imaginary parts of these eigenvalues will dictate how the homogeneous state behaves upon a perturbation. In this case, there is an explicit dependence on the mode numbers $(p, q)$, so when an instability occurs, there will be some preferred modes which will dominate over the others.

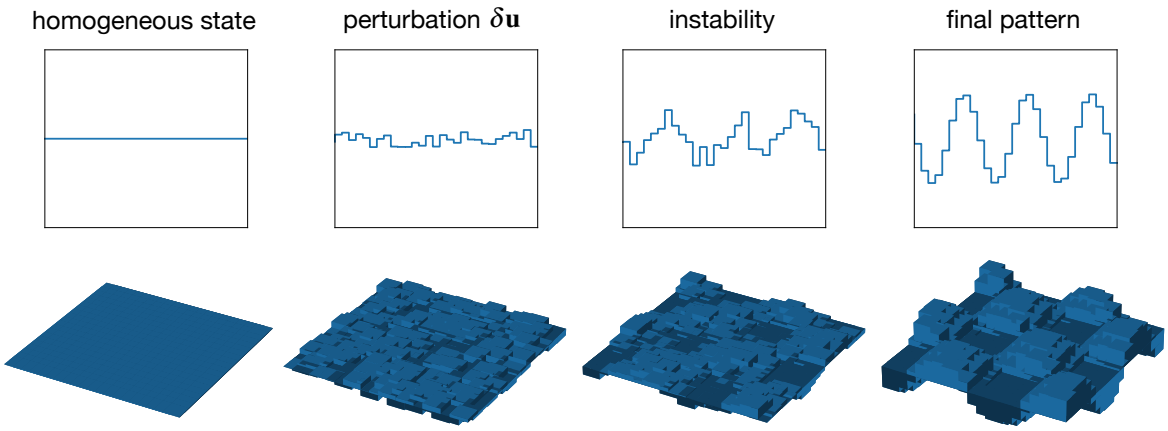



**Figure 3.8: Diffusion induced instability in a discrete lattice.** An homogeneous steady state (first panel) may lose stability due to diffusive coupling with its neighbouring cells. A perturbation (second panel) may destabilize the steady state, and the modes corresponding to the eigenvalues with largest real part grow and become dominant (third panel, instability). A new inhomogeneous steady state is reached with a spatial structure, which is modulated by the largest growing modes for parameters close to the transition point (last panel).

A particularly interesting type of instability common in reaction-diffusion systems is the *Turing instability* (or diffusion-induced instability), where a stable fixed point in the absence of spatial coupling becomes unstable when diffusion is introduced. This may lead to having $\mathrm{Re}(\sigma_{pq}) > 0$ and $\mathrm{Im}(\sigma_{pq}) = 0$, i.e. the system becomes unstable to perturbations of one or several modes $p, q$, and an inhomogeneous spatial state emerges (Figure 3.8). This type of instability will appear in Chapter 7, where the largest growing modes correspond to $(p, q) = (N/2, M/2)$, leading to salt-and-pepper patterns, where the activity of cells periodically alternates between ON and OFF states. Also in Chapter 7 we are going to encounter hybrid situations where modes with $\mathrm{Re}(\sigma_{pq}) > 0$ and $\mathrm{Im}(\sigma_{pq}) = 0$ appear together with other modes with $\mathrm{Re}(\sigma_{p'q'}) > 0$ and $\mathrm{Im}(\sigma_{p'q'}) > 0$, i.e. Turing modes and oscillatory modes will coexist in the system. This will lead to interesting behaviours such as transient homogeneous oscillations becoming arrested to form periodic patterns, or the formation of concentric circles.

### 3.2.3 Noise and the chemical Langevin equation

Gene regulation is an inherently random process, owing to the fact that the molecules involved are usually present in low numbers [Kaern et al., 2005, Elowitz et al., 2002]. It is acknowledged that these fluctuations—also called noise—are not always a detrimental force for biological systems [Tsimring, 2014]. In some cases these random effects can have dramatic consequences, as it happens, for example, in certain bacteria, where fluctuations are exploited to rapidly produce transcription factors controlling cellular differentiation [Süel et al., 2006]. Detailed accounts on the effects of noise in gene regulation can be found, for instance, in [Paulsson, 2005] and [Swain et al., 2002].

A common approach for incorporating noise in systems of molecular species such as those described in this chapter is through the so called chemical Langevin equation [Gillespie, 2000]. It consists of a continuous-time description of each species where stochastic effects appear as a multiplicative term, which is explicitly dependent on the interactions between molecules. For a single species whose concentration is denoted by $X$ (for example, a protein), produced with rate $P(X)$ and degraded with rate $D(X)$, the chemical Langevin equation can be written as:

$$\frac{dX}{dt} = P(X) - D(X) + \sqrt{|P(X)| + |D(X)|}\xi(t) \tag{3.37}$$

where $\xi(t)$ is an uncorrelated white Gaussian noise fulfilling $\langle \xi(t) \rangle = 0$, and autocorrelation $\langle \xi(t)\xi(t') \rangle = \frac{1}{\Omega}\delta(t - t')$, where $\Omega$ is the volume of the system, the conversion factor relating concentrations with protein numbers. In contrast to more general descriptions of stochastic systems via master equations, the Langevin approach works with continuous variables, allowing easier numerical implementations. In Chapter 7 we make use of this type of stochastic description to show that the presence of noise induces novel behaviours which are not predicted by its deterministic counterpart, such as noise-induced oscillations and pattern formation.

# Part II

# BRAVO and WOX5 in the stem cell niche

# Chapter 4

# Regulatory control at the *Arabidopsis* root stem cell niche

## Contents


**4.1 Introduction . . . . . 60**
**4.2 Experimental data and its interpretation . . . . . 61**
**4.3 Two possible circuits for the regulations between BRAVO and WOX5 . . . . . 66**
4.3.1 Modelling mutants and overexpressors . . . . . 69
**4.4 BRAVO and WOX5 directly interact to form a heterodimeric complex . . . . . 76**
4.4.1 The effect of additional sequestrators . . . . . 82
**4.5 The BRAVO-WOX5 complex is sufficient for the control of QC divisions . . . . . 84**
**4.6 Discussion . . . . . 89**


This chapter evaluates the interconnected role of the two transcription factors BRAVO and WOX5 in controlling stem cell niche homeostasis in the primary root of *Arabidopsis thaliana*. Building on our collaborators' experimental observations on promoter activities, we first propose two qualitatively distinct regulatory circuits between the two factors, which can recapitulate the behaviour of promoter expressions in wild-type and mutant plants. In one of the models, WOX5 is directly activated by BRAVO, while in the other, BRAVO indirectly activates WOX5 by alleviating its negative feedback. These interactions are effective, as multiple factors could be acting as intermediaries. The models are based on systems of coupled differential equations governing the time evolution of the expression of the BRAVO and WOX5 in the whole SCN. In light of the

absence of temporal data, they are studied in the stationary state. Exploring the model's parameters allows us to select the alleviation case as the most plausible candidate for the effective regulations between BRAVO and WOX5. Notably, a biochemical realization of the alleviation model can be introduced by considering the formation of an heterodimer complex between the two proteins, whose main function is to inactivate the transcriptional functions of the unbound proteins. Indeed, data from our collaborators show that BRAVO and WOX5 physically interact *in vitro*, thus providing additional experimental support to the model. This new approach naturally incorporates all the experimental observations and allows us to propose a simple framework for the regulation of QC division by BRAVO and WOX5.

The results presented in this chapter have been published in [Betegón-Putze et al., 2021] jointly with all the experimental data from our collaborators. Here we focus on the modelling part of this work, showing only the most relevant experiments related to the models.

## 4.1 Introduction

The development of the *Arabidopsis* root SCN is tightly controlled, both in time and space, by multiple signalling molecules, including transcription factors, phytohormones, small peptides, microRNAs, and reactive oxygen species [Aichinger et al., 2012, González-García et al., 2011, Berckmans et al., 2020, Yu et al., 2016, Knauer et al., 2013]. Transcription factors are the most widely explored, owing to their relatively easy quantification, primarily via fluorescent markers such as green fluorescent proteins (GFP) or through quantitative polymerase chain reaction (qPCR). As already mentioned in Chapter 2 (Section 2.1), the identity of these stem cells is controlled by the spatial convergence of several transcription factors, including SHR, SCR, and PLT genes [Aida et al., 2004, Shimotohno et al., 2018, Sabatini et al., 2003], together with their direct interaction with RETINOBLASTOMA-RELATED (RBR) proteins, which regulate the identity of QC cells [Sabatini et al., 2003, Cruz-Ramírez et al., 2012, Cruz-Ramírez et al., 2013]. This overlap coincides with the expression domain of the QC-specific transcription factor WUSCHEL-RELATED HOMEOBOX5 (WOX5), which has been shown to promote quiescence to QC cells through the regulation of cell cycle genes [Sarkar et al., 2007, Forzani et al., 2014]. Moreover, disruption of WOX5 activity has also been associated with overall disorganization of the QC and premature differentiation of columella stem cells [Sarkar et al., 2007, Pi et al., 2015]. More recently, brassinosteroids, the steroid hormones of plants, have also been shown to regulate QC activity through the MYB transcription factor BRAVO (BRASSINOSTEROIDS AT VASCULAR AND ORGANIZING CENTER), via its interaction with the BRI1-EMS-SUPPRESSOR 1 BES1 [Vilarrasa-Blasi et al., 2014].

While the regulations between SCR, SHR, PLTs have been well-studied, both

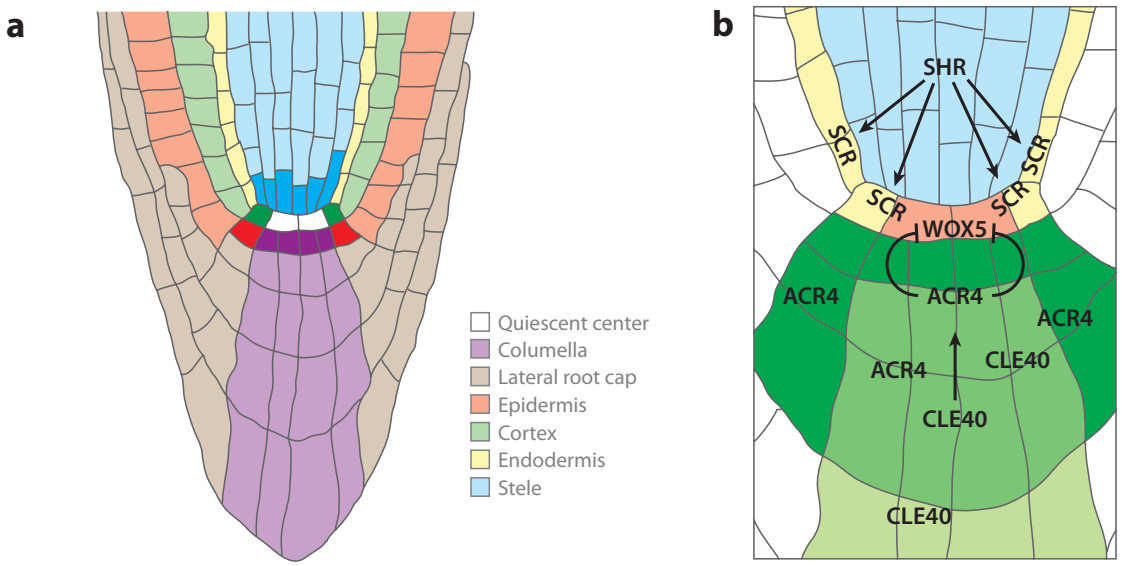



**Figure 4.1: Classic picture of SCN maintenance in the *Arabidopsis* root apical meristem. a)** Organization of the root stem cell niche. In white, cells in the quiescent center. Dark colors represent the stem cells surrounding the QC; dark blue cells are vascular initials; dark green marks the cortex and endodermis stem cells; dark purple are the columella stem cells; and dark red marks the stem cells for the epidermis and lateral root cap. **b)** The activity of WOX5 is confined to the QC, a regulation controlled by the convergence of SHR, SCR and PLT (not shown). Morover, the small peptide CLE40, expressed in differentiated columella cells, acts via its putative receptors ACR4 and CLV1 (not shown) to repress WOX5 expression. Adapted from [Aichinger et al., 2012].

genetically and through modelling, the role of BRAVO in the maintenance of QC identity still remains poorly understood, probably due to its recent characterization as a genuine transcription factor and the limited phenotype of *bravo* mutants, whose main feature is an increase in the frequency of QC division, with no apparent, large-scale disorders [Vilarrasa-Blasi et al., 2014]. As BRAVO and WOX5 have individually been shown to affect the frequency of QC division, we asked whether this happens independently of one another, or instead, their action involves a common mechanism. Moreover, BRAVO can regulate WOX5 expression, as evidenced by the decrease in WOX5 activity in *bravo* loss of function mutants [Vilarrasa-Blasi et al., 2014]. Our aim in the following sections is to understand the mutual regulations between BRAVO and WOX5 and how their collective action can help us understand their role as QC regulators.

## 4.2 Experimental data and its interpretation

Experimental evidence from our collaborators sheds light on the regulatory and molecular interactions between BRAVO and WOX5 and discloses a common role as regulators of primary and lateral root development [Betegón-Putze et al., 2021]. Here we use these data to infer the effective regulations between the

two, allowing us to propose specific mechanisms by which they may interact. Both BRAVO and WOX5 are expressed in QC cells and have been shown to promote their quiescent state, as loss of function mutations of either BRAVO (*bravo* mutants) or WOX5 (*wox5* mutants) show an increase in the frequency of QC divisions [Forzani et al., 2014, Vilarrasa-Blasi et al., 2014]. Figure 4.2E shows how QC divisions become more frequent in *bravo* and *wox5* mutants compared to WT (*Col-0*) plants. Plants with loss of function of both BRAVO and WOX5 (*bravo wox5* mutants) also show more divisions when compared to WT plants [Betegón-Putze et al., 2021]. Remarkably, all three mutants show a similar increase, pointing to non-additive effects in their control of QC division. Moreover, as shown in Figure 4.2F, while WOX5 clearly has an effect on CSC differentiation, BRAVO does not [Vilarrasa-Blasi et al., 2014, Sarkar et al., 2007]. The phenotypic similarities between single *wox5* and double *bravo wox5* mutants further suggest that the role of BRAVO is highly conditional on WOX5. To address whether these stem cell-specific defects account for general alterations in root growth and development, our collaborators also quantified changes in root architecture. Double mutant *bravo wox5* plants exhibit slightly but significantly shorter roots than the WT (Figure 4.18) and fewer lateral root density (Figure 4.2G). In the case of the lateral root density, 7-day-old *bravo wox5* seedlings show the same phenotype as the single mutants (Figure 4.2G), in agreement with previous reports for *wox5* mutants [Tian et al., 2014a]. Root growth defects become more exaggerated in *bravo wox5* double mutants than WT and single mutants in 10-day-old seedlings (Figure 4.18B), therefore supporting a joint contribution of BRAVO and WOX5 to overall root growth and architecture.

While the phenotypes of QC division and root architecture already hint at the mutual regulatory roles of BRAVO and WOX5—particularly the strong dependence of BRAVO upon WOX5—further potential regulatory interactions between the two transcription factors must be inferred otherwise. The most straightforward way to do this in practice is to analyze the promoter expression of each gene in loss of function mutants and compare them with the WT. These can be visualized through a GFP reporter, with the lines *pBRAVO:GFP* and *pWOX5:GFP*. Our collaborators further constructed the loss of function lines *bravo-1;pBRAVO:GFP* and *bravo-1;pWOX5:GFP*, which allow the visualization of the activity of the BRAVO and WOX5 promoters, respectively, in plants where BRAVO proteins are not functional; the lines *wox5-2;pBRAVO:GFP* and *wox5-2;pWOX5:GFP*, where WOX5 proteins are not functional; and the double mutant lines *bravo-1 wox5-2;pBRAVO:GFP* and *bravo-1 wox5-2;pWOX5:GFP*, where neither BRAVO nor WOX5 are functional. Moreover, our collaborators further generated the overexpression lines *35S:WOX5-GR* and *35S:BRAVO-Ei*, where WOX5 and BRAVO are placed under the control of the constitutive promoter 35S, and can be induced upon dexamethasone treatment; and the overexpression line *35S:BRAVO-Ei;pWOX5:GFP*, where *pWOX5:GFP* is placed under

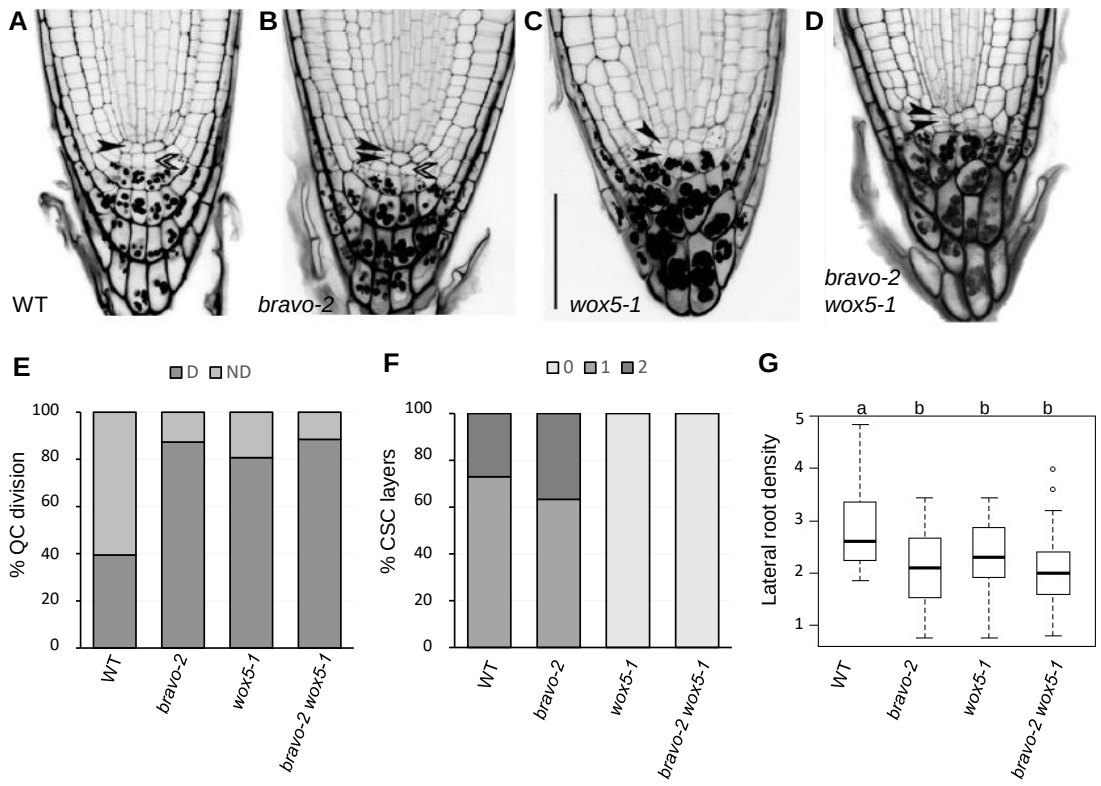



**Figure 4.2: BRAVO and WOX5 are required for the QC identity and stem cells maintenance. A-D)** Confocal images PI stained 6-day-old seedlings of WT (A), *bravo-2* (B), *wox5-1* (C) and *bravo-2 wox5-1* (D) mutants. Left black arrows indicate QC cells and right white arrows indicate CSC. Scale bar: 50 $\mu$m. **E)** Quantification of the QC divisions in 6-day-old roots expressed in percentage ($n > 50$, 3 replicates). D: QC divided; ND: QC non divided. **F)** Quantification of CSC layers in 6-day-old roots expressed in percentage ($n > 50$, 3 replicates). **G)** Lateral root density (number of lateral roots per mm of root length) of 7-day-old WT, *bravo-2*, *wox5-1* and *bravo-2 wox5-1* mutants ($n > 40, 2$ replicates). Different letters indicate statistically significant differences ($p$-value $< 0.05$ Student's $t$-test). Figure as in [Betegón-Putze et al., 2021].

the control of the constitutive promoter 35S fused with the BRAVO sequence, and is induced upon estradiol. With these lines, we can visualize the activity of each promoter when the opposite gene is constitutively expressed in the whole root. Thus, using GFP as a proxy for expression, all the above lines allow the direct visualization and subsequent quantification of each promoter's activity. These expression patterns can be seen in Figure 4.3A-G, Figure 4.18F,G and Figure 4.19C.

In *bravo* mutants, the activity of *pBRAVO:GFP* increases with respect to the WT and expands its domain towards the vasculature (Figure 4.3B,H), suggesting that BRAVO negatively regulates its own expression (we will explore this further in Chapter 5). Since this increase disappears in *bravo wox5* double mutants (Figure 4.20C), this means that the negative feedback of BRAVO must

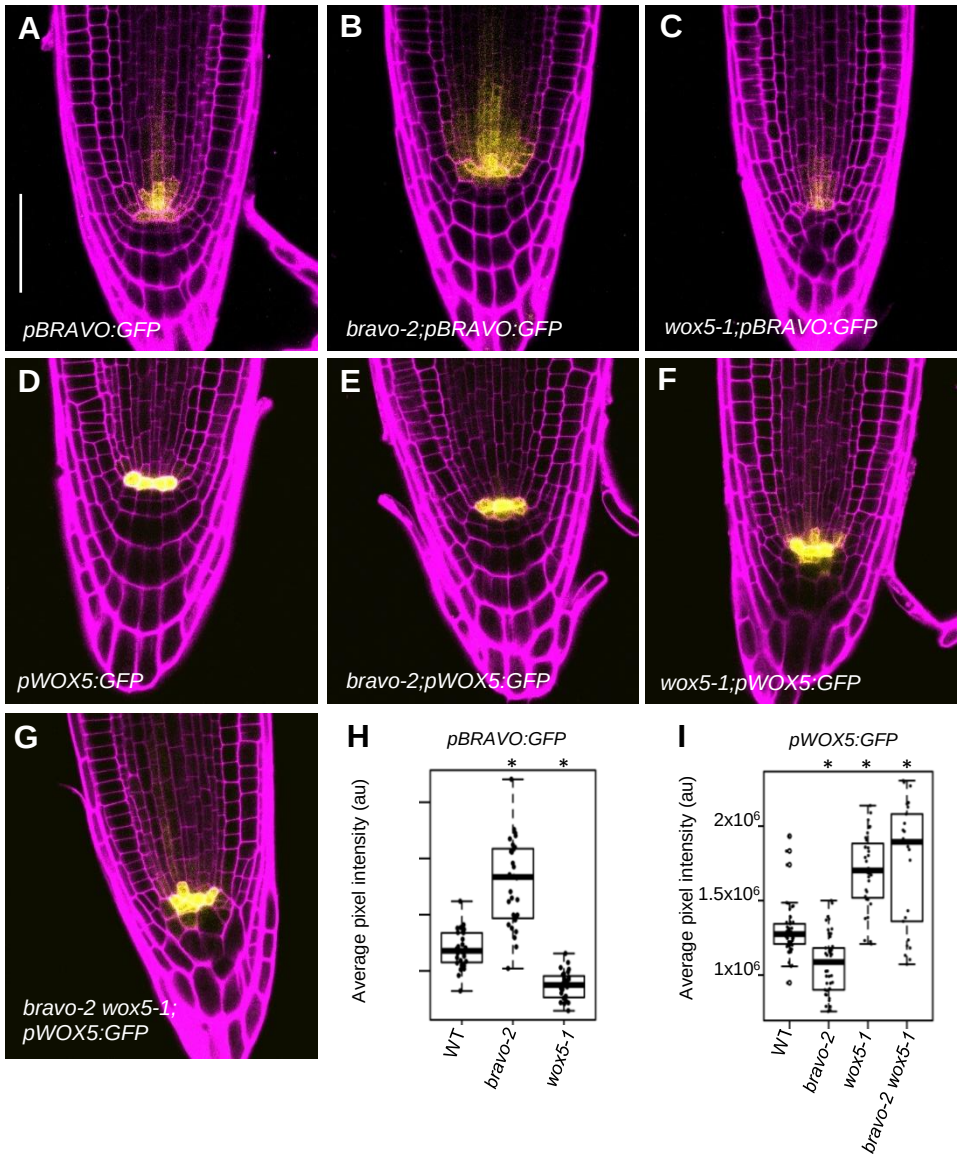



**Figure 4.3: GFP expression of *pBRAVO* and *pWOX5* in WT and mutants. A-G)** Confocal images of PI-stained 6-day-old roots, with GFP-tagged expression shown in yellow. A-C) *pBRAVO:GFP* in WT (A), *bravo-2* (B) and *wox5-1* (C) loss of function mutants. D-G) *pWOX5:GFP* in the WT (D), *bravo-2* (E), *wox5-1* (F) and *bravo-2 wox5-1* (G) mutants. Scale bar: 50 $\mu$m. **H-I)** Quantification of the total GFP signal integrated over a defined region of the roots in A-C (H) and D-G (I). Boxplots indicate the average pixel intensity of the GFP in the stem cell niche ($n > 25$, 3 biological replicates, $p$-value $< 0.05$ Student's $t$-test for each genotype versus the WT in the same condition). Quantification has been performed by integrating the GFP signal in each root across defined areas that included the whole SCN. Figure as in [Betegón-Putze et al., 2021].

be WOX5-dependent. Also, in *bravo* mutants, the activity of *pWOX5:GFP* suffers a slight but significant decrease when compared to the WT (Figure 4.3E,I), suggesting that BRAVO promotes the expression of WOX5. As we will see in the next section, this effective activation can be rationalized in two different

| Experiment | Result | Interpretation |
|---|---|---|
| *wox5-1:pBRAVO:GFP* | *pBRAVO:GFP* expression decreases with respect to the WT | WOX5 promotes *BRAVO* expression |
| *35S:WOX5-GR* (qPCR) | *pBRAVO:GFP* expression increases with respect to the WT | WOX5 promotes *BRAVO* expression |
| *35S:BRAVO-Ei:pWOX5:GFP* | *pWOX5:GFP* expression remains as in the WT | BRAVO does not promote *WOX5* further |
| *wox5-1:pWOX5:GFP* | *pWOX5:GFP* increases with respect to the WT | WOX5 negatively feeds back on its own expression |
| *bravo-2:pWOX5:GFP* | *pWOX5:GFP* expression decreases with respect to the WT | BRAVO promotes *WOX5* activity |
| *bravo-2:pBRAVO:GFP* | *pBRAVO:GFP* expression increases with respect to the WT | BRAVO negatively feeds back on its own expression |
| *bravo-2 wox5-1:pBRAVO:GFP* | *pBRAVO:GFP* expression decreases with respect to the WT, similarly to *wox5-1* mutants | WOX5 promotes *BRAVO* expression. The negative feedback of BRAVO requires WOX5 |
| *bravo-2 wox5-1:pWOX5:GFP* | *pWOX5:GFP* expression increases with respect to the WT, similarly to *wox5-1* mutants | The WOX5 regulation by BRAVO is conditional on WOX5 |

**Table 4.1:** Table summarizing the experimental observations of *pBRAVO:GFP* and *pWOX5:GFP* in WT plants, in *bravo*, *wox5* and *bravo wox5* mutants, and in the overexpression lines *35S:WOX5-GR* and *35S:BRAVO-Ei:pWOX5:GFP*. From these observations we can infer the possible interactions between the two transcription factors.

ways.

In *wox5* mutants, the activity of *pBRAVO:GFP* decreases, especially in the QC (Figure 4.3C,H), pointing to activation of BRAVO expression by WOX5. Finally, the domain of *pWOX5:GFP* activity expands in *wox5* mutants (Figure 4.3F,I), suggesting that WOX5 negatively regulates its own expression. A similar effect is observed *bravo wox5* double mutants (Figure 4.3G,I), pointing to a redundancy of BRAVO in *wox5* mutants. Therefore, the effective self-repression of WOX5 does not seem to be regulated by BRAVO.

Overexpression lines can give us further insight into the inferred regulations. When WOX5 is overexpressed via the 35S promoter, the expression of BRAVO (as measured by qPCR of root tips, see Figure 4.19) increases dramatically, further strengthening the hypothesis that WOX5 activates BRAVO. In contrast, the activity of WOX5 when placed under the 35S:BRAVO promoter does not change with respect to the WT, suggesting that BRAVO is not sufficient to induce an increase of WOX5 expression. In Table 4.1 we summarize how we interpret these effective interactions using the experimental results.

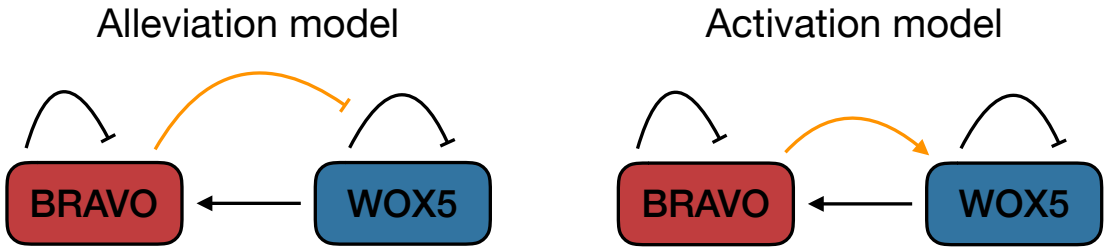



**Figure 4.4: Generic interactions between BRAVO and WOX5.** The activation and alleviation models share most of the interactions, namely the BRAVO activation by WOX5 and the self-repression of BRAVO and WOX5 (black arrows), but differ in how BRAVO regulates the expression of WOX5, i.e. in the alleviation model BRAVO represses the WOX5 self-repression, while in the activation model BRAVO induces the expression of WOX5 (yellow arrows).

## 4.3 Two possible circuits for the regulations between BRAVO and WOX5

To understand the regulations between BRAVO and WOX5[1], we propose two distinct mathematical models that can account for the experimental observations. This is motivated by the fact that some of the effective interactions between BRAVO and WOX5 cannot be unequivocally determined from the experimental data, as GFP measures the net effect of all the possible regulations. In particular, the fact that *pWOX5:GFP* does not change upon BRAVO overexpression suggests that either the activation is indirect, or that *pWOX5:GFP* is already saturated in the WT. In the first model, dubbed *alleviation model*, *BRAVO* indirectly activates *WOX5* by impairing the negative regulation *WOX5* exerts on its own promoter. In the second model, the *activation model*, *BRAVO* directly activates *WOX5* expression. The models are effective, i.e. they are assumed to encompass several possible transcriptional and post-transcriptional mechanisms, which may take place across the whole SCN and involve several intermediate molecules. As we will see, while both scenarios are able to reproduce experimental data, they differ in interpretation.

Three of the interactions are shared among both models: *WOX5* activates the expression of *BRAVO*, and *BRAVO* and *WOX5* negatively regulate their own expression. In Figure 4.4 we sketch a simplified diagram of the two mechanisms, the description of which is going to be explained along the following lines. Interactions common to both models are represented as black arrows, while those that make them different are drawn as yellow arrows. These common regulations are translated in mathematical form as follows. First, we define

[1]From now on we will use the following notation: we will write in regular font and capital letters when referring to the protein of a certain gene (e.g. BRAVO proteins), but in italic when referring to its mRNA (e.g. *BRAVO* expression)

the variables $B$ and $W$, describing the total mRNA expression of *BRAVO* and *WOX5* at the root tip, respectively. Each of these expressions is produced through the activity of their corresponding promoters, respectively denoted as $P_B$ and $P_W$, which will be functions of both $B$ and $W$. Therefore, in this framework, the mutual regulations between *BRAVO* and *WOX5* are implemented through their effect on the promoter activities $P_B$ and $P_W$. Thus, by further assuming that $B$ and $W$ are linearly degraded with rates $d_B$ and $d_W$, our models can be cast in the form of ordinary differential equations in the following way:

$$\frac{dB}{dt} = P_B(B,W) - d_B B \tag{4.1a}$$

$$\frac{dW}{dt} = P_W(B,W) - d_W W \tag{4.1b}$$

where the functions $P_B(B,W)$ and $P_W(B,W)$ will have different forms in each model. We implicitly assume that these functions integrate all the possible intermediate steps involved in gene regulation, including transcriptional and post-transcriptional processes within and between cells, with their corresponding intermediary molecules. However, as our aim is to model effective regulations, these intermediate steps will not be explicitly taken into account, but are altogether absorbed in the functionalities of $P_B$ and $P_W$. Due to these in-between processes, we expect the promoter functions to be non-linear. For both models we choose $P_B$ to have the same functionality, consisting of an activation term by *WOX5* and a negative feedback of *BRAVO* on its own expression (henceforth dubbed self-repression), as inferred from Table 4.1:

$$P_B(B,W) = \alpha\left(\frac{1+\varepsilon_B(K_B B)^2}{1+(K_B B)^2}\right)\left(\frac{1+\varepsilon_W(K_W W)^2}{1+(K_W W)^2}\right) \tag{4.2}$$

Here $\alpha$ represents the basal promoter activity of *BRAVO* (i.e. independent of *BRAVO* and *WOX5*), mathematically defined as the value of the promoter in the absence of both factors, $P_B(0,0) = \alpha$. The parameter $K_B$ sets the inhibition threshold of *BRAVO* activity by *BRAVO*, with inhibition strength $\epsilon_B < 1$, and $K_W$ sets the activation threshold of *BRAVO* activity by *WOX5*, with activation strength $\epsilon_W > 1$. This means that for large values of $B$ and $W$ (of the order of $B \gg 1/K_B$ (or $W \gg 1/K_W$)), the terms reach the values $\varepsilon_B$ and $\varepsilon_W$, respectively. Notice that the contribution of each factor on the functionality of the promoter is assumed to be independent of the other.

The difference between the activation and alleviation models lies in the functionality of the *WOX5* promoter. From Figure 4.3E,I, we can see a decrease in *pWOX5:GFP* activity in the *bravo* mutant, which would apparently indicate an activation of *WOX5* by *BRAVO*. In the activation model, where we assume this activation to take place, we propose the following functional form of the *WOX5* promoter:

$$P_W(B,W) = \gamma\left(\frac{W_0^2}{W_0^2+W^2}\right)\left(1+B_1\frac{B^2}{B_0^2+B^2}\right) \tag{4.3}$$

The parameter $\gamma$, represents the basal promoter activity of *WOX5* ($P_W(0,0) = P_W(B,0) = \gamma$), while $W_0$ sets the self-inhibition threshold of *WOX5*. $B_1$ represents the maximum value of the alleviation of *WOX5* by *BRAVO*, and $B_0$ is the threshold value corresponding to this alleviation. It is easy to see that in this model, the absence of *BRAVO* readily induces a decrease in *WOX5*, while an increase in *BRAVO* could instead potentially generate an increase. However, upon overexpressing BRAVO through a 35S promoter, no increase in *pWOX5:GFP* activity is observed (Figure 4.18B). This last piece of experimental data brings to mind another possible explanation for the apparent activation of *WOX5* by *BRAVO*: BRAVO could, instead of directly activate *WOX5*, alleviate the repression *WOX5* exerts on itself, thereby generating an effective activation. We model such alleviation mechanism through the following functional form of the *WOX5* promoter:

$$P_W(B,W) = \gamma\frac{W_0^2}{W_0^2+W^2\left(1+B_1\frac{B_0^2}{B_0^2+B^2}\right)^2} \tag{4.4}$$

Here $\gamma$ and $W_0$ are defined as in the activation model. $B_1$ and $B_0$ represent, respectively, the maximum repression rate of the *WOX5* self-repression by *BRAVO* and its corresponding threshold value. In the absence of *BRAVO*, the term multiplying $W^2$ in the denominator is equal to $(1+B_1)^2$, while in the presence of *BRAVO* the term is forcibly smaller, as $(1+B_1) > \left(1+B_1\frac{B_0^2}{B_0^2+B^2}\right)$ for $B > 0$. This means that in the presence of *BRAVO*, the self-repression of *WOX5* is alleviated, only being fully repressed if *BRAVO* is absent. By construction, in this model the role of *BRAVO* is conditional on the activity of *WOX5*, with the implication that single *wox5* and double *bravo wox5* mutants will behave in exactly the same manner.

The behaviour of these functions can be visualized in Figure 4.5, where $P_B$ and $P_W$ are plotted as a function of $B$ and $W$. For both models, the *BRAVO* promoter $P_B$ increases with *WOX5*, and three distinct regions can be characterized: one in which $W$ is high and *BRAVO* represses its own activity (light red region); one in which $W$ is also high but the low quantities of *BRAVO* do not allow self-repression to happen (dark red region); and one where $W$ is low, and the self-repressive effect of *BRAVO* is barely noticeable (white region). The *WOX5* promoter, for its part, is more dependent on *BRAVO* in the activation model that in the alleviation model. In particular, as the activity of *BRAVO* gets higher, for sufficiently low values of $W$ (so that *WOX5* self-repression is not large), $P_W$ strongly increases in the activation model but not as much in the alleviation model. This distinction will be important when comparing WT and

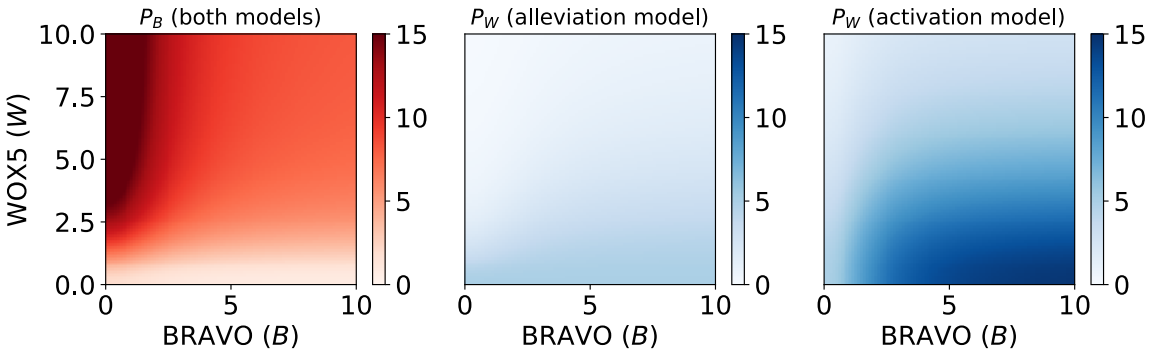



**Figure 4.5: Behaviour of $P_B$ and $P_W$ in the alleviation and activation models.** Heatmaps showing the behaviours of the functions $P_B(B,W)$ and $P_W(B,W)$, as defined by Equation 4.2, Equation 4.4 and Equation 4.3. Parameters are $\alpha = 2$, $\gamma = 5$, $K_B = 0.5$, $K_W = 0.5$, $\epsilon_B = 0.4$, $\epsilon_W = 10$, $W_0 = 5$, $B_0 = 2$, $B_1 = 2$, which have been chosen arbitrarily, only to show the qualitative behaviour of the functions.

mutants, as the results will tip the balance in favour of the alleviation model. The two models of *BRAVO* and *WOX5* interactions can thus be written as:

**Alleviation model**

$$\frac{dB}{dt} = \alpha\left(\frac{1+\varepsilon_B(K_B B)^2}{1+(K_B B)^2}\right)\left(\frac{1+\varepsilon_W(K_W W)^2}{1+(K_W W)^2}\right) - d_B B \tag{4.5a}$$

$$\frac{dW}{dt} = \gamma\frac{W_0^2}{W_0^2 + W^2\left(1 + B_1\frac{B_0^2}{B_0^2+B^2}\right)^2} - d_W W \tag{4.5b}$$

**Activation model**

$$\frac{dB}{dt} = \alpha\left(\frac{1+\varepsilon_B(K_B B)^2}{1+(K_B B)^2}\right)\left(\frac{1+\varepsilon_W(K_W W)^2}{1+(K_W W)^2}\right) - d_B B \tag{4.6a}$$

$$\frac{dW}{dt} = \gamma\left(\frac{W_0^2}{W_0^2+W^2}\right)\left(1 + B_1\frac{B^2}{B_0^2+B^2}\right) - d_W W \tag{4.6b}$$

In the next section we will explain how to use these models to make the comparison with experimental results.

### 4.3.1 Modelling mutants and overexpressors

The experiments shown in Figure 4.3 inform us about the promoter activities of *BRAVO* and *WOX5*. In the models proposed in the previous section we assume that $P_B$ and $P_W$ are a good proxy for comparison, the expressions of which can be found by solving the corresponding equations and substituting $B$ and $W$ into $P_B$ and $P_W$. While the equations of both models can be numerically solved at all times, the lack of temporal data on promoter expressions only allows static

comparisons between models and experiments. For this reason, we restrict ourselves to the study of the steady state of the system. This necessarily forces us to make again another assumption, namely that experimental observations of promoter activity are also in the stationary state.

Given the specific expressions for $P_B(B,W)$ and $P_W(B,W)$ for each model (here we don't consider a particular model, but a system for generic functions of $P_B(B,W)$ and $P_W(B,W)$), setting the equations to zero ($\frac{dB}{dt}=0$, $\frac{dW}{dt}=0$) lead to the pair of equations $B_s = P_B(B_s,W_s)/d_B$ and $W_s = P_W(B_s,W_s)/d_W$, where the subscript $s$ indicates that its values correspond to the stationary state. The remaining expressions have the form of algebraic equations that can be solved using standard numerical methods. The stationary solutions $B_s$ and $W_s$ can then be substituted into $P_B(B,W)$ and $P_W(B,W)$ to give the values of promoter activities in WT conditions. From now on, we will write the stationary values of the promoter expressions as $pB \equiv P_B(B_s,W_s)$ and $pW \equiv P_W(B_s,W_s)$. Thus, every time we write $pB$ or $pW$ we implicitly assume that we are in the stationary state. Specifically, in the WT we write $pB^{\mathrm{WT}} \equiv P_B(B_s,W_s)$ and $pW^{\mathrm{WT}} \equiv P_W(B_s,W_s)$.

To model *bravo* loss of function mutants, we simply set $B=0$, while for *wox5* mutants, $W=0$. Thus, denoting with the superscripts *bravo* and *wox5* the corresponding mutants, we can write the equations for these mutants as:

$$\frac{dW^{bravo}}{dt} = P_W(0,W^{bravo}) - d_W W^{bravo} \tag{4.7a}$$

$$\frac{dB^{wox5}}{dt} = P_B(B^{wox5},0) - d_B B^{wox5} \tag{4.7b}$$

where $P_B$ and $P_W$ have the same functional form as the WT (Equation 4.5 and Equation 4.6). Notice that while $B$ and $W$ are zero in their corresponding mutants, their promoter activities are not, and instead they change accordingly with the solution of their corresponding equations. After solving Equation 4.7, we define the promoter activities in these mutants as:

$$pB^{bravo} \equiv P_B(0,W^{bravo}), \quad pW^{bravo} \equiv P_W(0,W^{bravo}) \tag{4.8a}$$

$$pB^{wox5} \equiv P_B(B^{wox5},0), \quad pW^{wox5} \equiv P_W(B^{wox5},0) \tag{4.8b}$$

$$pB^{dm} \equiv P_B(0,0), \quad pW^{dm} \equiv P_W(0,0) \tag{4.8c}$$

where the subscript $s$ denoting stationarity has been dropped for clarity. We have also defined the promoters corresponding to *bravo wox5* double mutants, $pB^{dm}$ and $pW^{dm}$.

Overexpression is modelled by incorporating an additive constant in the pro-

| Parameter | Description | Value | Units |
|---|---|---|---|
| $\alpha$ | Basal production of *BRAVO* | 0.3 | nM $\text{min}^{-1}$ |
| $\gamma$ | Basal production of *WOX5* | 5 | nM $\text{min}^{-1}$ |
| $K_B$ | Threshold of *BRAVO* self-repression | 0.0017 | $\text{nM}^{-1}$ |
| $K_W$ | Threshold of *BRAVO* activation by *WOX5* | 0.02 | $\text{nM}^{-1}$ |
| $\varepsilon_B$ | Strength of *BRAVO* self-repression | 0.15 | – |
| $\varepsilon_W$ | Strength of *BRAVO* activation by *WOX5* | 10 | – |
| $W_0$ | Threshold of *WOX5* self-repression | 800 | nM |
| $B_0$ | Threshold of *BRAVO* repression of *WOX5* self-repression | 10 | nM |
| $B_1$ | Maximum value of *BRAVO* repression of *WOX5* self-repression | 1 | – |
| $d_B$ | *BRAVO* degradation | 0.01 | $\text{min}^{-1}$ |
| $d_W$ | *WOX5* degradation | 0.01 | $\text{min}^{-1}$ |
| $A_0$ | Change in basal activity in *BRAVO* overexpression | 10 | – |
| $G_0$ | Change in basal activity in *WOX5* overexpression | 10 | – |

**Table 4.2: Default parameters of the alleviation model.** Parameters are chosen to be biologically realistic and to qualitatively fit experimental results.

duction rate, in such a way that the production of *BRAVO* changes from $P_B$ to $P_B^{Boe} = P_B + \alpha A_0$, and the production of *WOX5* changes from $P_W^{Woe} = P_W + \gamma G_0$. The parameters $A_0$ and $G_0$ set the extent of the overexpression relative to the basal productions $\alpha$ and $\gamma$. In our case, the main goal of overexpressing a particular gene, say *WOX5*, is to see what is the corresponding effect on $pB$, the result of which can offer very useful information on their regulations.

Before actually comparing the results of the model with experiments, we are going to explore the model heuristically in order to find a set of parameters that make sense biologically, i.e. are within the range of values that can be found in the literature, and that at the same time are able to give the trends in promoter activities we see in the experiments. In eukaryotes, typical degradation rates of proteins and mRNAs are of the order of $\sim 0.1 - 0.001\text{min}^{-1}$ [Buchler et al., 2005, Buchler and Louis, 2008]. Production rates for proteins can be of the order of $0.1 - 100\text{nM min}^{-1}$ [Buchler et al., 2005, Schreiber et al., 2009], and we assume similar values for mRNA synthesis rates. Common values of dissociation constants in binding of transcription factors to promoters range from $0.01 - 100\text{nM}$ [Jung et al., 2018], while the rates of protein binding can take values of $0.001\text{nM}^{-1}$ to $1\text{nM}^{-1}$ [Buchler et al., 2005, Gerland et al., 2002].

Based on this data, we choose a default parameter set as described in Table 4.2 and Table 4.3, where we take into account biologically plausible ranges for each parameter. For example, we choose $\alpha = 0.3$ nM $\text{min}^{-1}$, while $\gamma = 5$ nM $\text{min}^{-1}$, revealing the higher synthesis of *WOX5* with respect to *BRAVO*, as experiments suggest. In order to show the inherent variability of the experiments, manifest even in plants within the same genotype, we solve the equations with different parameter sets, where each parameter is slightly varied from their default value. In particular, if $p_s = (\alpha, \gamma, K_B, \dots)$ is the default set of param-

| Parameter | Description | Value | Units |
|---|---|---|---|
| $\alpha$ | Basal production of *BRAVO* | 0.3 | nM $\text{min}^{-1}$ |
| $\gamma$ | Basal production of *WOX5* | 5 | nM $\text{min}^{-1}$ |
| $K_B$ | Threshold of *BRAVO* self-repression | 0.0015 | $\text{nM}^{-1}$ |
| $K_W$ | Threshold of *BRAVO* activation by *WOX5* | 0.03 | $\text{nM}^{-1}$ |
| $\varepsilon_B$ | Strength of *BRAVO* self-repression | 0.15 | – |
| $\varepsilon_W$ | Strength of *BRAVO* activation by *WOX5* | 10 | – |
| $W_0$ | Threshold of *WOX5* self-repression | 430 | nM |
| $B_0$ | Threshold of *WOX5* activation by *BRAVO* | 25 | nM |
| $B_1$ | Maximum activation of *WOX5* by *BRAVO* | 0.5 | – |
| $d_B$ | *BRAVO* degradation | 0.01 | $\text{min}^{-1}$ |
| $d_W$ | *WOX5* degradation | 0.01 | $\text{min}^{-1}$ |
| $A_0$ | Change in basal activity in *BRAVO* overexpression | 10 | – |
| $G_0$ | Change in basal activity in *WOX5* overexpression | 10 | – |

**Table 4.3: Default parameters of the activation model.** Parameters are chosen to be biologically realistic and to qualitatively fit experimental results.

eter values (Table 4.2 and Table 4.3), we create a uniform random distribution between $p_s/f$ and $fp_s$, where $f$ is a factor controlling the spread of the distribution. For convenience, we choose $f = 1.3$, meaning that the variability of each parameter value between plants is at most 30% from its default value.

In Figure 4.6 we show the stationary promoter activities of each model for $N = 1000$ simulations. Notice that in Figure 4.6 the promoter activities follow the same trends as their experimental counterparts (Figure 4.3H,I and Figure 4.19, Figure 4.20). Thus, for this set of parameters, both models recapitulate experimental observations on promoter expressions.

While these results already point to a good agreement between theory and experiments, a direct comparison may not be the best option. Since the GFP activity used to measure promoter activities has an arbitrary scale—which depends on the setting of the confocal microscope and on the actual production and degradation properties of the GFP molecule—instead of directly using the values of $pB$ and $pW$ and comparing them with their experimental counterparts, a better strategy is to compute the *ratios* between promoter activities in mutants with respect to WT (e.g. $pB^{bravo}/pB^{WT}$, $pW^{bravo}/pW^{WT}$, etc.). In doing so, we will effectively measure relative fold-changes in promoter activity, i.e. dimensionless quantities that will not depend on any arbitrary scale. First of all, however, and in order to get rid of redundant dependencies between parameters, it is convenient to write the models in non-dimensional form. To do this, we redefine time as $\tau \equiv td_B$, and define the new variables $b \equiv K_B B$, $b \equiv K_W W$, $\tilde{\alpha} \equiv \alpha K_B/d_B$, $\tilde{\gamma} \equiv \gamma K_W/d_W$, $b_0 \equiv B_0 K_B$, $w_0 \equiv W_0 K_W$ and $\delta \equiv d_W/d_B$. Then, we can write the non-dimensionalized version of the two models as:

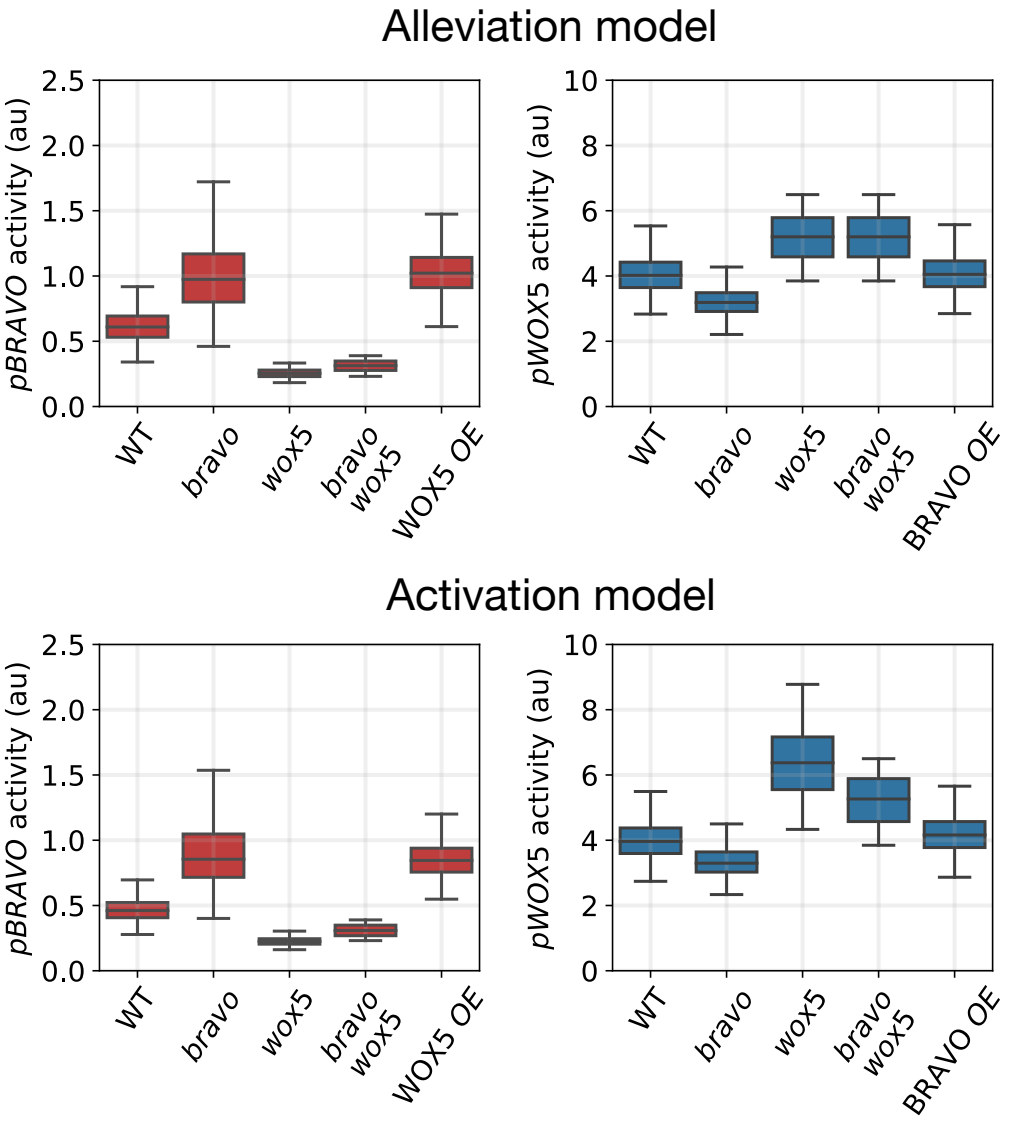



**Figure 4.6: Model results of $pB$ and $pW$ in WT and mutants.** Boxplots showing the distribution of $pB$ and $pW$ in WT, mutants and overexpression lines, for a random distribution of parameters between $p_s/f$ and $fp_s$, with $f = 1.3$ and $p_s$ the default parameter values (Table 4.2 and Table 4.3). These have been obtained by simulating the equations for $N = 1000$ combinations of the parameters. Box width represents the interquartile range ($IQR = Q3 - Q1$), where $Q_1$ and $Q_3$ denote the first and third quartiles of the promoter distributions, defined as the values $P(X \leq Q_1) = 0.25$ and $P(X \leq Q_3) = 0.75$, where $P(X \leq x)$ is the cumulative distribution function of the random variable $X$, in our case the value of the promoters. Thus the $IQR$ can be interpreted as the range of values of the promoters where half of the simulations end on. The horizontal line within each boxplot denotes the median of the distribution, while whiskers extend from $Q1-1.5IQR$ to $Q3+1.5IQR$. For each run, the WT, mutants and overexpressor scenarios are all computed with the same parameter values.

### Non-dimensional alleviation model

$$\frac{db}{dt} = \tilde{\alpha}\left(\frac{1+\varepsilon_B b^2}{1+b^2}\right)\left(\frac{1+\varepsilon_W w^2}{1+w^2}\right) - b \tag{4.9a}$$

$$\frac{dw}{dt} = \delta\left(\tilde{\gamma}\frac{w_0^2}{w_0^2 + w^2\left(1 + B_1\frac{b_0^2}{b_0^2+b^2}\right)^2} - w\right) \tag{4.9b}$$

| Parameter | Value | Parameter | Value |
|---|---|---|---|
| $\bar{\alpha}$ | 0.9 | $\bar{\alpha}$ | 0.9 |
| $\bar{\gamma}$ | 0.85 | $\bar{\gamma}$ | 0.75 |
| $\varepsilon_B$ | 0.15 | $\varepsilon_B$ | 0.15 |
| $\varepsilon_W$ | 10 | $\varepsilon_W$ | 10 |
| $B_0$ | 0.3 | $B_0$ | 0.75 |
| $w_0$ | 1.36 | $w_0$ | 0.645 |
| $B_1$ | 1 | $B_1$ | 0.5 |
| $A_0$ | 10 | $A_0$ | 10 |
| $G_0$ | 10 | $G_0$ | 10 |

**Table 4.4: Non-dimensional parameters of the alleviation (Left) and activation (Right) models.**

### Non-dimensional activation model

$$\frac{db}{dt} = \tilde{\alpha}\left(\frac{1+\varepsilon_B b^2}{1+b^2}\right)\left(\frac{1+\varepsilon_W w^2}{1+w^2}\right) - b \tag{4.10a}$$

$$\frac{dw}{dt} = \delta\left(\tilde{\gamma}\frac{w_0^2}{w_0^2+w^2}\left(1+B_1\frac{b^2}{B_0^2+b^2}\right) - w\right) \tag{4.10b}$$

With all these definitions, the basic framework for comparing the results of the mathematical model with the experiments is set. The particular values of the *BRAVO* promoters in the mutants are computed as follows:

$$pB^{bravo} = \tilde{\alpha}\frac{1+\varepsilon_W (w^{bravo})^2}{1+(w^{bravo})^2}, \quad pB^{wox5} = \tilde{\alpha}\frac{1+\varepsilon_B (b^{wox5})^2}{1+(b^{wox5})^2}, \quad pB^{dm} = \tilde{\alpha} \tag{4.11}$$

which are valid for both the alleviation and activation models. The activity of the *WOX5* promoter in the alleviation model reads, for each mutant:

$$pW^{bravo} = \tilde{\gamma}\frac{w_0^2}{w_0^2+(w^{bravo})^2(1+B_1)^2}, \quad pW^{wox5} = pW^{dm} = \tilde{\gamma} \tag{4.12}$$

While in the activation model:

$$pW^{bravo} = \tilde{\gamma}\frac{w_0^2}{w_0^2+(w^{bravo})^2}, \quad pW^{wox5} = \tilde{\gamma}\left(1+B_1\frac{B^2}{B_0^2+(b^{wox5})^2}\right), \quad pW^{dm} = \tilde{\gamma} \tag{4.13}$$

These expressions explicitly manifest the similarities and differences between the models when comparing WT and mutants. In particular, it puts into evidence the equivalence between *wox5* and *bravo wox5* mutants in the alleviation

model (Equation 4.12), and the differences between the same mutants in the activation model (Equation 4.13), a behaviour that was already observed in Figure 4.6.

To further test the behaviour of both models, we explore what is the effect of brassinosteroids (hereafter BL, for brassinolide, the most active brassinosteroid compound) to the fold-changes. Instead of modelling BL signalling through the introduction of new variables in the model, we take a simpler approach and consider their net effect on the levels of *BRAVO* and WOX5. In particular, we assume that BL directly affect their production rates $\tilde{\alpha}$ and $\tilde{\gamma}$. Since BL has an opposite role on the activity of *BRAVO* and *WOX5*—repressing the former but activating the latter (see Figure 4.21)—we assume that $\tilde{\alpha}$ and $\tilde{\gamma}$ are functions of the auxiliary variable $x$, which mimics BL signalling, and redefine $\alpha = \tilde{\alpha}/x$ and $\gamma = \tilde{\gamma}x/(x+9)$. In this way, $x = 1$ is associated with control conditions, as it coincides with the values used for the original simulations without BL. In Figure 4.7 we show the fold-changes of the promoters as a function of the auxiliary variable $x$, and display the experimental results as square marks on each line at $x = 1$. As expected, the effect of BL signalling ($x > 1$) makes the promoters less sensitive to the *bravo* mutants, as for hight BL the levels of BRAVO in the WT will already be low. This is in agreement with experiments in BL treated plants, where the fold-changes of *bravo* mutants with respect to the WT are close to one (Figure 4.21O,P).

To explore the possible outcomes of both models for different parameters, we choose the default parameter set of Table 4.4, and again generate uniform random distributions of parameters in the range between $p_s/f$ and $fp_s$, where now $p_s$ denote the non-dimensionalized set of parameters (Table 4.4), and choose the factor $f = 2$ so as to explore the results of the model with a wider parameter range. Figure 4.8 shows the promoter fold-changes of each WT/mutant pair obtained by solving the corresponding equations in the steady state. Experimental values of the fold-changes overlap with the model results, represented by the red and blue squares, with error bars denoting $\pm$ standard deviations (since promoter activities in the overexpressors are quantified via qPCR (see Figure 4.19), we do not explicitly mark the experimental results with squares).

Our results reveal that the two models behave in a similar manner with respect to the *BRAVO* promoter, but differ slightly in the *WOX5* promoter. In particular, while the alleviation model predicts, by construction, equal fold-changes for $pW^{wox5}/pW^{WT}$ and $pW^{dm}/pW^{WT}$, in the activation model these two quantities can be different. Notice that for certain combinations of parameters, the two fold-changes can even be less than one, meaning that in these mutants the promoter activity of *WOX5 decreases*. Since this is never observed in actual experiments, we suggest that *BRAVO* alleviation of *WOX5* self-repression is a more probable scenario than direct activation. Indeed, further parameter exploration, where variability is implemented in a wider range ($f = 5$) confirms that the activation model is less robust than the alleviation

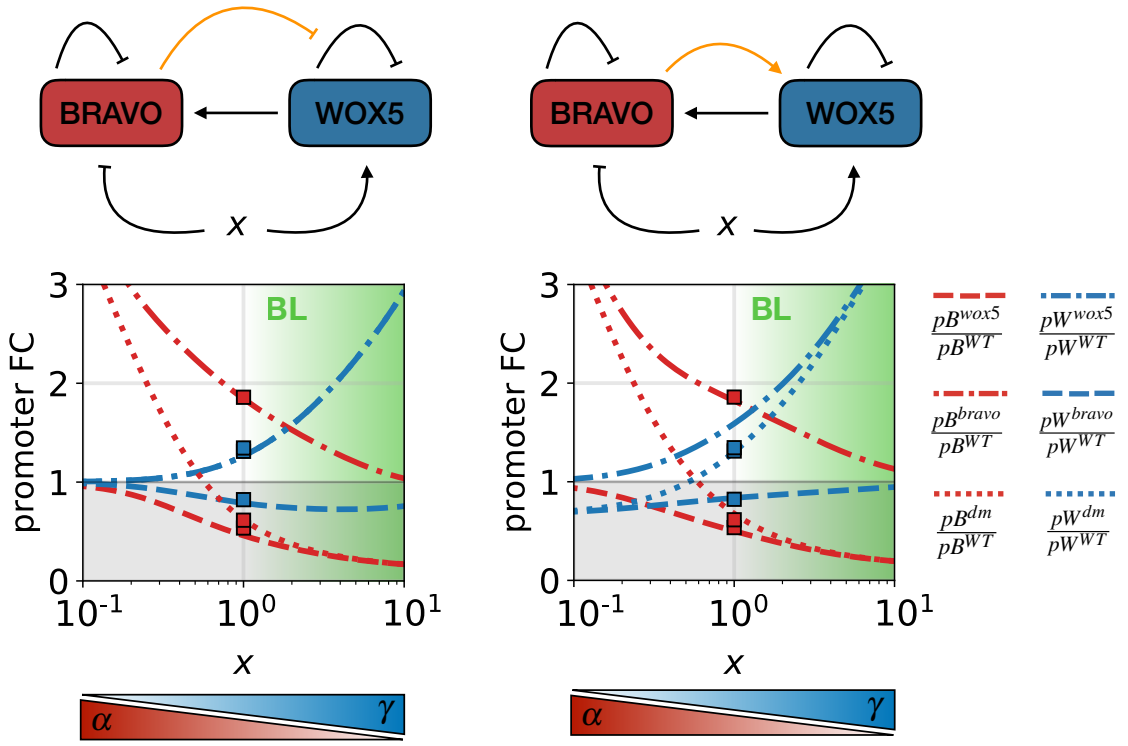



**Figure 4.7: Effect of brassinosteroids on promoter fold-changes.** Fold-changes in promoter activity in the mutants compared to the WT predicted by the alleviation (Left) and activation (Right) models, as a function of a control parameter $x$ which increases *WOX5* and reduces *BRAVO* promoter activities (see main text). $x = 1$ corresponds to control conditions, while $x > 1$ mimics exogenous BL application (green shaded area). The experimentally observed values in control conditions (computed as ratios of the median GFP) are drawn as red and blue markers. Error bars of these data are not depicted for clarity. In the plots, the regions of fold change $< 1$ (i.e. the promoter activity is reduced in the mutant) is shaded in gray to visually distinguish it from the region where the fold-change is $> 1$ (i.e. the promoter activity is increased in the mutant). Figure as in [Betegón-Putze et al., 2021].

model in predicting the promoter fold-changes as parameters are allowed to change (Figure 4.23).

## 4.4 BRAVO and WOX5 directly interact to form a heterodimeric complex

While the activation and alleviation models can well-reproduce the experimental results of promoter activities, it begs the question of which particular processes might generate each interaction. In particular, while direct activations or inhibitions, such as the activation of *BRAVO* by *WOX5*, the activation of *WOX5* by *BRAVO* in the activation model or the self-repressions, can be easily reconciled mechanistically—such as the binding of proteins to their corresponding promoters and the subsequent activation of repression of polymerase activity—the

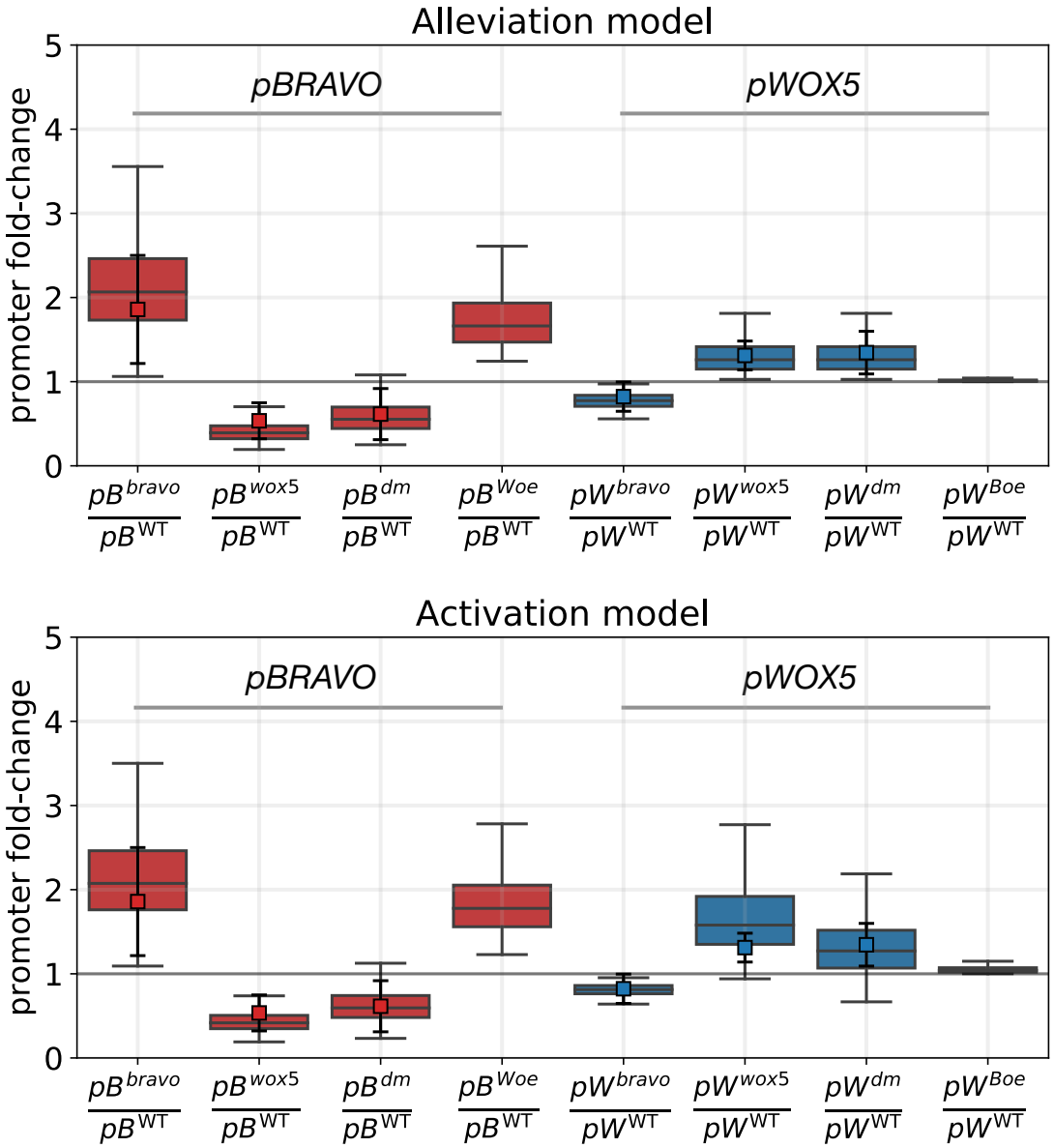



**Figure 4.8: Promoter fold-changes in the alleviation and activation models.** Boxplots showing the distribution of fold-changes of the BRAVO and WOX5 promoters in each mutant and overexpression lines over the WT, for a random distribution of the non-dimensionalized parameters between $p_s^n/f$ and $fp_s^n$, with $f = 2$. Results obtained by solving $N = 1000$ simulations of each model at the stationary state for the WT, mutants and overexpressor scenarios. For each run, the WT, mutants and overexpressor scenarios are all computed with the same parameter values. Experimental values of the fold-changes are represented by the red and blue squares overlaying the box plots, with error bars denoting ± standard deviations. Figure as in [Betegón-Putze et al., 2021].

specific mechanism of the alleviation model cannot be so directly interpreted. How can *BRAVO* alleviate *WOX5* self-repression, thereby generating an effective activation, to induce a decrease in *pWOX5:GFP* in the *bravo* mutant, while leaving its activity intact upon BRAVO overexpression?

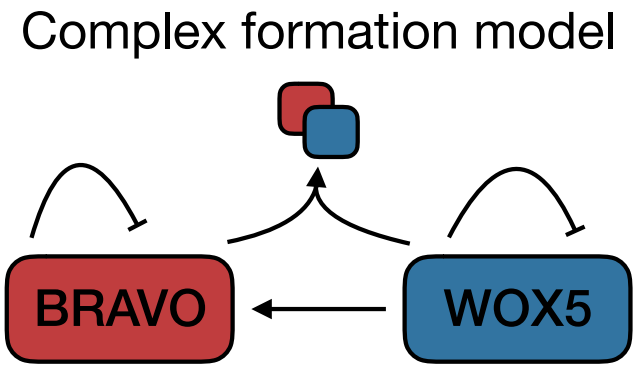



**Figure 4.9: Complex formation model.** Diagram of the interactions between BRAVO and WOX5 in the complex formation model. The interactions shared by the alleviation and activation models are also present on this model, while the interactions are here substituted by the formation of a complex between BRAVO and WOX5 proteins. Figure as in [Betegón-Putze et al., 2021].

To solve this puzzle, we make use of another piece of experimental data, in which our collaborators evaluate the possible physical interactions between the BRAVO and WOX5 proteins. They find that indeed the two proteins are able to bind *in vitro*, forming an heterodimeric complex (Figure 4.22B, G, K and L). This property of the proteins being able to bind to each other into a complex readily suggests a mechanistic explanation for the alleviation model: BRAVO, by binding to WOX5, prevents WOX5 from repressing (either directly or indirectly) its own expression. Hence, BRAVO alleviates the self-repression of WOX5 by means of a post-transcriptional sequestering mechanism.

To do this, we construct a third mathematical model, which we name *complex formation model*, where instead of considering promoter activities as the main variables, we explicitly model the dynamics of BRAVO and WOX5 proteins, and specifically include the formation of a complex. This model is to be viewed as applying to QC cells, where the complex is mostly formed, contrasting with the previous models where the activities of *BRAVO* and *WOX5* were comprised the whole domain of promoter expression observed in the root tip. For clarity, we call the new variables $B$ and $W$, but taking into account that they now represent protein concentrations at the QC, not the whole genetic expression as in the alleviation and activation models. We denote by $C_{BW}$ the concentration of the complex. For simplicity, we assume that the binding between BRAVO and WOX5 happens only through pair-wise reactions, with no higher order complexes involving BRAVO or WOX5 oligomers. Thus, by considering mass-action kinetics these interactions will contribute to the dynamics of BRAVO and WOX5 a reaction term proportional to the product $BW$. With these new ingredients, and keeping the regulations that are common in alleviation and activation models (i.e. the BRAVO and WOX5 self-regulations and BRAVO activation by WOX5), the dynamics of the complex formation model can be cast in the form of differential equations as:

**Complex formation model**

$$\frac{dB}{dt} = \alpha\left(\frac{1+\varepsilon_B(K_B B)^2}{1+(K_B B)^2}\right)\left(\frac{1+\varepsilon_W(K_W W)^2}{1+(K_W W)^2}\right) - \lambda_{BW}BW + \mu_{BW}C_{BW} - d_B B \tag{4.14a}$$

$$\frac{dW}{dt} = \gamma\frac{W_0^2}{W_0^2+W^2} - \lambda_{BW}BW + \mu_{BW}C_{BW} - d_W W \tag{4.14b}$$

$$\frac{dC_{BW}}{dt} = \lambda_{BW}BW - \mu_{BW}C_{BW} - d_C C_{BW} \tag{4.14c}$$

Here $\lambda_{BW}$ and $\mu_{BW}$ measure, respectively, the binding and unbinding rates of BRAVO and WOX5 proteins. Notice that implicitly in the construction of Equation 4.14 is the assumption that the BRAVO-WOX5 complex $C_{BW}$ does not regulate the production of neither BRAVO nor WOX5, but acts only as a mechanism to reduce the levels of unbound (free) WOX5 and BRAVO proteins. In constructing (4.14) we make the assumption that mRNA activities are very fast compared those of their corresponding proteins, and so the parameters $\alpha$ and $\gamma$ carry information about both transcription and translation (see Section 3.1 in Chapter 3). As before, the regulations involved in the promoters could take place through intermediate molecules, which are not modelled. While in this case the production of BRAVO is the same as the alleviation and activation models, the production of WOX5 only involves a term of self-repression.

The effects of having the new binding reaction of BRAVO and WOX5 are manifold: on the one hand, due to BRAVO and WOX5 being partially sequestered into an inactive complex, the levels of free proteins might be lower in the WT than in mutants. Indeed, in the *bravo* mutant, the levels of free WOX5 proteins may increase as they are released from the binding with BRAVO. At the same time, however, if WOX5 increases it will exert higher repression to its own promoter, thus reducing its production. On the other hand, in the *wox5* mutant, while BRAVO proteins are released, the promoter activity of BRAVO will invariably decrease due to the absence of WOX5, thus reducing its production.

The effect of complex formation is particularly revealing from Figure 4.10, where we show the fold-changes in protein activity of BRAVO (left) and WOX5 (right) in their complementary mutants with respect to the WT, for different values of the parameters $\lambda_{BW}$, $\epsilon_W$ (left) and $W_0$ (right). As shown in Figure 4.10 (left), if complex formation is weak, i.e. $\lambda_{BW}$ takes small values, the activation of BRAVO by WOX5 (measured by $\epsilon_W$) dominates, which induces a decrease of BRAVO protein levels in *wox5* mutants (pink region). As $\lambda_{BW}$ increases, BRAVO becomes more and more sequestered by WOX5, reducing its protein levels in the WT, up to a point where sequestration becomes dominant over activation, thereby inducing an increase in BRAVO protein activity in *wox5*

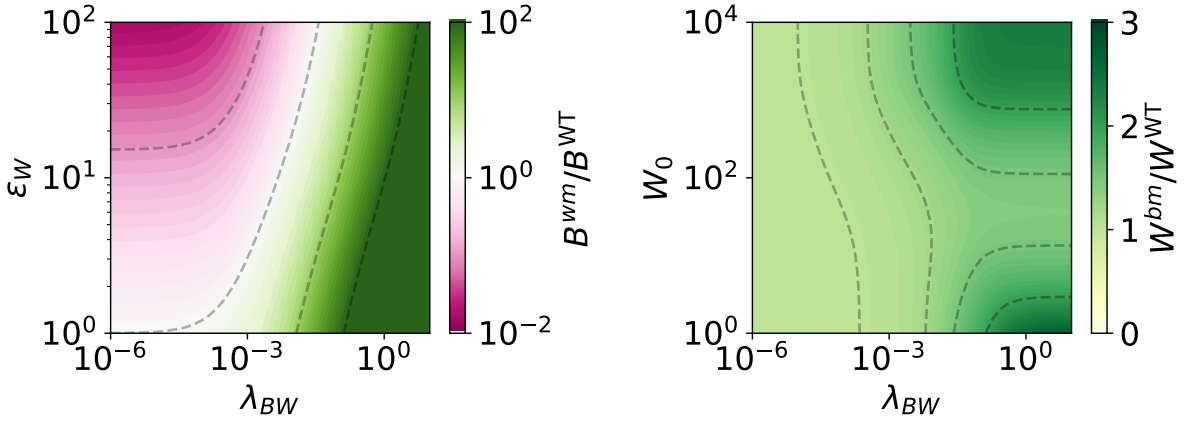



**Figure 4.10: Protein fold-changes in the complex formation model.** Heatmaps showing the fold-changes in protein concentration of BRAVO (left) and WOX5 (right) in their complementary mutants with respect to the WT, for different values of the parameters $\lambda_{BW}$, $\epsilon_W$ (left) and $W_0$ (right). Dashed lines show the contour lines with values $0.1, 1, 10, 100$ in the left figure, and with values $1.01, 1.2, 1.5, 2$ in the right figure. Figure as in [Betegón-Putze et al., 2021].

mutants (green region). In the simulations, we choose $\epsilon_W = 10$, $\lambda_{BW} = 0.01$ nM$^{-1}$ min$^{-1}$, which correspond to a BRAVO fold-change of $\sim 1$, that is, the effects of BRAVO sequestration and activation by WOX5 are on more or less equal footing. In Figure 4.10 (right) we can see the alleviation of WOX5 self-repression due to sequestration at play. For small $\lambda_{BW}$, the fold-change in activity is one, as there is no feedback from BRAVO to WOX5; as $\lambda_{BW}$ increases, complex formation makes free WOX5 levels to decrease, thus generating an increase in the fold-change in the *bravo* mutant. In the simulations, $W_0$ is chosen to be $W_0 = 415$ nM, which induces a WOX5 fold change of $\sim 1.5$, enough to generate a decrease in $P_W$ activity in the *bravo* mutant.

As before, we model *bravo* and *wox5* loss of function mutants by setting $B = 0$ and $W = 0$, respectively. The promoter values in the mutants are:

$$pB^{bravo} = \alpha \frac{1 + \varepsilon_W (K_W W^{bravo})^2}{1 + (K_W W^{bravo})^2}, \quad pB^{wox5} = \alpha \frac{1 + \varepsilon_B (K_B B^{wox5})^2}{1 + (K_B B^{wox5})^2}, \quad pB^{dm} = \alpha \tag{4.15}$$

$$pW^{bravo} = \gamma \frac{W_0^2}{W_0^2 + (W^{bravo})^2}, \quad pW^{wox5} = pW^{dm} = \gamma \tag{4.16}$$

As we did with the alleviation and activation models, we explore the behaviour of the fold-change in promoter activity by taking sets of parameters drawn from random uniform distributions. In Figure 4.11 we show how the fold-changes behave using the parameters shown in Table 4.5. While qualitatively the model reproduces well the experimental results, some of the fold-changes

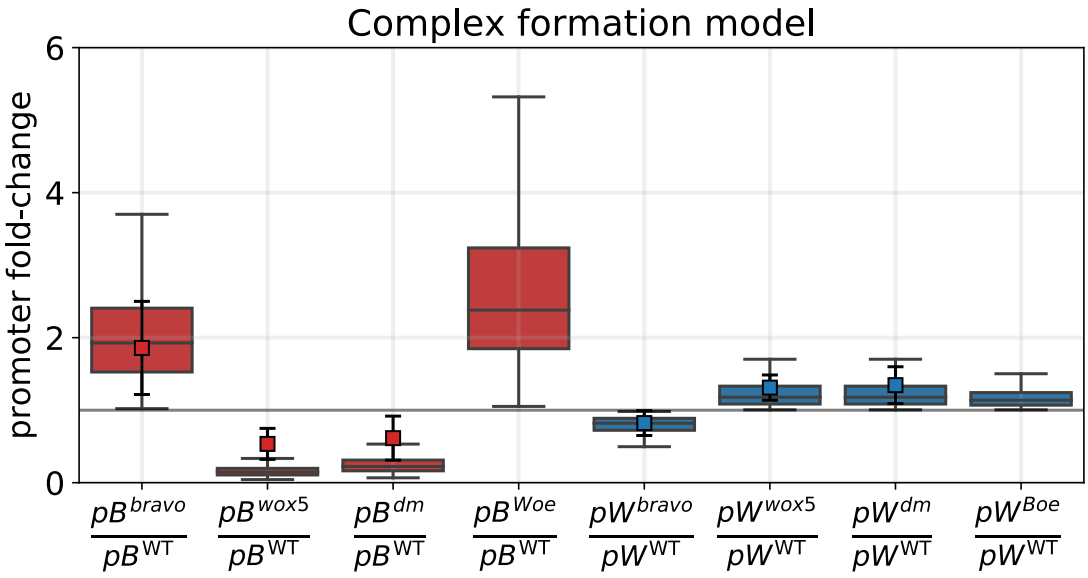



**Figure 4.11: Promoter fold-changes in the complex formation model.** Boxplots showing the distribution of fold-changes of the BRAVO and WOX5 promoters in each mutant and overexpression lines over the WT, for a random distribution of parameters between $p_s^n/f$ and $fp_s^n$, with $f = 2$. Results obtained by solving $N = 1000$ simulations of each model at the stationary state for the WT, mutants and overexpressor scenarios. For each run, the WT, mutants and overexpressor scenarios are all computed with the same parameter values. Experimental values of the fold-changes are represented by the red and blue squares overlaying the box plots, with error bars denoting ± standard deviations. Figure as in [Betegón-Putze et al., 2021].

deviate in absolute numbers. In particular, the fold-changes $pB^{wox5}/pB^{WT}$ and $pB^{dm}/pB^{WT}$ are smaller than the ones predicted by the experiments. This is consistent with the experimental observation that, in the QC, the decrease of *pBRAVO:GFP* in *wox5* and *bravo wox5* plants is more exaggerated than when considering the whole SCN (see Figure 4.3C and Figure 4.20C). Another difference between this model and the alleviation and activation models concerns the overexpression of BRAVO. In this case, a slight increase in $pW$ can be observed, as upon BRAVO overexpression BRAVO proteins are able to sequester WOX5, thus preventing WOX5 to repress itself. This situation cannot happen in the other models, where the effect of BRAVO on WOX5 activity is almost saturated in the WT. Again, given that this effect is small, and the values of $pW^{Boe}/pW^{WT}$ are within the error range we consider valid, we conclude that the complex formation model is a good candidate for the regulatory interactions between BRAVO and WOX5.

For comparison in Figure 4.12 we show how the promoter fold-changes behave when we do not consider the formation of the complex. While most are similar to the original case, the WOX5 promoter does not change in *bravo* mutants compared to the WT, as there is no feedback between BRAVO and WOX5. Due to the same reason, the WOX5 promoter does not change upon BRAVO

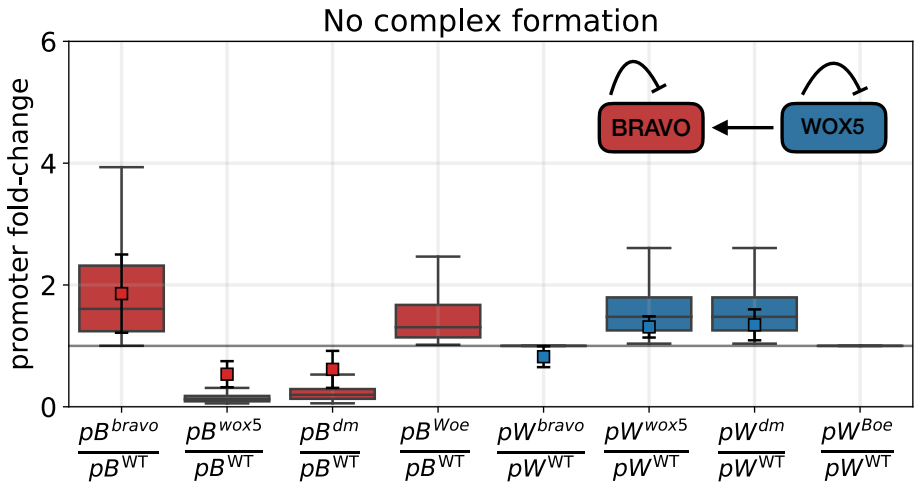



**Figure 4.12: Promoter fold-changes without complex formation.** When there is no complex formation the fold-change $pW^{bravo}/pW^{WT} = 1$, as BRAVO does no regulate WOX5. This is in disagreement with experimental results, where this fold-change is less than one. Figure as in [Betegón-Putze et al., 2021].

overexpression. Therefore, in the BRAVO-WOX5 circuit, the complex acts as a coupling mechanism between BRAVO and WOX5 activities.

| Parameter | Description | Value | Units |
|---|---|---|---|
| $\alpha$ | Basal production of BRAVO | 0.3 | nM $\text{min}^{-1}$ |
| $\gamma$ | Basal production of WOX5 | 5 | nM $\text{min}^{-1}$ |
| $K_B$ | Threshold of BRAVO self-repression | 0.1 | $\text{nM}^{-1}$ |
| $K_W$ | Threshold of BRAVO activation by WOX5 | 0.005 | $\text{nM}^{-1}$ |
| $\varepsilon_B$ | Strength of BRAVO self-repression | 0.5 | |
| $\varepsilon_W$ | Strength of BRAVO activation by WOX5 | 10 | |
| $W_0$ | Threshold of WOX5 self-repression | 415 | nM |
| $\lambda_{BW}$ | Binding rate of the complex | 0.01 | $\text{nM}^{-1}$ $\text{min}^{-1}$ |
| $\mu_{BW}$ | Unbinding rate of the complex | 0.02 | $\text{min}^{-1}$ |
| $d_B$ | BRAVO degradation | 0.01 | $\text{min}^{-1}$ |
| $d_W$ | WOX5 degradation | 0.01 | $\text{min}^{-1}$ |
| $d_C$ | Complex degradation | 0.01 | $\text{min}^{-1}$ |
| $A_0$ | Change in basal activity in BRAVO overexpression | 10 | – |
| $G_0$ | Change in basal activity in WOX5 overexpression | 10 | – |

**Table 4.5: Parameters of the complex formation model.** Parameters are chosen to be biologically realistic and to qualitatively fit experimental results.

### 4.4.1 The effect of additional sequestrators

To see whether the complex formation model is robust when additional factors are able to bind to BRAVO and WOX5, we extended the model to include the possible competition of other factors. Indeed, WOX5 has been shown to bind to the TOPLESS (TPL) correpressor to control CSC differentiation [Pi et al.,

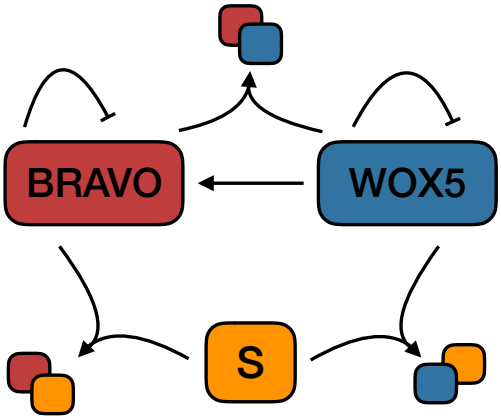



**Figure 4.13: Complex formation model in the presence of an additional sequestrator.** Diagram of the interactions when an additional sequestrator $S$ can bind both BRAVO and WOX5. Depending on the binding strengths of the sequestrator, the effect of complex formation between BRAVO and WOX5 may become impaired. Figure as in [Betegón-Putze et al., 2021].

2015], while the role of BRAVO in the brassinosteroid pathway has been shown to involve its binding with BES1 [Vilarrasa-Blasi et al., 2014]. Our collaborators have shown that further physical interactions can take place between these factors, including binding between WOX5 and BES1 and between BRAVO and TOPLESS (Figure 4.22). To asses how these additional interactions can affect the behaviour of BRAVO and WOX5, we model the presence of these factors through a single variable $S$, representing for example TPL, BES1 or both, as possible binding partners of BRAVO and WOX5. For simplicity, we allow $S$ to bind both BRAVO and WOX5, but not BRAVO-WOX5 complex, and assume that the resultant heterodimers do not affect the promoter activities of BRAVO nor WOX5. Therefore, by binding to BRAVO or WOX5, $S$ may prevent some of their mutual regulations to take place (Figure 4.13). The equations of this new model read:

$$\frac{dB}{dt} = \alpha \frac{1+\varepsilon_B (K_B B)^2}{1+(K_B B)^2} \frac{1+\varepsilon_W (K_W W)^2}{1+(K_W W)^2} - \lambda_{BW} BW + \mu_{BW} C_{BW} - \\ - \lambda_{BS} BS + \mu_{BS} C_{BS} - d_B B \tag{4.17a}$$

$$\frac{dW}{dt} = \gamma \frac{W_0^2}{W_0^2 + W^2} - \lambda_{BW} BW + \mu_{BW} C_{BW} - \lambda_{WS} WS + \mu_{WS} C_{WS} - d_W W \tag{4.17b}$$

$$\frac{dS}{dt} = \alpha_S - \lambda_{BS} BS + \mu_{BS} C_{BS} - \lambda_{WS} WS + \mu_{WS} C_{WS} - d_S S \tag{4.17c}$$

$$\frac{dC_{BW}}{dt} = \lambda_{BW} BW - \mu_{BW} C_{BW} - d_{C_{BW}} C_{BW} \tag{4.17d}$$

$$\frac{dC_{BS}}{dt} = \lambda_{BS} BS - \mu_{BS} C_{BS} - d_{C_{BS}} C_{BS} \tag{4.17e}$$

$$\frac{dC_{WS}}{dt} = \lambda_{BW} BW - \mu_{BW} C_{BW} - d_{C_{WS}} C_{WS} \tag{4.17f}$$

(4.17g)

where $C_{BS}$ and $B_{WS}$ denote the concentrations of the BRAVO-$S$ and the WOX5-$S$ complexes, respectively. Our results show that the mechanism of BRAVO driving alleviation of WOX5 self-repression holds in the presence of this competing factor, as long as the levels of the competing factors remain low enough to allow BRAVO and WOX5 to perform their functions (see Figure 4.14). If the synthesis rate of the sequestrator ($\alpha_S$) is too high, the mechanisms by which BRAVO and WOX5 regulate each other may become impaired, leading to fold-changes which do not match experimental results (Figure 4.24). Moreover, analysis of the model revealed that the cross-regulations between BRAVO and WOX5 expressions remain less sensitive to the presence of the sequestering factor $S$ when this competing factor can bind both factors separately than if it could bind only one of them (Figure 4.15).This is more relevant for BRAVO-mediated regulations since BRAVO is produced in a lesser amount than WOX5.

## 4.5 The BRAVO-WOX5 complex is sufficient for the control of QC divisions

The specific transcriptional interactions between BRAVO and WOX5, together with the formation of a complex with a possible maximum at the location of the QC, begs the question of how may the BRAVO-WOX5 circuit modulate QC divisions. Since there is little information about the specific molecular targets of each factor—the regulation of cyclins by WOX5 [Forzani et al., 2014] and the control of brassinosteroid-induced QC division by BRAVO [Vilarrasa-Blasi et al., 2014]—but no knowledge about how these two pathways might converge,

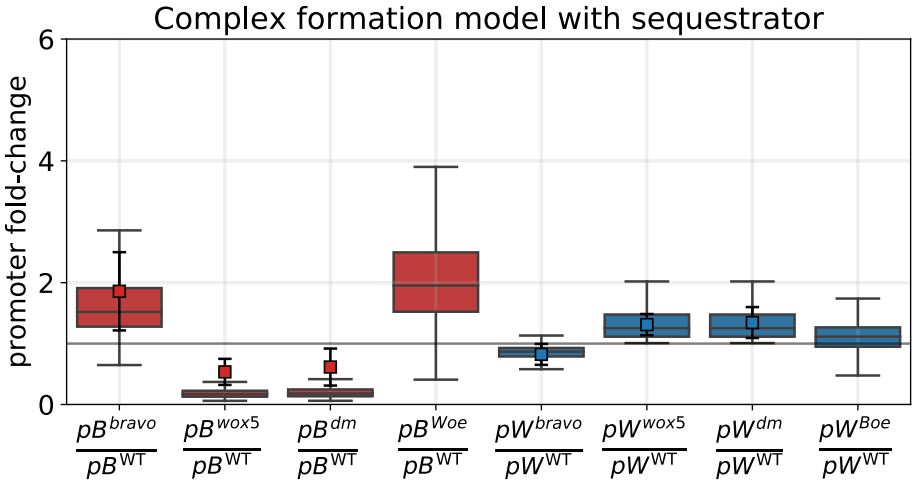



**Figure 4.14: Promoter fold-changes in the complex formation model with an additional sequestrator.** For relatively low values of sequestrator production ($\alpha_S = 0.1$ in this figure), the model still reproduces the experimental trends in promoter activity. Figure as in [Betegón-Putze et al., 2021].

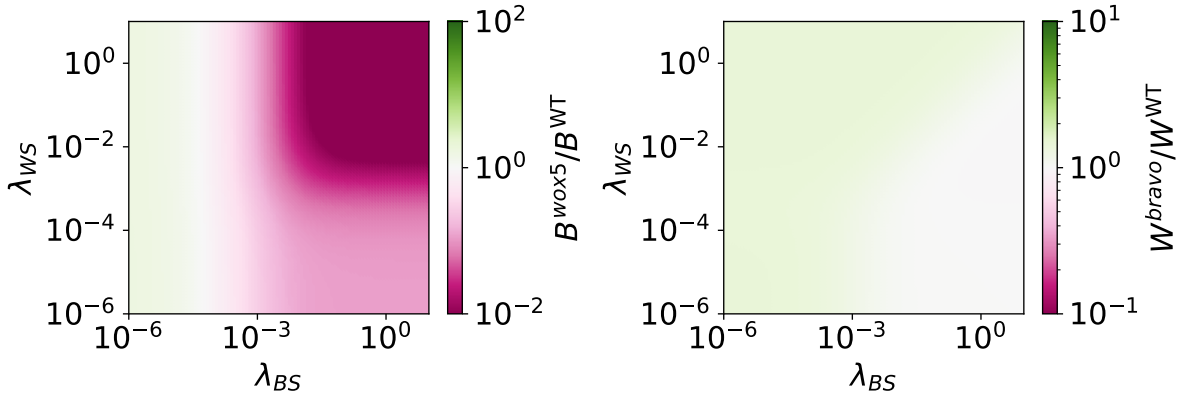



**Figure 4.15: The effect of sequestrator binding strengths on protein fold changes. Left:** When BRAVO does not bind much with the sequestrator $\lambda_{BS}$, WOX5 is able to sequester BRAVO, and thus in the *wox5* mutant the concentration of free BRAVO proteins will slightly increase (green region). For large $\lambda_{BS}$, $S$ sequesters BRAVO, and depending on the strength of the WOX5-S binding ($\lambda_{WS}$) the increase in BRAVO protein concentration in the *wox5* mutant will be more or less pronounced (purple regions). **Right:** In the *bravo* mutant, on the other hand, the increase in WOX5 concentration with respect to the WT depends less on the values of $\lambda_{BS}$ and $\lambda_{WS}$, because in the WT the concentration of WT is already at high values compared to those of BRAVO. Figure as in [Betegón-Putze et al., 2021].

we again tackle the problem through mathematical modelling. The cell division phenotypes of Figure 4.2E, when examined in the light of the mutual interactions between BRAVO and WOX5 studied in the previous section, indicate that these two pathways are probably not independent, but closely interlinked.

From the observed interactions between BRAVO and WOX5, we can conceive several ways by which the two might operate to promote quiescence to QC cells.

For instance, the fact that double mutants have the same proportion of QC divisions than single mutants could mean that the molecular element required to repress QC divisions is the BRAVO-WOX5 complex itself, as it would be absent in both single and double mutants. Conversely, on might independently favor BRAVO or WOX5 as the main factors repressing QC divisions, in such a way that QC divisions increase in double mutants just like in single mutants because both BRAVO and WOX5 transcripts decrease in these mutants.

To distinguish among these possibilities, we build a simple model of QC regulation contemplating all possible scenarios. We assume that the frequency of QC divisions is controlled by three distinct contributions: one mediated by BRAVO (denoted by $T_B$), one mediated by WOX5 ($T_W$) and one mediated by the combined action of BRAVO and WOX5, hereafter named *joint contribution* ($T_{BW}$). While the latter might implicate the BRAVO-WOX5 heterodimer, it is not an implicit assumption of the model. With these definitions, we define the frequency of plants with a divided QC to be inversely proportional to the value of each contribution:

$$F = \frac{F_0}{1 + T_B + T_W + T_{BW}} \tag{4.18}$$

where $F_0$ is associated with the frequency of plants with a divided QC in *bravo wox5* double mutants, as is the value of $F$ in the absence of all contributions (i.e. when $T_B = T_W = T_{BW} = 0$, then $F = F_0$). In single mutants, the contributions are $T_B = 0$ in the case of the *bravo* mutant, $T_W = 0$ in the *wox5* mutants, and $T_{BW} = 0$ for both cases. Since BRAVO and WOX5 regulate each other, in single mutants the contributions of the non-mutated genes will change. For example, in *wox5* mutants, since the activity of BRAVO is strongly down-regulated, we expect its contribution on QC quiescence to decrease. To take this into account we define, for each mutant, a proportionality factor accounting for the fold-change in repression strength due to mutual regulations. Specifically, in *wox5* mutants the BRAVO contribution changes by a factor $q_B^{wox5} > 0$ when compared with the $T_B^{\mathrm{WT}}$ in the WT, i.e. $T_B^{wox5} \equiv T_B^{\mathrm{WT}} q_B^{wox5}$. Similarly, the individual contribution of WOX5 changes by a factor $q_W^{bravo} > 0$ in *bravo* mutants compared to the WT, $T_W^{bravo} \equiv T_W^{\mathrm{WT}} q_W^{bravo}$. Thus, in WT and in mutants, we can define the frequency of plants with a divided QC as:

$$F^{\mathrm{WT}} = \frac{F_0}{1 + T_B^{\mathrm{WT}} + T_W^{\mathrm{WT}} + T_{BW}^{\mathrm{WT}}} \tag{4.19a}$$

$$F^{bravo} = \frac{F_0}{1 + T_W^{bravo}} = \frac{F_0}{1 + q_W^{bravo} T_W^{\mathrm{WT}}} \tag{4.19b}$$

$$F^{wox5} = \frac{F_0}{1 + T_B^{wox5}} = \frac{F_0}{1 + q_B^{wox5} T_B^{\mathrm{WT}}} \tag{4.19c}$$

$$F^{dm} = F_0 \tag{4.19d}$$

A direct consequence of these definitions is that small values ($\ll 1$) of $q_W^{bravo}$ ($q_B^{wox5}$) represent strong upregulation of WOX5 (BRAVO) by BRAVO (WOX5), while large values ($\gg 1$) represent strong down-regulation of WOX5 (BRAVO) by BRAVO (WOX5). Since the values of $F^{\mathrm{WT}}, F^{bravo}, F^{wox5}$ and $F^{dm}$ can be inferred from experimental data (Figure 4.2), the previous system constitutes an algebraic system of four equations and four variables, which can be easily solved. In particular, these values are $F^{\mathrm{WT}} = 0.39$, $F^{bravo} = 0.87$, $F^{wox5} = 0.81$ and $F^{dm} = 0.89$.

The values of $q_W^{bravo}$ and $q_B^{wox5}$ are associated with the changes in the amounts of BRAVO and WOX5 proteins in the single mutants, and how these changes influence QC division. Because the specific values of these changes cannot be measured, we estimate them via the fold-changes in promoter expression in the mutants with respect to the WT. For instance, since in *bravo* mutants the promoter fold-change in *pWOX5:GFP* is $\sim 0.8$ (Figure 4.3I), we used as a first approximation $q_W^{bravo} = 0.8$. The fact that *wox5* mutants exhibit phenotypes which are not observed in *bravo* mutants (such as a disorganized SCN and premature CSC differentiation) also suggests that $q_W^{bravo}$ might be close to one, i.e. in the *bravo* mutant the effect of WOX5 on QC division is very redundant. On the other hand, since *pBRAVO:GFP* decreases dramatically in the QC of *wox5* mutants, we expect $q_B^{wox5}$ to be small, as in these mutants BRAVO is presumably at very low levels. While the estimate for $q_B^{wox5}$ based on the fold-change of *pBRAVO:GFP* expression in *wox5* mutants would be $q_B^{wox5} \sim 0.5$ (Figure 4.3H), this value is obtained by measuring the GFP intensity in the whole SCN. This decrease is more pronounced in the QC (Figure 4.3C), so lower values of $q_B^{wox5}$ are to be expected.

In Figure 4.16 we show the strength of each contribution $T_B^{WT}, T_W^{WT}, T_{BW}^{WT}$ as a function of $q_B^{wox5}$, for a fixed value of $q_W^{bravo} = 0.8$, together with their associated errors (shaded envelope, see Section 4.A in the appendix for details in the calculation of these errors). A first feature of the results is that the contribution mediated by WOX5 is very small. On the other hand, the contribution mediated by BRAVO is large if $q_B^{wox5}$ is small, i.e. if BRAVO is highly dependent of WOX5. This scenario corresponds to BRAVO acting downstream of WOX5 to repress QC divisions. In this very same region, our results indicate that the joint contribution can also be important, and could even facilitate QC divisions (negative values of $T_{BW}^{WT}$). For intermediate and large values of $q_B^{wox5}$, the model predicts that the only relevant contribution is the one where BRAVO and WOX5 act together. This suggests that the joint contribution is sufficient to describe the QC division phenotype independently of how strong the cross-regulations between BRAVO and WOX5 are. The possibility of this joint contribution being mediated by the BRAVO-WOX5 complex is therefore tempting.

Finally, one might also consider the effect of additional factors impairing the contributions of BRAVO and WOX5 in QC division. As shown in Figure 4.10,

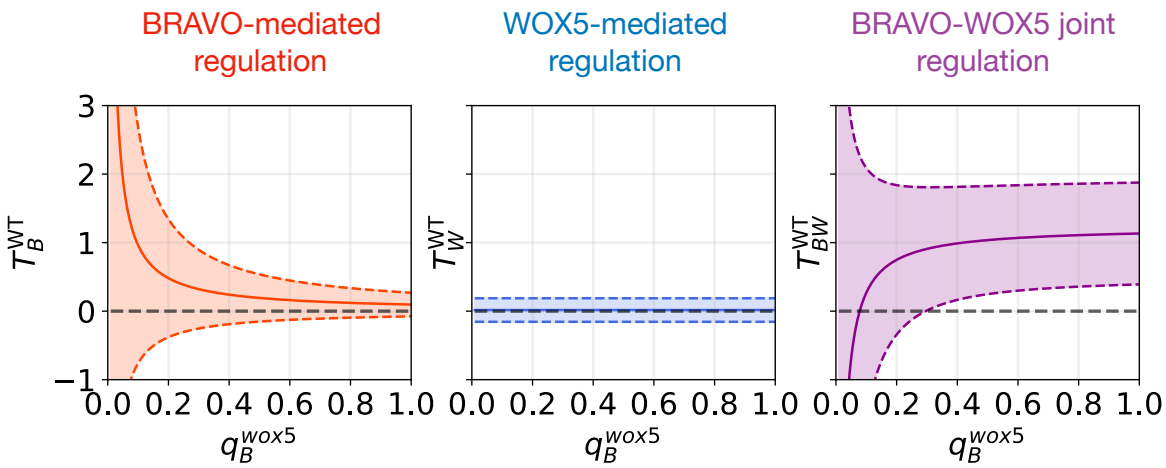



**Figure 4.16: BRAVO and WOX5 have a joint role in repressing QC divisions.** Computational estimation of the contributions of BRAVO-mediated ($T_B^{\mathrm{WT}}$), WOX5-mediated ($T_W^{\mathrm{WT}}$) and BRAVO-WOX5 joint ($T_{BW}^{\mathrm{WT}}$) regulations of QC divisions in the WT, as a function of the attenuating factor of BRAVO contribution in the *wox5* mutant, $q_B^{wox5}$. Continuous lines represent the best estimated values, while dashed lines are the enveloping confidence intervals (i.e. $T_B^{\mathrm{WT}} \pm \delta T_B^{\mathrm{WT}}$). The horizontal grey dashed lines mark the zero lines. For a wide range of $q_B^{wox5}$ values, the joint contribution of BRAVO and WOX5 is the only one relevant. The individual contribution of BRAVO becomes significant only for small values of $q_B^{wox5}$. In all three panels, we set $q_W^{bravo} = 0.8$. Positive contributions correspond to repression of QC divisions, while negative contributions correspond to activation of QC divisions. Figure as in [Betegón-Putze et al., 2021].

in *wox5* mutants BRAVO proteins are able to increase, decrease or remain as in the WT depending on parameter values. With the parameters used to fit experimental results, however, this change is small (Table 4.3). In the presence of an additional sequestrator, however, this change in BRAVO concentration is highly dependent on the relative values of the binding rates $\lambda_{BS}$ and $\lambda_{WS}$ (Figure 4.15). In this mutant, the competing factor would sequester BRAVO more than in the WT. Hence, smaller values of $q_B^{wox5}$ than those predicted heuristically from fold-changes in promoter expression could also be possible. In contrast, since the change in WOX5 proteins is small in the presence of the sequestrator (Figure 4.15), small, highly variable values of $q_W^{bravo}$ are not expected.

Overall, these results suggest that BRAVO and the BRAVO-WOX5 complex, but not WOX5 alone, are the main drivers of QC divisions. While this seems to challenge the currently established role of WOX5 as a repressor of QC divisions, the contradiction is only apparent, as the function of WOX5 must be viewed, in light of our results, not as an independent force but as part of a larger mechanism acting in conjunction with its partner BRAVO.

## 4.6 Discussion

In this chapter we have shown that simple mathematical models are able to recapitulate the promoter expressions of BRAVO and WOX5 in WT, mutants, and overexpressors. Moreover, we find that their interactions at both transcriptional and post-transcriptional levels have important implications in their role as repressors of QC division. In particular, our modelling approach supports the formation of a BRAVO-WOX5 complex, and favours the possibility that it is this very complex which controls QC divisions in the *Arabidopsis* root. While the presence of competing factors might impair this mechanism, binding to both proteins makes the cross-regulation between BRAVO and WOX5 expressions less sensitive to the amount of competing factors. This suggests that promiscuity of protein-interacting partners can be a mechanism to enable modular regulations of gene expression, as has already been suggested [Antebi et al., 2020, Su et al., 2020].

The interactions proposed in the models need to be considered effective, in the sense that they can be the result of multiple, direct and indirect, regulatory mechanisms. For instance, the self-repression of WOX5 may involve a negative feedback where WOX5 activates a repressor or represses an activator. In this context, the interactions between auxin-ARF and auxin-IAA, as well a those of PLT genes, have all been shown to involve negative feedback loops with WOX5 [Tian et al., 2014b, Burkart et al., 2019], and could be the ultimate responsibles for the self-repression we considered in our models. The induction of BRAVO by WOX5 could also be indirect, being mediated by a downstream target of WOX5. In addition, the apparent self-repression of BRAVO probably occurs through intermediate molecules, as in tobacco leaves BRAVO has been shown to activate itself by directly binding its own promoter [Vilarrasa-Blasi et al., 2014].

Our analysis further supports that the joint regulation of BRAVO and WOX5 is sufficient to explain the QC division phenotypes. This could take place by several means, although the finding that BRAVO and WOX5 can physically interact strongly suggests that the resulting complex might be involved. At a mechanistic level, the BRAVO-WOX5 complex could directly interact with the CYCLIN-D3:3, as has been shown to occur for WOX5 [Forzani et al., 2014]. Although the joint action is sufficient, other scenarios cannot be discarded. For example, while *bravo* mutant phenotypes only differ in the frequency of QC divisions, *wox5* and *bravo wox5* mutants also display a disorganized SCN morphology and premature CSC differentiation. This indicates that the effect of WOX5 on BRAVO is strong, but not viceversa. In light of these observations, BRAVO alone could be the main factor repressing QC divisions, and the similar division phenotypes observed in *bravo*, *wox5* and *bravo wox5* mutants would be a consequence of the strong regulation of *BRAVO* by *WOX5*.

Our model also provides an easy explanation for the phenotypes of increased

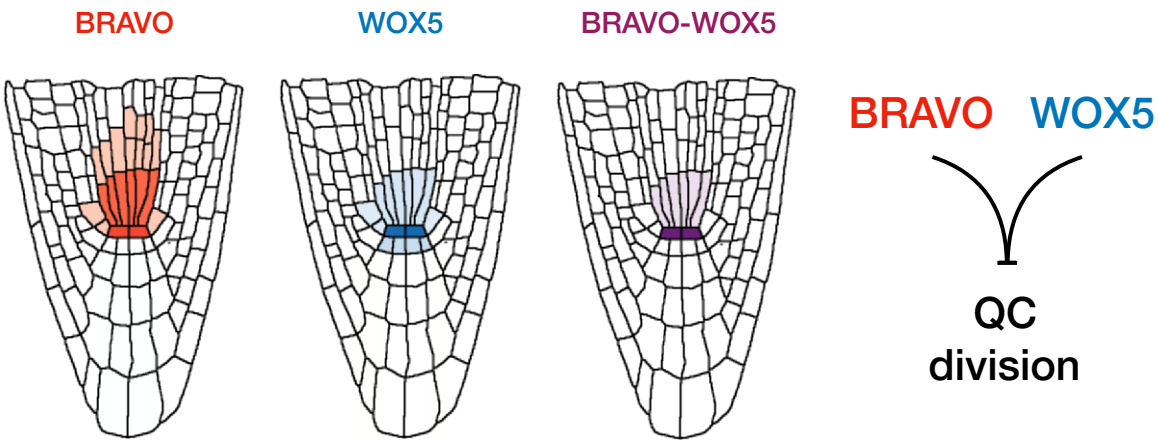



**Figure 4.17: Regulation of QC division by BRAVO and WOX5.** Sketch representing the spatial distribution of BRAVO, WOX5 and their product BRAVO × WOX5, which can be interpreted as the protein complex. Their joint interaction peaks at the QC, where repression of cell division occurs.

QC divisions in plants treated with BL [González-García et al., 2011]. BL has opposite effects on *BRAVO* and *WOX5*, repressing the former but activating the latter. Therefore, based on our findings that BRAVO and the BRAVO-WOX5 complex contribute more to QC division frequency than WOX5 alone, the low levels of *BRAVO* induced by BL treatment will lead to a highly divided QC.

Finally, our study sets a framework for future studies on the interplay between WOX5 and BR signalling in the control of CSC differentiation. WOX5 is known to repress CSC differentiation [Pi et al., 2015, Sarkar et al., 2007]. However, upon BL treatment, and in *bes1-D* gain of function mutants, CSC differentiate prematurely [González-García et al., 2011], in apparent contradiction with the inhibitory role associated with WOX5. One option comes from assuming that BL-induced CSC differentiation is independent from WOX5 and overrides the WOX5-mediated repression. In this case, a tug-of-war between WOX5-mediated repression and BL-dependent activation of CSC differentiation would tip the balance in favor of BR. Another possibility is that BR downstream effectors such as BES1-D inactivate WOX5 and/or impair its function. As WOX5 and BES1-D physically interact, an increase of BES1-D upon BL may boost WOX5 sequestration into WOX5-BES1-D complexes. Assuming this binding weakens the original function of WOX5, CSC differentiation would no longer be repressed by WOX5 in the presence of BL. Moreover, the fact that BES1-D directly interacts with TOPLESS, and TOPLESS needs WOX5 to inhibit CSC differentiation [Pi et al., 2015], suggests that in plants treated with BL the function of WOX5 may be further impaired due to the majority of TPL being bound to BES1-D.

Overall, the results shown in the chapter reveal that a simple regulatory network can account for the experimental observations of the promoter expressions of *BRAVO* and *WOX5*, and support the hypothesis that a complex between

the two factors is involved in the control of QC division. Since the regulation of SCN maintenance explicitly depends on the position of regulatory signals, a natural next step is extending the model to include spatial dependences, which may shed some light on the expression patterns of *BRAVO* and *WOX5*. In the next chapter (Chapter 5), these spatial dependences are explored, further illuminating the regulatory principles underlying stem cell maintenance in the *Arabidopsis* root apical meristem.

# Appendix

## 4.A Error propagation for QC division contributions

To estimate the errors associated with the variability of QC divisions in each phenotype, we think of QC divisions as Bernoulli trials, i.e. we take $N$ independent experiments for each genotype, and associate a probability $p$ of observing a QC with at least one divided cell. By defining $N_k$ as the number of roots that have a divided QC, this probability is $p = N_k/N$, with an associated standard deviation of $\sigma = \sqrt{\frac{p(1-p)}{N}}$. For each genotype, we take a conservative view and use $N = 15$ for computing the errors, to avoid underestimation. By defining $a \equiv F^{\mathrm{WT}} = 0.39$, $b \equiv F^{bravo} = 0.87$, $c \equiv F^{wox5} = 0.81$ and $d \equiv F^{dm} = 0.89$, i.e., the values of the frequency of QC division in each genotype, the errors corresponding to the contributions $T_B^{WT}$, $T_W^{WT}$, $T_{BW}^{WT}$ are:

$$\delta T_B^{\mathrm{WT}} = \frac{1}{q_B^{wox5}} \sqrt{\left(\frac{\delta d}{c}\right)^2 + \left(\frac{d}{c^2}\delta c\right)^2} \tag{4.20a}$$

$$\delta T_W^{\mathrm{WT}} = \frac{1}{q_W^{bravo}} \sqrt{\left(\frac{\delta d}{b}\right)^2 + \left(\frac{d}{b^2}\delta b\right)^2} \tag{4.20b}$$

$$\delta T_{BW}^{\mathrm{WT}} = \sqrt{\left(\delta d\left(\frac{1}{a} - \frac{1}{q_B^{wox5}c} - \frac{1}{q_W^{bravo}b}\right)\right)^2 + \left(\frac{d}{a^2}\delta a\right)^2 + \left(\frac{d}{q_W^{bravo}b^2}\delta b\right)^2 + \left(\frac{d}{q_B^{wox5}c^2}\delta c\right)^2} \tag{4.20c}$$

In Figure 4.16 we plot the quantities $T_B^{WT} \pm \delta T_B^{\mathrm{WT}}$, $T_W^{WT} \pm \delta T_W^{\mathrm{WT}}$, $T_{BW}^{WT} \pm \delta T_{BW}^{\mathrm{WT}}$ as dashed lines. In Figure 4.25 we show the same results but taking $N = 100$.

## 4.B Numerical methods

In the stationary state (i.e. when time derivatives are equal to zero), all models reduce to either single algebraic equations or systems of algebraic equations. To solve them numerically, we used custom-made software including the *fsolve* rou-

tine embedded in Python (Python Software Foundation, https://www.python.org/), which uses a modification of Powell's hybrid method for finding zeros of a system of nonlinear equations.

# 4.C Supplementary Figures

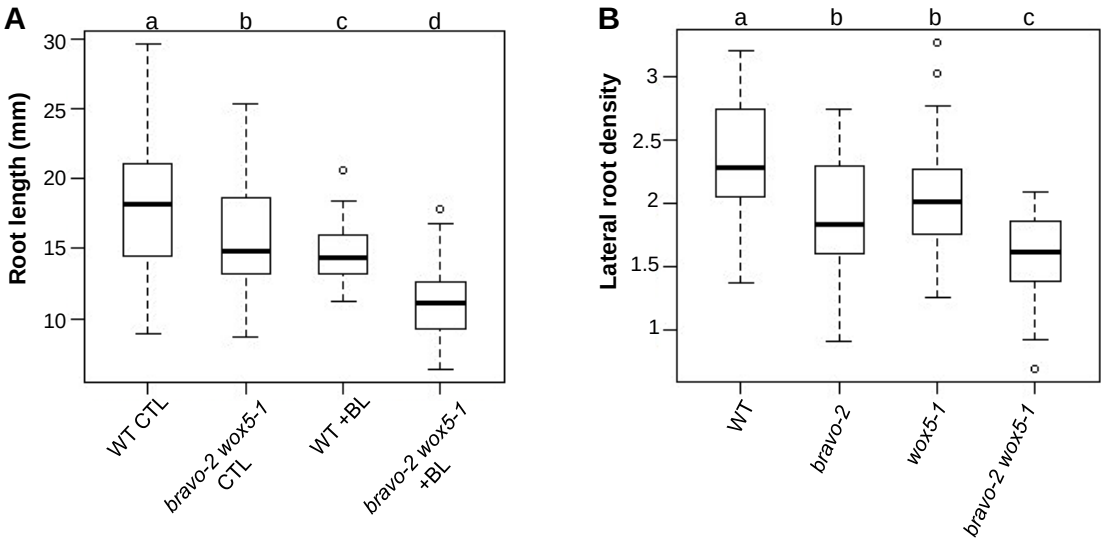



**Figure 4.18: BRAVO and WOX5 promote primary root growth and lateral root development. A)** Root length of 6-day-old WT and *bravo-2 wox5-1* mutants in control and after BL treatment ($n > 30$, 3 replicates). Different letters indicate statistically significant differences ($p$-value $< 0.05$ Student's $t$-test).**B)** Lateral root density (number of lateral roots per mm of root length) of 10-day-old WT, *bravo-2*, *wox5- 1* and *bravo-2 wox5-1* mutants ($n > 52$, 3 replicates). Different letters indicate statistically significant differences ($p$-value $< 0.05$ Student's $t$-test). Figure as in [Betegón-Putze et al., 2021].

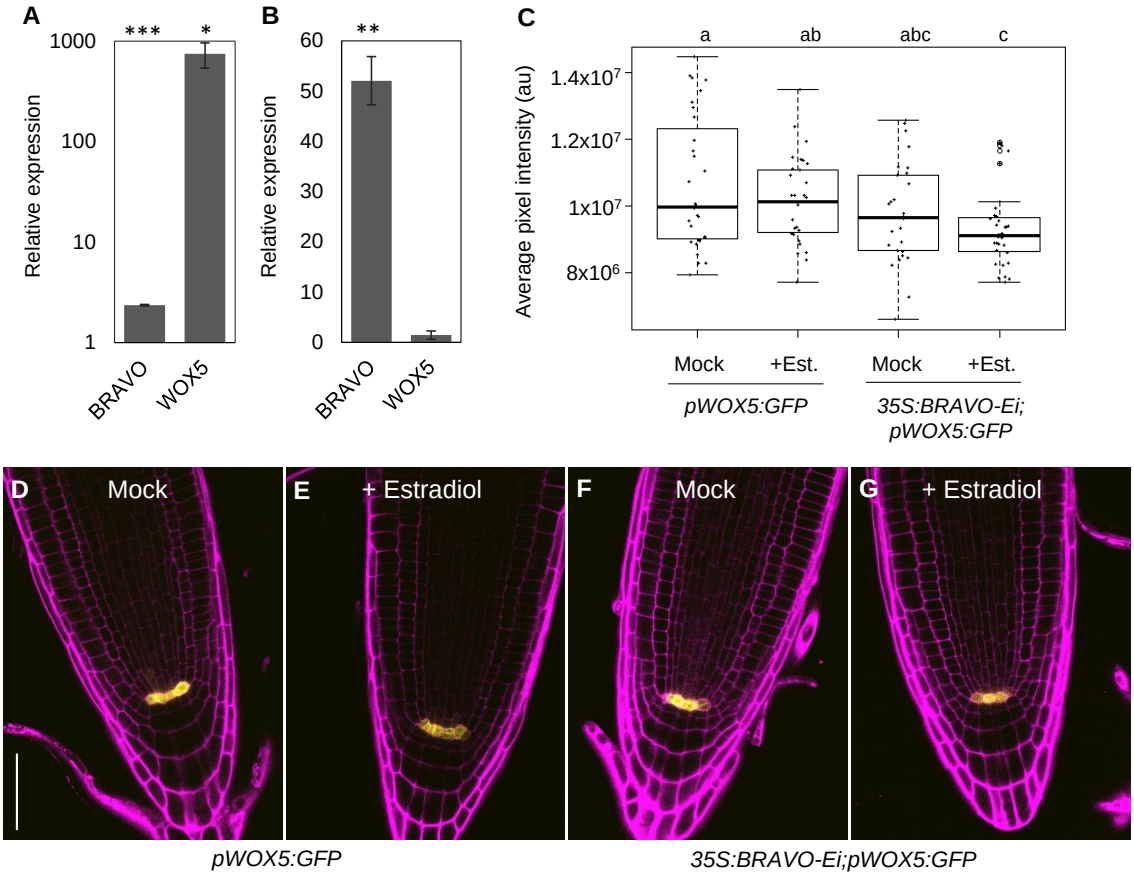



**Figure 4.19: BRAVO and WOX5 expression patterns in overexpressing lines. A)** Bars show the relative expression of *BRAVO* and *WOX5* in *35S:WOX5-GR* lines when induced with 1 $\mu$M Dexamethasone for 24 hours. Values in control conditions are not represented, as are equal to 1. Data obtained from two independent biological replicates. Asterisks indicate significant differences (* $p$-value $< 0.05$, *** $p$-value $< 0.001$ Student's $t$-test). **B)** Bars show the relative expression of *BRAVO* and *WOX5* in *35S:BRAVO-Ei* lines when induced with 30 $\mu$M $\beta$-estradiol for 24 hours. Values in control conditions are not represented, as are equal to 1. Data obtained from three independent biological replicates. Asterisks indicate significant differences (** p-value $< 0.01$ Student's $t$-test). **C)** Quantification of the GFP fluorescent signal of the roots in D-G. Boxplot indicating the average pixel intensity of the GFP in the stem cell niche. ($n > 29$, 3 biological replicates. Different letters indicate statistically significant differences ($p$-value $< 0.05$ Student's $t$-test). **D-G)** Confocal images of PI-stained 6-day-old roots. GFP-tagged expression is shown in yellow. *pWOX5:GFP* in WT and *35S:BRAVO-Ei* background in control (D, F) and after 6 days 30 $\mu$M $\beta$-estradiol induction (E, G). Scale bar: 50 $\mu$m. Figure as in [Betegón-Putze et al., 2021].

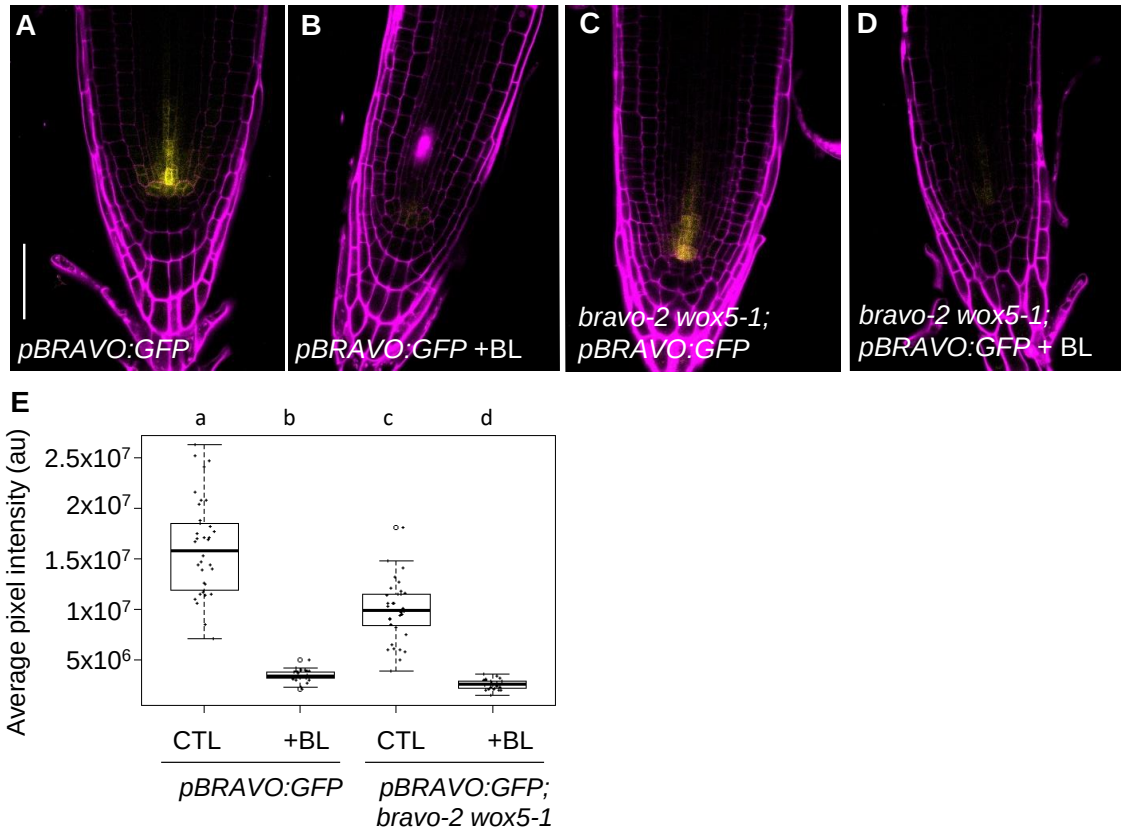



**Figure 4.20: BRAVO expression in the *bravo wox5* mutant background. A-D)** Confocal images of PI-stained 6-day-old roots. GFP-tagged expression is shown in yellow. *pBRAVO:GFP* in WT and *bravo-2 wox5-1* background in control (A, C) and after BL treatment (B, D). Scale bar: 50 $\mu$m. **E)** Quantification of the GFP fluorescent signal of the roots in A-D in the stem cell niche. Different letters indicate statistically significant differences ($p$-value $< 0.05$ Student's $t$-test). Different confocal settings were used in these images to those in Figure 4.3 and Figure 4.21. Figure as in [Betegón-Putze et al., 2021].

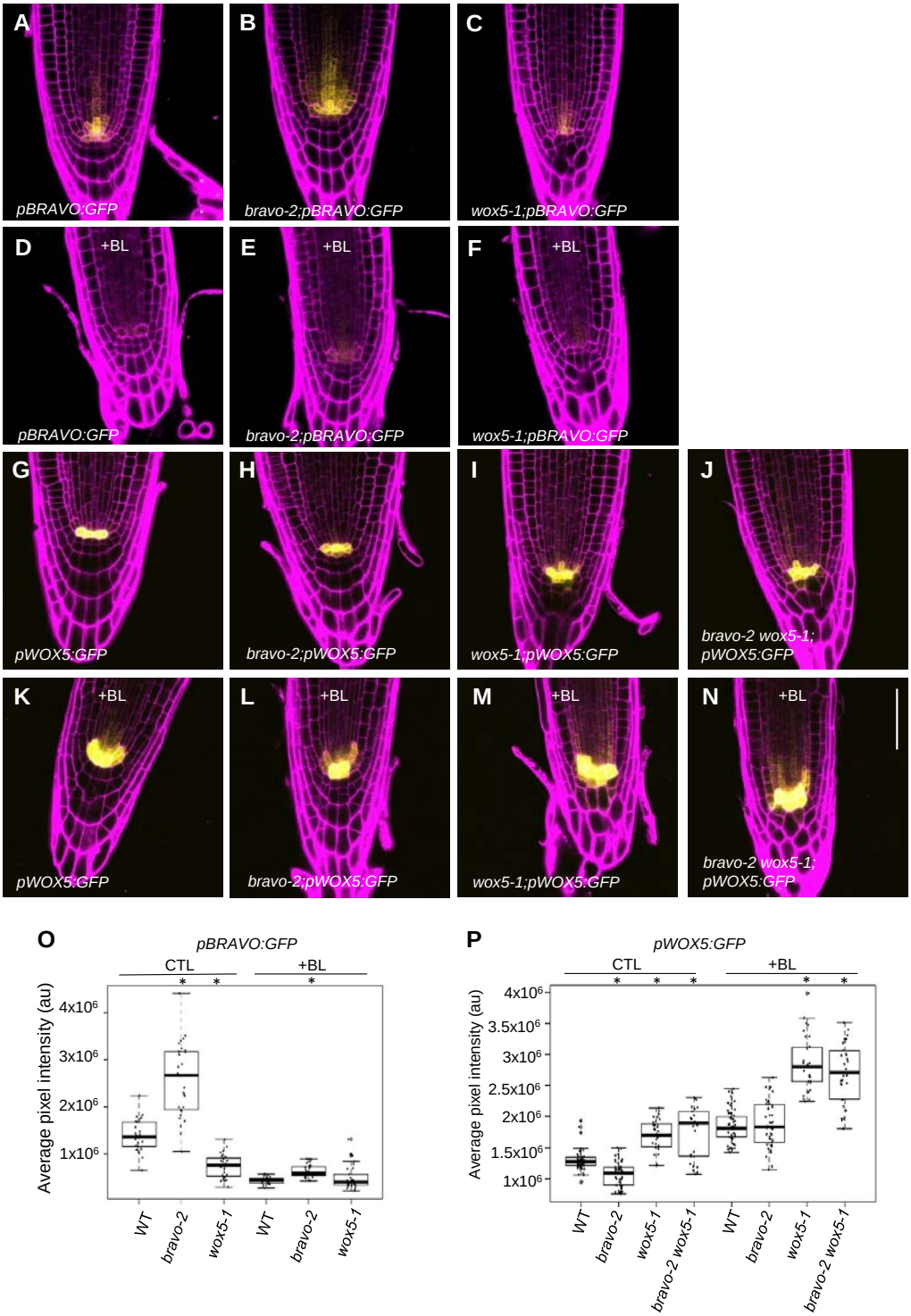



**Figure 4.21: BRAVO and WOX5 expression is BL regulated. A-N)** Confocal images of PI-stained 6-day-old roots. GFP-tagged expression is shown in yellow. A-C) pBRAVO:GFP in WT, *bravo-2* and *wox5-1* knockout backgrounds in CTL (A-C) and after 48h 4nM BL treatment (D-F). G-N) *pWOX5:GFP* in WT, *bravo-2*, *wox5-1* and *bravo-2 wox5-1* knockout backgrounds in CTL (G-J) and after 48h 4 nM BL treatment (K-N). Images in control conditions are the same that are shown in Figure 2. Scale bar: 50 $\mu$m. **O,P)** Quantification of the GFP fluorescent signal of the roots in A-F (O) and G-N (P). Boxplot indicating the average pixel intensity of the GFP in the stem cell niche. ($n > 25$, 3 biological replicates, *$p$-value $<$ 0.05 Student's $t$-test for each genotype versus the WT in the same condition). Quantification of lines in control conditions are the same as those shown in Figure 4.3. These results (together with Figure 4.20) suggest that the mutual regulation of BRAVO and WOX5, as well as their self-regulation, is not significantly altered by BL treatment. Figure as in [Betegón-Putze et al., 2021].

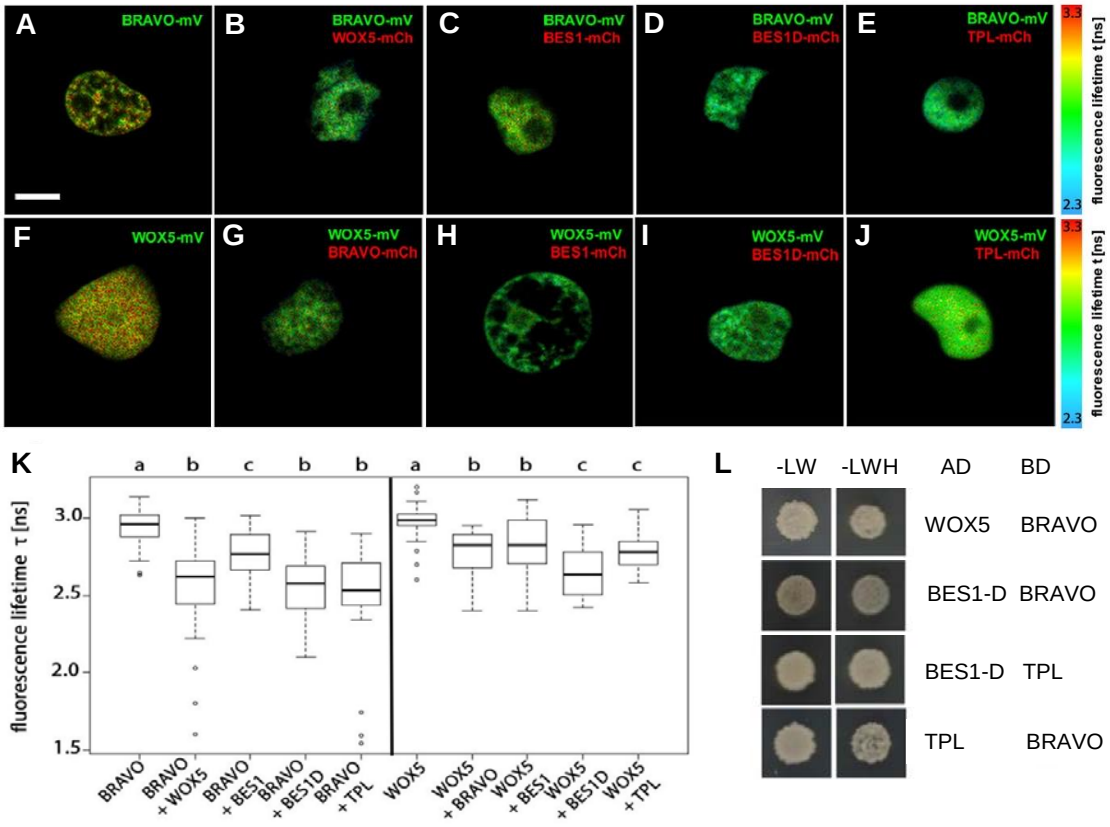



**Figure 4.22: BRAVO physically interacts with WOX5. A-J)** Interaction of BRAVO with WOX5 (B), BES1 (C), BES1D (D) and TPL (E); and interaction of WOX5 with BRAVO (G), BES1 (H), BES1D (I) and TPL (J) measured by FRET-FLIM. GFP fluorescence lifetime $\tau$ [ns] has been measured in transiently expressing *Nicotiana benthamiana* leaf epidermal cells. GFP fluorescence lifetime fitted pixel-wise with a mono-exponential model of BRAVO and WOX5 interactions. mV: mVenus; mCh: mCherry. Scale bar: 5 $\mu$m. **K)** Fluorescence-weighted average lifetimes of BRAVO and WOX5 interactions fitted with a double-exponential model of the indicated samples are summarized in the boxplots. Statistical significance has been tested by one-way ANOVA with a Sidakholm post-hoc test. Different letters indicate statistically significant differences ($p$-value $< 0.01$; $n > 20$). **L)** Yeast two-hybrid assay showing BRAVO interacting with WOX5, BES1-D and TPL. In the left column yeast cells were grown on control media, and in the right column yeast cells were grown on control media lacking Leu, Trp and His, indicating an interaction between the proteins. Using Förster resonance energy transfer measured by fluorescence lifetime microscopy (FRET-FLIM) [Long et al., 2017] (Figure 4.22) and yeast two-hybrid assays. Figure as in [Betegón-Putze et al., 2021].

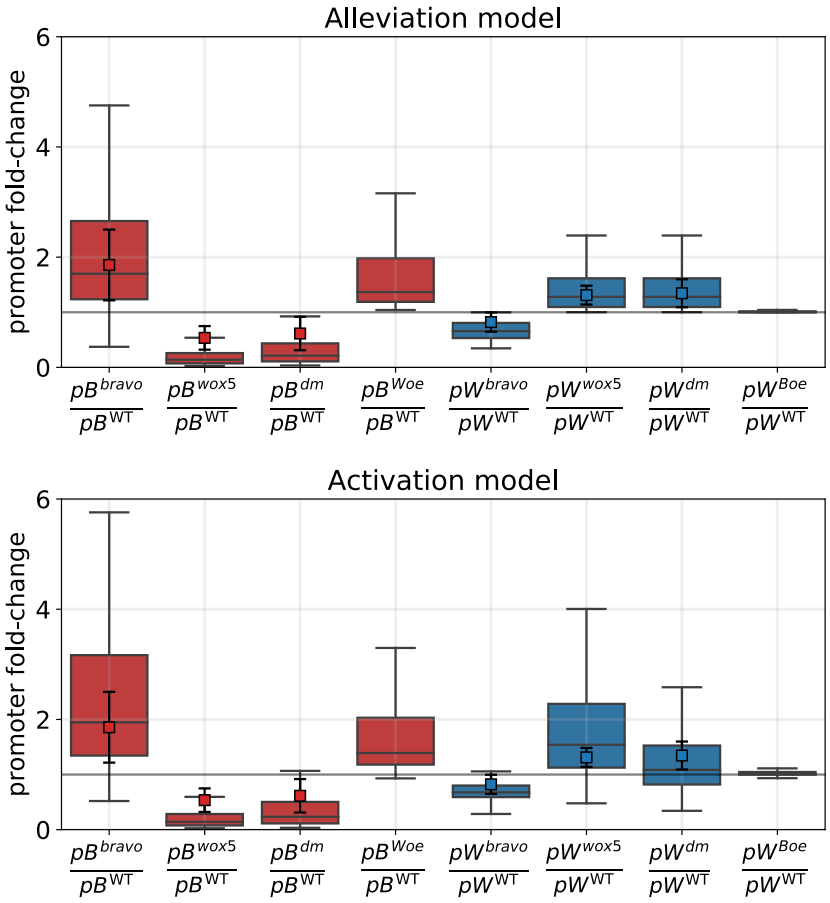



**Figure 4.23: Promoter fold-changes in the alleviation and activation models for higher parameter variability.** When parameters are allowed to change with a broader range, the activation model makes worse predictions than the alleviation model, particularly in the WOX5 promoter. In this case, we choose $f = 5$. Figure as in [Betegón-Putze et al., 2021].

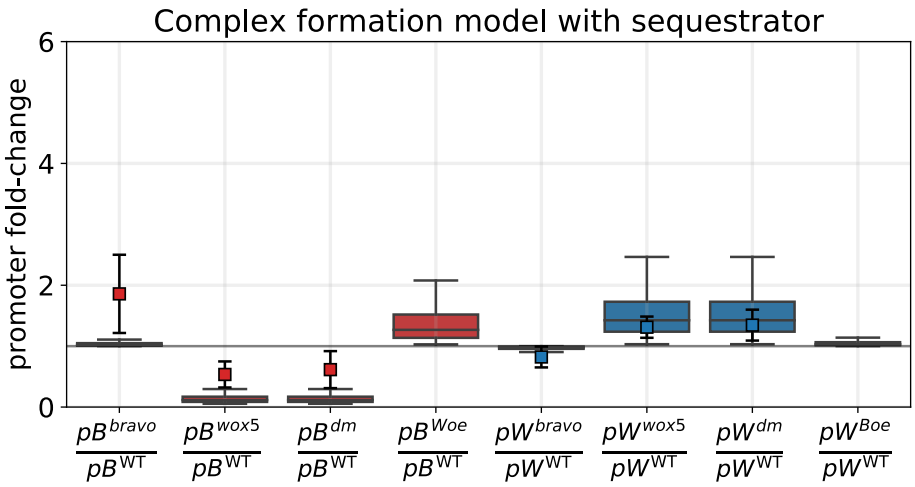



**Figure 4.24: Promoter fold-changes in the complex formation model with an additional sequestrator with high activity.** When the sequestrator has a larger production rate ($\alpha_S = 2$ in this figure), the promoter fold-change become impaired, and the model is not able to reproduce experimental results. Figure as in [Betegón-Putze et al., 2021].

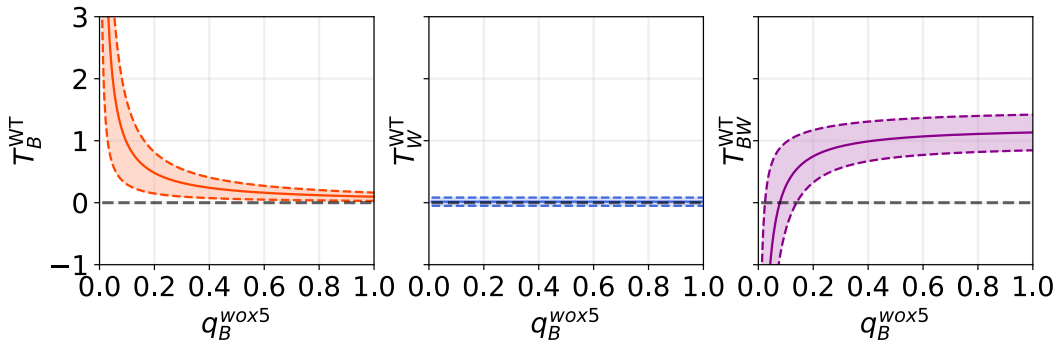



**Figure 4.25: Higher $N$ reduces the error of QC division contributions.** For a large number of simulations (emulating roots), the error associated with the contributions of QC division decreases. Results are for $N = 100$. Figure as in [Betegón-Putze et al., 2021].

# Chapter 5

# BRAVO restricts its own expression in the stem cell niche

## Contents


**5.1 Introduction . . . . . 104**
**5.2 Modelling BRAVO self-confinement in the root SCN 106**
5.2.1 Confinement through immobilization of WOX5 . . . . 106
5.2.2 Confinement through inactivation of WOX5 . . . . . 114
5.2.3 Confinement through the repression of a mobile activator 118
**5.3 Modelling BRAVO self-confinement in a realistic root layout . . . . . 122**
**5.4 Discussion . . . . . 129**


This chapter is based on the results presented in Chapter 4, and extends them to include spatial effects. Here, the main goal is to understand how BRAVO regulates its own promoter expression in space, in such a way that in loss of function *bravo* mutants, its domain of expression expands. Through mathematical modelling, we find that in WT conditions BRAVO is able to confine its own expression domain in the stem cell niche by attenuating the activity of a mobile activator, which can be WOX5 or one of its targets. Incidentally, these mechanisms also confine the spatial domain of WOX5 activity. We show that this attenuation can occur either through sequestration – thus making the connection with the hypothesis proposed in Chapter 4 – or of through direct repression. Modelling these situations in a simplified, 1D framework reveals that indeed confinement emerges as a direct outcome of the model's interactions, without the need to fine-tune parameters. Making the extension to a

realistic root layout, where the cellular geometry of the root and differential diffusion through the cytoplasm and cell walls is taken into account, shows that this mechanism allows *BRAVO* expression to be confined within few cells. We propose that attenuation of a diffusible activator can be a general mechanism for a gene to self-confine its activity to a small region while at the same time maintain signalling between cells. The results of this chapter are available as a preprint at bioR$\chi$iv [Mercadal et al., 2021].

## 5.1 Introduction

Stem cell niches (SCNs) constitute a reservoir of undifferentiated cells whose main role is to sustain growth and replace old or damaged tissues [Sablowski, 2007]. Usually, SCNs consist of just a few number of cells, which maintain their pluripotency through the integration of short-range signals produced by localized sources or *organizing centers*, groups of cells which keep neighbouring cells in a stem cell state [Scadden, 2006, Spradling et al., 2001]. As daughters of these organizing cells are placed outside the reach of these signals they begin to differentiate and give rise to more specialized cell types [Sablowski, 2004]. In animals, typical signals preserving stem cell identity come in the form of diffusible ligands, such as the *Decapentaplegic* (*Dpp*) and *Hedgehog* (*Hh*) morphogens in *Drosophila* which, among other functions, control the number of ovarian germline cells by preventing their differentiation [Xie and Spradling, 1998, Chen and McKearin, 2003, Zhang and Kalderon, 2001]; the *Hh* mouse homolog *Sonic hedgehog* (*Shh*), which is required for the maintenance of neural progenitors in the stem cell niche located at the subventricular zone of the mouse forebrain [Machold et al., 2003, Palma et al., 2005, Han et al., 2008]; or the *Wnt* pathway, which is involved in hematopoietic stem cell renewal [Fleming et al., 2008, Nemeth and Bodine, 2007], in the differentiation of cells in the intestinal crypt [Ootani et al., 2009, Farin et al., 2016] and in the control of brain cell precursors [Nusse et al., 2008, Rattis et al., 2004]. In all cases, overproduction of these signals leads to an increase in the frequency of division of stem cells, enlarging their otherwise limited domain and often leading to the malfunctioning of the surrounding tissues and organs [Spradling et al., 2001].

In plants, mobile factors with morphogen-like characteristics having a role in stem cell maintenance include phytohormones such as auxin [van Berkel et al., 2013, Grieneisen et al., 2007], reactive oxygen species like hydrogen peroxide ($H_2O_2$) and superoxide ($O_2^{\bullet -}$) [Kong et al., 2018, Lv et al., 2018, Yu et al., 2016, Huang et al., 2019], small microRNAs [Knauer et al., 2013, Skopelitis et al., 2018], as well as transcription factors like PLETHORA [Aida et al., 2004, Mähönen et al., 2014].

In the *Arabidopsis* root, the SCN is specified by the constant balance between external signalling and local communication, restricting the location of stem cells to a small, well-defined region (see Figure 4.1 in the previous chapter).

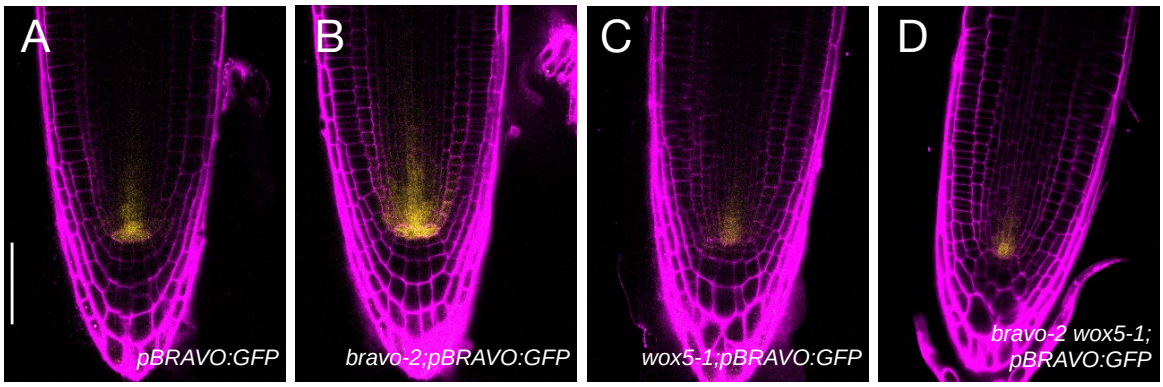



**Figure 5.1: *pBRAVO* activity in WT and in loss of function mutants.** Confocal images of PI-stained 6-day-old roots. GFP-tagged expression is shown in yellow. Activity of the BRAVO promoter in WT (A) and *bravo-2* (B), *wox5-1* (C) and *bravo-2 wox5-1* (D) knockout backgrounds. Scale bar: 50$\mu$m. The promoter activity of BRAVO expands its domain in the *bravo-2* mutant. This suggests that BRAVO confines its own expression to the QC and VI in the WT. The expansion is not observed in *wox5-1* mutants nor in *bravo-2 wox5-1* double mutants, suggesting that such confinement requires WOX5. Results from the same set of experiments as Figure 4.2. Figure as in [Mercadal et al., 2021].

Direct cell-cell contact from the QC to its surrounding stem cells is important for stem cell identity [van den Berg et al., 1997, Liu et al., 2017] and can involve the transport of short-range signals from the QC. Recent studies have revealed that WOX5, specifically expressed at the QC, is able to move towards adjacent cells [Clark et al., 2020], and itself has been proposed to act as the short-range signal to repress columella stem cell differentiation [Pi et al., 2015], albeit recent results challenge this view [Berckmans et al., 2020]. While short-range signalling is thought to ensure that stem cell numbers are restrained and the SCN does not become displaced from the growing root tip, it is yet unclear how this is achieved [Scheres, 2007, Rahni et al., 2016, Matosevich and Efroni, 2021].

As indicated in Chapter 4, both WOX5 and BRAVO have been independently shown to repress QC divisions [Vilarrasa-Blasi et al., 2014, Forzani et al., 2014]. The results presented in Chapter 4 support the hypothesis that the two transcription factors mutually promote their activity and that they form a complex that may be relevant in the regulation of QC divisions [Betegón-Putze et al., 2021]. In addition, the experimental results show that the expression of the *BRAVO* promoter, restricted to the QC and VI in WT plants, expands its domain of expression towards the vasculature, cortex and endodermis, in *bravo* loss of function mutants (Figure 5.1A,B). This suggests that BRAVO actively confines its own expression domain. Moreover, this expansion is not observed in the double mutant *bravo wox5* when compared to the WT and to the single mutant *bravo* (Figure 5.1D), pointing to a mechanism which is strongly WOX5-dependent. In this chapter, we address the question of how BRAVO achieves this self-confinement.

## 5.2 Modelling BRAVO self-confinement in the root SCN

To decipher the mechanisms by which the self-confinement of BRAVO can be accomplished, we use an approach that takes advantage of the known interactions between the BRAVO and WOX5 proteins obtained in Chapter 4 and study their behaviour in a spatial setting, where protein transport through diffusion is explicitly taken into account. Recent results suggests that the action of WOX5 may not be exclusively restricted to QC cells, but to the SCN as a whole. Indeed, WOX5 proteins have been shown to move towards the columella [Pi et al., 2015] and to the VI [Berckmans et al., 2020, Clark et al., 2020], thus allowing us to explore the consequences its mobile nature on the activity of BRAVO. While the mobility of WOX5 has been experimentally tested *in planta* (with plasmodesmata as possible tranport channels) [Berckmans et al., 2020, Clark et al., 2020], the intercellular BRAVO transport has not been investigated. The BRAVO protein has a molecular weight of about $\sim$ 36 kDa, compared to the smaller WOX5, with $\sim$ 20 kDa [TAIR, 2017]. Moreover, the plasmodesmata size exclusion limit, i.e. the maximum size the protein is allowed to have in order to move through plasmodesmata, is estimated to range from $\sim 27 - 54$ kDa in the boundaries between QC/cortex and QC/columella stem cells [Rim et al., 2011][1]. In light of these observations, in all models we assume BRAVO proteins are immobile, contrasting to the mobile nature of WOX5.

### 5.2.1 Confinement through immobilization of WOX5

This first model takes into account that BRAVO and WOX5 form a complex (as in Chapter 4 and [Betegón-Putze et al., 2021]). It is loosely based on the interactions between BRAVO and WOX5 proposed in the complex formation model of Chapter 4, where WOX5 activates *BRAVO* expression, and both proteins interact into a higher order complex that does not regulate neither *BRAVO* nor *WOX5*[2]. Additionally, we assume WOX5 proteins diffuse from its production source, i.e. the QC, and are therefore able to activate *BRAVO* in a larger domain. In contrast, BRAVO proteins are assumed to be immobile. The BRAVO-WOX5 complex, owing to its larger size, is not expected to move from cell to cell either. With all these assumptions, the mechanism by which BRAVO self-confines becomes apparent: WOX5 proteins, produced in QC cells

[1] All these values may change depending on different environmental conditions and developmental stages, particularly through the regulation of callose deposition [Yadav et al., 2014].

[2] We will use the term *inactive* to refer to the inability of the complex to regulate BRAVO or WOX5, but this does not mean that the complex cannot regulate other proteins. We do not want to convey the idea that the BRAVO-WOX5 complex has no role in regulating other factors, only that its effect on the BRAVO/WOX5 circuit is purely post-transcriptional.

and being able to move to the VI, are able to activate *BRAVO* therein. In turn, BRAVO proteins sequester WOX5 into an immobile complex, thus preventing its movement to other cells and the subsequent activation of *BRAVO* expression. Hence, the activation of the *BRAVO* promoter by WOX5 is spatially confined by BRAVO itself, a restriction which becomes released when BRAVO no longer immobilizes WOX5, e.g. in *bravo* loss of function mutants.

To see whether the above-mentioned rationale is sound, we translate the previous assumptions intof mathematical form, by considering the dynamics of the BRAVO and WOX5 proteins in one spatial dimension. We denote the concentration of BRAVO and WOX5 proteins as $B(x,t)$ and $W(x,t)$, respectively, where $x$ and $t$ denote, respectively, the spatial position and time. For simplicity, in the model BRAVO is induced by WOX5 in a linear fashion. Moreover, based on the results of the previous chapter, we assume that the complex does not regulate the expression of neither *BRAVO* nor *WOX5*. With all this, the dynamics of $B(x,t)$ and $W(x,t)$ follow:

$$\frac{\partial B(x,t)}{\partial t} = \alpha W(x,t) - \lambda B(x,t)W(x,t) - d_B B(x,t) \tag{5.1a}$$

$$\frac{\partial W(x,t)}{\partial t} = \gamma_{QC}(x) - \lambda B(x,t)W(x,t) - d_W W(x,t) + D_W \frac{\partial^2 W(x,t)}{\partial x^2} \tag{5.1b}$$

Here, the parameter $\alpha$ (which has units of inverse time, $\mathrm{s}^{-1}$) measures the rate at which BRAVO proteins are produced. WOX5 is synthesized at a constant rate $\gamma_{QC}(x)$, where the subscript and the explicit spatial dependence indicate that it is only produced at the QC. We choose $\gamma_{QC}(x)$ to be a rectangular function of the form

$$\gamma_{QC}(x) = \begin{cases} 0 & \text{if } |x| \geq L_{QC}/2 \\ \gamma & \text{if } |x| < L_{QC}/2 \end{cases} \tag{5.2}$$

where $L_{QC}$ is defined as the total length of the QC region. This implies that WOX5 production will only occur in the region delimited by $-\frac{L_{QC}}{2} \leq x \leq \frac{L_{QC}}{2}$, with constant production rate $\gamma$. Degradation of BRAVO and WOX5 is controlled by the parameters $d_B$ and $d_W$, respectively. The movement of WOX5 is controlled by the diffusion coefficient $D_W$. Finally, complex formation between BRAVO and WOX5 is mediated by the parameter $\lambda$. By writing the complex formation term as $\lambda B(x,t)W(x,t)$ we implicitly assume that either binding is irreversible, or the dynamics of complex formation are very fast compared to the other reactions and that the complex can be degraded. In the former case $\lambda$ can simply be interpreted as the rate of complex formation (i.e., binding). To see what $\lambda$ represents in the latter case, consider Equation 5.1 but with all the

reactions involving complex formation:

$$\frac{\partial B(x,t)}{\partial t} = \alpha W(x,t) - \lambda B(x,t)W(x,t) + \delta C(x,t) - d_B B(x,t) \tag{5.3a}$$

$$\frac{\partial W(x,t)}{\partial t} = \gamma_{QC}(x) - \lambda B(x,t)W(x,t) + \delta C(x,t) - d_W W(x,t) + D_W \frac{\partial^2 W(x,t)}{\partial x^2} \tag{5.3b}$$

$$\frac{\partial C(x,t)}{\partial t} = \lambda B(x,t)W(x,t) - \delta C(x,t) - d_C C(x,t) \tag{5.3c}$$

Where $\delta$ represents the unbinding rate of the complex, and $d_C$ its degradation. If the dynamics of the complex are very fast, we can assume the third equation is approximately in the steady state, leading to an expression for $C(x) = \frac{\lambda B(x)W(x)}{\delta + d_C}$. Upon substitution to the other equations, we obtain:

$$\frac{\partial B(x,t)}{\partial t} = \alpha W(x,t) - \frac{\lambda d_C}{\delta + d_C} B(x,t)W(x,t) - d_B B(x,t) \tag{5.4a}$$

$$\frac{\partial W(x,t)}{\partial t} = \gamma_{QC}(x) - \frac{\lambda d_C}{\delta + d_C} B(x,t)W(x,t) - d_W W(x,t) + D_W \frac{\partial^2 W(x,t)}{\partial x^2} \tag{5.4b}$$

These equations have the same form as Equation 5.1 but with the redefinition of $\lambda \to \frac{\lambda d_C}{\delta + d_C}$. Therefore, if the complex is not irreversible $\lambda$ also encodes information about complex degradation and dissociation.

Now we want to compare how the spatial profile of the BRAVO promoter changes in the *bravo* mutant with respect to the WT. As in Chapter 4, we model the *bravo* mutant by setting $B(x,t) = 0$ and solving the remaining equations. As we do not have available temporal data, these equations will be solved in the stationary state. The promoter activities of BRAVO and WOX5 in the stationary state are defined as $pB(x) = \alpha W_s(x)$ and $pW(x) = \gamma_{QC}(x)$, respectively, where $W_s(x)$ denotes the spatial profile of WOX5 in the stationary state, as indicated by the subscript $s$.

In order to find $W_s(s)$ and $B_s(s)$ in the WT, we solve Equation 5.1 by setting the time derivatives to zero. Upon substituting $B(x)$ into the equation for $W(x)$, the system simplifies to the following second order differential equation:

$$D_W \frac{d^2 W(x)}{dx^2} = -\gamma_{QC}(x) + \left( \frac{\lambda \alpha W(x)}{\lambda W(x) + d_B} + d_W \right) W(x) \tag{5.5}$$

where the subscript $s$ has been dropped for clarity. The above equation can be interpreted as WOX5 diffusing from the spatially extended source at $-\frac{L_{QC}}{2} \leq x \leq \frac{L_{QC}}{2}$, with a *nonlinear* degradation rate, given by $d'_W[W(x)] =$

$d_W + \frac{\lambda\alpha W(x)}{\lambda W(x)+d_B}$. In the last section of this chapter we will discuss the relevance of this nonlinear degradation in the context of robust morphogen gradients. In the *bravo* mutant, degradation is no longer nonlinear. To see this, we model the *bravo* mutant by setting $B(x,t) = 0$ in Equation 5.1 and solving the remaining equation for $W(x)$ in the steady state:

$$D_W \frac{d^2W(x)}{dx^2} = -\gamma_{QC}(x) + d_W W(x) \tag{5.6}$$

The solution $W(x)$ of this equation decays exponentially as $x$ gets away from the QC. Therefore, the spatial profile of BRAVO activity is different in the WT than in the *bravo* mutant.

In Figure 5.2B,C we show the stationary activity profiles $pW(x)$ (inset), $pB(x) = \alpha W_s(x)$, $B_s(x)$ and $W_s(x)$ in the WT (continuous lines) and in the *bravo* mutant (dashed lines). As expected, the profile of $pB(x)$ in the *bravo* mutant spreads (Figure 5.2B) due to WOX5 being able to diffuse larger distances, as it is not sequestered by BRAVO (Figure 5.2C). Therefore, our results show that since the domain of $pB(x)$ expands in the *bravo* mutant, the immobilization by sequestration mechanism is able to confine the expression of *BRAVO* expression in the WT.

Notice the stationary profile of $W_s(x)$ in the WT is not symmetric, but decays in a different fashion above and below the QC, a behaviour caused by the presence and absence, respectively, of BRAVO proteins (Figure 5.2C). Above the QC, WOX5 activates BRAVO, making the gradient of WOX5 proteins to be steeper than below the QC, where BRAVO cannot be activated. Hence, the presence of BRAVO makes the WOX5 gradient more abrupt, restricting the spatial domain where WOX5 protein is concentrated, and consequently confining its own expression domain (recall that in this simplified model *BRAVO* expression is proportional to WOX5 levels). In the *bravo* mutant, the gradient of WOX5 proteins expands and the profile becomes symmetric with respect to the QC due to the absence of WOX5 sequestration by BRAVO. Consequently, the domain where the *BRAVO* promoter is activated also expands proportionally.

The expansion of $pB(x)$ in the *bravo* mutant can potentially be much larger than that shown in Figure 5.2C, depending on the sequestration rate $\lambda$ or the diffusion coefficient $D_W$. However, the parameters for the profiles shown in the figure are chosen to qualitatively match the experimental results of *pBRAVO:GFP*, where the expansion, while noticeable, is not very pronounced (see Figure 5.1A). Indeed, we can quantify the expansion of the simulated profile of $pB(x)$ in the *bravo* mutant with respect to the WT as follows. We first define $x_{VI}$ to be the position where the VI region ends, in our case $x_{VI} = \frac{3}{2}L_{QC}$ (light gray region), and compute the activity of the *BRAVO* promoter at this point, $pB^{WT}(x_{VI})$. For the *bravo* mutant, we define $x^{bravo}$ to be the position at which the *BRAVO* promoter in the *bravo* mutant takes the value $pB^{WT}(x_{VI})$, i.e. $pB^{bravo}(x^{bravo}) = pB^{WT}(x_{VI})$ (see Figure 5.2B). Then, we can quantify the

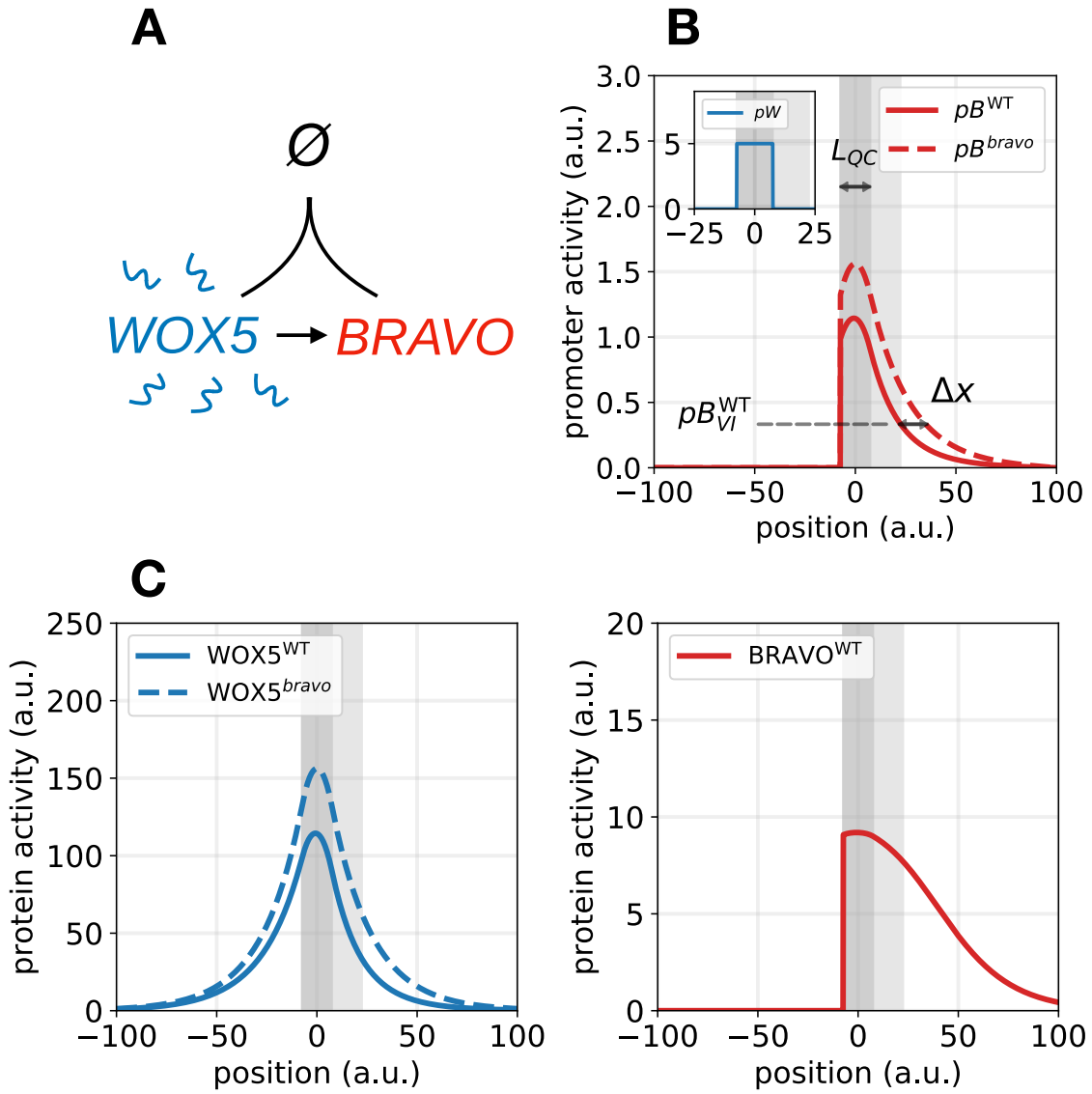



**Figure 5.2: Immobilization by sequestration model. A)** Cartoon displaying the models' interactions: WOX5 diffuses (wavy lines) and activates (arrow) BRAVO. In turn, BRAVO immobilizes WOX5 by sequestering it into an immobile and inactive complex (depicted as $\emptyset$). **B)** Stationary profiles of BRAVO and WOX5 promoter activities, $pB(x)$ and $pW(x)$, in the WT (continuous lines) and in the *bravo* mutant (dashed lines). The QC region (dark gray, where $pW$ is active) has a size $L_{QC}$. For simplicity, the VI region (light gray) is set to be of the same size as the QC. The value of $pB(x)$ in the WT at the end of the VI is denoted by $pB_{VI}^{WT}$. The quantity $\Delta x$ measures the relative expansion of $pB$ in the *bravo* mutant as compared with $pB$ in the WT. Confinement is said to occur when $\Delta x > 0$. **C)** Stationary protein activity profiles of WOX5 and BRAVO in WT (continuous lines) and in the *bravo* mutant (dashed lines) corresponding to the simulations in B). In all panels, parameter values are $\alpha = 0.01$, $\gamma = 5$, $\lambda = 0.001$, $d_W = d_B = 0.01$ and $D_W = 0.01$ (see Table 5.2).

expansion of the domain of *BRAVO* expression via the quantity:

$$\xi = \frac{x_{VI} - x^{bravo}}{L_{QC}} \equiv \frac{\Delta x}{L_{QC}} \tag{5.7}$$

With this definition, $\xi$ measures the difference in expression in WT and *bravo* mutants relative to the size of the QC. Upon close inspection, one can readily see that changes in $\xi$ might come as a consequence of two qualitatively distinct processes: through an increase in the total activity of $pB$ (for example, by increasing $\alpha$); or through a spread in the distribution, without necessarily having an increase in $pB(x)$ activity (e.g. by increasing $D_W$). In Figure 5.3 we show how changing the parameters $\alpha$, $\lambda$ and $D_W$ induce changes in the stationary profile of $pB(x)$.

Moreover, experimental data of WT roots indicates that in the QC the BRAVO promoter is $\sim 0.2$ times the value of the WOX5 promoter [Clark et al., 2019] (i.e., the condition $pB^{WT}(x_{QC})/pW^{WT}(x_{QC}) \sim 0.2$), and that BRAVO is not only expressed in the QC, but in the VI as well [Vilarrasa-Blasi et al., 2014, Betegón-Putze et al., 2021]. To evaluate whether these conditions are met in our simulations, we define the ratio between the WT activities of $pB(x)$ at $x_{VI}$ and of $pW(x)$ at $x_{QC}$:

$$R = \frac{pB^{WT}_{VI}}{pW^{WT}_{QC}} \tag{5.8}$$

In the experiments, this quantity remains within a certain interval close to $R \simeq 0.05 - 0.2$ [Betegón-Putze et al., 2021]. In Figure 5.4, we show how $R$ and $\xi$ change as a function of the binding rate $\lambda$, and for different values of the BRAVO production rate $\alpha$ (other parameters remain fixed, see Table 5.2). Red crosses mark the values of $\alpha, \lambda$ used in Figure 5.2A,B, which verify the condition of $0.05 < R < 0.2$.

Additional consequences of this model and their relevance for comparing with experimental data are worth mentioning. Importantly, the mechanism explicitly requires WOX5 to be mobile. As shown in Figure 5.3, if WOX5 has a large diffusion coefficient ($D_W = 0.05$, compared with $D_W = 0.01$ in Figure 5.2), the expression domain of *BRAVO* in the WT spreads too far away from the QC, and its absolute values are too low, in disagreement with experimental observations (Figure 5.1, Figure 4.2 [Betegón-Putze et al., 2021]). Indeed, WOX5 diffusion has been reported to be rather small [Berckmans et al., 2020, Clark et al., 2020]. Increasing the production rate of BRAVO, $\alpha$, also leads to dramatic changes in the promoter profile, while increasing $\lambda$ (while keeping $\alpha$ small) may still produce profiles which are in agreement with experimental data (Figure 5.3).

Sequestration of WOX5 by BRAVO (mediated by the parameter $\lambda$) is also necessary for BRAVO to confine its own expression (Figure 5.4). Yet, high sequestration (large $\lambda$ and high synthesis rate $\alpha$) can lead to an overly exaggerated confinement, with BRAVO being highly expressed at the QC but not in VI

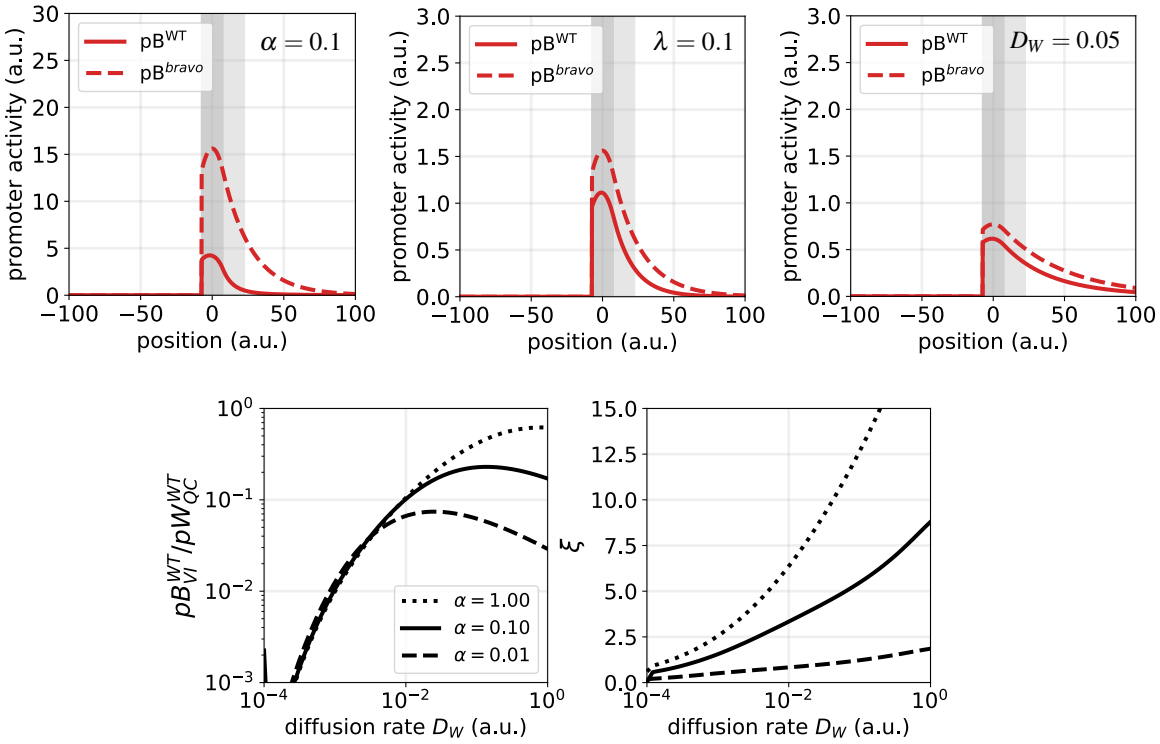



**Figure 5.3: Parameter dependence of $pB(x)$ in the immobilization by sequestration model.** (Top) Change in the spatial profile of $pB(x)$ for different values of the parameters $\alpha$, $\lambda$ and $D_W$ (see Table 5.2 for default values). (Bottom) The effect of WOX5 diffusion on the quantities $pB^{WT}_{VI}/pW^{WT}_{QC}$ and $\xi$, for different values of $\alpha$. Here we see how at least some (non-zero) value of WOX5 diffusion is needed to induce an expansion of $pB(x)$ in the *bravo* mutant, while too much diffusion can even be detrimental for the expansion. The profiles of $B(x)$, $W(x)$, $pW(x)$ corresponding to these figures are shown in Figure 5.18.

cells, a situation which would be in disagreement with the experimentally observed WT expression (Figure 5.1A). Low sequestration of WOX5 by BRAVO at the QC is expected in the *Arabidopsis* root since the expression of *BRAVO* in the SCN and the amount of *BRAVO* RNA transcripts are low compared to those of *WOX5* (we take as an approximate value $WOX5^{WT}_{QC} \approx 5BRAVO^{WT}_{QC}$) [Vilarrasa-Blasi et al., 2014, Betegón-Putze et al., 2021, Clark et al., 2019]. Overall, these results suggest that the *immobilization by sequestration* mechanism is a plausible candidate to explain the observed self-confinement of *BRAVO* expression.

Since sequestration is a key ingredient for this mechanism to work, one could argue that the presence of other molecules also binding to BRAVO and/or WOX5 might impair or even destroy the confinement. Indeed, as mentioned in Chapter 4, it is known that WOX5 and BRAVO proteins can bind to additional molecules, such as TOPLESS and BES1 [Vilarrasa-Blasi et al., 2014, Betegón-Putze et al., 2021]. Since these are relatively large molecules ($\sim$ 39 kDa and $\sim$ 124 kDa, respectively [TAIR, 2017]) it would be possible for them to immobilize WOX5. Therefore, assuming that BRAVO is activated by WOX5 outside

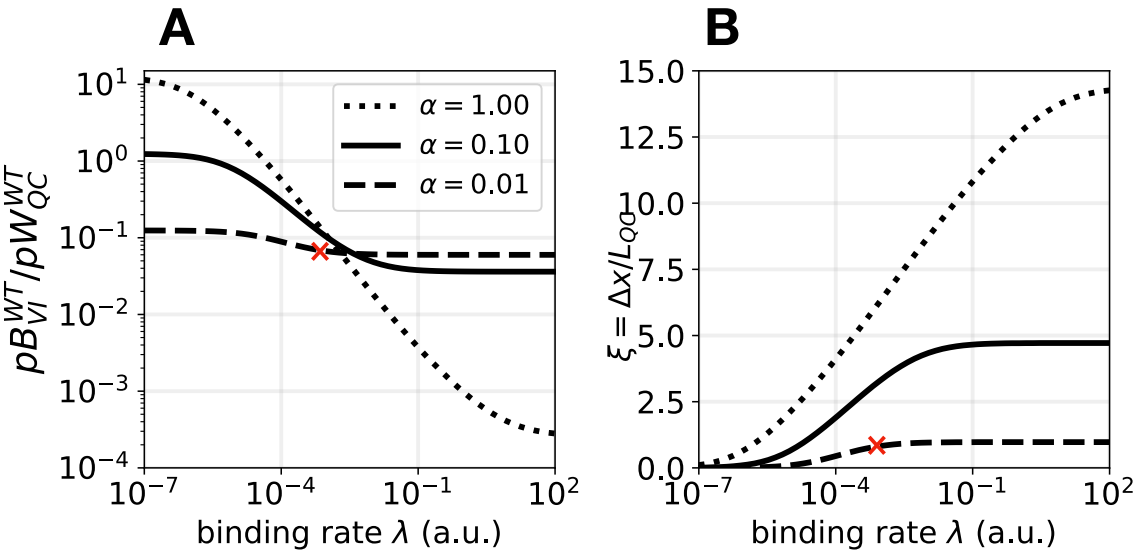



**Figure 5.4: Expansion and expression ratios in the immobilization by sequestration model.** Effect of the binding rate $\lambda$ and the BRAVO synthesis rate $\alpha$ on $R$ (A) and $\xi$ B). The curves drawn in B) correspond to the same $\alpha$ values as in A). The red crosses in D) and E) mark the values of $\alpha$ and $\lambda$ used for the simulations in Figure 5.2. Larger values of $\alpha$ increase the expansion but lead to $pB \approx pW$ at the QC in the WT (Figure 5.18), which is not experimentally supported [Betegón-Putze et al., 2021, Clark et al., 2019]. In both panels, parameter values are $\gamma = 5$, $d_W = d_B = 0.01$ and $D_W = 0.01$ (see Table 5.2).

the QC, these other molecules can also help to confine *BRAVO* expression, by preventing the movement of WOX5. To test this possibility, we introduce the presence of a generic sequestrator $S$ to the BRAVO-WOX5 system. If $S$ can bind both BRAVO and WOX5, the new equations are:

$$\frac{\partial B(x,t)}{\partial t} = \alpha W(x,t) - \lambda B(x,t)W(x,t) - \lambda_{BS}B(x,t)S(x,t) - d_B B(x,t) \tag{5.9a}$$

$$\frac{\partial W(x,t)}{\partial t} = \gamma_{QC}(x) - \lambda B(x,t)W(x,t) - \lambda_{WS}W(x,t)S(x,t) - d_W W(x,t) + D_W \frac{\partial^2 W(x,t)}{\partial x^2} \tag{5.9b}$$

$$\frac{\partial S(x,t)}{\partial t} = \alpha_S - \lambda_{Bs}B(x,t)S(x,t) - \lambda_{BS}B(x,t)S(x,t) - \lambda_{WS}W(x,t)S(x,t) - d_S S(x,t) \tag{5.9c}$$

where $S(x,t)$ represents the concentration of the sequestrator $S$. We assume that $S$, whether or not is bound to BRAVO or WOX5, does not regulate the production any of them; its only role is to sequester its proteins. The new

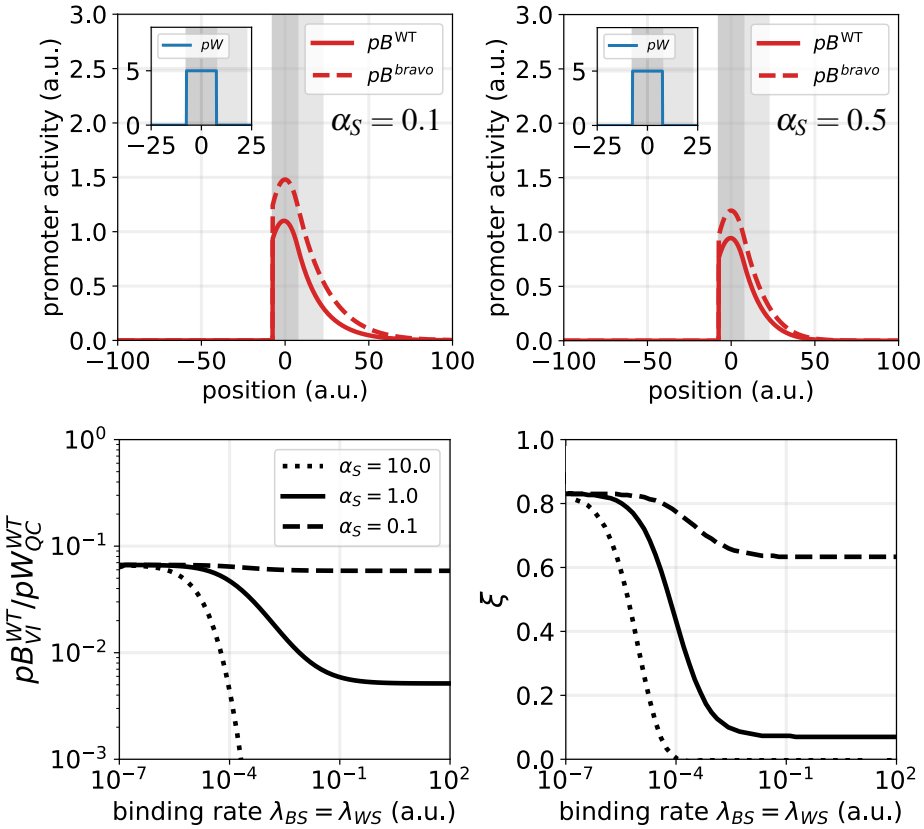



**Figure 5.5: The presence of an additional sequestrator impairs BRAVO self-confinement.** (Top) Profiles of BRAVO promoter activity for different values of sequestrator production $\alpha_S$. (Bottom) The effect of sequestrator production ($\alpha_S$) and sequestration rates ($\lambda_{BS}, \lambda_{WS}$) on the expansion of $pB(x)$. While for low values of $\alpha_S$, $\lambda_{BS}$ and $\lambda_{WS}$, the quantities $pB^{WT}_{VI}/pW^{WT}_{QC}$ and $\xi$ remain similar to the original model, an increase in their values weakens the expansion of $pB(x)$. The profiles of $B(x)$, $W(x)$, $pW(x)$ and $S(x)$ corresponding to these figures are shown in Figure 5.19. Figure as in [Mercadal et al., 2021].

parameters $\alpha_S$ and $d_S$ represent the production and degradation of $S$ proteins, respectively; the parameters $\lambda_{BS}$ and $\lambda_{WS}$ denote the rates fo complex formation between $S$ and BRAVO and $S$ and WOX5, respectively. Modelling this scenario (Figure 5.5) shows that for large activity of the sequestrator $S(x)$ (large $\alpha_S$), the expansion of $pB(x)$ in the *bravo* mutant becomes compromised, as WOX5 proteins are not able to increase nor diffuse because they become sequestered (see Figure 5.19 for the distributions of $W(x)$ and $S(x)$). Therefore, in order to maintain the self-confinement of *BRAVO* expression in the presence of an additional sequestrator, its effect on BRAVO and WOX5 must be small.

### 5.2.2 Confinement through inactivation of WOX5

The self-confinement of *BRAVO* expression in the *immobilization by sequestration* model requires WOX5 to diffuse. Experiments suggest that, while mobile, WOX5 does not move very large distances [Berckmans et al., 2020, Clark

| Parameter | Description | ISAS |
|---|---|---|
| $\alpha_S$ | Protein production rate of $S$ | 0.1 |
| $d_S$ | Degradation rate of $S$ proteins | 0.01 |
| $\lambda_{BS}$ | Complex formation rate between BRAVO and $S$ | 0.001 |
| $\lambda_{WS}$ | Complex formation rate between WOX5 and $S$ | 0.001 |

**Table 5.1: Additional parameters for the immobilization by sequestration model with an additional sequestrator (ISAS).** In the model with an additional sequestrator $S$, the effect of the sequestrator has to be small for the mechanism of BRAVO self-confinement to take place. The remaining parameters are the same as in the original immobilization by sequestration model. The units of all parameter values are arbitrary.

et al., 2020]. Therefore, this small diffusion may not be sufficient to explain the self-confinement of *BRAVO* expression observed in real roots. Since activation of *BRAVO* by WOX5 could happen through intermediary molecules, we asked whether the binding between the two proteins could still be sufficient to drive self-confinement if WOX5 is activating *BRAVO* not directly, but through a highly mobile WOX5 target, hereafter named $X$. This mechanism also assumes that the BRAVO-WOX5 complex is transcriptionally inactive, i.e., does not regulate the activity of $X$. Hence BRAVO, by binding to WOX5, prevents WOX5 from activating $X$ (Figure 5.6A). To evaluate this scenario, we again formulated a minimal model, in this case named *attenuation by sequestration* model, and studied its implications by numerically simulating WT and *bravo* mutant backgrounds, as done in the previous section. In this minimal model, neither WOX5 nor BRAVO can diffuse, but $X$ can. As in the previous section, the complex is not explicitly modelled. The equations of this model are:

$$\frac{\partial B(x,t)}{\partial t} = \alpha X(x,t) - \lambda B(x,t)W(x,t) - d_B B(x,t) \tag{5.10a}$$

$$\frac{\partial X(x,t)}{\partial t} = \beta W(x,t) - d_X X(x,t) + D_X \frac{\partial^2 X(x,t)}{\partial x^2} \tag{5.10b}$$

$$\frac{\partial W(x,t)}{\partial t} = \gamma_{QC}(x) - \lambda B(x,t)W(x,t) - d_W W(x,t) \tag{5.10c}$$

where we introduce the new parameters $\beta$, $d_X$ and $D_X$, characterizing the production, degradation and diffusion of the intermediary factor $X$, respectively.

In this model the BRAVO promoter in the stationary state is $pB(x) = \alpha X_s(x)$, where $X_s(x)$ denotes the concentration profile of the intermediary in the stationary state, while the WOX5 promoter is defined as in the previous case, $pW(x) = \gamma_{QC}(x)$, with $\gamma_{QC}$ only affecting the QC region (Equation 5.2). In the appendix we describe an alternative version of this model where WOX5 is also allowed to diffuse (Figure 5.22). The expansion factor $\xi$ and the ratio $R$ are again computed via Equation 5.7 and Equation 5.8, respectively.

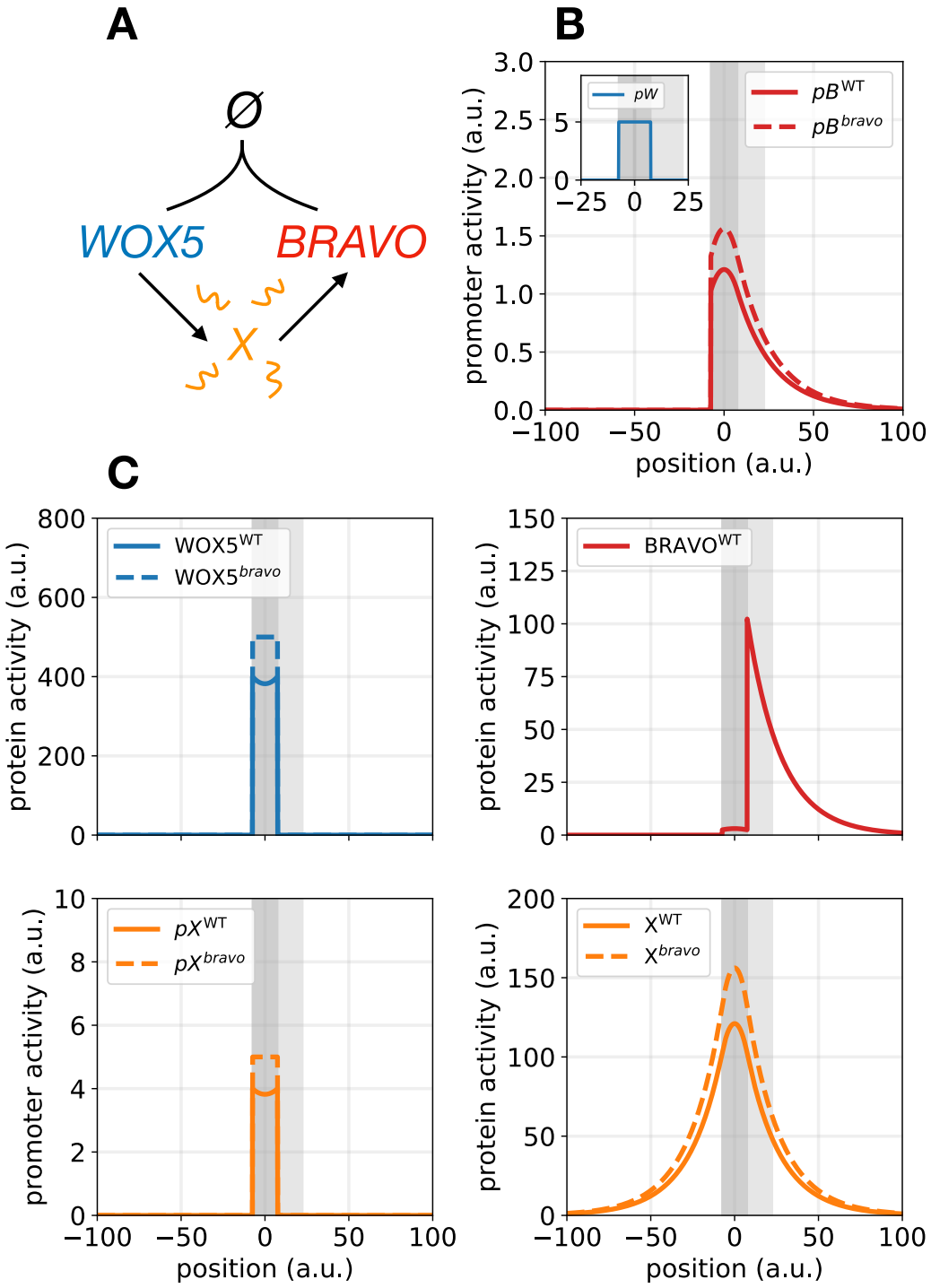



**Figure 5.6: Attenuation by sequestration model.** **A)** Cartoon of the interactions: WOX5 activates a highly diffusible intermediary $X$, which in turn activates BRAVO. BRAVO sequesters and inactivates WOX5 and thus prevents the activation of $X$. **B)** Stationary activity profiles of $pB$ and $pW$ in WT (continuous lines) and in the *bravo* mutant (dashed lines). **C)** Stationary profiles of BRAVO ($B$), WOX5 ($W$) and $X$ protein activities, as well as promoter activity $pX$, in WT (continuous lines) and in the *bravo* mutant (dashed lines) corresponding to the simulations in B). Parameters as in Table 5.2.

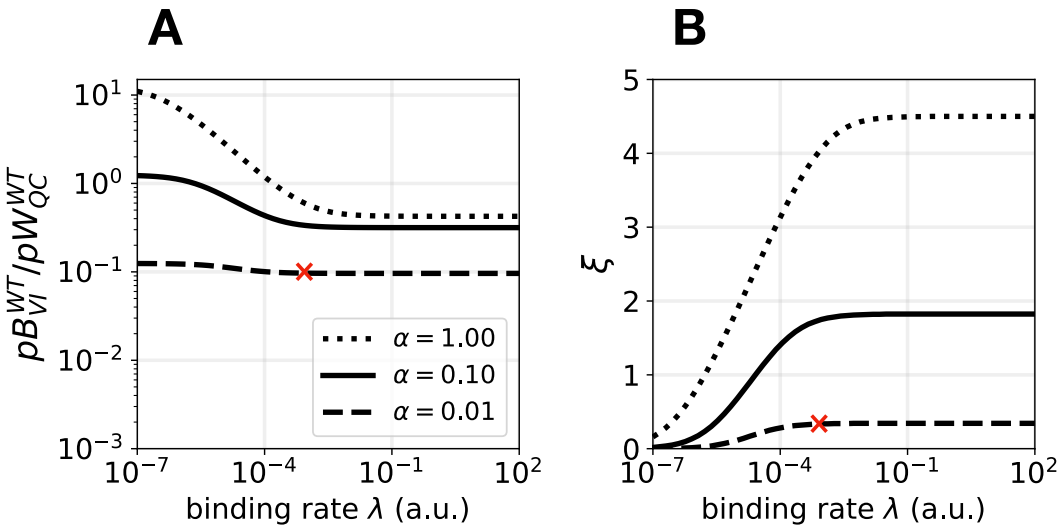



**Figure 5.7: Expansion and expression ratios in the attenuation by sequestration model.** Effect of the binding rate $\lambda$ and of the BRAVO synthesis rate $\alpha$ on $pB_{VI}^{WT}$ (A) and on $\xi$ (B). Parameters as in Table 5.2.

In this mechanism, because WOX5 is sequestered by BRAVO, $X$ becomes less activated at the QC, leading to a smaller range of $pB(x)$ activity, compared to the case when BRAVO is absent, i.e., in the *bravo* mutant (Figure 5.6B). In this case the expansion in the *bravo* mutant inevitably comes with an increase in absolute values of $pB(x)$ (Figure 5.6B). Mathematically, the very structure of the model's interactions do not allow an expansion without an increase in absolute values of $pB(x)$. This happens because even though complex formation between BRAVO and WOX5 occurs, its effect on $pB(x)$ only affects the QC region, as it is here where WOX5 is produced and activates $X$. Therefore, the tails of the distribution of $X(x)$ will decay exponentially in all cases, contrary to what happens in the *immobilization by sequestration* model, where the effective nonlinear degradation generates wider tails.

The results show that this mechanism requires WOX5 to be highly sequestered by BRAVO to drive noticeable self-confinement. If this is the case, in *bravo* mutants WOX5 proteins are released in high quantities, being able to activate $X$ (Figure 5.7). For this to happen, the activity of the *BRAVO* promoter in the WT needs to be strongly expressed (similarly to *WOX5*) at the QC (Figure 5.8). However, in *Arabidopsis* roots, we expect a low sequestration of WOX5 by BRAVO, as the activity of the *WOX5* promoter is significantly higher than that of the *BRAVO* promoter (Figure 5.1A,V).

Altogether, these arguments suggest that the *attenuation by sequestration* mechanism is not able to generate a true *BRAVO* expansion – i.e. without compromising the other conditions – and is therefore not a good candidate for the confinement of *BRAVO* expression in the *Arabidopsis* primary root SCN.

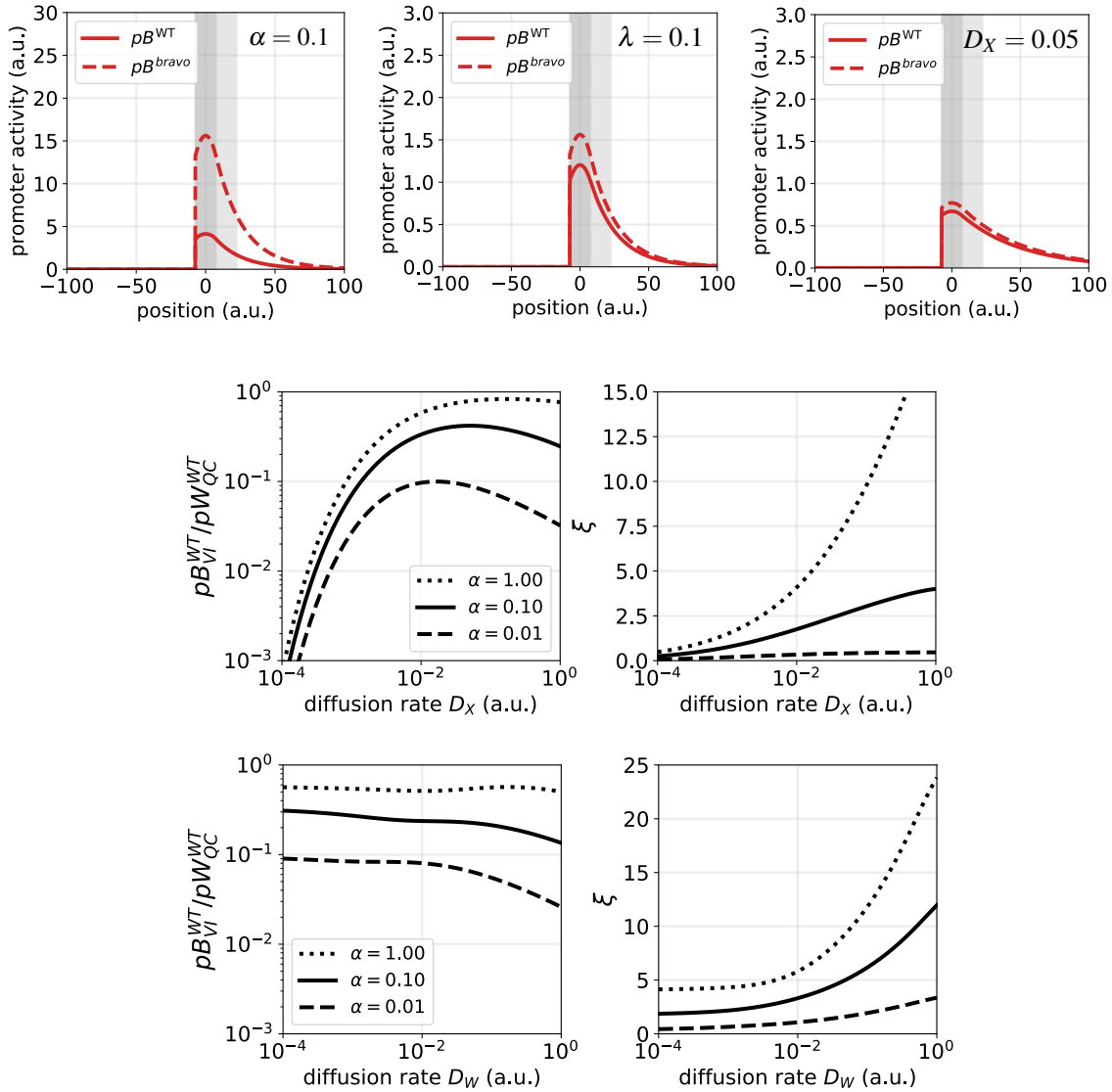



**Figure 5.8: Parameter dependence of $pB(X)$ in the attenuation by sequestration model.** (Top) Change in the spatial profile of $pB(x)$ for different values of the parameters $\alpha$, $\lambda$ and $D_X$ (see Table 5.2 for default values). (Middle) The effect of $X$ diffusion on the quantities $pB_{VI}^{WT}/pW_{QC}^{WT}$ and $\xi$, for different values of $\alpha$. While the value of $pB_{VI}^{WT}/pW_{QC}^{WT} \sim 0.1$ for $\alpha = 0.01$ and $D_X = 0.01$ (default values), $\xi$ remains at low values compared to Figure 5.4B. (Bottom) The effect of introducing diffusion of WOX5 in the model. Keeping the rest of parameters with the default values, the diffusion of WOX5 promotes expansion of $pB(x)$ in the *bravo* mutant (larger $\xi$), while keeping $pB_{VI}^{WT}/pW_{QC}^{WT} \sim 0.1$ (see Figure 5.22 for the model with WOX5 diffusion). The profiles of $B(x)$, $W(x)$, $X(x)$, $pW(x)$ and $pX(x)$ corresponding to these figures are shown in Figure 5.20.

### 5.2.3 Confinement through the repression of a mobile activator

The *attenuation by sequestration* mechanism indicates that a transcription factor can confine its own expression by reducing the production of its mobile

activator. Based on this, we envisaged a third scenario which does not have the limitations imposed by sequestration. In this new scenario, BRAVO represses the production of its activator, $Z$, which is mobile and is activated by WOX5 (Figure 5.9A). We call this the *repression* model, with corresponding equations:

$$\frac{\partial B(x,t)}{\partial t} = \alpha Z(x,t) - d_B B(x,t) \tag{5.11a}$$

$$\frac{\partial Z(x,t)}{\partial t} = \frac{\beta W(x,t)}{1 + cB(x,t)} - d_Z Z(x,t) + D_Z \frac{\partial^2 Z(x,t)}{\partial x^2} \tag{5.11b}$$

$$\frac{\partial W(x,t)}{\partial t} = \gamma_{QC}(x) - d_W W(x,t) \tag{5.11c}$$

Similar to the previous case, the parameters $\beta$, $d_Z$ and $D_Z$ describe the production, degradation and diffusion of $X$, respectively, while the new parameter $c$ sets the threshold of $Z$ repression by BRAVO. In this case, promoter activities in the stationary state are given by $pB(x) = \alpha X_s(x)$, $pZ(x) = \frac{\beta W_s(x)}{1+cB_s(x)}$ and $pW = \gamma_{QC}(x)$, where again the subscript $s$ indicates that the concentration profiles are the ones corresponding to the stationary state.

Simulations indicate that the *repression* mechanism is also able to induce the confinement of *BRAVO* expression (Figure 5.9B) and, as with previous mechanisms, shows that the action of WOX5, mediated by its target $Z$, becomes spatially restricted in the WT, while it expands in the *bravo* mutant (Figure 5.9B). The *repression* mechanism relies on the repression of $Z$ by BRAVO (Figure 5.9C) and on the mobility of $Z$ (Figure 5.11). Albeit movement of $Z$ is required for this mechanism to drive *BRAVO* self-confinement, the results indicate that large diffusion coefficients would drive *BRAVO* expression in the WT scenario to be too faint and large when compared to the expression in *Arabidopsis* root SCN (Figure 5.11, Figure 5.21, Figure 5.1). This suggests that $Z$ should not have a very large diffusion coefficient.

As opposed to the *attenuation by sequestration* mechanism, the *repression* mechanism does not require a very strong *BRAVO* expression in the WT scenario to drive noticeable self-confinement (since the concentration threshold of BRAVO to repress $Z$ can be low). Accordingly, *BRAVO* expressions lower than that of *WOX5*, like those in the *Arabidopsis* root SCN, are consistent with strong self-confinement through repression (Figure 5.9B). Further analysis of the model shows that strong repression drive more self-confinement but can result in unrealistic $pB(x)$ profiles in the WT, which are limited only to the QC and not reaching the VI cells (Figure 5.10). In addition, strong repression involves not only spatial confinement but also a dramatic reduction of *BRAVO* expression at the QC in the WT scenario compared to the *bravo* mutant (Figure 5.11). However this strong change in expression levels at the QC is not observed experimentally [Betegón-Putze et al., 2021] (Figure 5.1A,B). Taken together these results indicate that if the *repression* mechanism takes place at the SCN of *Ara-*

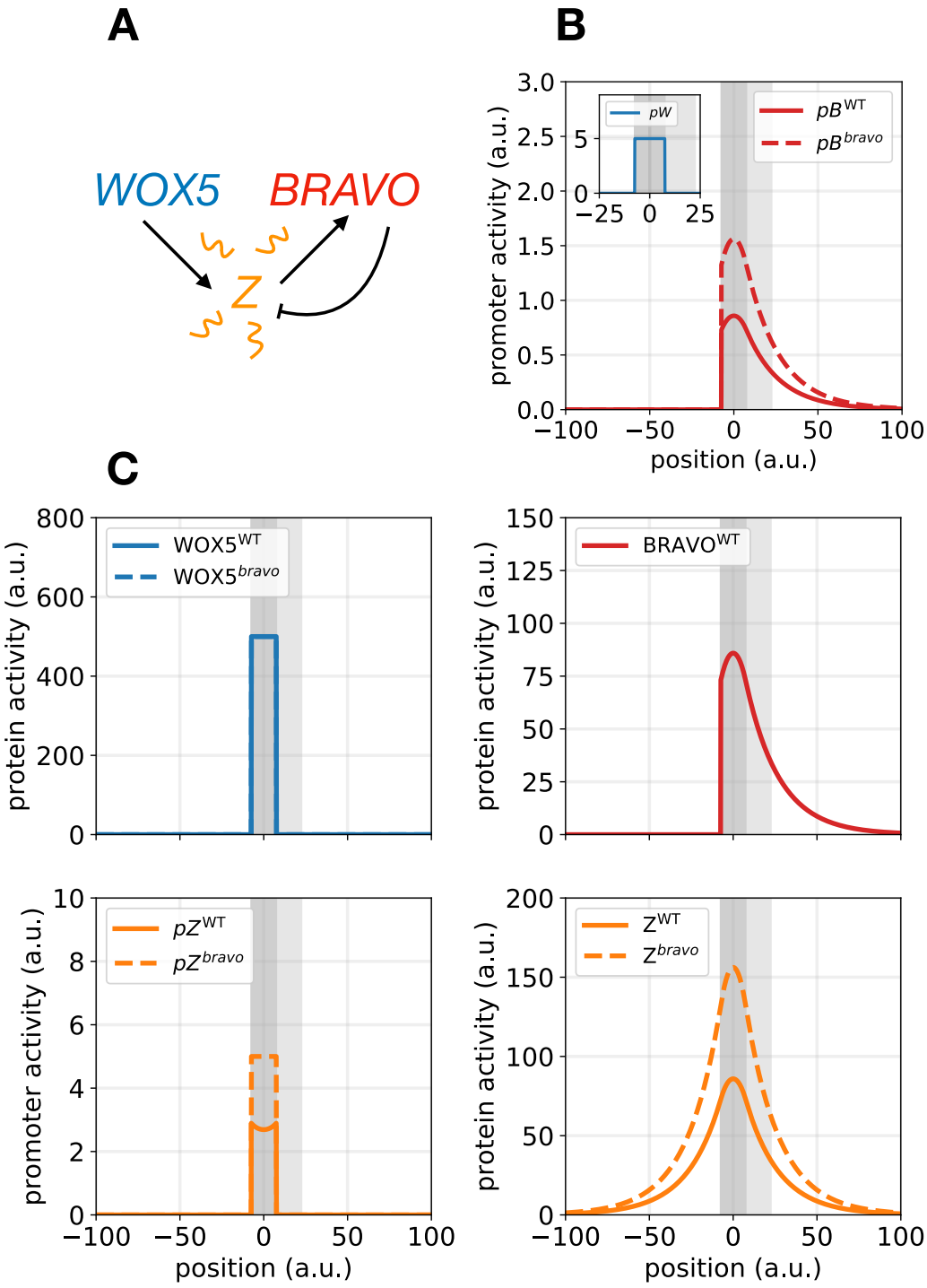



**Figure 5.9: Repression model. A)** Sketch of the interactions: WOX5 activates a diffusible factor $Z$, which activates BRAVO. BRAVO, in turn, is able to repress (blunt arrow) the activity of $Z$. **B)** Stationary activity profiles of $pB$ and $pW$ in WT (continuous lines) and in the *bravo* mutant (dashed lines) obtained with the repression model. **C)** Stationary profiles of BRAVO ($B$), WOX5 ($W$) and $Z$ protein activities as well as promoter activity $pZ$, in WT (continuous lines) and in the *bravo* mutant (dashed lines) corresponding to the simulations in B). Parameters as in Table 5.2.

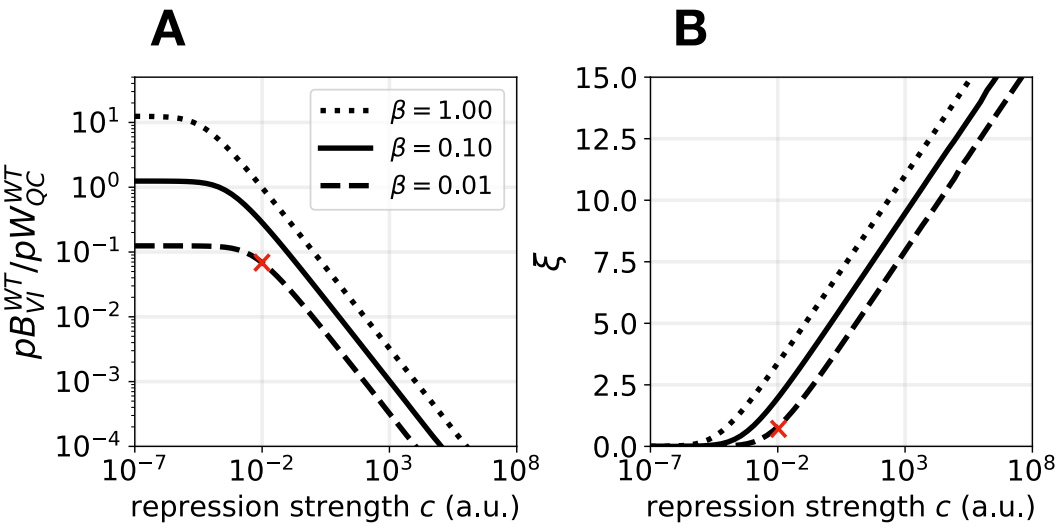



**Figure 5.10: Expansion and expression ratios in the repression model.** Effect of the repression strength $c$ and of the $Z$ synthesis rate $\beta$ on $pB_{VI}^{WT}$ (D) and on $\xi$ (E). Larger $\beta$ and $c$ values lead to larger expansions but involve a very strong increase of $pB$ levels in the *bravo* mutant (see Figure 5.21) which is not in agreement with experiments (Figure 5.1). Parameters as in Table 5.2.

*bidopsis* to confine the *BRAVO* expression domain, then BRAVO represses the WOX5 target $Z$ only weakly.

| Parameter | Description | IS | AS | R |
|---|---|---|---|---|
| $\alpha$ | Protein production rate of BRAVO | 0.01 | 0.01 | 0.01 |
| $\gamma_{QC}$ | Protein production rate of WOX5 | 5 | 5 | 5 |
| $\beta$ | Protein production rate of $X$ | – | 0.01 | 0.01 |
| $c$ | Threshold of $Z$ repression by BRAVO | – | – | 0.01 |
| $\lambda$ | Binding rate between BRAVO and WOX5 | 0.001 | 0.001 | 0.001 |
| $d_B$ | Degradation rate of BRAVO proteins | 0.01 | 0.01 | 0.01 |
| $d_W$ | Degradation rate of WOX5 proteins | 0.01 | 0.01 | 0.01 |
| $d_X$ | Degradation rate of $X$ proteins | – | 0.01 | – |
| $d_Z$ | Degradation rate of $Z$ proteins | – | – | 0.01 |
| $D_W$ | Diffusion coefficient of WOX5 proteins | 0.01 | – | – |
| $D_X$ | Diffusion coefficient of $X$ proteins | – | 0.01 | – |
| $D_Z$ | Diffusion coefficient of $Z$ proteins | – | – | 0.01 |

**Table 5.2: Default parameters of the *immobilization by sequestration* (IS), *attenuation by sequestration* (AS) and *repression* (R) models.** The units of all parameter values are arbitrary.

Reported transcriptomics of QC cells from our collaborators have revealed that most of the genes whose mRNA levels are differentially regulated in *wox5-1* and *bravo-1* mutants show opposite de-regulations [Betegón-Putze et al., 2021], thus opening the possibility of one of these genes to act as the intermediate factor

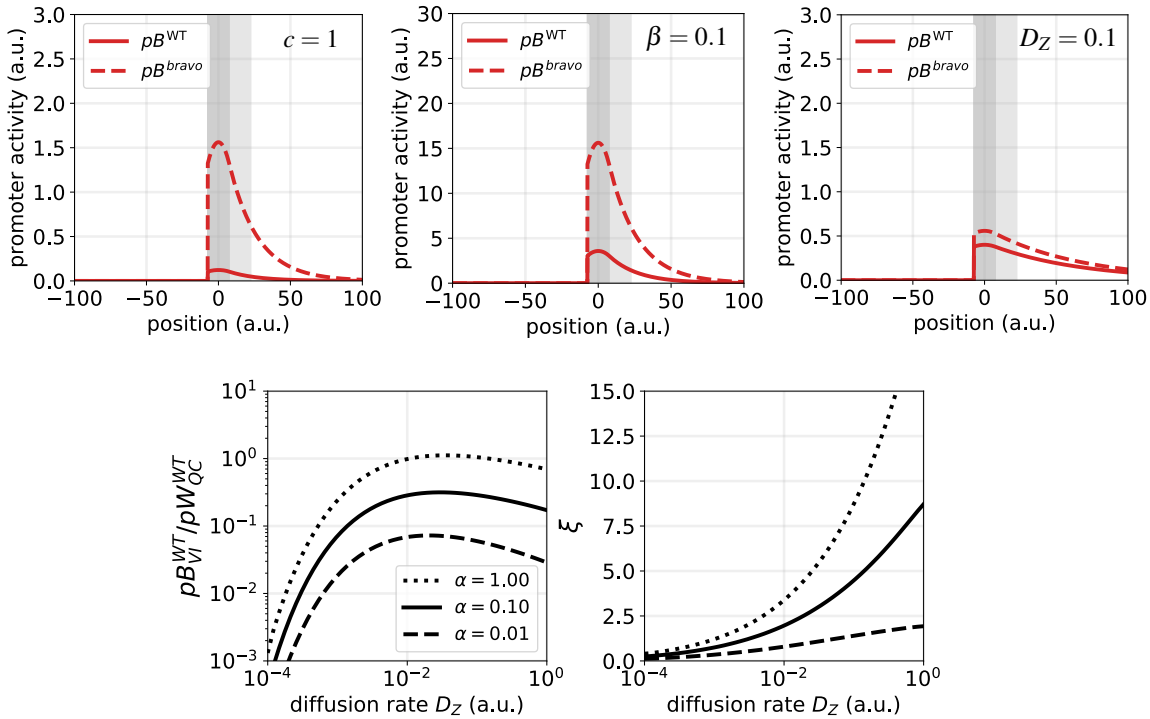



**Figure 5.11: Parameter dependence of $pB(X)$ in the repression model.** (Top) Change in the spatial profile of $pB(x)$ for different values of the parameters $c$, $\beta$ and $D_Z$ (see Table 5.2 for default values). (Bottom) The effect of introducing diffusion of $Z$ in the model. Keeping the rest of the parameters with the default values, the diffusion of $Z$ promotes expansion of $pB(x)$ in the *bravo* mutant (larger $\xi$), while keeping $pB^{WT}_{VI}/pW^{WT}_{QC} \sim 0.05 - 0.1$. The profiles of $B(x)$, $W(x)$, $Z(x)$, $pW(x)$ and $pZ(x)$ corresponding to these figures are shown in Figure 5.21.

$Z$, which in our model is downregulated in the *wox5* mutant but upregulated in the *bravo* mutant. Hence, transcriptomic data in the QC [Betegón-Putze et al., 2021] suggest several candidates for $Z$.

## 5.3 Modelling BRAVO self-confinement in a realistic root layout

The results of the simplified models suggest that both the *immobilization by sequestration* and the *repression* mechanisms are plausible candidates to explain the self-confined expression of *BRAVO* in the *Arabidopsis* root SCN. However, it remains unclear whether the diffusion of WOX5 is sufficiently large to make the *immobilization by sequestration* mechanism sufficient, and whether the weak repression required in the *repression* model is enough to produce the confinement observed in real roots. To address these issues, we modelled these mechanisms on realistic root layouts, where the cellular geometry of the roots is explicitly incorporated. We assumed both mechanisms to be present at the same time

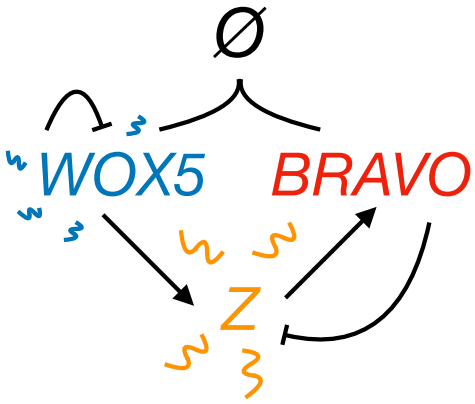



**Figure 5.12: Diagram of the mixed model.** Mixed WOX5 is able to diffuse, self-repress and activate a highly mobile intermediary $Z$. This intermediary activates BRAVO, which in turn feeds back on $Z$ to repress its activity. BRAVO and WOX5 can bind into an immobile and inactive complex.

(which incidentally incorporates the *attenuation by sequestration* mechanism as a side-effect). In Figure 5.12 we show a diagram with the interactions of the hereafter named *mixed model*. In this new framework, WOX5 can move between cells and is able to activate a mobile target $Z$, which in turn activates BRAVO. BRAVO feeds back on $Z$ to repress its activity and together with WOX5 they are able to bind into a transcriptionally inactive complex which, like BRAVO, can not move from cell to cell. Because of this, as in the previous sections, the complex is not explicitly modelled. Besides modelling the dynamics of BRAVO and WOX5, we also considered the dynamics of GFP proteins produced by the BRAVO and WOX5 promoters, which we denote by *pBRAVO:GFP* and *pWOX5:GFP*. For GFP, the production is set to be proportional to the promoter activity of the corresponding gene, and their degradation is set to be linear (just as for the remaining molecules). In addition, GFP are assumed to be mobile, both within and between cells.

We evaluate this mixed model in realistic root geometries to assess whether it can predict the changes in expression observed in *Arabidopsis* roots. The implementation of the mixed model in realistic root geometries takes into account the realistic shape of cells and the presence of cell walls. The 2-dimensional geometry of WT and *bravo* mutant roots were considered separately, by using different layouts.

In the computational implementation of the model, the inside of the cells (cytoplasmic regions) and the cell walls are characterized by distinct dynamics and diffusion coefficients. Specifically, in all the pixels belonging to the cell's interior, molecules can be produced, regulated, degraded, can sequester other molecules and are able to diffuse. Inside the cell walls, however, molecules are only able to diffuse. Regarding differences in diffusion, for example, the diffusion coefficient of WOX5 in the region is defined as $D_W^{cyt}$, while for cell walls $D_W^{wall}$. By

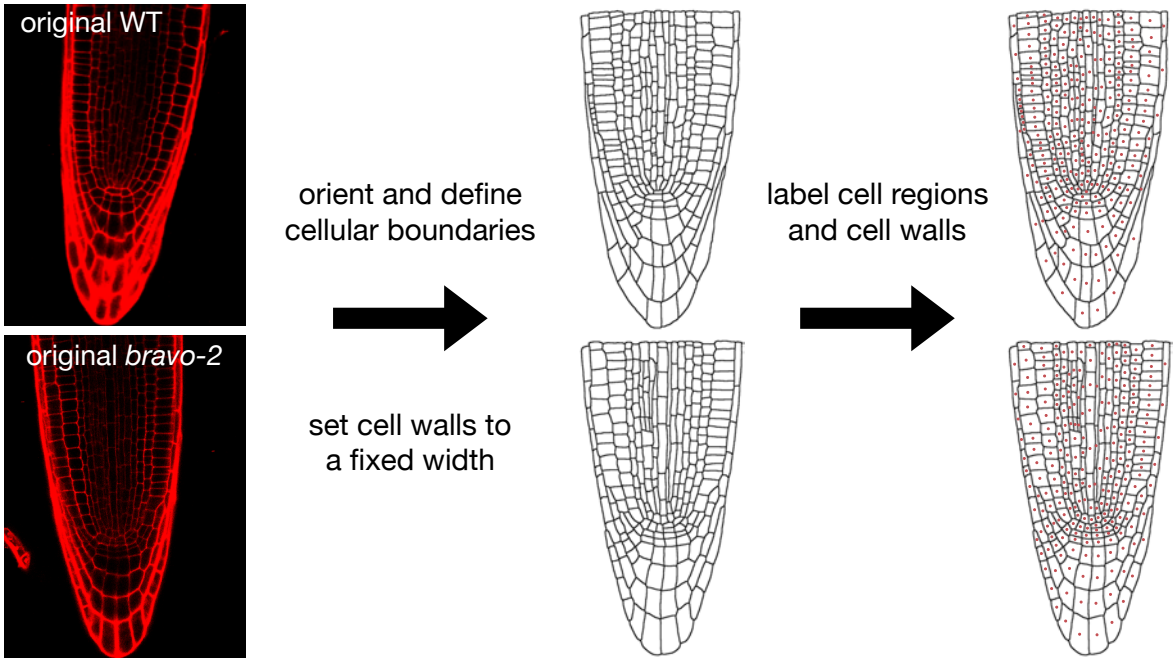



**Figure 5.13: Construction of a realistic root layout.** We select two root tips, representative for WT and *bravo-2* mutants, from a confocal image of the root where cell walls are PI-stained (red). We first orient and rescale the roots so that both can be compared. As a result proportions are slightly modified from the original image. This initial step is optional. We then reset a fixed width for the cell walls (2 pixels in the simulation). Subsequently, we label the images to define each cellular region (marked as red dots located at the centroid of each cell).

imposing the condition $D_W^{cyt} > D_W^{wall}$ we take into account that larger diffusion occurs inside the cell compared to intercellular diffusion (i.e. proteins move more freely within the cell than between cells). With this assumption the physical boundaries between cells are naturally incorporated, leading to discontinuities in the concentration profiles of molecular factors. These are to be expected for any molecule diffusing freely inside the cytoplasm but moving only occasionally from cell to cell, as it may happen, for example, in plasmodesmata-mediated transport. For simplicity (and lack of evidence), we assume that BRAVO can only move inside the cell, and we set $D_B^{cyt} > 0$, $D_B^{wall} = 0$. Conversely, WOX5 and $Z$ proteins can move inside the cytoplasm with diffusion coefficients $D_W^{cyt}$ and $D_Z^{cyt}$, respectively, and between cells with diffusion coefficients $D_W^{wall}$ and $D_Z^{wall}$, respectively. The diffusion coefficient of GFP and WOX5 proteins is assumed to be similar, both in the cytoplasm and in the cell wall, since both proteins have aminoacid sequences of similar lengths ($\sim$ 20 kDa for WOX5 and $\sim$ 27 kDa for GFP [TAIR, 2017]). Because GFP proteins are able to diffuse from cell to cell, they can reach cells where there is no promoter activity. The interactions between BRAVO and WOX5 can be directly mapped into the realistic root layout by defining the corresponding equations to each pixel of the layout and implementing the conditions of each region.

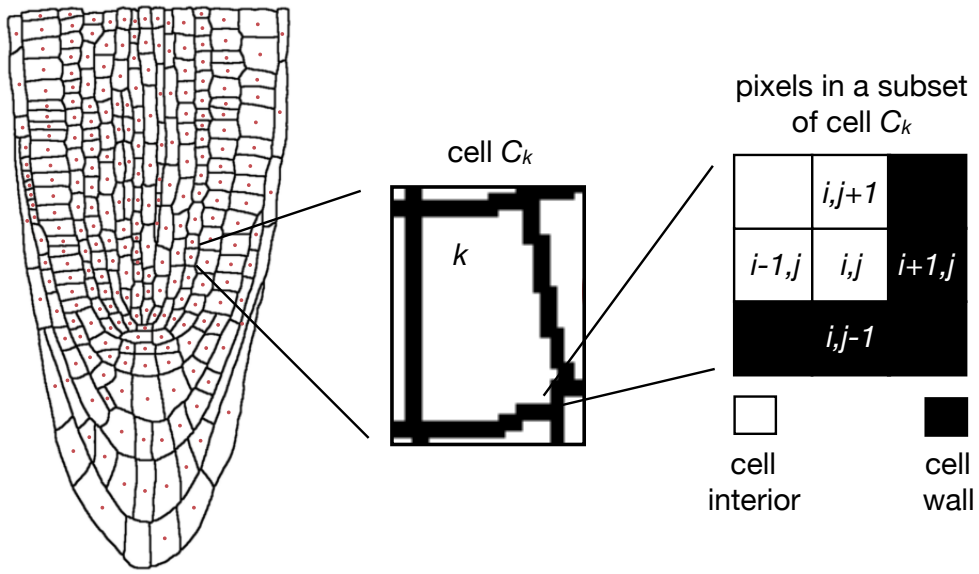



**Figure 5.14: Pixel type assignment in the segmented root layout.** Each region $k$ contains a set of pixels $C_k$ (defining the cell's interior) which are surrounded by pixels corresponding to cell walls. To each pixel type (i.e. cell wall or cell interior) there will be an associated diffusion coefficient. Further details on the construction and implementation of the realistic root layout can be consulted in Section 5.B in the appendix.

Finally, cells are classified by cell type. We defined nine different cell types: quiescent center, vascular initials, vascular cells, cortex, endodermis, epidermis, columella stem cells, columella cells, and lateral root cap cells (the same types shown in Figure 2.4). This classification enables setting different dynamics of molecular species in distinct cell types. We set the activation of BRAVO by WOX5 only in the QC, vascular initials, vascular cells, cortex and endodermis, but not in the remaining cell types (Figure 5.15). This last assumption is based on the experimental observation that *BRAVO* is expressed only in inner tissues, from the SCN upwards. For simplicty, WOX5 is only allowed to be produced at the QC (Figure 5.15, albeit recent observations show that low values of promoter expression are also present in the vascular initials [Berckmans et al., 2020, Clark et al., 2020]). Diffusion and degradation are set to occur in all cell types.

In this mixed model, the equations for each protein can be written in general

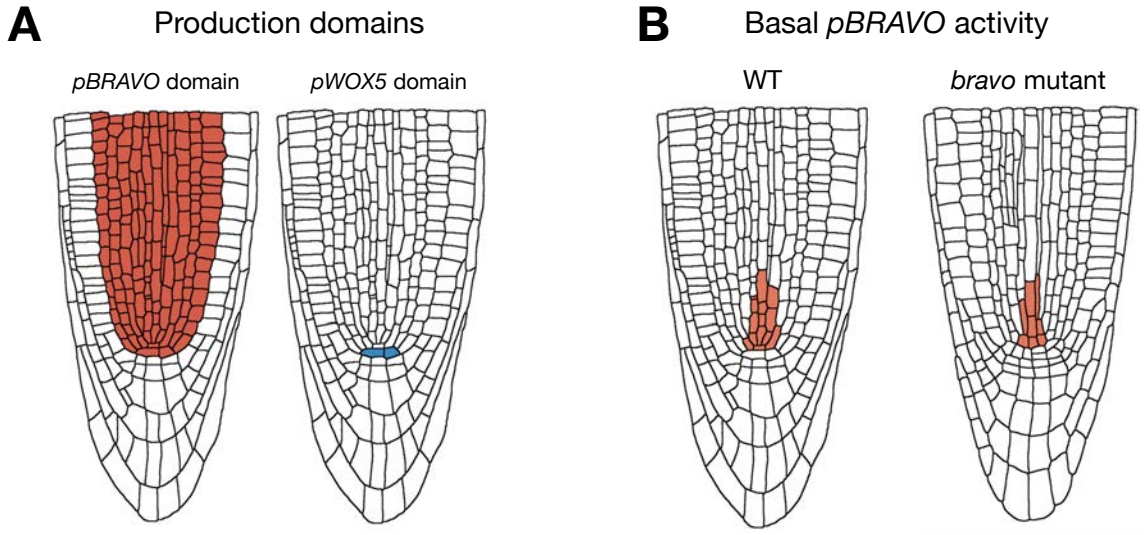



**Figure 5.15: Cellular domains where production of BRAVO and WOX5 is enabled in the simulations. A)** The production terms of BRAVO and WOX5 are restricted to the red and blue domains respectively. The GFP reporters of their promoters are produced only in these domains. In this way, we only allow $B$ and $B_{GFP}$ to be activated by $Z$ in the QC, vasculature, cortex and endodermis, while $W$ and $W_GFP$ are only produced at the QC. This does not prevent WOX5 and GFP to be present in other tissues, which they can reach through diffusion. **B)** BRAVO is assumed to have basal levels of production only in the first cells of the vasculature. This consideration comes from the fact that in *bravo wox5* double mutants, basal expression of $pBRAVO : GFP$ can still be observed, with a spatial pattern similar to the one shown in red in the figure. The GFP reporter of the BRAVO promoter is set to have a basal activity only in the red domain. Since WT and *bravo* mutant roots differ in morphology, the cells with basal BRAVO activity are not exactly the same.

form as:

$$\frac{\partial B(x,t)}{\partial t} = P_B\Big(x, Z(x,t)\Big) - \lambda B(x,t)W(x,t) - d_B(x)B(x,t) \tag{5.12a}$$

$$\frac{\partial Z(x,t)}{\partial t} = P_Z\Big(W(x,t), B(x,t)\Big) - d_Z(x)Z(x,t) + \nabla\Big[D_Z(x)\nabla Z(x,t)\Big] \tag{5.12b}$$

$$\begin{aligned}\frac{\partial W(x,t)}{\partial t} &= P_W\Big(x, W(x,t)\Big) - \lambda B(x,t)W(x,t) - d_W(x)W(x,t) + \\ &+ \nabla\Big[D_W(x)\nabla W(x,t)\Big]\end{aligned} \tag{5.12c}$$

where the promoter activities $P_B\Big(x, Z(x,t)\Big)$, $P_Z\Big(W(x,t), B(x,t)\Big)$, $P_W\Big(W(x,t)\Big)$ will have different values depending on the cell type. Moreover, both the promoter activities, the degradations $d_B(x)$, $d_Z(x)$, $d_W(x)$ and the diffusion coefficients $D_Z(x)$, $D_W(x)$ will have different values depending on whether the spatial position $x$ belongs to the cell's cytoplasm or the cell membrane. In particular, the promoters will only be active in the cytoplasm, but not in cell

walls. To avoid the possible drawbacks caused by linear synthesis rates used in the minimal models of the previous sections (such as the lack of saturation and thresholds of activity), here we used transcriptional regulations described by Hill functions, with basal activity and saturation values. In order to account for the increase in the domain of *WOX5* expression in the *wox5* mutant, we included a negative feedback of WOX5 activity, a regulation that induces a decrease in WOX5 activity in the *bravo* mutant, as sequestration of BRAVO by WOX5 allows the WOX5 promoter to be less repressed in the WT (much like we have seen in Chapter 4). The promoter activities have the form:

$$P_B\big(x, Z(x,t)\big) = \begin{cases} 0 & \text{if } x \in \text{cell wall} \\ \alpha_0(x,t) + \alpha \frac{Z(x,t)^3}{k_B^3 + Z(x,t)^3} & \text{if } x \in \text{cytoplasm} \end{cases} \tag{5.13}$$

$$P_Z\big(W(x,t), B(x,t)\big) = \begin{cases} 0 & \text{if } x \in \text{cell wall} \\ \beta \frac{W(x,t)}{k_Z + W(x,t)} \frac{1}{1 + cB(x,t)} & \text{if } x \in \text{cytoplasm} \end{cases} \tag{5.14}$$

$$P_W\big(W(x,t)\big) = \begin{cases} 0 & \text{if } x \in \text{cell wall} \\ \gamma_{QC}(x) \frac{k_W^3}{k_W^3 + W(x,t)^3} & \text{if } x \in \text{cytoplasm} \end{cases} \tag{5.15}$$

Here $\alpha_0(x)$ is the basal production rate of BRAVO, present only in the pixels corresponding to the cells shown in Figure 5.15B. The expression of BRAVO regulated by the factor $Z$ is controlled by $\alpha$, which measures the maximum strength of this regulation, and is set to be non-zero only in the cells shown in Figure 5.15A; and by the threshold $k_B$, which controls the levels of $Z$ necessary for BRAVO activation. The factor $Z$ is activated by WOX5 with maximum rate $\beta$, and activation threshold $k_Z$. This activation is modulated by the repression of $Z$ by BRAVO, the effect of which is controlled by the parameter $c$. The production of WOX5 is mediated by the parameter $\gamma_{QC}$, which in this case comprises only the region corresponding to QC cells (Figure 5.15A). In addition, WOX5 is able to repress its own expression, with a repression threshold controlled by the parameter $k_W$. Degradation of all species is assumed to be:

$$d_B(x) = \begin{cases} 0 & \text{if } x \in \text{cell wall} \\ d_B & \text{if } x \in \text{cytoplasm} \end{cases}, \quad d_Z(x) = \begin{cases} 0 & \text{if } x \in \text{cell wall} \\ d_Z & \text{if } x \in \text{cytoplasm} \end{cases}$$

$$d_W(x) = \begin{cases} 0 & \text{if } x \in \text{cell wall} \\ d_W & \text{if } x \in \text{cytoplasm} \end{cases} \tag{5.16}$$

And the diffusion coefficients

$$D_Z(x) = \begin{cases} D_Z^{wall} & \text{if } x \in \text{cell wall} \\ D_Z^{cyt} & \text{if } x \in \text{cytoplasm} \end{cases}, \quad D_W(x) = \begin{cases} D_W^{wall} & \text{if } x \in \text{cell wall} \\ D_W^{cyt} & \text{if } x \in \text{cytoplasm} \end{cases} \tag{5.17}$$

The promoter activity of the each transcription factor is measured through an additional equation representing the expression of its corresponding GFP reporter:

$$\begin{aligned} \frac{\partial B_{GFP}(x,t)}{\partial t} &= P_B\big(x, Z(x,t)\big) - d_{GFP}(x) B_{GFP}(x,t) + \\ &+ \nabla\big[D_{GFP}(x)\nabla B_{GFP}(x,t)\big] \end{aligned} \tag{5.18a}$$

$$\begin{aligned} \frac{\partial Z_{GFP}(x,t)}{\partial t} &= P_Z\big(W(x,t), B(x,t)\big) - d_{GFP}(x) Z_{GFP}(x,t) + \\ &+ \nabla\big[D_{GFP}(x)\nabla Z_{GFP}(x,t)\big] \end{aligned} \tag{5.18b}$$

$$\begin{aligned} \frac{\partial W_{GFP}(x,t)}{\partial t} &= P_W\big(W(x,t)\big) - d_{GFP}(x) W_{GFP}(x,t) + \\ &+ \nabla\big[D_{GFP}(x)\nabla W_{GFP}(x,t)\big] \end{aligned} \tag{5.18c}$$

Notice that the production rate of GFP proteins is the same as their corresponding proteins. The degradation and diffusion coefficient of GFP are the same for all proteins, but still vary depending on whether the position corresponds to the cell's interior or cell walls. In particular, GFP degradation $d_{GFP}(x)$ is assumed to be zero in cell walls and $d_{GFP}$ in the cytoplasm. GFP diffusion is $D_{GFP}^{wall}$ in cell walls and $D_{GFP}^{cyt}$ in the cytoplasm.

All the equations of this section described up to this point equations correspond to the WT scenario. In *bravo* mutants the same equations, with the same parameter values apply, but the activity of BRAVO is set to zero, $B(x,t) = 0$. Notice that in this mutant, the reporter for BRAVO GFP activity, $B_{GFP}$, is described as in the WT, but with the values of other factors computed for the *bravo* mutant, i.e. with $B(x,t) = 0$.

In Figure 5.16, *pBRAVO:GFP* corresponds to the variable $B_{GFP}(x,t)$, i.e. the activity of the BRAVO promoter as seen through its GFP reporter, while $B(x,t)$ represents the BRAVO protein concentration. In Figure 5.17 the promoter expressions of each protein are defined likewise.

With the parameters shown in Table 5.3, we found that the mixed model can explain the behaviour of *pBRAVO:GFP* in the WT and the expansion of its domain in the *bravo* mutant (compare Figure 5.16 with Figure 5.1A,B). This self-confinement additionally induces WOX5 proteins and the diffusible target $Z$ to be confined, as shown in Figure 5.23. WOX5 diffusion is set to be low enough such that its promoter activity, in the absence of any regulatory factor, is mostly confined at the QC, VI and CSC (Figure 5.22), as found experimen-

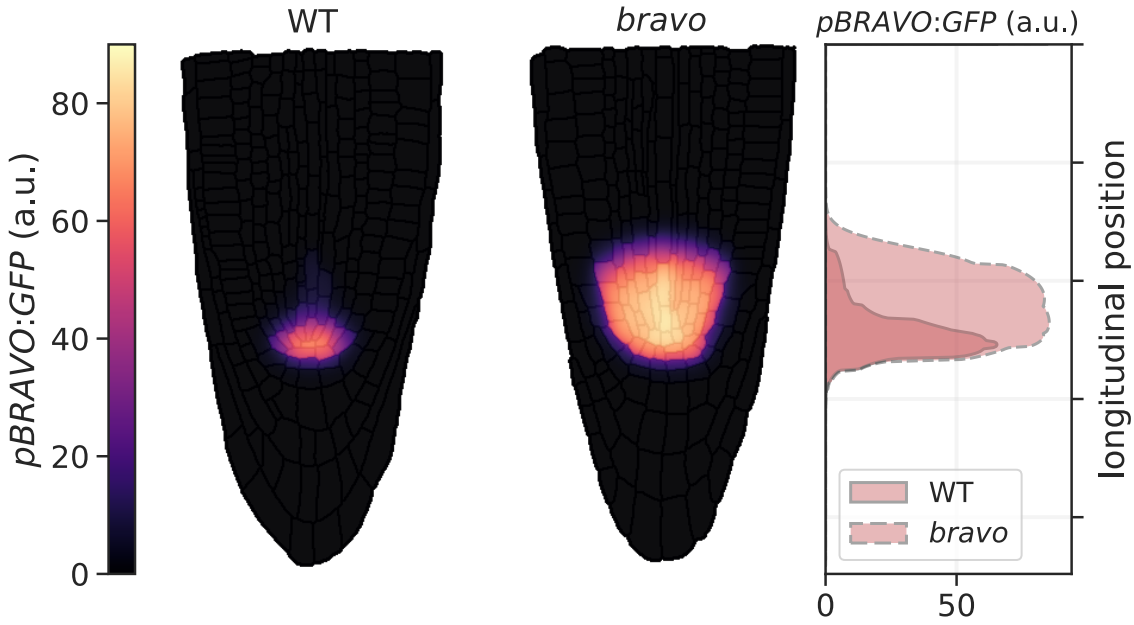



**Figure 5.16: *pBRAVO:GFP* simulated in realistic root layouts.** Simulation results for the stationary activity of *pBRAVO:GFP* in WT (left root) and in *bravo* mutant (right root) *bravo* mutant for the mixed model. The rightmost panel depicts the activity of *pBRAVO:GFP* along the longitudinal midline (vertical axis). In the WT, *pBRAVO:GFP* is confined to the SCN, but it expands in the *bravo* mutant. The stationary profiles of all other molecules are depicted in Figure 5.23.

tally. This small diffusion is sufficient to drive a realistic self-confinement only through the *immobilization by sequestration* mechanism (Figure 5.16A). However, this only happens if activation of BRAVO by WOX5 occurs through a non-diffusible WOX5-target $Z$ (Figure 5.17A). For a diffusible $Z$, the *repression* mechanism is required to drive self-confinement (compare Figure 5.16A with Figure 5.17C). Under these circumstances, sequestration between BRAVO and WOX5 facilitates a higher expression of *BRAVO* in the WT (Figure 5.17C).

## 5.4 Discussion

In this chapter, we have shown that a simple spatial model where WOX5 can diffuse and activate BRAVO, together with the binding between BRAVO and WOX5 proteins, is sufficient to explain the expression patterns of the *BRAVO* promoter and, in particular, its confinement to the SCN. We investigated three regulatory mechanisms for self-confined expression (*immobilization by sequestration*, *attenuation by sequestration*, and *repression*). These three mechanisms share that the emergence of self-confinement involves a negative feedback with a mobile activator and an immobile inhibitor. Each of the three mechanisms can be understood as a different regulatory way for this negative feedback to be accomplished: by immobilizing or reducing the activator's production, which

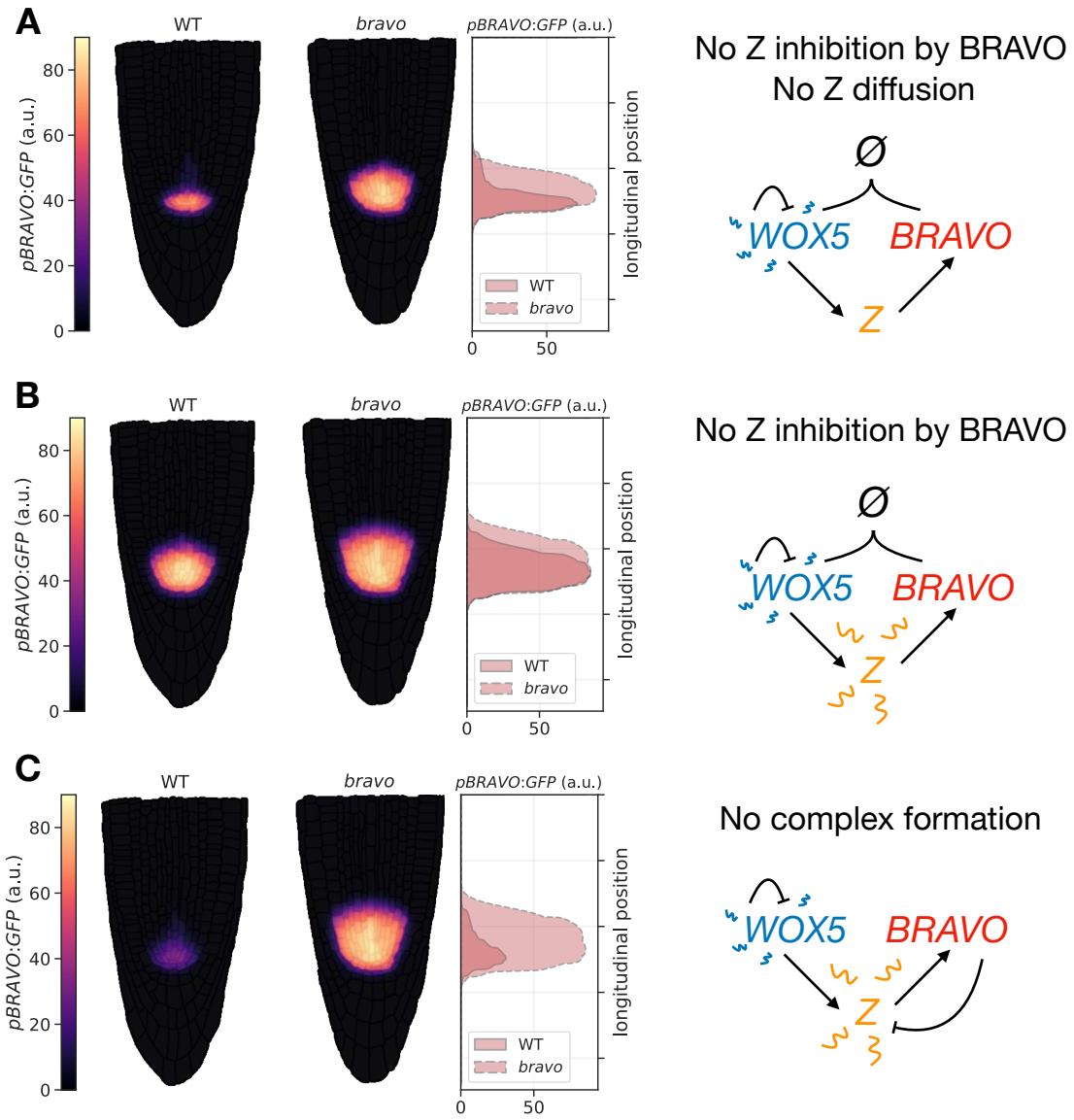



**Figure 5.17: *pBRAVO:GFP* simulated in variants of the mixed model. A)** Confined expression of *pBRAVO:GFP* can still be obtained when $Z$ does not diffuse and is not repressed by BRAVO (this corresponds to the *immobilization by sequestration* mechanism). The expansion in the *bravo* mutant is less pronounced than in the mixed model. **B)** Removing the repression of $Z$ by BRAVO induces a larger expansion of *pBRAVO:GFP* in the WT, with similar absolute levels as in the *bravo* mutant. Hence, little confinement is achieved in the WT. **C)** If there is no binding between BRAVO and WOX5, the activity of *pBRAVO:GFP* in the WT decreases dramatically due to stronger repression through $Z$.

may happen through sequestration or repression. Therefore they can be encompassed within a general framework of self-confinement, which could go under the name of *attenuation of a mobile activator*. All these mechanisms drive the self-confinement of both the repressor and the activator. Yet, despite their similarities, they are not equivalent, as each has its distinct characteristics, as our analysis revealed. The most noticeable feature is perhaps the fact that the im-

| Parameter | Description | Value |
|---|---|---|
| $\alpha_0$ | Basal production rate of BRAVO proteins | 0.01 |
| $\alpha$ | Regulated production rate of BRAVO proteins | 0.1 |
| $\gamma_{QC}$ | Production rate of WOX5 proteins | 2 |
| $\beta$ | Production rate of $Z$ proteins | 6 |
| $k_B$ | Threshold of BRAVO activation by $Z$ | 10 |
| $k_Z$ | Threshold of $Z$ activation by WOX5 | 1 |
| $k_W$ | Threshold of WOX5 self-repression | 1 |
| $c$ | Threshold of $Z$ repression by BRAVO | 10 |
| $\lambda$ | Binding rate between BRAVO and WOX5 | 0.005 |
| $d_B$ | Degradation rate of BRAVO proteins | 0.005 |
| $d_W$ | Degradation rate of WOX5 proteins | 0.005 |
| $d_Z$ | Degradation rate of $Z$ proteins | 0.005 |
| $D_W^{cyt}$ | Diffusion coefficient of WOX5 proteins in the cytoplasm | 0.2 |
| $D_W^{wall}$ | Diffusion coefficient of WOX5 proteins in cell walls | 0.1 |
| $D_Z^{cyt}$ | Diffusion coefficient of $Z$ proteins in the cytoplasm | 1.2 |
| $D_Z^{wall}$ | Diffusion coefficient of $Z$ proteins in cell walls | 0.6 |
| $D_{GFP}^{cyt}$ | Diffusion coefficient of GFP proteins in the cytoplasm | 0.1 |
| $D_{GFP}^{wall}$ | Diffusion coefficient of GFP proteins in cell walls | 0.01 |
| $d_{GFP}$ | Degradation rate of GFP proteins | 0.001 |

**Table 5.3: Default parameters of the mixed model in the realistic root layout.** All parameter values are indicated in arbitrary units of concentration, time and space.

mobilization mechanism involves a change in the gradient profile of the activator (Figure 5.2) whereas the other mechanisms do not. Furthermore, the opposite regulation of WOX5 and BRAVO to common targets as inferred by transcriptional profiling [Betegón-Putze et al., 2021] supports the scenario where this confinement is induced by a negative regulation between BRAVO and factor activated by WOX5 (the *repression* mechanism).

A different mechanism to drive self-confined expression has been proposed to confine WUSCHEL (WUS)—a homolog of WOX5 expressed in the shoot apical meristem of *Arabidopsis*. According to it, WUS protein restricts its own expression by activating its repressor, CLAVATA3 (CLV3), which is highly mobile [Yadav et al., 2011, Zhou et al., 2018]. Both this mechanism and the *attenuation of a mobile activator* analyzed in this chapter have in common that a negative feedback is responsible for self-confinement. However, in the *attenuation of a mobile activator* the strongly mobile component is the activator and not the repressor. The generic process of *attenuation of a mobile activator* is thus a distinct mechanism for self-confinement and, because of its minimal assumptions, we expect it, or a variant thereof, to take place in very different developmental contexts. For instance, Hedgehog signalling confines its own expression in the Drosophila wing by activating one of its repressors, the nuclear zinc finger

*Master of thickveins* (*mtv* [Bejarano et al., 2007]). Thus, this self-confinement may be framed within the *attenuation of a mobile activator* mechanism, where Hedgehog acts as the mobile activator ($Z$ in the repressor model) and *mtv* as the immobile repressor.

The mechanism of *immobilization by sequestration* can be related to mechanisms for robust morphogen gradient profiles [Eldar et al., 2003, Shilo and Barkai, 2016]. Morphogens are ligand molecules produced at localized sources that can diffuse between cells, generating activity gradients that can be subsequently interpreted by gene regulatory networks, activating or repressing sets of genes in a concentration-dependent manner. It has been proposed that the sequestering of the morphogen by receptors might lead to an effective non-linear degradation of the ligand, resulting in concentration profiles that are robust to changes in the rate of production at the source [Eldar et al., 2003]. We could make the correspondence between such models and ours by identifying WOX5 as a morphogen and BRAVO as the receptor. In agreement with what has been described for morphogen gradients induced by non-linear degradation [Eldar et al., 2003], we find that the gradient of WOX5 decays much more abruptly in the presence of BRAVO, suggesting that the specific regulations between BRAVO and WOX5 may be tuned to achieve robust activity profiles.

Modelling of root tissues has been most commonly done in terms of simplified rectangular geometries, where cells and cell walls are subdivided in squares or rectangles [Grieneisen et al., 2007, Tian et al., 2018]. In the shoot, models have been implemented with cellular layouts with diffusing molecules between cells but not within [Jönsson et al., 2005, Yadav et al., 2011, Voß et al., 2014]. Here, by using pixels as the basic unit for discretization, we can realistically model the shapes of cells and consider both the regulation within and between cells. A pixel-based approach has also been used to model hormonal crosstalk in the *Arabidopsis* root [Liu et al., 2017]. Mathematically, our framework can be characterized as a reaction-diffusion model in heterogeneous media. The inhomogeneities appear due to the presence of cell walls, which have different diffusion coefficients than cell interiors. Furthermore, this realistic root layout can be extended to include internal structures such as nuclei or cell-to-cell communication channels like plasmodesmata. Therefore, it has the potential to evaluate much more complex scenarios in a manageable way.

In a broader context, the similarities between stem cell niche organization in animals and plants may represent the outcome of convergent evolution [Dinneny and Benfey, 2008]. Multicellularity – a necessary condition for the emergence of stem cell niches – is thought to have evolved independently in both kingdoms [Grosberg and Strathmann, 2007, Knoll, 2011], implying that their presence in widely disparate organisms may be a direct consequence of developmental constraints and not of historical contingencies. Similar mechanisms of niche regulation are therefore to be expected, not through common genes or molecules but through more general regulatory principles. The fact that stem cell niches

consist of narrow regions of few cells clustered together, in opposition to large numbers of cells distributed over the whole organism, possibly emerged as a way to ensure a proper balance between centralized renewal and genome integrity by minimizing deleterious mutations, which may be able to spread across whole-cell lineages [Sena et al., 2009, Yoshiyamaa et al., 2009]. Indeed, the smaller the population of stem cells and the lower their division rate, the less likely deleterious mutations to accumulate in differentiated tissues [Cannataro et al., 2017].

In *Arabidopsis*, signals from the SCN such as BRAVO and WOX5 allow cells to communicate between them and with other cell types, at the same time as they create boundaries within which local information can be transmitted. Indeed, QC cells have been shown to influence neighbouring cell types such as the CSC, where WOX5 plays a crucial role as a signalling agent [Pi et al., 2015, Berckmans et al., 2020]. Through this work, we propose the very same happens towards the vasculature, with *BRAVO* acting as the signalling molecule by actively restraining its own expression from reaching cells far away from its source, ensuring that the small microenvironment of the SCN remains confined within the root. Mechanisms like the ones proposed here involve very general principles that contribute to the understanding of stem cell populations not only in plants but in multicellular organisms on the whole.

# Appendix

## 5.A Numerical solution of steady state expression profiles of the one-dimensional models

To numerically solve the ODEs resulting from the steady state approximation of the one-dimensional reaction-diffusion models studied in the first part of this chapter, we take a domain of size $D = [-600, 600]$, and a QC of size $L_{QC} = 15$ (located at the center of the domain, i.e. at $[-7.5, 7.5]$), and implement the *solve_bvp* routine embedded in the Python-based *SciPy* library [Virtanen and SciPy 1.0 Contributors, 2020], with a spatial step of $\delta x = 0.05$. Boundary conditions are set to $W(x \to \pm\infty) = 0$, but since the source is small compared to the size of the domain, these conditions don't affect the profile close to the center, at the QC position.

## 5.B Construction of realistic root layouts

In order to build a realistic root layout with which we can subsequently implement the corresponding reaction-diffusion equations, we start by taking a confocal image of the root with PI-stained cell walls and we apply a segmentation routine which divides the root into its constituent cellular regions and cell walls (Figure 5.13). To do this, we make extensive use of the *scikit-image* collection of Python-based algorithms [van der Walt et al., 2014]. In particular, we first define the cellular boundaries with the *threshold_otsu* method, which transforms the original image into a thresholded binary image where only cell wall pixels remain. We then *skeletonize* to obtain a cell wall with a fixed width. We then apply the *label* function to the modified image, which labels the distinct cellular regions. Specifically, each label constitutes the collection of pixels belonging to the particular region. With this routine, we can access each cell as an individual entity, and we can modify its properties (e.g. by assigning them different parameters in the simulations) accordingly. The cell wall and the outside of the root are classified as single regions. The interactions between BRAVO and WOX5 can be directly mapped into the realistic root layout by defining the corresponding equations to each pixel of the layout and implementing the conditions of each region.

# 5.C Numerical implementation of heterogeneous reaction-diffusion equations in the realistic root layout

To solve the dynamics of BRAVO, WOX5 and $Z$ in the realistic root layout, we simulate a reaction-diffusion equation with heterogeneous diffusion coefficients, where diffusion is explicitly dependent on the spatial position. In our case, this coefficient will depend on whether the lattice point corresponds to the interior of the cell or the cell wall, with respective diffusion coefficients of $D^{cyt}$ and $D^{wall}$. These can be encompassed into a single, spatially-dependent coefficient $D(x, y)$, where $x, y$ carry the information of the root layout. For an arbitrary function $u(t, x, y)$, we discretize time in steps of size $\Delta t$, so that after $k$ steps, $t_k = k\Delta t$. Space is discretized in steps of size $(\Delta x, \Delta y)$, so that $(x_i, y_i) = (i\Delta x, j\Delta y)$. The numerical solution of the reaction-diffusion equation for the a generic variable $u(t, x, y)$ with the forward time central space (FTCS) scheme is given by:

$$u_{ij}^{k+1} = u_{ij}^{k} + \Delta t\left(\nabla[D_{ij}\nabla u_{ij}^{k}] + f(\mathbf{u}_{ij}^{k})\right)$$

where $\mathbf{u} \equiv (u_1, u_2, \ldots, u_n)$ represents the dependence of other variables on the reaction terms $f(\mathbf{u}_{ij}^{k})$. The spatial discretization of $\nabla(D_{ij}\nabla u_{ij}^{k})$ is given by [Lee, 2017]:

$$\nabla(D_{ij}\nabla u_{ij}^{k}) = \frac{1}{\Delta x^2}\left(\frac{1}{2}(D_{ij}+D_{i+1,j})(u_{i+1,j}-u_{ij})-\frac{1}{2}(D_{ij}+D_{i-1,j})(u_{ij}-u_{i-1,j})\right)+$$

$$+\frac{1}{\Delta y^2}\left(\frac{1}{2}(D_{ij}+D_{i,j+1})(u_{i,j+1}-u_{ij})-\frac{1}{2}(D_{ij}+D_{i,j-1})(u_{ij}-u_{i,j-1})\right)$$

Where the indexes in $D_{ij}$ will specify whether $D = D^{cyt}$ or $D = D^{wall}$. In all the simulations we set $\Delta x = \Delta y = 1$, with a lattice size of $(L_x, L_y) = (228, 448)$ for WT roots and $(L_x, L_y) = (231, 448)$ for *bravo* mutant roots. We run the simulations up to $T = 3000$, with a time step of $\Delta t = 0.1$ (we have checked that the same results are obtained for smaller values of $\Delta t$). We take this time point as corresponding to the stationary state. The diffusion coefficient outside the root layout is set to be zero, restricting the domain of the equations to the root's interior. Additionally, this condition automatically implements reflecting boundary conditions at the root borders.

# 5.D Supplementary Figures

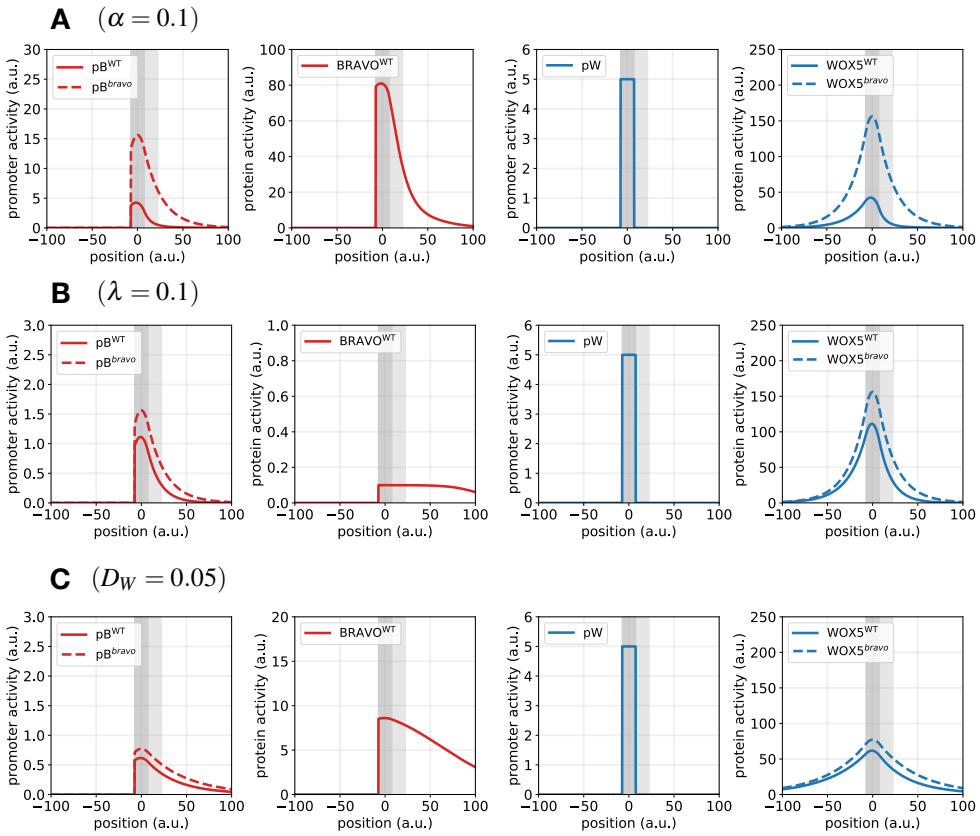



**Figure 5.18: Immobilization by sequestration model for different parameter values.** Stationary profiles of $pB(x)$, $B(x)$, $pW(x)$ and $W(x)$ in WT (continuous lines) and in the *bravo* mutant (dashed lines), for the parameter values **A)** $\alpha = 0.1$, **B)** $\lambda = 0.1$ and **C** $D_W = 0.05$. The rest of the parameters are the same as in Figure 5.2. **A)** Increasing the production rate of BRAVO from $\alpha = 0.01$ (original) to $\alpha = 0.1$ (this figure), induces an increase in the levels of $pB(x)$ which come close to the values of $pW(x)$, a behavior we do not observe in the experiments. **B)** Letting the rate of complex formation change from $\lambda = 0.001$ (original) to $\lambda = 0.1$ (this figure), does not affect much on the spatial profile of $pB(x)$ (compare with Figure 5.2B), but the levels of free BRAVO decrease dramatically due to higher sequestration by WOX5. Such low values of BRAVO are able to extend far from the QC and VI domains. **C)** Increasing the diffusion of WOX5 from $D_W = 0.01$ (original) to $D_W = 0.05$ (this figure) induces a dramatic expansion of WOX5 levels, and consequently an expansion of $pB(x)$. Again, this situation is not realistic.

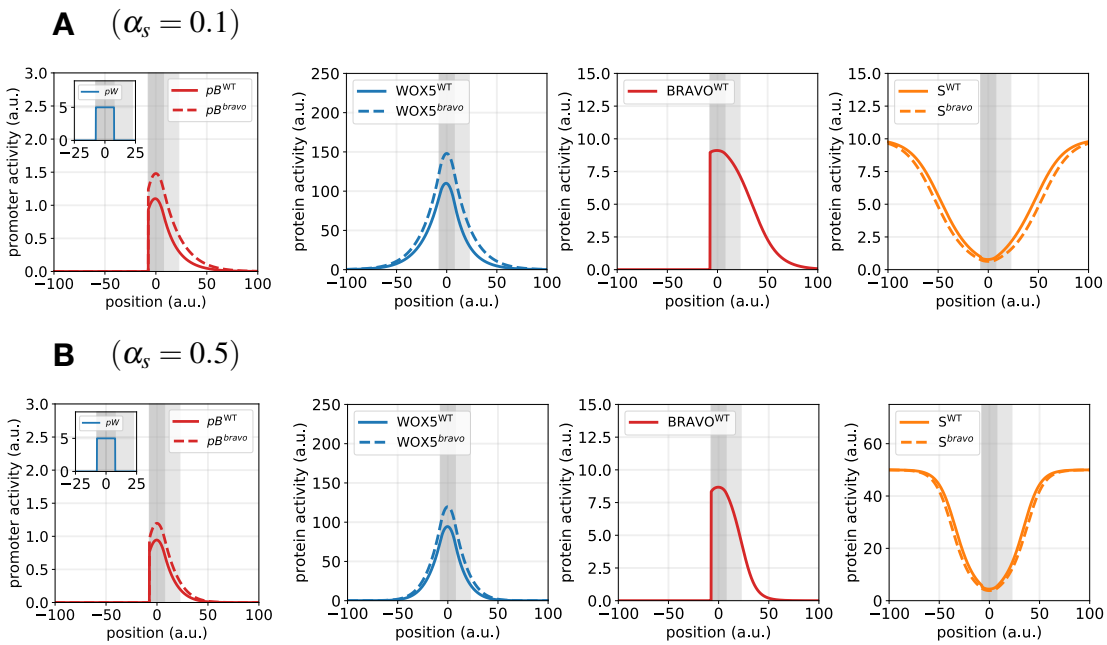



**Figure 5.19: Immobilization by sequestration model with an additional sequestrator. A,B)** Stationary profiles of $pB(x)$, $B(x)$, $pW(x)$, $W(x)$ and $S(x)$ for different values of the production of the additional sequestrator $\alpha_S$, **A)** $\alpha_s = 0.1$ **B)** $\alpha_S = 0.5$. The rest of the parameters are the same as in Figure 5.2. While an expansion of $pB(x)$ in the *bravo* mutant is still possible for low values of $\alpha_S$ (as shown in **A**), sequestration by the additional factor $S$ can impair the expansion of $pB(x)$ due to a the impossibility of WOX5 to increase in the *bravo* mutant, as a consequence of being sequestered by $S(x)$ (**B**).

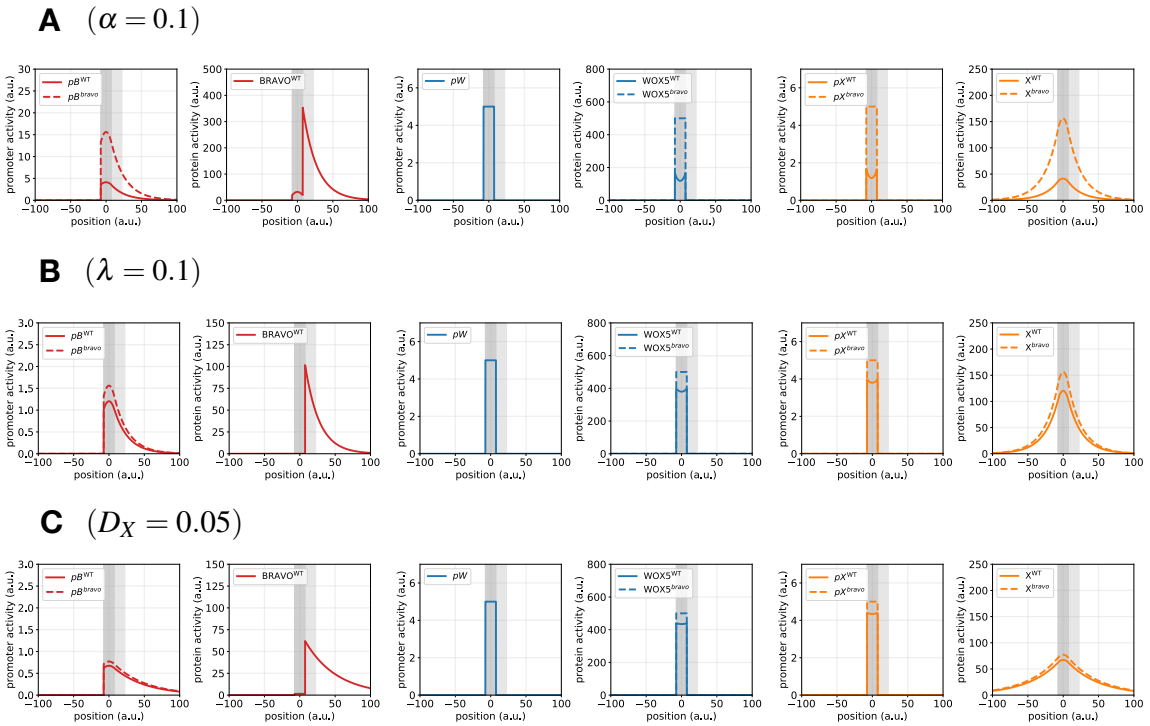



**Figure 5.20: Attenuation by sequestration model for different parameter values.** Stationary profiles of $pB(x)$, $B(x)$, $pW(x)$, $W(x)$, $pX(x)$ and $X(x)$ for the parameter values **A)** $\alpha = 0.1$, **B)** $\lambda = 0.1$ and **C)** $D_X = 0.05$. The rest of the parameters are the same as in Figure 5.6. **A)** Increasing the production rate of BRAVO from $\alpha = 0.01$ (original) to $\alpha = 0.1$ (this figure), induces an increase in the levels of $pB(x)$ too high to match the experiments. The bump in the profile of $B(x)$ is a direct consequence of sequestration only happening in the QC, as in this model WOX5 does not diffuse. **B)** As the rate of complex formation changes from $\lambda = 0.001$ (original) to $\lambda = 0.1$ (this figure), the bump in $B(x)$ disappears, as more free BRAVO is sequestered by WOX5. In this case, the profiles of $pB(x)$ are very similar to the ones in Figure 5.6. **C)** Increasing the diffusion of $X$ from $D_X = 0.01$ (original) to $D_X = 0.05$ (this figure) induces an expansion in BRAVO levels, and a less pronounced expansion in $pB(x)$ due to the little accumulation of $X$ in the QC.

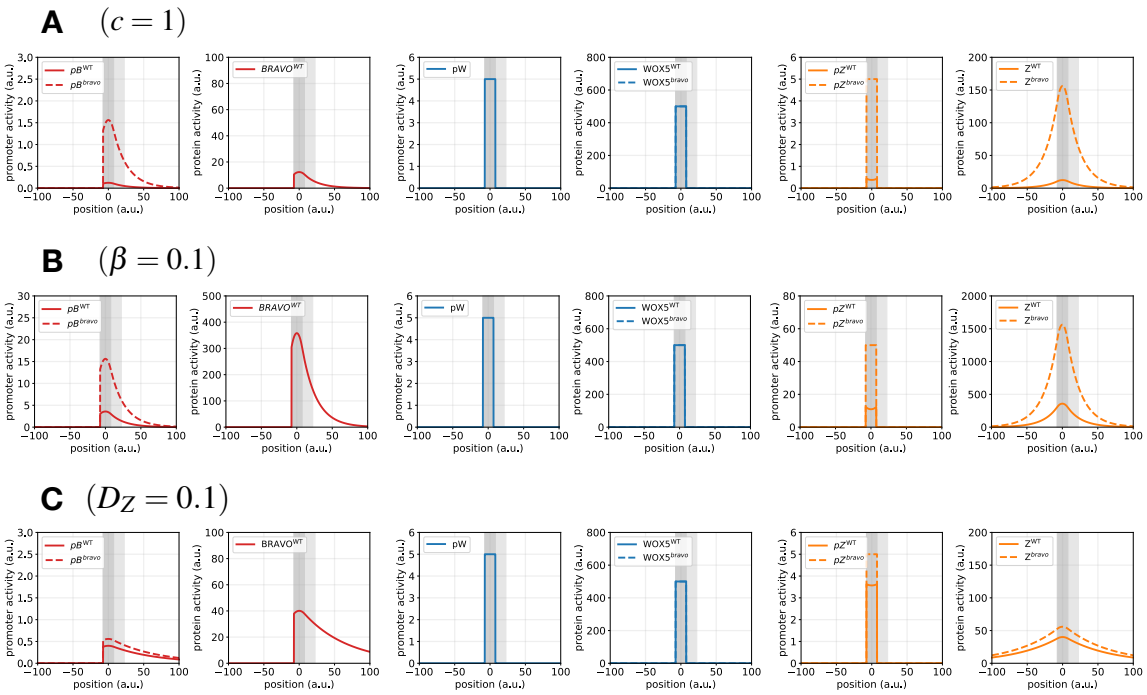



**Figure 5.21: Repression model for different parameter values.** Stationary profiles of $pB(x)$, $B(x)$, $pW(x)$, $W(x)$, $pZ(x)$ and $Z(x)$ for the parameter values A) $c = 1$, B) $\beta = 0.1$ and C) $D_Z = 0.1$. The rest of the parameters are the same as in Figure 5.9. **A)** Increasing the repression threshold of $Z$ by BRAVO from $c = 0.01$ (original) to $c = 1$ (this figure), lead to very low levels of $pB(x)$ in the WT, which imply a dramatic expansion in the *bravo* mutant, which is not realistic. This happens because the levels of $Z(x)$ in the WT are very low due to high inhibition by BRAVO. **B)** Increasing the production rate of $Z$ from $\beta = 0.01$ (original) to $\beta = 0.1$ (this figure), also produces a decrease in the WT activity of $pB(x)$, as $Z(x)$ will be at higher values and will activate. **C)** Increasing the diffusion of $Z$ from $D_Z = 0.01$ (original) to $D_Z = 0.1$ (this figure), leads to the spreading of $pB(x)$, which again is not a realistic situation.

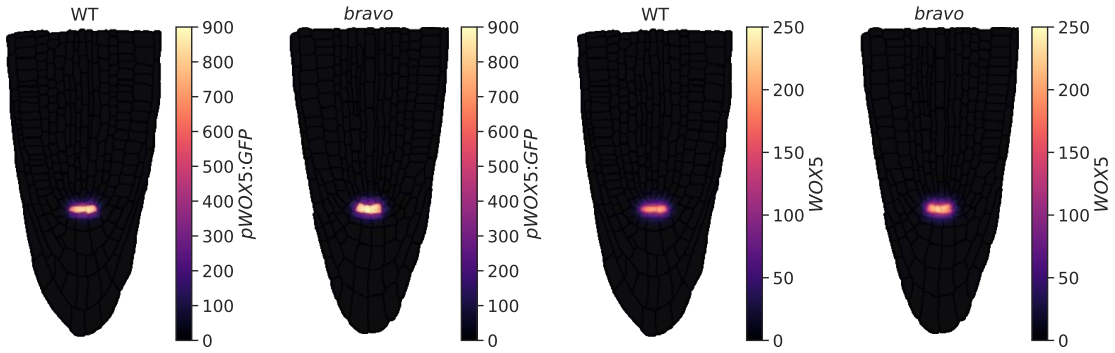



**Figure 5.22: Activity of *pWOX5:GFP* and *WOX5* in the absence of other regulatory factors.** When WOX5 is only allowed to be produced at the QC, degrade and diffuse, the expression pattern in the stationary state is as shown in the figure.

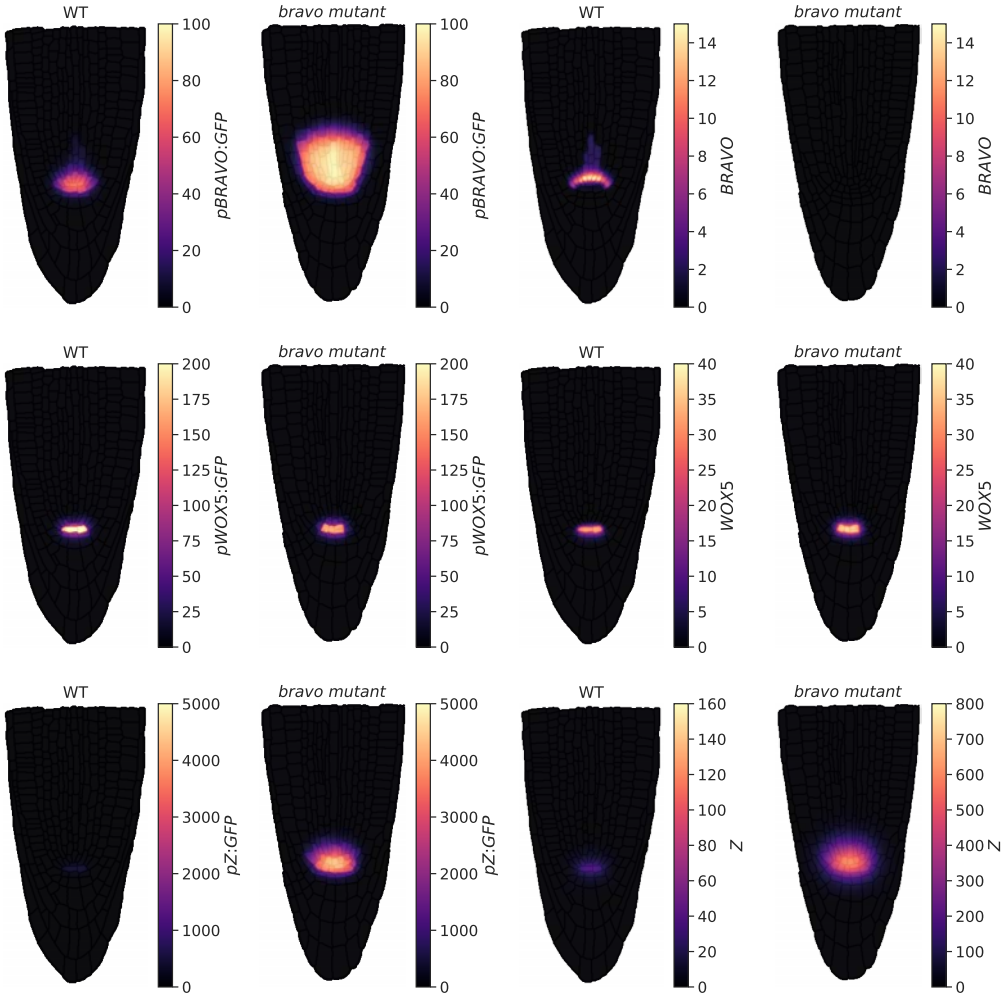



**Figure 5.23: Stationary profiles of all proteins and GFP reporters of promoters corresponding to Figure 5.16 (Mixed Model).** The results are shown for the WT and the *bravo* mutant. The first two panels correspond to the same results shown in Figure 5.16.

# Part III

# Lateral inhibition by diffusion

# Chapter 6

# Formation of rhizoids in *Marchantia polymorpha*

## Contents


**6.1 Introduction . . . . . 146**
**6.2 A null model: cell-autonomous random decisions for rhizoid precursor patterns . . . . . 150**
**6.3 A model with self-activation and lateral inhibition through diffusion . . . . . 156**
6.3.1 Model formulation . . . . . 156
6.3.2 The model recapitulates rhizoid patterns in WT and mutants . . . . . 160
**6.4 A balance between randomness and lateral-inhibition by diffusion . . . . . 163**
6.4.1 Model predictions . . . . . 163
6.4.2 Experiments support the model predictions . . . . . 168
**6.5 Discussion . . . . . 172**


In this chapter, we study the molecular mechanisms involved in the formation of rhizoid precursor cells in the epidermis of *Marchantia polymorpha* gemmae. Recent experiments suggest that the spatial distirbution of these precursors emerge as a consequence of lateral inhibition interactions [Thamm et al., 2020], yet the molecular mechanisms for how this happens are not well-understood. We first show that a null model where rhizoid precursors appear cell-autonomously and at random locations within the gemma epidermis cannot fully explain the experimentally observed distributions previously reported by others [Thamm et al., 2020], as expected. By recognizing the statistical limitations of the data—such as the low frequency of large clusters—we then propose appropriate measures for quantifying the structure of rhizoid patterns, which

focus on local instead of global properties of the clusters. We then propose a reaction-diffusion mechanism in a discrete cellular lattice where the two genes RSL1 and FRH1, known for their role in the regulation of rhizoid cell specification, interact in a spatially dependent negative feedback loop to induce the formation of small filamentous clusters of rhizoid precursors, in a way reminiscent to lateral inhibition. We compare the results of our model with data obtained from our collaborators and show that it can predict with high precision the structure of rhizoid patterns in all the proposed measures. Particularly, the model predicts that both lateral inhibition and randomness are important factors controlling the spatial distribution of rhizoid precursors. Moreover, we show that our model can recapitulate the patterns observed in gain and loss of function mutants, reported elsewhere [Thamm et al., 2020, Honkanen et al., 2018].

## 6.1 Introduction

In the early-diverging land plant *Marchantia polymorpha*, rhizoids in the gemma epidermis are formed from a field of initially equivalent epidermal cells, which are specified on the first day after germination (see subsection 2.1.2 for further details). Up to this day, little is known about the genetic factors controlling such specification, but recent experiments have shed light on some of them. By analyzing loss of function mutants that do not develop rhizoids, Proust *et al* have recently identified that the transcription factor MpRSL1 is involved in rhizoid specification [Proust et al., 2016]. In the gemma of *Marchantia*, rhizoid precursor cells—i.e., cells which will eventually become rhizoids—express MpRSL1 (henceforth simply RSL1), marking differentiated cells from non-rhizoid (epidermal) cells [Proust et al., 2016]. Moreover, gemmae of gain of function mutants of RSL1 display supernumerary rhizoids, further confirming RSL1 as a rhizoid specifying factor [Proust et al., 2016].

Recently, RSL1 has been shown to interact with the microRNA MpFRH1 (henceforth simply FRH1). The underlying genetic circuit has been suggested to be important in controlling rhizoid cell specification, as wild-type patterns are altered in loss of function and overexpression mutants of both genes [Proust et al., 2016, Honkanen et al., 2018, Thamm et al., 2020]. Furthermore, these observations support the idea that RSL1 and FRH1 interplay in a negative feedback loop, with RSL1 activating FRH1 and FRH1 repressing the expression of RSL1. Due to the presumed mobile nature of microRNAs, these interactions would generate a mechanism akin to lateral inhibition, where the activity of FRH1 in a cell represses the activity of FRH1 in its neighbours [Thamm et al., 2020]. In this chapter, we use these recent observations to build a theory on rhizoid pattern formation, incorporating the known interactions between the two components and exploring their consequences.

While rhizoid's morphological structure, density, and location within the

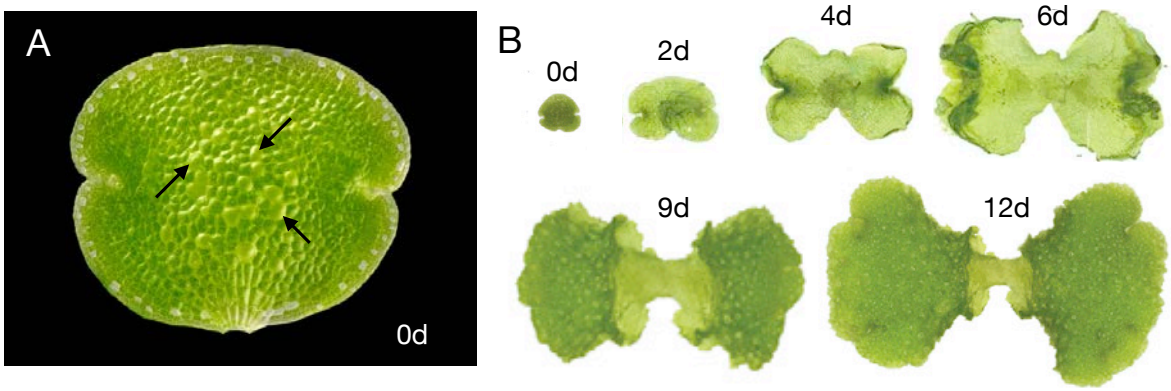



**Figure 6.1: Developmental stages of *Marchantia polymorpha*. A)** 1-day-old gemma, showing epidermal cells, rhizoid precursor cells (arrows) and oil body cells (small grey cells in the boundaries) (image from Wikipedia). **B)** Time-lapse of some developmental stages of *Marchantia* (adapted from [Solly et al., 2017]).

*Marchantia* thallus have been well-characterized [Shimamura, 2016, Cao et al., 2014], their emergence and spatial distribution in the first stages of *Marchantia* development have only recently been addressed. Thamm, Saunders, and Dolan have given the first detailed analysis of such spatial patterns [Thamm et al., 2020], with the observation that rhizoid precursor cells of 1-day-old gemmae tend to develop individually, yet some stick together to form filamentous, one-dimensional chains of cells, in apparent opposition to the clusters one would expect if rhizoids were located randomly in the tissue (Figure 6.2).

To characterize the patterns of rhizoid precursors, Thamm, Saunders, and Dolan make use of two main measures: the frequency of cluster sizes and the average number of neighbours of a cell belonging to a cluster of a certain size [Thamm et al., 2020]. The first quantity is obtained by counting the number of clusters—how many groups of interlinked rhizoid precursors—of each size and dividing by the total number of clusters. For clusters consisting of $k$ cells, we denote the frequency of cluster sizes by $f_k = C_k / \sum_i C_i$, where $C_k$ is the number of clusters of size $k$ (isolated rhizoid precursors are counted as clusters of size $k = 1$). The second quantity, denoted by $n_k$, is defined as the average number of neighbours which are also rhizoid precursors, for a particular cell belonging to a cluster of size $k$. In Figure 6.3 and Figure 6.4 we show the experimental data on these two quantities as adapted from [Thamm et al., 2020].

While the cluster-size distribution $f_k$ only conveys global information about the structure of the clusters, $n_k$ encodes properties about their actual shape. It will be useful to first consider a particular limit case, which constitutes a lower bound on the possible relationship between $n_k$ and $k$. This limit case consists of clusters assembled as one-dimensional, filamentous chains of rhizoid precursors [Thamm et al., 2020]. It's easy to see that for one such cluster of size (or in this case, length) $k$, the number of neighbours is 2 for cells in the interior of the chain, and 1 for the two cells at the tips of the chain, making a total

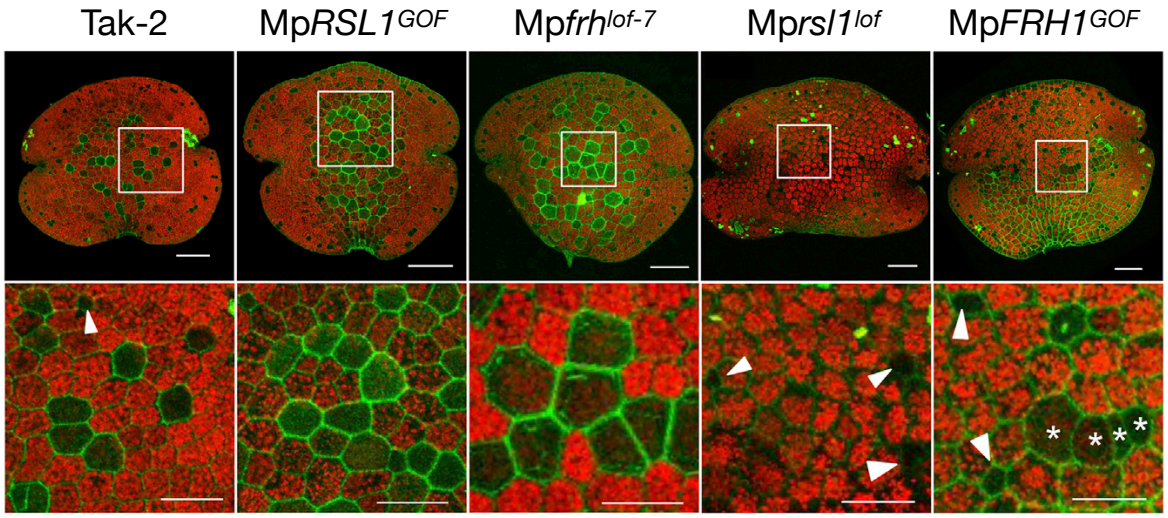



**Figure 6.2: Distribution of rhizoid precursors in WT (Tak-2) and mutants.** In WT plants, rhizoid precursors are either isolated or forming filamentous structures, generally with two or three cells (and sometimes more). In plants with RSL1 gain of function and *frh1* loss of function mutants, this filamentous nature is partially lost, and display instead more clumped clusters, as well as a higher density of rhizoid precursors. The opposite happens in *rsl1* loss of function and FRH1 gain of function mutants, where rhizoids barely develop. White arrowheads indicate the presence of oil body cells. Image adapted from [Thamm et al., 2020].

of $2 + 2(k-2) = 2k-2$. Dividing this quantity by $k$, we obtain the average number of neighbours for a cell in a cluster of size $k$, resulting in the curve $n_k = 2 - 2/k$ (green curve in Figure 6.3). In WT plants, the experimentally measured $n_k$ falls close to $2 - 2/k$, suggesting that indeed clusters tend to be filamentous [Thamm et al., 2020]. In gain of function mutants of $RSL1$ ($RSL1^{GOF}$) these values deviate from the $2 - 2/k$ curve, as the filamentous nature of clusters is lost[1] (Figure 6.4, [Thamm et al., 2020]). Similarly, in loss of function mutants of FRH1 ($frh1^{lof}$), the filamentous nature of clusters is also lost, and more clumped groups of cells can be observed (Figure 6.4, [Thamm et al., 2020]).

With these data at hand, together with the molecular interactions between RSL1 and FRH1 described previously, Thamm, Saunders, and Dolan [Thamm et al., 2020] suggest that patterns of rhizoid precursors must involve a mechanism analogous to lateral inhibition, in which rhizoid precursors prevent neighbouring cells to acquire the same fate. To test this hypothesis, they used a model based on a cellular automata on a 2-dimensional, regular hexagonal array of cells, beginning with an initial random distribution of rhizoid precursors and sequentially changing epidermal cells to rhizoid precursors according to a basic rule: within the existing groups of rhizoid precursors, new precursors can

[1] In Figure 6.3 and Figure 6.4 we use standard deviations for the error bars in order to show the results as displayed in [Thamm et al., 2020], but we must bear in mind that experimental values of $n_k < 2 - 2/k$ are not possible, as $2 - 2/k$ constitutes a lower bound for $n_k$.

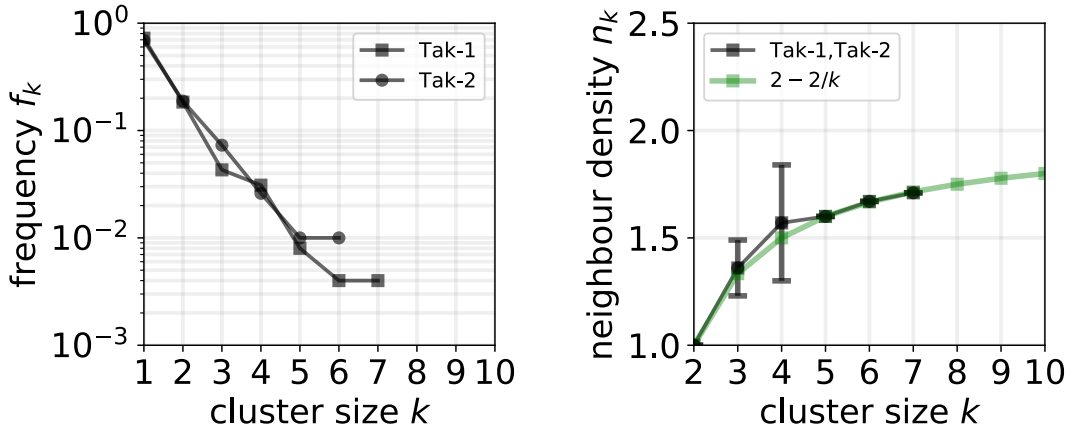



**Figure 6.3: Distribution of cluster sizes and average neighbour density of rhizoid precursors in experimental data from WT (Tak-1 and Tak-2) plants.** Data taken from [Thamm et al., 2020] and plotted similarly to Figure 2B, D and Figure 5E in [Thamm et al., 2020].

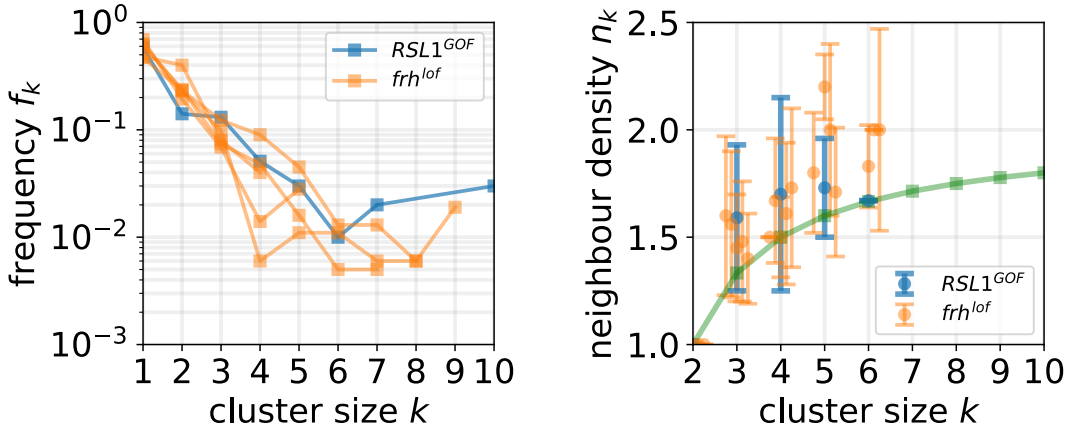



**Figure 6.4: Distribution of cluster sizes and average neighbour density of rhizoid precursors in $RSL1^{GOF}$ and $frh1^{lof}$ plants.** Data taken from [Thamm et al., 2020] and plotted similarly to Figure 2B,D and Figure 5E in [Thamm et al., 2020].

become integrated into the group, but only near the cells with exactly one neighbouring precursor. Through this rule, lateral inhibition is explicitly imposed, inevitably leading to the formation of one-dimensional, filamentous clusters, in good agreement with their experimental data in the WT. To model $frh1^{lof}$ and $RSL1^{GOF}$ mutants, they allow rhizoid precursors to become integrated into an existing cluster without any restriction regarding their neighbours. The distributions of rhizoid precursors in these mutants are well-described by the cellular automata model without lateral inhibition. Importantly, in this model, for a predetermined initial density of rhizoid cells, additional precursor cells appear *sequentially* in the already formed clusters. As we will see, this will differ from our proposed model, where clusters emerge dynamically through cell-to-cell interactions.

Despite the simplicity of the cellular automata model—which does not consider any genetic interactions between RSL1 and FRH1—the results of [Thamm et al., 2020] strongly advocate for lateral inhibition as an integral mechanism to explain the structure of rhizoid precursor patterns observed in WT gemmae. This leads them to suggest that, among possible mechanisms, the negative feedback between RSL1 and FRH1 may determine the filamentous nature of rhizoid patterns. However, how rhizoid cells are specified from a field of initially equivalent cells, how patterns are dynamically formed, and what are the specific contributions of RSL1 and FRH1 in generating such patterns still remain open questions. In this chapter, we tackle these questions through a mathematical model that takes into account the known genetic interactions between RSL1 and FRH1.

## 6.2 A null model: cell-autonomous random decisions for rhizoid precursor patterns

Our first approach assumes that the process underlying rhizoid precursor specification is cell-autonomous, that is, it involves each cell performing a random binary decision. Therefore, the location at which a precursor appears will be independent of the others. We call this the *null model*. To see what this hypothesis implies for $f_k$ and $n_k$, we consider a discrete hexagonal lattice of size $N \times N$ cells (as defined in Chapter 3 of Part I) where cells can either become rhizoid precursors (hereafter denoted as ON cells) with probability $p$ or epidermal cells (OFF) with probability $q = 1 - p$. In other words, for a given value of $p$, a hexagonal layout is generated with a specific distribution of ON and OFF cells (Figure 6.5). To emulate the tissue layout of the *Marchantia* gemma epidermis, we choose a lattice size of $14 \times 14$, consistent with the average number of cells enclosing the regions where rhizoid precursors appear. With this set-up, the density of ON cells—that is, the fraction of cells in the ON state with respect to the total number of cells—is controlled by the value of $p$: the larger $p$, the larger the density. For a small lattice, this density will only be approximately equal to $p$, as each different realization of the random process will lead to different proportions of ON/OFF cells. Only when the lattice approaches an infinite size will the density be strictly equal to $p$, as the previous proportion in this limit becomes exact. Thus, having a relatively small lattice will invariably bring about deviations from this average density.

By fixing the size of the lattice ($14 \times 14$ in our case), the statistics of the null model—including $f_k$ and $n_k$—are completely determined by the value of the single, free parameter $p$. We choose a value of $p$ similar to the values for the density of rhizoid precursor cells. Experimentally, this proportion ranges from 0.1 to 0.2 [Thamm et al., 2020, Thamm, 2019]. In Figure 6.5 we show different examples of patterns of rhizoid precursors (ON, green cells) obtained with the

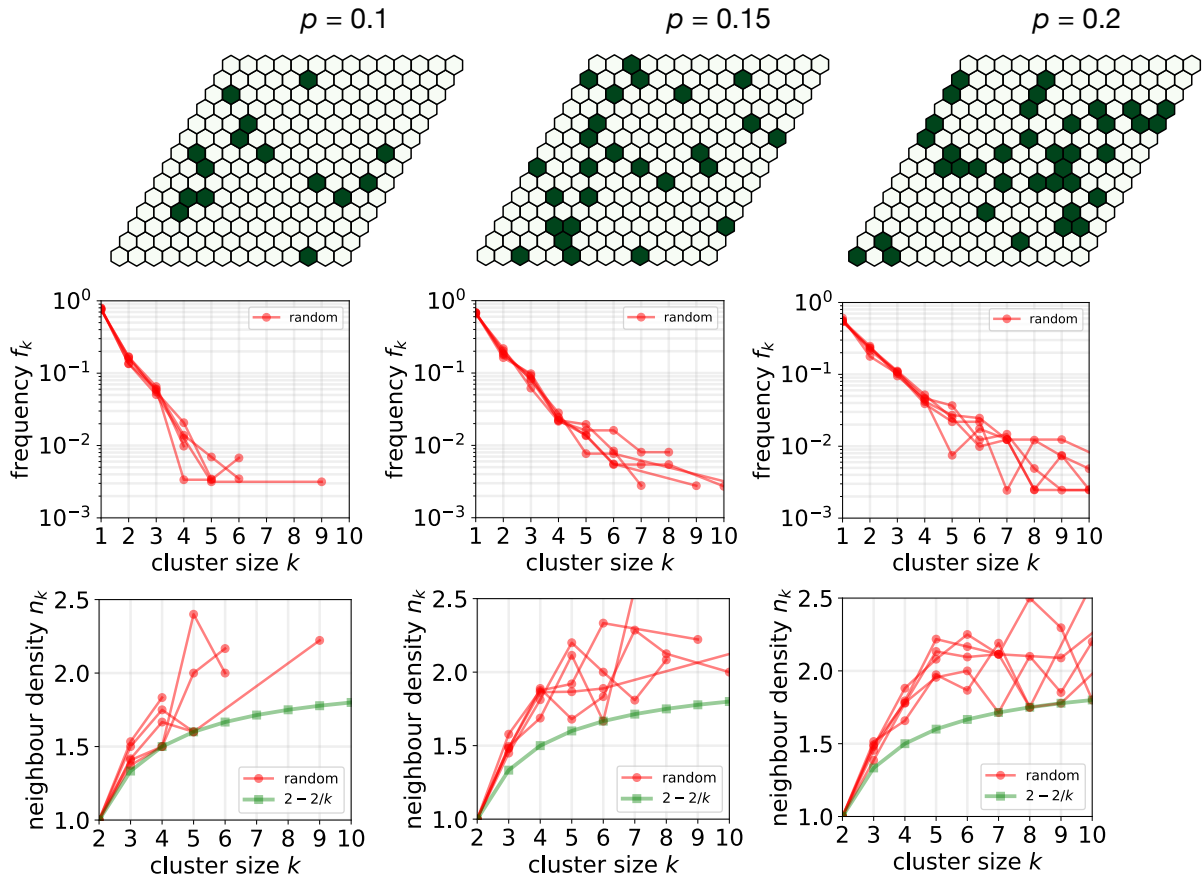



**Figure 6.5: Distributions of ON cells predicted by the null model and their statistics. Top row:** Rhizoid precursor patterns (in green) for different values of $p$, chosen to be similar to the density of rhizoid precursors observed in WT plants (rhizoid density in WT $\simeq 0.15$ [Thamm et al., 2020]). As the probability increases, the proportion of ON cells in the lattice also increases. **Middle-bottom row:** In red, five realizations of $f_k$ (middle) and $n_k$ (bottom) for the same values of $p$. Each realization has been obtained by averaging $N_{sim} = 20$ random lattices of size $14 \times 14$ cells, similar to the experiments used in [Thamm et al., 2020] ($20 - 30$ gemma for each genotype). Since the lattice is finite, large clusters become misrepresented in the statistics, resulting in large deviations of the corresponding frequencies. Analytical values of $n_k$ corresponding to filamentous clusters ($n_k = 2 - 2/k$) are plotted in green.

null model, for this range of values of $p$. As expected, larger clusters emerge as $p$ increases.

To understand the structure of the clusters exhibited by this null model, we defined new complementary measurements. For instance, we could have two different sets of clusters, one in which all are filamentous and another where they are not, and we could nonetheless have the same distribution of cluster sizes. Thus, while $f_k$ does give us information about the spatial structure of the pattern, it does not inform us about the structure of clusters *themselves*. Since most of the experimentally observed clusters consist of 1, 2, 3, or 4 cells (in [Thamm et al., 2020], only four 5-clusters, three 6-clusters and, one 7-cluster

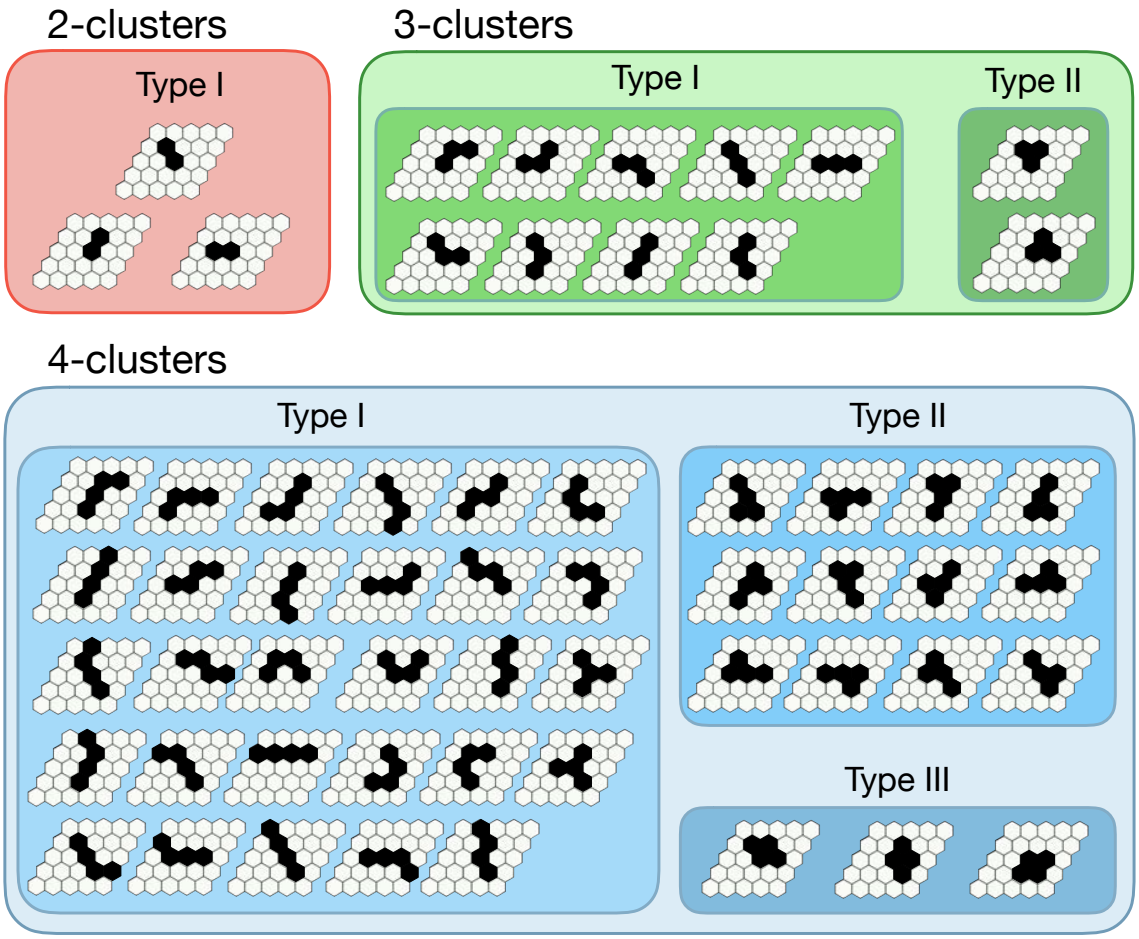



**Figure 6.6: Distinct configurations of clusters of 2, 3 and 4.** In a hexagonal lattice, there can be 3 clusters of two (red background) all of the same type; 11 clusters of three (green background), distributed among 9 clusters of type I and 2 of type II; and 44 clusters of four (blue background), of which 29 are of type I, 12 are of type II and 4 are of type III. For practical reasons, we do not show the number of configurations of clusters larger than four, but we can compute their type frequencies numerically.

are described for WT plants), here we propose two additional measures to assess the local properties of clusters. The first, which we denote by $F_r^k$, is the fraction of clusters of size $k$ and type $r$ among the totality of clusters, where here the type is defined by its average number of ON neighbours (or, equivalently, depending on the number of OFF cells in their boundary). For clusters of size $k$, there are $k-1$ types (except for isolated cells, which have $k=1$ and there is only one type), so that for 2-clusters, there is only one type, for 3-clusters two types, for 4-clusters three types, and so on (Figure 6.6). Notice that, for all sizes $k$, clusters of type I are those we call filamentous, as are the ones falling into the curve $n_k = 2 - 2/k$. The value of $n_k$ for clusters of types I, II, III, etc, will be above the curve $n_k = 2 - 2/k$.

The second measure, denoted by $g_l^k$, describes, for clusters of size $k$, the fraction of cells that have $l$ ON neighbours, where $l$ runs from 0 to $k-1$. For

example, for 1-cell clusters (i.e. isolated cells) the fraction $F_r^1 = 1$, while $g_0^1 = 1$ and $g_1^1 = 0$, as isolated cells have no ON neighbours. For clusters of two, it is easy to see that $F_r^2 = 1$, because there is only one type of cluster, and $g_0^2 = 0$, $g_1^2 = 1$, because all cells in 2-clusters have 1 ON neighbour. In general, for each $k$ we have the conditions $\sum_r^{k-1} F_r^k = 1$ and $\sum_l^{k-1} g_l^k = 1$, as all fractions must sum up to one. For clusters of three or more, it is harder to compute these quantities analytically, as we need to know, on the one hand, all different types of clusters and how many neighbours cells have within such clusters, and on the other hand, the probability of occurrence of each type of cluster in a null model. Still, for clusters of three and four, one can compute the analytical expressions for these frequencies (see the Appendix of this chapter).

For a given $p$, the null model predicts specific values of $f_k$, $n_k$, $F_r^k$ and $g_l^k$, which we will eventually use to compare with the experimental observations of our collaborators. For instance, in Figure 6.7 (Top) we show the values of $n_k$ of the null model (red curves), together with the fraction of clusters of each type $F_r^k$. In this plot, the $F_r^k$ are represented as circles whose area is proportional $F_r^k$, and are centered at the values of $k$ and the $n_k$ corresponding to the type $r$. The numbers above the circles represent the total number of clusters of each size. For example, in the left panel we show the results obtained for a simulation of $N = 40$ lattices, similar to the number of WT gemmae considered in [Thamm et al., 2020]. In our case, we obtain 54 clusters of 3, the majority of which are of type I, while some are of type II. In the same panel, only 2 clusters of 7 appear, 1 of type I and 1 of type II. Due to the low number of lattices, few large clusters appear, and the curve $n_k$ exhibits high variability. This contrasts with the right panel, where we simulate $N = 1000$ lattices. In this case, larger clusters appear, and the curve $n_k$ follows a more regular shape, with less variability. Notice, however, that very large clusters are still rare. In Figure 6.7 (Bottom) we show the results of an additional simulation for $N = 40$, with typical cluster configurations for each type.

As in [Thamm et al., 2020] there is no information about the local cluster structure, we can only compare the results of null model with the experiments via the quantities $f_k$ and $n_k$, but not through $F_r^k$ and $g_l^k$. These will be used in the next sections, when comparing the results of our modelling with experiments from our collaborators. The distinct information provided by $f_k$ and $n_k$ is evidenced in Figure 6.8. While the frequency of cluster sizes $f_k$ matches quite well with experimental results of [Thamm et al., 2020] in the WT, the null model overestimates the average number of neighbours, well surpassing the limits allowed by the experimental deviations. Therefore, we conclude that, despite giving good results for $f_k$, the null model cannot predict the distribution $n_k$ in the WT. As already pointed out in [Thamm et al., 2020], the deviation from a null model in the WT can be resolved by assuming that the specification of rhizoid precursors is not so cell-autonomous after all but involves inhibitory interactions between neighbouring cells, preventing ON cells to cluster together

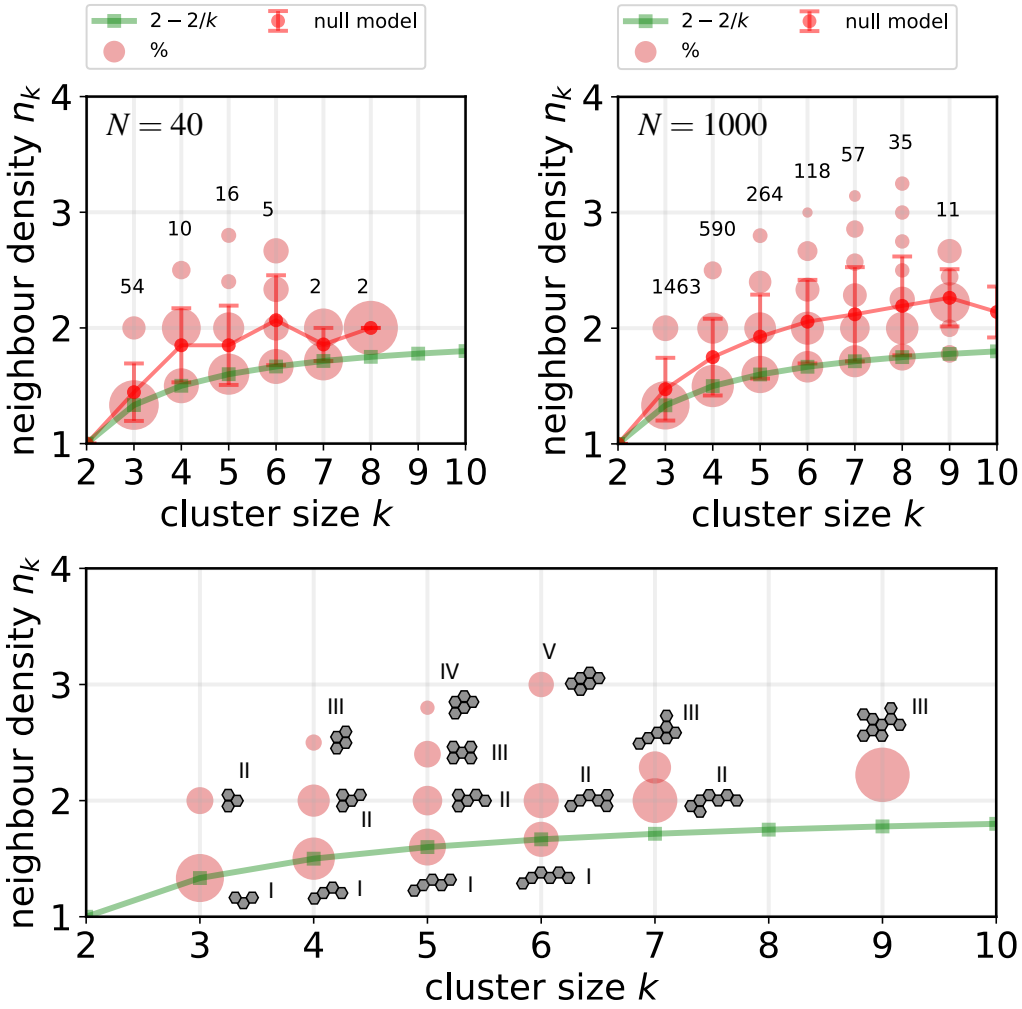



**Figure 6.7: Mean neighbour density with the fraction $F_r^k$ of cluster types for the null model. Top:** Average neighbour density separated by each cluster type obtained by simulating the null model in $N = 40$ (left) and $N = 1000$ (right) hexagonal lattices of size $14 \times 14$ and with ON probability $p = 0.15$. The area of the circles represents the proportion of clusters of each type, $F_r^k$. The number above the circles denote the total number of clusters of that size. The red curves represent the average of $n_k$ over all simulations, with error bars denoting plus and minus the standard deviations of the average $n_k$. **Bottom:** Additional simulation with $N = 40$ showing the fraction of cluster types and typical configurations of each type.

in two-dimensional structures.

In contrast, as shown in Figure 6.9, the null model recapitulates the experimental observations in $RSL1^{GOF}$ and $frh1^{lof}$ mutants, both in $f_k$ and $n_k$. This supports the hypothesis that lateral inhibition requires FRH1, and its effect is negligible when RSL1 is overexpressed, in agreement with the conclusions of [Thamm et al., 2020]. As explained previously, RSL1 is a rhizoid promoting factor, and FRH1 has been shown to repress RSL1. The fact that both epidermal and rhizoid cell types arise in the gemmae of $frh1^{lof}$ mutants, and do

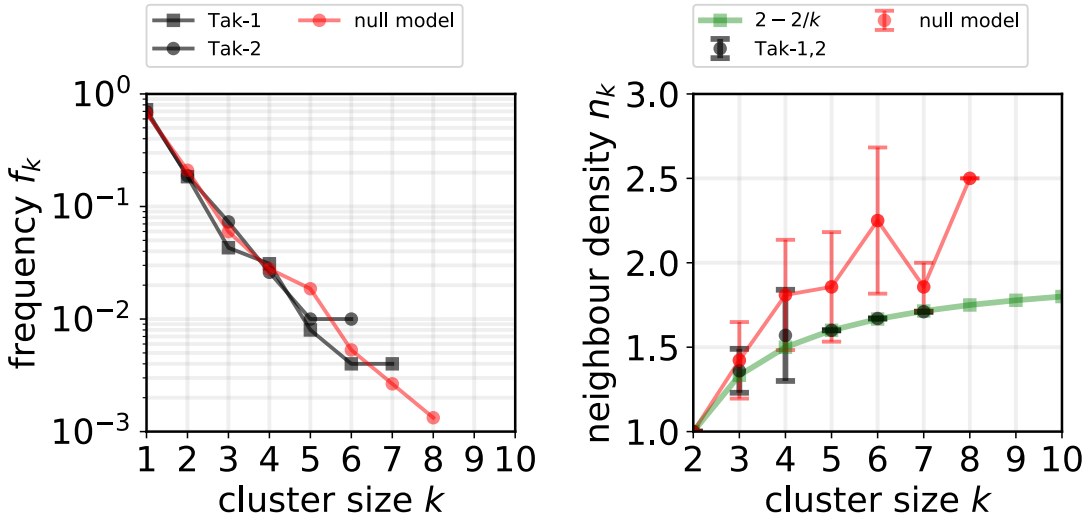



**Figure 6.8: Comparison between the null model and experimental WT distributions.** Frequency of cluster sizes and average number of neighbours in the random lattice model (red) compared with their experimental counterparts in the WT (black, data from [Thamm et al., 2020]). The curves of the null model are averaged over $N = 40$ simulations in a $14 \times 14$ lattice with $p = 0.15$. Error bars denote $\pm$ the standard deviations of $n_k$. The green curve corresponds to $n_k = 2 - 2/k$.

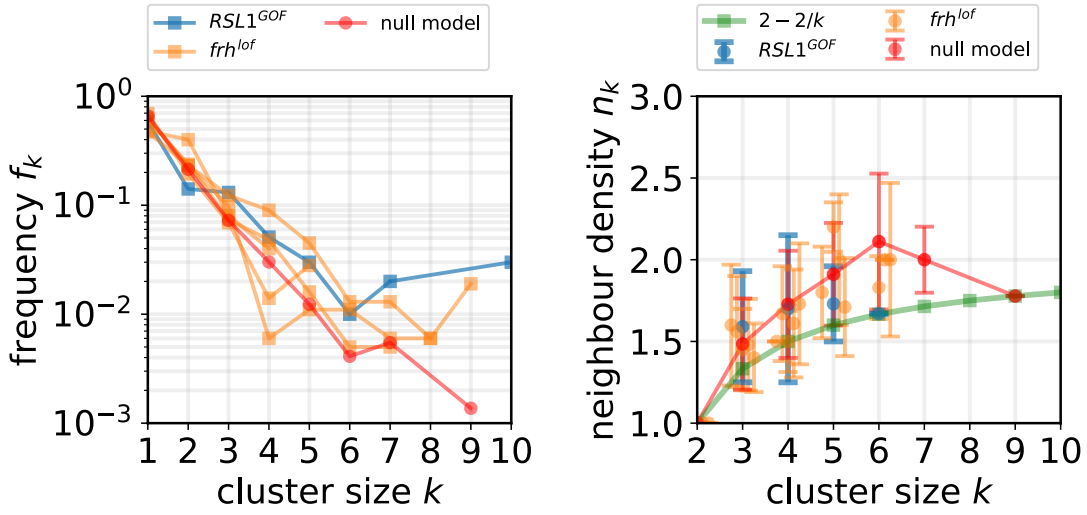



**Figure 6.9: Comparison between the null model and experimental mutant distributions.** Frequency of cluster sizes and average number of neighbours in the null model (red) compared with their experimental counterparts in the mutants (black, data from [Thamm et al., 2020]). The curves of the null model are averaged over $N = 40$ simulations in a $14 \times 14$ lattice with $p = 0.2$. Error bars denote $\pm$ the standard deviations of $n_k$. The green curve corresponds to $n_k = 2 - 2/k$.

so with a distribution that can be explained with a random, cell-autonomous Bernoulli process, suggests that RSL1 can control cell-fate decisions without the need of FRH1. The ability of RSL1 to control multiple cell-fate decisions on its own can be understood by framing the process of rhizoid specification as a

bistable system. This can be achieved simply by assuming that RSL1 regulates its own activity through a positive feedback loop. With this framework, the fate of each cell will depend on the initial state (i.e., the initial concentration of RSL1, for instance). We will explore this further in the next section, where we propose a dynamic model of rhizoid precursor specification where this positive feedback loop is considered explicitly.

## 6.3 A model with self-activation and lateral inhibition through diffusion

While the cellular automata model proposed by Thamm, Saunders and Dolan [Thamm et al., 2020] indeed suggests that a lateral inhibition mechanism can account for the distribution of rhizoid precursor cells observed experimentally, it does not provide any mechanistic explanation about how the interactions between RSL1 and FRH1 are able so generate such patterns. They recognize the potential role of FRH1 as a non-cell-autonomous repressor of RSL1—thereby generating lateral inhibition—yet the details on the mutual regulations between the two factors, and particularly how the presumed movement of FRH1 from cell to cell affects their dynamics and final distributions remain to be assessed. Thus, in this section we propose a simple model for the regulations between RSL1 and FRH1, where we take into account the experimental data provided by Thamm, Saunders and Dolan, and Honkanen *et al* [Thamm et al., 2020, Honkanen et al., 2018]. Our approach rests upon dynamical systems theory, where the dynamic and spatial interactions between RSL1 and FRH1 are explicitly modelled. This dynamic theory of rhizoid pattern formation reveals that the underlying negative feedback loop between RSL1 and FRH1, together with the diffusion of FRH1 and a presumed self-activation of RSL1, is able to explain all the known phenotypes observed for WT, loss of function and overexpressor mutants, without the need to impose any ad hoc rules.

### 6.3.1 Model formulation

The distribution of rhizoids in *frh1* and *rsl1* loss of function mutants, together with the phenotypes observed in RSL1 and FRH1 gain of function plants, serve as the starting point of our study [Proust et al., 2016, Honkanen et al., 2018, Thamm et al., 2020]. As already shown, loss of function mutants lacking RSL1 activity do not develop rhizoids, while plants overexepressing RSL1 develop supernumerary, ectopic rhizoids in place of flat epidermal cells (Figure 6.2). On the other hand, loss of function *frh1* mutants show a similar phenotype than the RSL1 gain of function, with an excess of rhizoids, while gain of function of FRH1 plants resemble *rsl1* mutants, with no rhizoids (Figure 6.2). Furthermore, as mentioned before, RSL1 promotes the expression of FRH1 [Honkanen et al., 2018], which in turn represses RSL1 [Proust et al.,

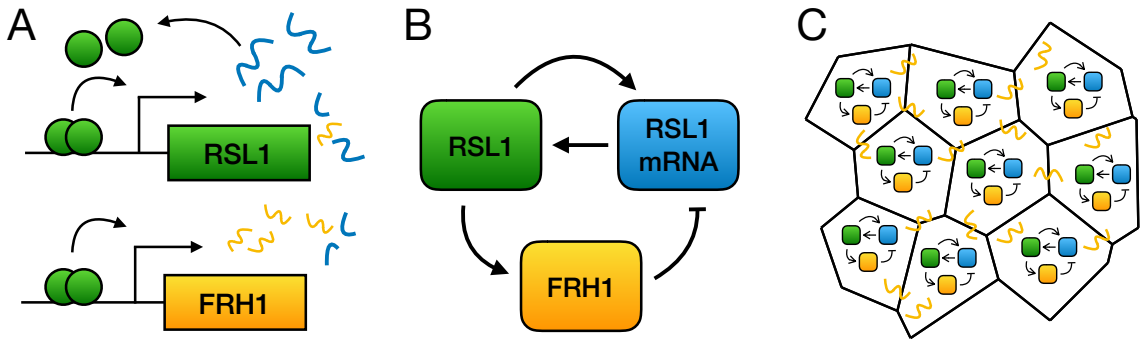



**Figure 6.10: Interactions between RSL1 and FRH1 considered in the model. A**) Explicit regulations, where RSL1 proteins (green circles) activate the expression of both RSL1 mRNA (blue curly lines) and FRH1 miRNA (yellow curly lines), and FRH1 represses RSL1 through mRNA cleavage. **B**) The effective interactions of the model in a single-cell, showing a negative feedback loop between RSL1 and FRH1 together with a RSL1 positive feedback. **C**) Each cell following these regulations is coupled with neighbouring cells via diffusion of the FRH1 miRNA.

2016, Thamm et al., 2020]. Thus, a negative feedback loop between RSL1 and FRH1 seems to be at play. FRH1 being a miRNA, the repression is presumed to occur through cleavage of the RSL1 mRNA, which is therefore prevented from becoming translated into protein. Moreover, the fact that $frh1^{lof}$ plants still develop rhizoids suggests that RSL1 alone has the ability to control rhizoid fates. This bistability in cellular states that can be easily achieved by assuming RSL1 promotes its own expression. To study the resulting system, we begin by defining the concentrations of RSL1 mRNA, RSL1 protein and FRH1 miRNA as $m$, $R$ and $F$, respectively. We consider, as in the null model, a hexagonal lattice where cells are labelled with the indices $i, j$, and assign the variable $m_{ij}$, $R_{ij}$ and $F_{ij}$ to each cell. Then, our model consists on the following set of coupled differential equations:

$$\frac{dm_{ij}}{dt} = a_0 + a\frac{R_{ij}^{n_R}}{k_R^{n_R} + R_{ij}^{n_R}} - k_c m_{ij} F_{ij} - d_m m_{ij} \tag{6.1a}$$

$$\frac{dR_{ij}}{dt} = b m_{ij} - d_R R_{ij} \tag{6.1b}$$

$$\frac{dF_{ij}}{dt} = g_0 + g\frac{R_{ij}^{n_F}}{k_F^{n_F} + R_{ij}^{n_F}} - d_F F_{ij} + D\nabla^2 F_{ij} \tag{6.1c}$$

where $\nabla^2 F_{ij}$ is the discrete Laplacian in a hexagonal lattice, defined as Equation 3.16 in Chapter 3. In this system, transcription of RSL1 mRNA happens with a constant rate $a_0$, but is promoted by RSL1 proteins with maximum strength $a$, activation threshold $k_R$ and cooperativity exponent $n_R$. RSL1 mRNA degradation involves two contributions, one dependent of the FRH1

miRNA (cleaving) with rate $k_c$, and another representing constant degradation of the mRNA by other means, with rate $d_m$. The protein RSL1 is translated from the mRNA at constant rate $b$, while also being linearly degraded with rate $d_R$. Transcription of FRH1 happens with a basal rate $g_0$, and can be enhanced by the binding of RSL1 proteins to the FRH1 promoter, with maximum rate $g$, activation threshold $k_F$, and cooperativity exponent $n_F$. Finally, FRH1 can also be linearly degraded with constant rate $d_F$, and is able to move from cell to cell with diffusion coefficient $D$.

In Figure 6.10 we show a diagram of the interactions between the factors considered in the model. RSL1 is expressed in the whole gemma epidermis, and is able to self-activate. RSL1 proteins can cell-autonomously activate the expression of the miRNA FRH1, which in turn is able to move to other cells and repress RSL1 activity through mRNA cleavage. The system Equation 6.1 has the form of an activator-inhibitor system, with self-activation of RSL1 and long-range inhibition of FRH1. As detailed in Section 2.2 of Chapter 2, these kind of systems are known for their ability to generate patterns [Meinhardt and Gierer, 2000, Meinhardt, 1982]. Activator-inhibitor systems where only the inhibitor diffuses have been studied for the patterning of prestalk/prespore in the slime mold *Dictyostelium discoideum* [Meinhardt, 1983].

Since we are interested in the capacity of these interactions to generate the distribution of rhizoid precursors observed experimentally, we will first reduce the full system so that its analysis becomes more manageable. The first approximation consists of assuming that the dynamics of the RSL1 mRNA are very fast compared to RSL1 proteins. Then, letting Equation 6.1a be equal to zero and writing $m_{ij}$ as a function of $R_{ij}$ and $F_{ij}$, we can substitute it into the second equation to obtain:

$$\frac{dR_{ij}}{dt} = b\frac{a_0 + a\frac{R_{ij}^{n_R}}{k_R^{n_R}+R_{ij}^{n_R}}}{d_m + k_c F_{ij}} - d_R R_{ij} \tag{6.2}$$

The second approximation consists of assuming that the diffusion of FRH1 is very fast, and therefore instead of explicitly considering the dynamics of diffusion, we model its the effect on RSL1 in a particular cell as an average over neighbours and the FRH1 in the original cell [Saiz et al., 2020, Mori et al., 2008]. Then, we can finally write:

$$\frac{dR_{ij}}{dt} = b\frac{a_0 + a\frac{R_{ij}^{n_R}}{k_R^{n_R}+R_{ij}^{n_R}}}{d_m + k_c \langle F_{ij}\rangle} - d_R R_{ij} \tag{6.3}$$

where $\langle F_{ij}\rangle = \frac{1}{7}(F_{i+1,j-1} + F_{i+1,j} + F_{i,j-1} + F_{i,j+1} + F_{i-1,j} + F_{i-1,j+1} + F_{ij})$ (with the hexagonal labelling scheme defined in Figure 3.5). For simplicity, when simulating these lattices we always consider periodic boundary conditions. Finally, by assuming that the dynamics of FRH1 are also fast compared to RSL1,

we can write $F_{ij}$ as a function of $R_{ij}$, which upon substitution gives:

$$\frac{dR_{ij}}{dt} = b\frac{a_0 + a\frac{R_{ij}^{n_R}}{k_R^{n_R}+R_{ij}^{n_R}}}{d_m + \frac{k_c}{d_F}\langle g_0 + g\frac{R_{ij}^{n_F}}{k_F^{n_F}+R_{ij}^{n_F}}\rangle} - d_R R_{ij} \tag{6.4}$$

We can adimensionalize the previous system to get rid of redundant parameters:

$$\frac{dR_{ij}}{dt} = \frac{\alpha_0 + \frac{R_{ij}^{n_R}}{R_A^{n_R}+R_{ij}^{n_R}}}{1 + \gamma_0 + \langle\gamma\frac{R_{ij}^{n_F}}{R_B^{n_F}+R_{ij}^{n_F}}\rangle} - R_{ij} \tag{6.5}$$

where $R$ and $t$ have been rescaled to $R \to Rd_m d_R/ab$ and $t \to t/d_R$. The relations between the original and new parameters are described in Table 6.1.

| Parameter | Relation | Value |
|---|---|---|
| $\alpha_0$ | $a_0/a$ | 0.2 |
| $R_A$ | $k_R d_m d_R/ba$ | 0.6 |
| $R_B$ | $k_F d_m d_R/ba$ | 1 |
| $\gamma_0$ | $g_0 k_c/d_F d_m$ | 0.1 |
| $\gamma$ | $g k_c/d_F d_m$ | 0.6 |

**Table 6.1: Parameters of the simplified adimensional model.** Parameters are chosen to be biologically realistic and to qualitatively fit experimental results.

To understand the possible patterns this model is able to generate, it is convenient to first understand its behaviour in a single cell, without interactions between neighbours. In this case, the equation for a single cell corresponds to Equation 6.5 but for the single variable $R$ and without the averaging brackets:

$$\frac{dR}{dt} = \frac{\alpha_0 + \frac{R^{n_R}}{R_A^{n_R}+R^{n_R}}}{1 + \gamma_0 + \gamma\frac{R^{n_F}}{R_B^{n_F}+R^{n_F}}} - R \equiv f(R) \tag{6.6}$$

The steady states of this equation can be understood by taking the function $f(R)$ as defined above, and computing the values of $R$ when $f(R) = 0$. As shown in Figure 6.11, for the parameters chosen in Table 6.1, the system can be bistable for certain values of $\alpha_0$, meaning that the final value of $R$ will depend on initial conditions. Cells with high $R$ will be rhizoid precursors, while cells with low $R$ will be epidermal cells. Notice that in this bistable regime, since there are no cell-to-cell interactions the system effectively behaves like the null model, where the initial condition $R_0 = R(t = 0)$, together with the dynamics of Equation 6.6, plays the role of the probability $p$, setting the final density of rhizoid precursors (see Figure 6.19).

The fact that in $frh1$ loss of function mutants rhizoids still appear, suggests that RSL1 can generate the two cellular fates without the need of cell-to-cell

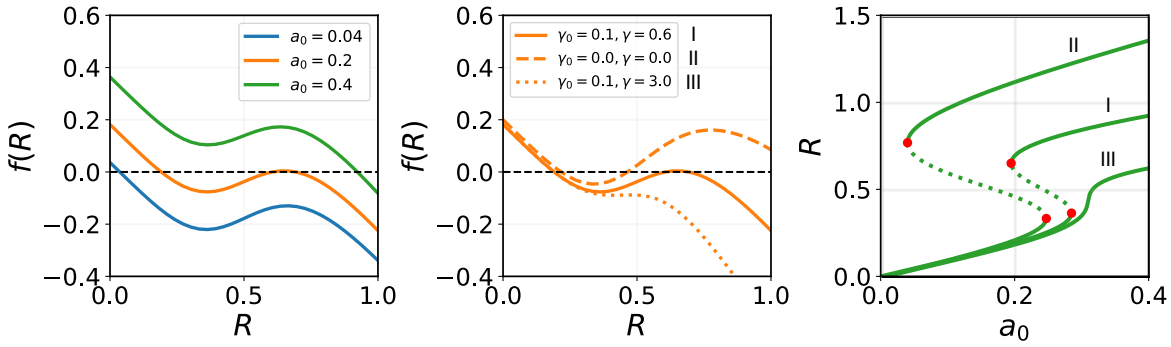



**Figure 6.11: Steady states of the model for a single cell. Left:** Curves $\frac{dR}{dt} = f(R)$ as a function of $R$, for different values of $\alpha_0$, showing the transition monostability ($\alpha_0 = 0.04$), bistability ($\alpha_0 = 0.2$) and again to monostability ($\alpha_0 = 0.4$). **Middle:** The curves $\frac{dR}{dt} = f(R)$ for different combinations of $\gamma_0, \gamma$, and with $\alpha_0 = 0.2$. The cases $\gamma_0 = \gamma = 0$ (II) and $\gamma_0 = 0.1, \gamma = 3$ (III) are intended to mimic loss of function and overexpression mutants of FRH1, respectively. **Right:** Bifurcation diagram showing the steady states of $R$ as a function of $\alpha_0$, and for the different combinations of $\gamma_0, \gamma$ I, II and III. The system can be bistable for certain values of $\alpha_0$, $\gamma_0$ and $\gamma$. Continuous (dashed) lines represent stable (unstable) fixed points. Red dots denote saddle-node bifurcations. The rest of the parameters as in Table 6.1.

coupling. In the uncoupled version of our model, this corresponds to setting $\gamma_0 = \gamma = 0$. As shown in Figure 6.11, in this mutant the cell-autonomous system is in the bistable regime (Middle panel, dashed curve), for the parameter set shown in Table 6.1. Moreover, the system remains bistable even when $\gamma_0$ and $\gamma$ are different than zero, although being close to the saddle-node bifurcation separating monostability from bistability (Middle panel, continuous curve). If $\gamma$ takes higher values (for example, in $FRH1^{GOF}$), the system only has a single steady state with low $R$ (Middle panel, dotted curve), i.e., all cells become epidermal cells. Now that we understand the possible behaviours of the uncoupled, cell-autonomous system, what happens when we introduce cell-to-cell coupling?

### 6.3.2 The model recapitulates rhizoid patterns in WT and mutants

We perform simulations of the diffusively coupled system with the parameter set shown in Table 6.1. To set the initial state of $R_{ij}$ in the hexagonal lattice, we assign at each cell $i, j$ values taken from a uniform distribution of the form $R_{ij}|_{t=0} = R_0\mathcal{U}[0, 1]$, where $\mathcal{U}[0, 1]$ has a size of $N \times N$ (the size of the lattice). As seen in Figure 6.12, the resulting patterns are characterized by displaying mostly single-cell or two-cell rhizoid precursor clusters, together with larger filamentous clusters, with the exception of some non-filamentous 3-clusters.

By quantifying the cluster-size distribution $f_k$ and the average neighbour density $n_k$, we can compare the results of the model with the experimental data in [Thamm et al., 2020]. In Figure 6.25 we show these results in the WT, where we simulate $N = 40$ gemmae with the parameter set in Table 6.1.

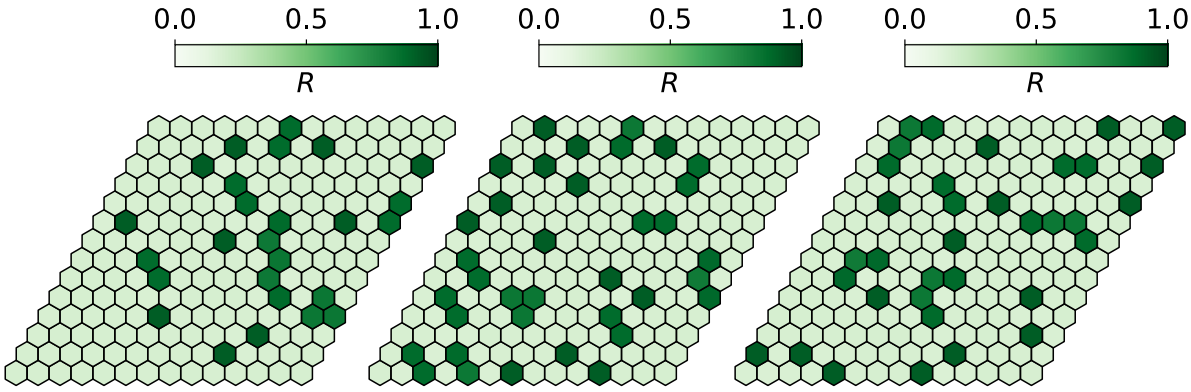



**Figure 6.12: Three examples of WT patterns obtained with the simulations.** Typical patterns obtained by solving the equations of the mathematical model in a $14 \times 14$ hexagonal grid. The three examples correspond to the same parameter set (Table 6.1), but initial conditions differ from one another. In particular, initial conditions are set to be $R_{ij}|_{t=0} = R_0\mathcal{U}[0,1]$, with $R_0 = 0.67$, where the uniform distribution of random numbers is different in each example. While most clusters consist of 1, 2 or 3 cells, larger clusters are also possible, although less probable. Clusters tend to be filamentous, but in some cases non-filamentous clusters may also appear.

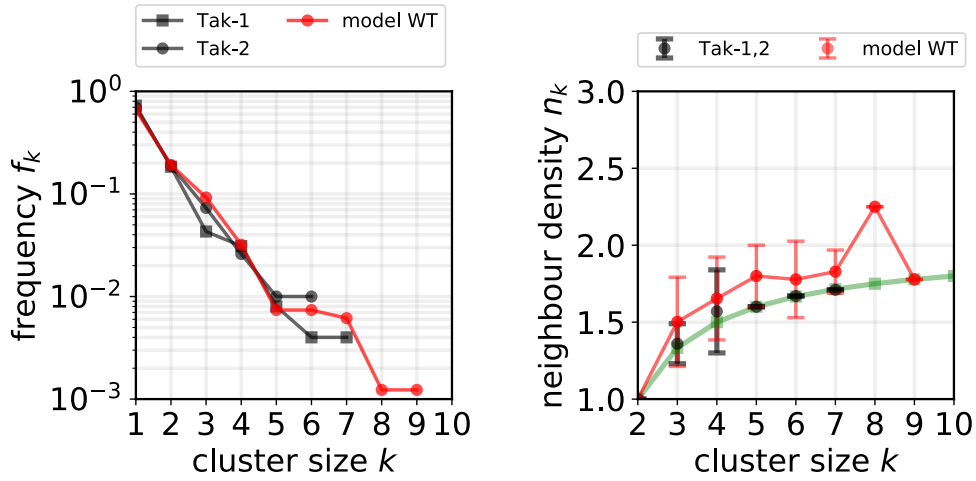



**Figure 6.13: Comparison of $f_k$ and $n_k$ between the model and experiments in [Thamm et al., 2020] in the WT.** Frequency of cluster sizes and average number of neighbours in the model (red) compared with their experimental counterparts in the WT (black). The red curve in the right panel represents the average of $n_k$ over all simulations. Results obtained from $N = 40$ simulations in a $14 \times 14$ hexagonal lattice, similar to the experiments in [Thamm et al., 2020]. Parameters values are those shown in Table 6.1. Initial conditions are $R_{ij}|_{t=0} = R_0\mathcal{U}[0,1]$, with $R_0 = 0.67$.

The results of our model are consistent with experimental observation of both $f_k$ and $n_k$. In particular, we observe values of $n_k$ slightly higher than those in the experiments. This reflects the fact that most rhizoid precursor clusters appearing in the simulations are filamentous, but some still have cells with more than two precursor neighbours. The presence of non-filamentous clusters

of size 3 and 4 in the experiments suggest that larger, non-filamentous clusters could still appear. The filamentous nature of large clusters observed in the experiments of [Thamm et al., 2020] might be related to low statistics, as the total number of such clusters is low—four 5-clusters, three 6-clusters and a single 7-cluster.

With the model we can also simulate mutant phenotypes, by tuning the parameters controlling each interaction. For example, $frh1$ and $rsl1$ loss of function mutants can be implemented by lowering the values of $\gamma_0$ (and/or $\gamma$) and $\alpha_0$, respectively. Gain of function mutants, on the other hand, can be implemented by increasing the same parameters. In Figure 6.14 we show the patterns obtained in these mutants. In $rsl1^{lof}$ and $FRH1^{GOF}$ mutants, since the activity of RSL1 decreases, few or no rhizoid precursors are able to emerge. The $rsl1^{lof}$ loss of function mutant is implemented by setting $\alpha_0 = 0$, i.e., RSL1 is not produced. Therefore, as RSL1 is a rhizoid-promoting factor, no rhizoids can appear in this mutant. In the case of the $FRH1^{GOF}$ mutant we set $\gamma = 3$ (contrasting with $\gamma = 0.6$ in the WT), such that cell competition induced by lateral inhibition increases, but not to the point of repressing all rhizoids.This is consistent with experimental results of $FRH1^{GOF}$ mutants, where a small fraction of rhizoid precursors can still be observed (see Figure 6.2). In the model, for larger values of $\gamma$, no rhizoids can appear, as there is too much inhibition. In $RSL1^{GOF}$ and $frh1^{lof}$, since the activity of RSL1 increases, the density of rhizoid precursors also increases. In $frh1^{lof}$ mutants we set $\gamma_0 = \gamma = 0$, and therefore the system becomes spatially decoupled. In this modelled mutant, the decision between rhizoid precursor and epidermal cell is cell-autonomous, and will only depend on the initial value of $R$ in each cell, just as in the null model. In the $RSL1^{GOF}$ mutant, conversely, even though the density of rhizoid precursors becomes larger, lateral inhibition is still acting, as FRH1 is highly activated by RSL1. However, in this case the threshold for inhibition is larger, and rhizoid precursor cells can form larger and more compact clusters.

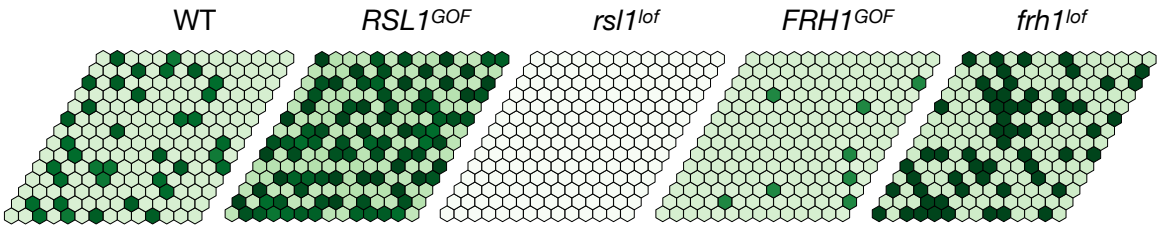



**Figure 6.14: Patterns in WT and mutant phenotypes obtained with the model.** WT simulation obtained with parameters as in Table 6.1. For the mutants, $\alpha_0$, $\gamma_0$ and $\gamma$ are modified with respect to the original parameters. We $\alpha_0 = 0.3$ for $RSL1^{GOF}$; $\alpha_0 = 0$ in $rsl1^{lof}$; $\gamma = 3$ in $FRH1^{GOF}$; and $\gamma_0 = \gamma = 0$ in $frh1^{lof}$. All initial conditions are set to $R_{ij}|_{t=0} = R_0\mathcal{U}[0, 1]$, with $R_0 = 0.67$.

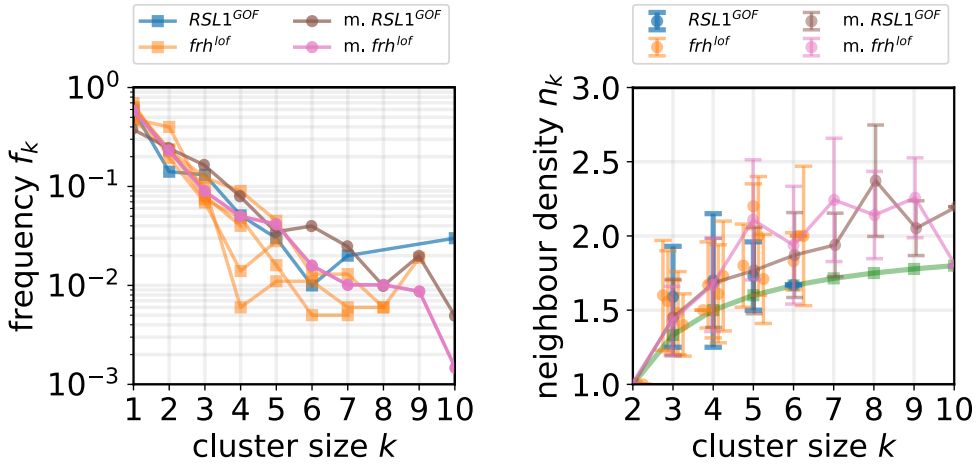



**Figure 6.15: Comparison of $f_k$ and $n_k$ between the model and experiments in [Thamm et al., 2020] in mutants.** From the default parameter set in Table 6.1, we take $\alpha_0 = 0.25$ to model $RSL1^{GOF}$ mutants and $\gamma_0 = \gamma = 0$ to model $frh1^{lof}$ mutants. For $RSL1^{GOF}$ mutants we perform $N = 10$ simulations, similar to the number gemmae in the experiments of [Thamm et al., 2020]. For $frh1^{lof}$ mutants, $N = 40$, again similar to experiments of [Thamm et al., 2020]. Initial conditions are $R_{ij}|_{t=0} = R_0\mathcal{U}[0, 1]$, with $R_0 = 0.67$ in $RSL1^{GOF}$ mutants and $R_0 = 0.57$ in $frh1^{lof}$ mutants.

## 6.4 A balance between randomness and lateral-inhibition by diffusion

The way patterns are created in this model differs from the cellular automata model proposed in [Thamm et al., 2020]. While in their model clusters are created sequentially, by allowing new rhizoid precursors to emerge from existing clusters given a set of rules, the clusters exhibited by our model are formed *dynamically* as a consequence of the interactions in the reaction-diffusion model. As we have seen, the initial conditions of $R_{ij}(t)$ set the initial density of rhizoid precursor cells, whose state later becomes modified by the lateral inhibition of FRH1, turning off cells that would otherwise become rhizoid precursors. This initial distribution is assumed to be random, so that there is variability in the values of $R$. Therefore, rhizoid precursor patterns obtained by the model appear through the interplay between random initial conditions and lateral inhibition by diffusion.

### 6.4.1 Model predictions

The temporal evolution of typical rhizoid patterns in the WT is shown in Figure 6.16. Starting with an initial distribution of $R_{ij}$, cells that initially have high values of $R$ tend to develop into rhizoid precursors, while those with low $R$ become epidermal cells. If by chance there are some cells with high initial $R$ that happen to have neighbours also with high $R$, lateral inhibition may turn off

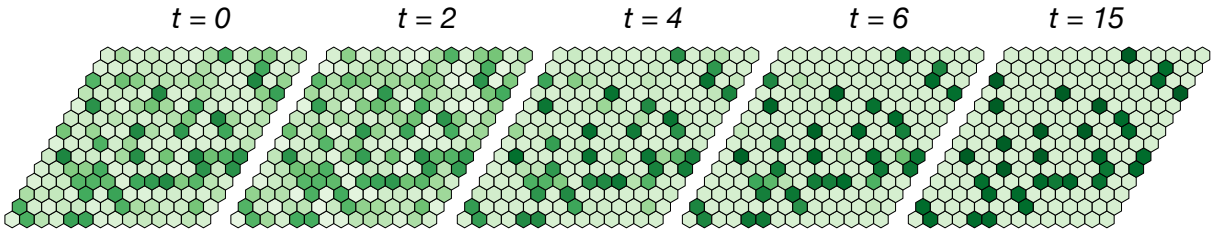



**Figure 6.16: Time evolution of rhizoid precursor patterns.** Computational results of the dynamics of rhizoid precursor patterns in the WT. The system begins with a random initial distribution of $R_{ij}$, which becomes progressively specified due to the action of bistability on one hand, and lateral inhibition on the other, preventing cells which would become specified from reaching the ON state. Parameters as in Table 6.1. Initial conditions $R_{ij}|_{t=0} = R_0\mathcal{U}[0,1]$, with $R_0 = 0.67$.

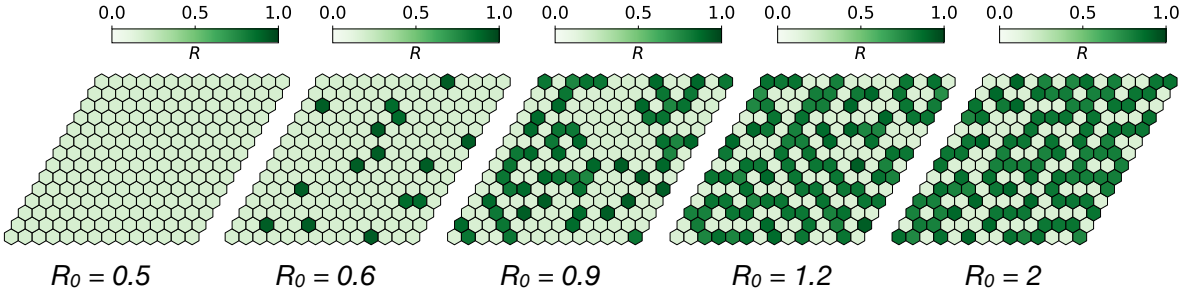



**Figure 6.17: Rhizoid precursor patterns for different values of $R_0$.** The final patterns highly depend on the initial conditions. For small $R_0$, rhizoid precursor cells do not appear, but they progressively emerge as $R_0$ increases. For values of $R_0$ larger than $\sim 1.2$, the structure of the final patterns are similar, as the influence of lateral inhibition prevents higher densities of rhizoid precursors. Parameters as in Table 6.1. Initial conditions are implemented as $R_{ij}|_{t=0} = R_0\mathcal{U}[0,1]$, where the factor $R_0$ changes from panel to panel.

some of these cells, which would otherwise become rhizoid precursors. Depending on the values of the parameters and initial conditions, more or less adjacent cells will be able to remain rhizoid precursors without lateral inhibition turning off any of them, as the threshold for inactivation will be different.

In our model, randomness introduced via the initial conditions plays an important role in the specification of rhizoid precursors. In Figure 6.17 we show the different patterns obtained when initial conditions are implemented via $R_{ij}|_{t=0} = R_0\mathcal{U}[0,1]$, where $R_0$ changes from panel to panel. For the parameter values in Table 6.1, both epidermal and rhizoid precursor states are stable, and so the final fate a cell will acquire will depend both on initial conditions and the strength of lateral inhibition it receives from its neighbours. When $R_0$ is small, all cells develop as epidermal, as the homogeneous state where all cells have low $R$ is always stable. This can be formally seen by studying Equation 6.5 through linear stability analysis (not shown). Larger initial values of $R_0$ are needed for some cells to leave the basin of attraction of the epidermal state and reach the high $R$, rhizoid precursor state. As $R_0$ increases, more and more

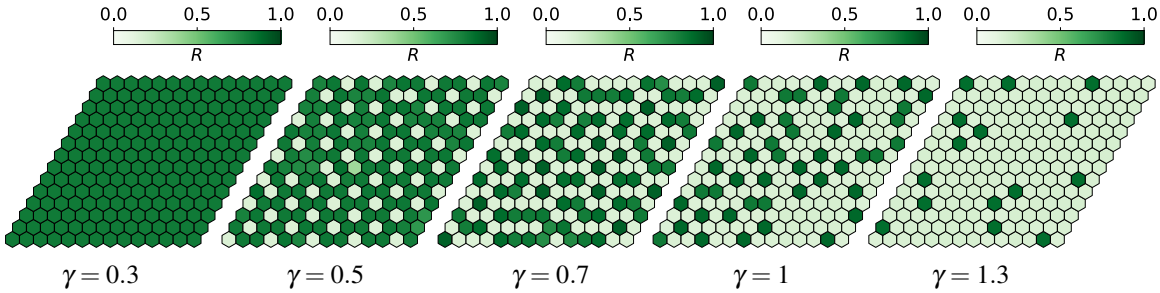



**Figure 6.18: Distinct patterns emerge as the coupling strength changes.** Changing the coupling strength via the parameter $\gamma$ modulates the kind of patterns the system can display. For low $\gamma$ and initial conditions close to the high $R$ homogeneous state ($R_{ij}|_{t=0} = 1 + 0.1\mathcal{U}[0, 1]$) the system remains in that state, as it is stable. As $\gamma$ increases, the homogeneous state loses stability and patterns with different rhizoid precursor densities and cluster structures appear. Parameters as in Table 6.1.

cells become rhizoid precursors. As the density of these precursors increases, however, the influence of lateral inhibition becomes noticeable, leading to the emergence of filamentous clusters. Notice that above a certain values of $R_0$ the structure of rhizoid precursor patterns no longer changes (in Figure 6.17, compare panel with $R_0 = 1.2$ and $R_0 = 2$). This happens because the homogeneous state where all cells becomes rhizoids (high $R$) is not stable in this parameter regime. When initial conditions are too high, cell-to-cell competition through lateral inhibition is so strong that a large proportion of cells eventually end up with low $R$, forming the characteristically filamentous clusters.

This can be seen more clearly by fixing the initial conditions in this high $R$ homogeneous state, adding a small spatial variability in initial conditions, and see the final patterns for different values $\gamma$, the parameter controlling the coupling strength (Figure 6.18). For small $\gamma$ ($\gamma = 0.3$), since lateral inhibition is small, all cells remain rhizoid precursors, as the homogeneous state with all cells having high $R$ is stable. As $\gamma$ increases and lateral inhibition becomes larger ($\gamma = 0.5$), this homogeneous state loses stability, generating salt-and-pepper patterns where isolated epidermal cells are surrounded by rhizoid precursors, with a characteristic periodicity. As $\gamma$ increases further, patterns consist on filamentous clusters and isolated rhizoid precursors ($\gamma = 0.7$), which progressively become less and less common ($\gamma = 1$), until only isolated rhizoid precursors can appear ($\gamma = 1.3$). For still larger values of $\gamma$, the only stable state corresponds to all cells having low $R$, i.e., all cells become epidermal.

For completeness, in Figure 6.19 we show how the system behaves when there is no cell-to-cell interaction. As described in the previous section, when coupling is absent—Equation 6.6, when we drop out the brackets in Equation 6.5—, the decision to become rhizoid precursor or epidermal cell is cell-autonomous, just as in the null model, with initial conditions controlling the final fate of each cell. As $R_0$ increases, the proportion of rhizoid precursors becomes larger, just as it happened in the null model when the probability $p$ increased. This means that

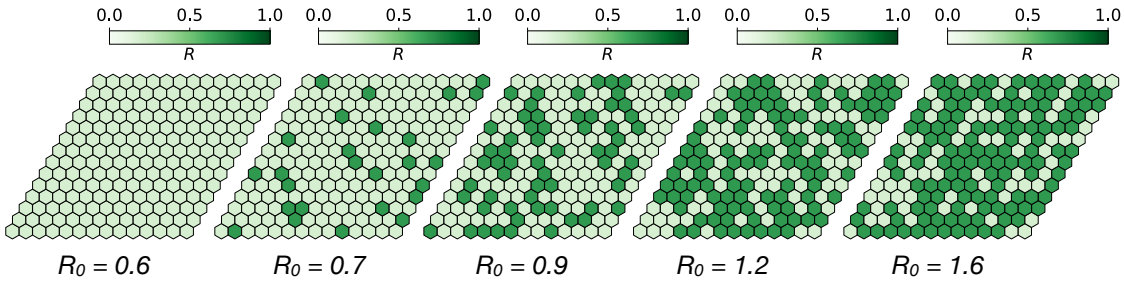



**Figure 6.19: The uncoupled system behaves as the null model.** If the system is uncoupled, i.e. there are no interactions between cells, the fate of each cell only depends on initial conditions, as the system is in the bistable regime. Parameters as in Table 6.1. Initial conditions implemented via $R_{ij}|_{t=0} = R_0\mathcal{U}[0,1]$.

the system is bistable even though inhibition of RSL1 by FRH1 still happens at the level of single cells.

The activator-inhibitor model has clear predictions concerning the frequency of cluster types $F_r^k$ and the fraction $g_l^k$ (as defined in Section 6.2). If lateral inhibition is indeed influencing the local structure of rhizoid clusters, we expect the proportion of filamentous clusters in the activator-inhibitor model to be larger than in the null model. Moreover, rhizoid precursors will tend to have few precursor neighbours compared to those in the null model. In Figure 6.20 and Figure 6.21 we show these results for 3, 4 and 5-clusters, were the predictions of the activator-inhibitor model (model) are compared side-by-side with those corresponding to all clusters being filamentous (fil.), those predicted by the null model (null), and those predicted by the activator-inhibitor model but without diffusive cell-to-cell interactions (model no diff.). In each case, the results have been obtained by simulating $N = 40$ gemmae lattices. Strikingly, both in the activator-inhibitor model, the model without diffusion and in the null model, clusters of size 3 have similar values for the fraction of clusters types and the fraction of rhizoid precursors with 1 or 2 precursor neighbours. This means that for these clusters lateral inhibition is not strong enough to induce any change in their structure, thus making their statistical properties effectively random. Conversely, for clusters of 4 and 5, the activator-inhibitor model predicts that these fractions will fall closer to the filamentous category, reflecting the effect of lateral inhibition in preventing clumped aggregations of many cells. In the case where there is no cell-to-cell interactions, these fractions again resemble those of null model, as expected.

These results give us some hints about how rhizoid precursors may interact—or, in other words, which are the rules—to allow the formation of the patterns we observe experimentally. First, it tells us that a rhizoid precursor cell can still remain a rhizoid precursor even in the presence of two precursor cells as its neighbours. This contrasts with the modelling approach of [Thamm et al., 2020], where a specific rule prevent rhizoids from having more than two rhizoid neighbours. Second, there seems to be a maximum number of neighbouring cells

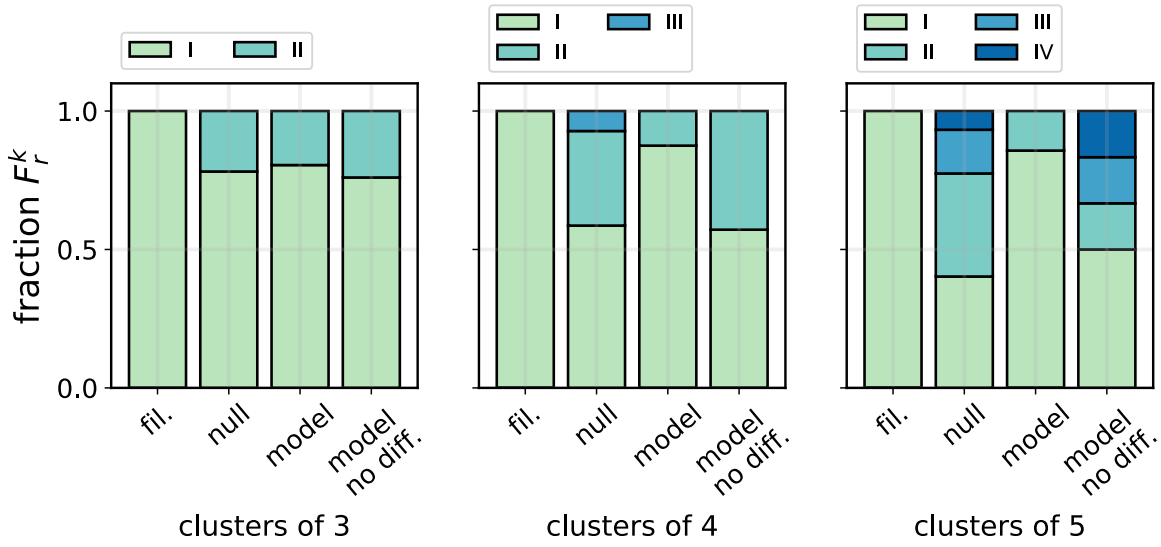



**Figure 6.20: Fraction of cluster types $F_r^k$ for 3, 4 and 5-clusters.** Comparison of the fractions of cluster types between the filamentous model (fil.), the null model (null), the activator-inhibitor model (model) and the activator inhibitor model without the diffusive cell-to-cell coupling (model no diff.). For the null model, $p = 0.15$. For the dynamical model, initial conditions are implemented with $R_0 = 0.67$.

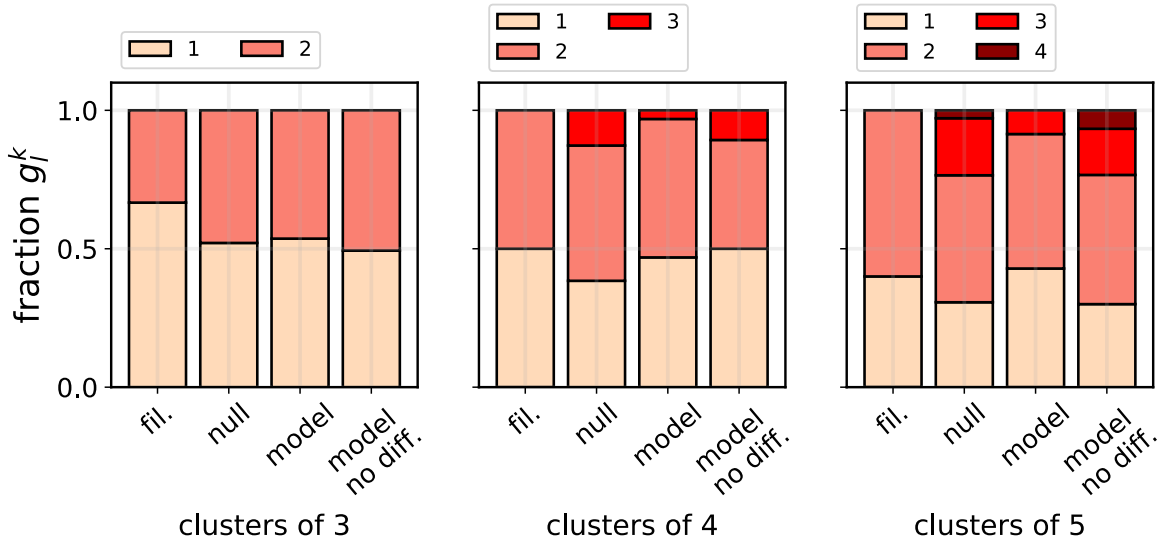



**Figure 6.21: Fraction of cells with $l$ neighbours $g_l^k$ for 3, 4 and 5-clusters.** Comparison of the fraction of precursor cells with different number of precursor neighbours for each cluster size between the filamentous model (fil.), the null model (null), the activator-inhibitor model (model) and the activator inhibitor model without the diffusive cell-to-cell coupling (model no diff.). For the null model, $p = 0.15$. For the dynamical model, initial conditions are implemented with $R_0 = 0.67$.

at which point a cell cannot be a rhizoid precursor, as previously suggested by [Thamm et al., 2020]. In particular, the model does not generate any 5-cluster of type IV (see Figure 6.7), suggesting that these are not stable.

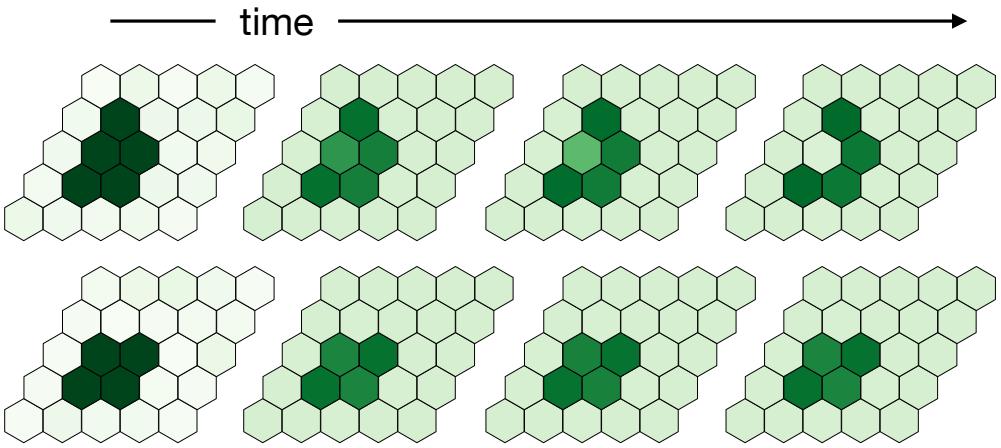



**Figure 6.22: Large compact clusters are not stable.** The model predicts that cells with more than 3 rhizoid precursor neighbours will not be able to become rhizoid precursors. Initial conditions are $R_{ij}|_{t=0} = 1 + R_0\mathcal{U}[0,1]$ for cells in the clusters, with $R_0 = 0.01$, and $R_{ij}|_{t=0} = 0$ for cells outside the clusters. Parameters as in Table 6.1.

Indeed, if we test the stability of these clusters when isolated from any other cluster, we see that 5-clusters of type IV are not stable, and turn into a filamentous 4-cluster. Therefore, the model predicts that cells with more than 3 rhizoid precursor neighbours will not be able to become rhizoid precursors. However, we must bear in mind that clusters do not appear isolated, but surrounded by other cells with variable values of $R$, all of which might affect to the final outcome of the cluster.

### 6.4.2 Experiments support the model predictions

To further compare the predictions of our model with experiments, our collaborators generated additional data of rhizoid precursor distributions by growing Tak-1 (WT) gemmae and staining chloroplasts with a chlorophyll autofluorescense dye. The goal of performing these experiments is twofold: first, with these data we will be able to compute not only the cluster-size distribution $f_k$ and the mean neighbour density $n_k$, but the fractions $F_r^k$ and $g_l^k$ as well; second, to have sufficient cluster statistics, thus allowing proper comparison between the activator-inhibitor model and the experiments. In Figure 6.23 we show 3 examples of such gemmae, where rhizoid precursors appear as dark cells—as they lack chloroplasts—contrasting with the bright, purple epidermal cells. The small, dark cells in gemmae boundaries are not rhizoid precursors, but oil body cells.

By plotting $f_k$ and $n_k$, we see that our data are consistent with that of [Thamm et al., 2020], as shown in Figure 6.24, although in our case not all clusters of 4 and 5 are filamentous. We can now make use of these experiments to compute the experimental values of $F_r^k$ and $g_l^k$, which will give us information about the local properties of the clusters.

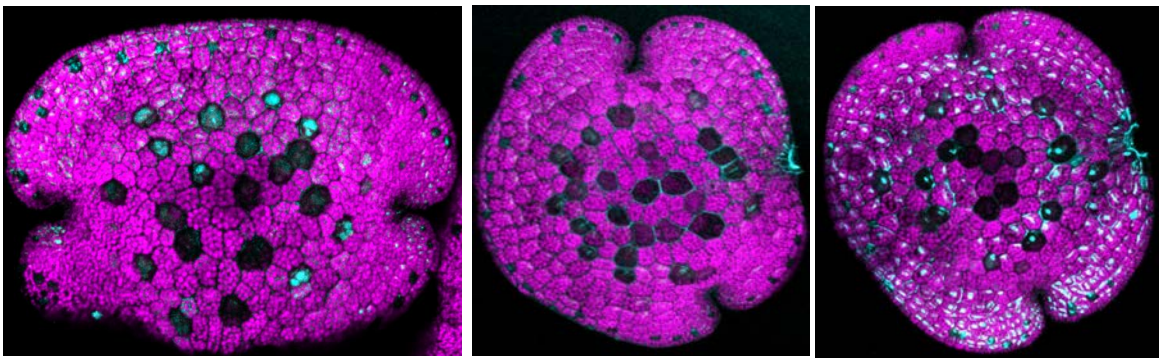


**Figure 6.23: Three examples of Tak-1 gemmae.** Our collaborators generated 41 gemmas distributed among 5 independent replicas. We obtained a total of 630 clusters, distributed in 441 individual cells, 120 clusters of 2 cells, 37 clusters of 3 cells, 19 clusters of 4 cells, 7 clusters of 5 cells, 3 clusters of 6 cells, 2 clusters of 8 cells and a single cluster of 9 cells.

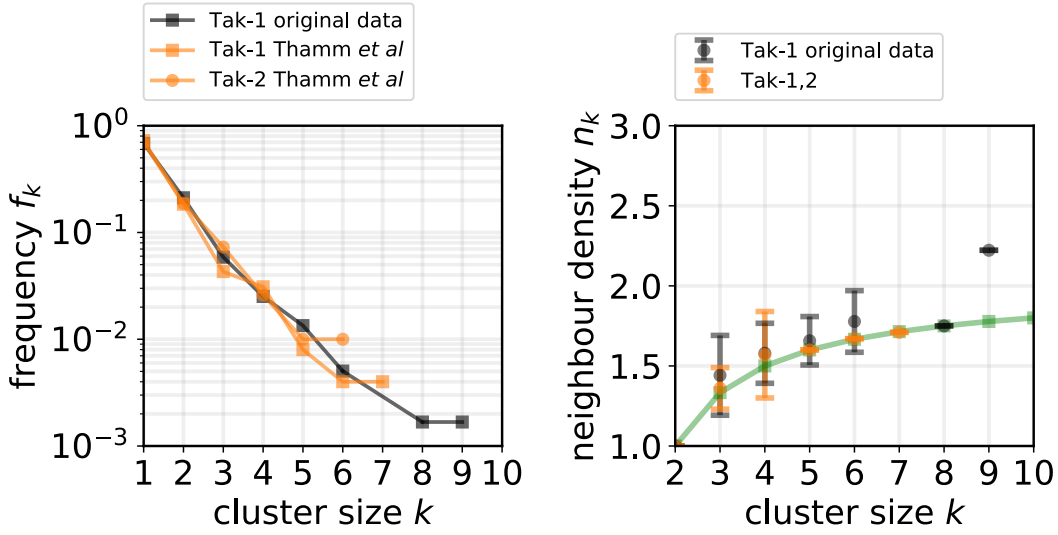



**Figure 6.24: Comparison between data from [Thamm et al., 2020] and data from our collaborators.** Data from our collaborators is consistent with the data presented in [Thamm et al., 2020]. However, it reveals that not all large clusters are filamentous, and some are composed of cells with more than two neighbours, as inferred by the deviation from the curve $2-2/k$. This contrasts with previously published data, where all 5, 6 and 7-clusters were filamentous.

By simulating many lattices with this parameter set, we can compare the results of the model with the experiments. As we see in Figure 6.25, the results of the simulations in this parameter regime fit very well both the experimental cluster-size distribution $f_k$ and the neighbour density $n_k$. Moreover, by comparing the fraction of cluster types $F_r^k$ and the fraction of cells with $l$ neighbours $g_l^k$ in 3,4 and 5-clusters, we see that the model also recapitulates very well experimental results (Figure 6.26 and Figure 6.27). Notice that the model predicts that $g_l^k$ for 3-clusters behaves as in the null model, while for clusters of 4 and 5 it falls closer to the filamentous regime. More importantly, while in

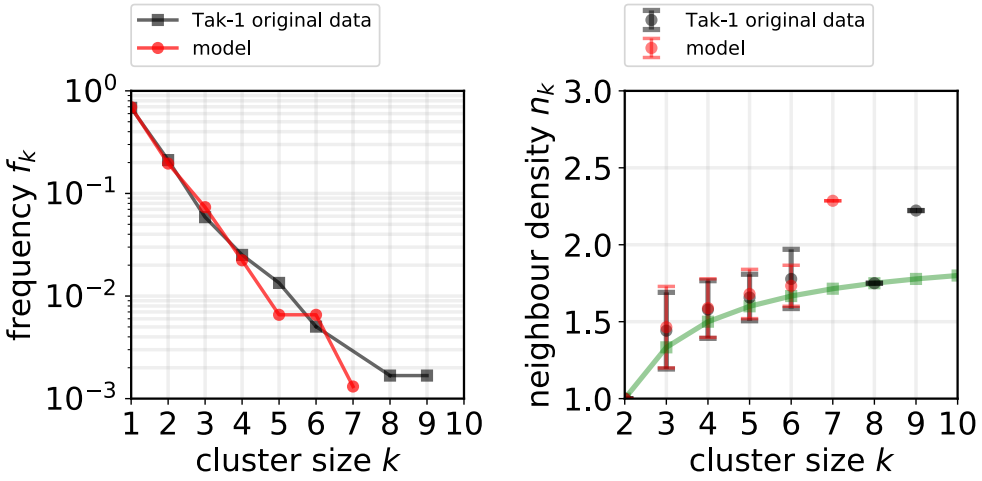



**Figure 6.25: Simulated cluster-size distribution and average neighbour density.** Frequency of cluster sizes and average number of neighbours in the model (red) compared with their experimental counterparts in the WT (black). The area of the circles represent the proportion of clusters of each type only for clusters of size 3, 4 and 5. The red curve in the right panel represents the average of $n_k$ over all simulations. The numbers above the circles represent the total number of clusters for each size. Results come from $N = 40$ simulations in a $14 \times 14$ hexagonal lattice with the parameters of Table 6.1. Initial conditions are implemented with $R_0 = 0.67$.

the null model clusters of type III and VI can be observed, they do not appear in the dynamical model[1]. Remarkably, this is just what we see in the experiments. However, the presence of precursors with three precursor neighbours in the experiments and in the model contrasts with the impossibility of these configurations in the filamentous case. Altogether, the model suggests—and so far the experiments validate—that rhizoids precursors patterns in the WT are generated through the contribution of two main forces: randomness caused by different initial conditions (which may come from heterogeneity in the cellular tissue of the gemma epidermis) and lateral inhibition due to the interactions between RSL1 and FRH1.

The data from our collaborators reveals new features which can not be inferred by only looking at the data in [Thamm et al., 2020]. In particular, while both datasets include clusters of 3 and 4 cells which are not filamentous, our data shows that this also happens for larger clusters, contrasting with Thamm's data where all clusters of 5, 6 and 7 cells were filamentous in the WT Figure 6.24. This tells us that, while clusters do tend to be filamentous—i.e. cells can have two neighbours without being turned OFF—there is no rule preventing the appearance of non-filamentous clusters, where cells have more than two neighbours.

[1] In fact, there is no rule preventing such clusters to appear, but the probability of observing them in a small sample of gemmae ($N = 40$ in the simulations, $N = 41$ in our experiments) is very low.

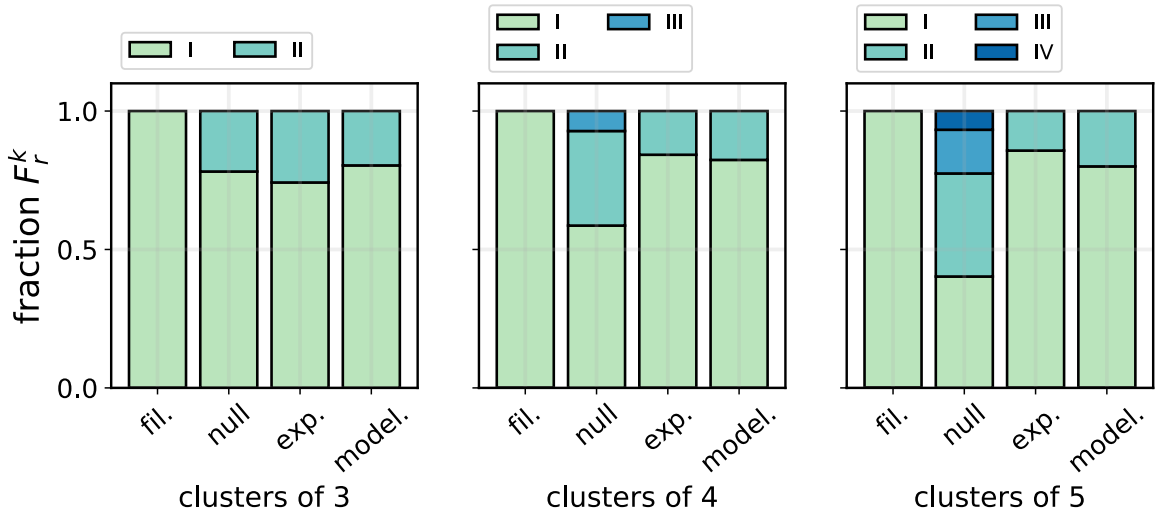



**Figure 6.26: Fraction of cluster types $F_r^k$ for 3, 4 and 5-clusters.** Comparison of the fraction cluster types for each cluster size between the filamentous model, the null model, experiments and the dynamical model. Results come from the same simulations as in Figure 6.25. For the null model, $p = 0.15$. For the dynamical model, initial conditions are implemented with $R_0 = 0.67$.

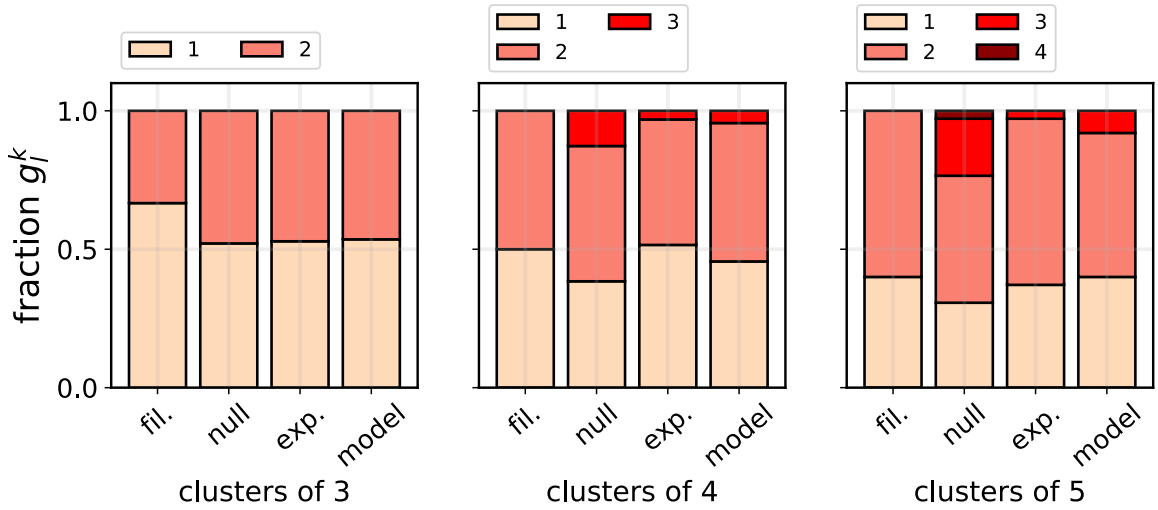



**Figure 6.27: Fraction of rhizoid precursors with $l$ rhizoid precursor neighbours $g_l^k$ for 3,4 and 5-clusters.** Comparison between the filamentous model, the null model, experiments and the dynamical model. Results come from the same simulations as in Figure 6.25. For the null model, $p = 0.15$. For the dynamical model, initial conditions are implemented with $R_0 = 0.67$.

We do not see, however, any cell with more than three neighbours, suggesting that a threshold of lateral inhibition at which a surrounded cell is no longer able to remain ON is 3 rhizoid neighbours. For example, in Figure 6.28A we show a cluster of 6 precursor cells with three of them having three precursor neighbours, far from being filamentous but still stable. For the chosen param-

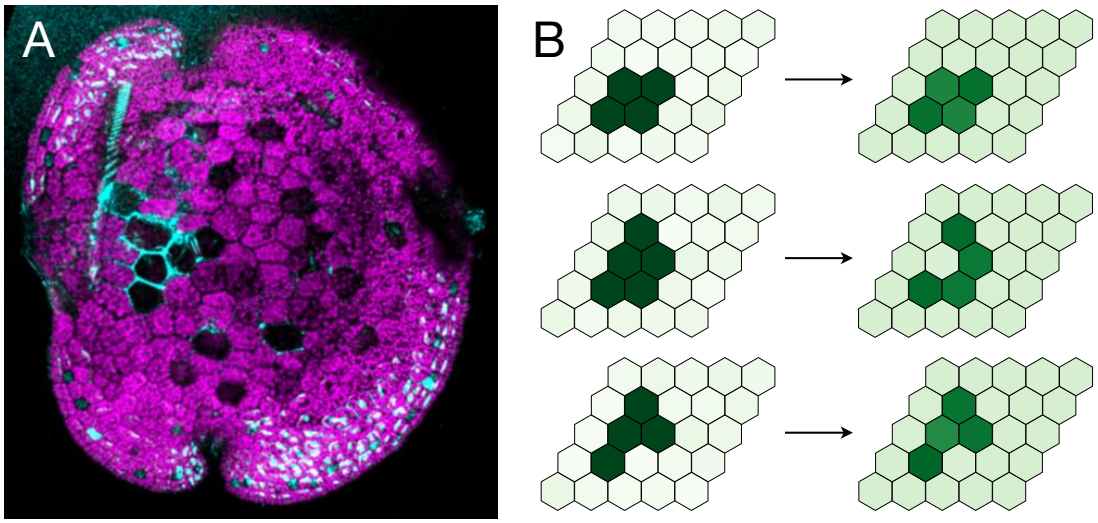



**Figure 6.28: Stability of clusters. A)** A non-filamentous cluster of six cells, with three of them having three rhizoid neighbours. **B)** Time-evolution of some clusters obtained with the model with parameters as in Table 6.1, showing how cells with four neighbours are turned off due to lateral inhibition, while cells with three neighbours can remain rhizoid precursors. No cells with more than three neighbours have been observed in experimental data.

eter values Table 6.1, this rule holds in our simulations. In Figure 6.28B we see that with these parameters, while a compact 4-cluster, where two precursor cells have three neighbours and the other two have two neighbours is stable, a 5-cluster created by adding an extra cell makes the surrounded cell unstable, leading to a filamentous 4-cluster. In contrast, a 4-cluster with only one cell with three neighbours, two cells with two neighbours and a cell with only one neighbour remains stable. Due to the low density of rhizoid precursors, large, non-filamentous clusters will appear with very low frequency, but as shown in Figure 6.28, their stability will depend on their particular shape, in some cases leading to filamentous structures. Therefore, even though some non-filamentous clusters are stable, the explicit dynamics of the system inevitably favours filaments.

## 6.5 Discussion

In this chapter, we have shown that a simple mathematical model based on a RSL1 positive feedback loop and a negative feedback between RSL1 and the FRH1 miRNA is sufficient to explain the formation of rhizoid patterns in the *Marchantia* gemma epidermis. The model is able to predict both the rhizoid distributions for WT plants as well as *frh1* loss of function and RSL1 overexpressor mutants, in agreement with experimental observations [Thamm et al., 2020]. While several interactions such as the activation of FRH1 by RSL1 and the repression of RSL1 by FRH1 have already been described elsewhere [Honkanen et al., 2018, Thamm et al., 2020], our model advances the presence

of a new regulation, namely a positive feedback loop in the activity of RSL1, which is able to generate bistability in epidermal cell states. Crucially, this bistability is key for understanding the spatial distribution of rhizoid precursors observed experimentally, which have a strong random component. From this initially random distribution mediated by the RSL1 bistability, the movement of FRH1 from cell to cell acts by turning off cells with too many precursor neighbours, depriving them from an otherwise rhizoid fate. This self-activation plus lateral inhibition mechanism ultimately leads to an over-representation of small clusters, together with larger clusters that tend to be filamentous.

The simplification of the mathematical model from three variables to one, although useful for analysing the system—as it reduces the number of parameters and initial conditions that have to be specified—, comes with its associated drawbacks. For instance, simulations of the model show that in order to obtain rhizoid precursor distributions with the statistical characteristics of the experiments, the initial distribution of RSL1 must already determine which cells will become rhizoids—those with initially high RSL1. Simulations of the three-variable model show that rhizoid precursor distributions similar to the experiments can be obtained without rhizoids being specified by their initial value of RSL1, but instead form after a transient time where both RSL1 mRNA, RSL1 proteins and FRH1 interplay.

For our model to make sense, FRH1 must have the ability to move between cells. While the intercellular transport of FRH1 has not yet been observed, its status as a microRNA is highly suggestive for such a process to occur. Indeed, while it is not known whether intercellular miRNA movement is widespread among plants, many miRNA have already been observed to act far away from its original expression domain [Chitwood and Timmermans, 2010, Skopelitis et al., 2018]. For example, in the *Arabidopsis* root miR165/6 has been shown to act downstream the SHR/SCR pathway to non-cell autonomously control the activity of class III HD-ZIP genes, by moving from the endodermis to the stele and determining cellular fates therein [Carlsbecker et al., 2010, Miyashima et al., 2011]. A gradient of miR166 has also been shown to confer positional information to generate sharp boundaries of activity in developing leaf primordia [Skopelitis et al., 2017]. In the *Arabidopsis* shoot apical meristem, miR394 has been shown to move from the epidermal cells to the stem cell niche to repress the activity of LCR, which in turn controls of the WUS/CLV3 module, thus regulating the activity of stem cells as the tip grows [Knauer et al., 2013].

Notice that the spatial coupling between cells is implemented via the movement of the miRNA FRH1. For simplicity, the intracellular mobility of FRH1 is modelled as passive diffusion, though other mechanisms may mediate its range and specificity [Chitwood and Timmermans, 2010]. Indeed, microRNAs in plants have been shown to act non-cell autonomously, acting in a strikingly similar way morphogen gradients do in order to generate reliable patterns [Skopelitis et al., 2017, Skopelitis et al., 2018, Chitwood et al., 2009]. Other forms of intra-

cellular mobility such as exosome transport, could for example generate bursts of miRNA activity in recipient cells, constituting an important source of heterogeneity in the otherwise linear nature of passive diffusion, potentially generating much richer pattern configurations [Liu and Chen, 2018].

In *Marchantia*, the functions of microRNAs are less known. We now know that only seven microRNAs are conserved across land plants [Lin and Bowman, 2018], so little can be drawn from *Arabidopsis* studies, where most of the research on small RNAs has been focused on. Only few microRNAs in *Marchantia* have known targets [Lin et al., 2016]. For example, MpmiR166a targets Mp$C3HDZ1$, a class III HD-ZIP protein, but its role is yet to be uncovered [Lin et al., 2016]. The MpmiR160 targets the auxin response factor Mp$ARF3$ [Lin et al., 2016], and has been shown to control the transition to reproductive development, including processes such as gemmae and air chamber formation, and the development of rhizoids [Flores-Sandoval et al., 2018, Mutte et al., 2018]. More recently, the microRNA MpmiR529c has been shown to target $SPL$ transcription factors, also involved in the development of reproductive structures [Tsuzuki et al., 2019, Kohchi et al., 2021].

The general mechanism of cell specification mediated by lateral inhibition induced by mobile factors is not an exclusive feature of *Marchantia* rhizoids. In *Arabidopsis*, the spatial distribution of leaf trichomes, root hairs and stomata have also been shown to involve mechanisms similar to lateral inhibition, where mobile factors play a prominent role [Torii, 2012, Horst et al., 2015]. The specification of rhizoid precursors represents yet another instance of such mechanisms.

The value of having an uniformly distributed array of specialized cells can readily be envisaged. As rhizoids function to anchor the plant to the soil, they provide robustness in the face of external disturbances such as wind or floods. A uniform distribution of rhizoids also assures an even distribution of resources (water and nutrients) across the plant's epidermis, deviations from which would lead to asymmetries in their allocation. How evolution has led to these specific distributions is hard to answer. One could argue that an optimization process is taking place, where rhizoid formation is spatially organized to optimize surface covering, while maintaining a specific proportion of rhizoid/epidermal cells to avoid the energetic costs of building rhizoids. Thus, a trade-off between energy expenditure and resource allocation would be at play. However, we must take caution when assigning precise evolutionary explanations to such specific traits—explanations which to this day, as many evolutionary explanations, remain untested—as they may fall under the category of what Rudiyard Kipling originally called—and Stephen J. Gould later appropiated and popularized—"just so stories", or narratives for evolutionary adaptations which are appealing but untestable [Gould, 1978]. Alternatively, this kind of patterning might by a side-effect of a yet unrecognized process which has been subject to adaptive selection, thus deeming the specific distribution of rhizoids an evolutionary

spandrel [Gould and Lewontin, 1979].

Several questions thus come to mind in order to tackle such problems. For instance, are similar mechanisms conserved among bryophytes? Do other closely related liverworts such as *Conocephalum conicum* or *Blasia pusilla* display similar types of rhizoid distributions? As of today, rhizoid formation in liverworts is still poorly understood, but the recently disclosed mechanisms underlying their development in *Marchantia* lay the first stone to a hopefully burgeoning field, of which the combination of experimental and theoretical work will be essential. Only further exploration with newly emerging model organisms, phylogenetic reconstructions of early land plant lineages, together with a sound theoretical understanding of the signalling pathways underlying their characteristic traits will shed light on the hitherto evolutionary significance in the process of land colonization that took place more that half a billion years ago, and the molecular and physical basis that made such remarkable transition possible.

# Appendix

## 6.A Analytical expressions for $f_k$, $n_k$, $F_r^k$ and $g_l^k$ in the null model

We first need to count all the ways clusters can be arranged in a hexagonal lattice. For example, for clusters of one ON cell, i.e., consisting of isolated cells, the expected proportion in an infinite lattice with probability parameter $p$ is just $P_1 = p(1-p)^6$, as both the ON probability and the probability of the neighbours being OFF must be taken into account. For clusters of two, it is relatively straightforward to show that in a hexagonal lattice, there are only 3 equivalent configurations (Figure 6.6). Again, we need to consider both the probability of 2 ON cells being neighbours, i.e., $p^2$, and the probability that boundary cells of such cluster are OFF, i.e., $(1-p)^8$, because all clusters have a boundary of 8 OFF cells. Therefore the probability of obtaining a 2-cluster is:

$$P_2 = 3p^2(1-p)^8 \tag{6.7}$$

For clusters of 3 ON cells, things get more complicated. There are 11 possible configurations of 3-clusters in a hexagonal lattice (Figure 6.6). Still, configurations now have different shapes and numbers of boundary cells, which must be considered when computing the total proportion. In particular, there are two types of 3-clusters—with either 10 or 9 OFF cells in their boundary—, and so each of their probabilities must be weighted by the number of clusters of each type. We can write the probability of appearance of a 3-cluster as:

$$P_3 = 9p^3(1-p)^{10} + 2p^3(1-p)^9 \tag{6.8}$$

where the numbers 9 and 2 reflect the number of configurations of each type, and the exponents 10 and 9 denote the number of OFF neighbours in their respective boundaries. These quantities allow us to compute the values of $F_r^k$ in the null model with parameter $p$:

$$F_1^3 = \frac{9p^3(1-p)^{10}}{9p^3(1-p)^{10} + 2p^3(1-p)^9}, \quad F_2^3 = \frac{2p^3(1-p)^9}{9p^3(1-p)^{10} + 2p^3(1-p)^9} \tag{6.9}$$

with $F_1^3 + F_2^3 = 1$. Moreover, with these quantities we can write in a concise way the average number of neighbours $n_3$, via the relation:

$$n_3 = \frac{1}{3}(4F_1^3 + 6F_2^3) \tag{6.10}$$

where the values 4 and 6 in front of $F_1^3$ and $F_2^3$ indicate the sum of all neighbours in cells within clusters of type I and II, respectively. We can also write closed-form expressions for $g_1^3$ and $g_2^3$, by counting the proportion of cells with one or two neighbours among all cluster types:

$$g_1^3 = \frac{2}{3}F_1^3, \quad g_2^3 = \frac{1}{3}F_1^3 + F_2^3 \tag{6.11}$$

where the fractions 2/3 and 1/3 represent the proportions of cells with one or two neighbours, respectively, in clusters of type I. Since clusters of type II only have cells with two neighbours, the factor accompanying $F_2^3$ is just 1. Notice that $g_1^3 + g_2^3 = F_1^3 + F_2^3 = 1$, as it must be. A similar procedure allows us to write analytical expressions of $F_r^k$ and $g_l^k$ for 4-clusters, again by counting the number of possible configurations and cluster types of size 4 (Figure 6.6):

$$P_4 = 27p^4(1-p)^{12} + 12p^4(1-p)^{11} + 3p^4(1-p)^{10} + 2p^4(1-p)^{12} \tag{6.12}$$

and therefore

$$F_1^4 = \frac{27p^4(1-p)^{12} + 2p^4(1-p)^{12}}{27p^4(1-p)^{12} + 12p^4(1-p)^{11} + 3p^4(1-p)^{10} + 2p^4(1-p)^{12}} \tag{6.13}$$

$$F_2^4 = \frac{12p^4(1-p)^{11}}{27p^4(1-p)^{12} + 12p^4(1-p)^{11} + 3p^4(1-p)^{10} + 2p^4(1-p)^{12}} \tag{6.14}$$

$$F_3^4 = \frac{3p^4(1-p)^{10}}{27p^4(1-p)^{12} + 12p^4(1-p)^{11} + 3p^4(1-p)^{10} + 2p^4(1-p)^{12}} \tag{6.15}$$

with $F_1^4 + F_2^4 + F_3^4 = 1$. The quantity $n_4$ can be derived from the above expressions through the relation:

$$n_4 = \frac{1}{4}(6F_1^4 + 8F_2^4 + 10F_3^4) \tag{6.16}$$

The fractions of cells with 1, 2 and 3 neighbours can be written as:

$$g_1^4 = \frac{1}{2}F_1^4 + \frac{1}{4}F_2^4, \quad g_2^4 = \frac{1}{2}F_1^4 + \frac{1}{2}F_2^4 + \frac{1}{2}F_3^4, \quad g_3^4 = \frac{1}{4}F_2^4 + \frac{1}{2}F_3^4 \tag{6.17}$$

And again, $g_1^4 + g_2^4 + g_3^4 = 1$. One could in principle go on counting all the

possible configurations of larger clusters. However, clusters of 5 or more are seldom observed in the *Marchantia* gemma epidermis, so proper comparison with experimental data can only be done with 2, 3 and 4-clusters, for which analytical expressions can be obtained, as shown here.

The values of $F_r^k$ and $g_l^k$ in the null model have been computed using these analytical expressions, and have been compared with the simulated results. The similarity between these two results supports the view that the computational implementation of $F_r^k$ and $g_l^k$ is correct.

# Chapter 7

# Diffusion induced lateral inhibition patterns

## Contents


**7.1 Introduction . . . . . 182**
**7.2 The reversible mixed feedback loop . . . . . 185**
7.2.1 Dynamics and stability of fixed points . . . . . 186
7.2.2 The RMFL with intrinsic noise . . . . . 194
**7.3 The diffusively coupled mixed feedback loop . . . . . 195**
7.3.1 Two-cell system . . . . . 197
7.3.2 The RMFL in cellular lattices . . . . . 199
7.3.3 Noise-induced phenomena . . . . . 206
**7.4 Discussion . . . . . 208**


In this chapter, we study a modified version of the mixed feedback loop (MFL) proposed by François and Hakim [François and Hakim, 2005], where two proteins form a complex, and one of them regulates the production of the other. It is well-established that depending on the nature of transcriptional interactions—repression or activation—the MFL can display bistability or oscillations, respectively, as well as monostability in both cases. Contrary to the original formulation of the MFL—where the complex is assumed to form irreversibly—in this modified version we allow for complex reversibility, and find that when the transcriptional regulation is repressive the system can be both monostable, bistable and oscillatory, all without invoking a change in the qualitative nature of gene regulations, namely from transcriptional repression to transcriptional activation. By analyzing the system through linear stability analysis, we find how each regime depends on critical parameters such as transcriptional rates or complex degradation and discuss the relevance of the

multi-functional nature of the circuit. We further study the circuit when the diffusion of the complex is introduced. The introduction of spatial coupling confers a much richer range of spatiotemporal behaviours, many of which can be mapped into processes often encountered in developmental contexts, including the formation of salt-and-pepper patterns akin to those obtained by classic cell-to-cell Notch-Delta lateral inhibition, bulk oscillations, travelling waves and spatial chimeras—states where stable patterns and oscillations coexist in different spatial regions. We study in detail the conditions for these regimes to appear and discuss their relevance for developmental systems. The multiple dynamical regimes displayed by this modified version of the mixed feedback loop encapsulate a major theme in evolutionary developmental biology, namely the harnessing and reusing of already existing molecular components to perform functionally distinct tasks in contextually different stages, as embodied by the notion of evolution as a "tinkerer" [Jacob, 1977].

## 7.1 Introduction

A major goal in developmental systems biology is to understand how gene regulatory networks operate across the organism and over time to reliably specify each particular cell type, tissue, and organ, with the robustness and precision so characteristic of biological forms. At the same time, it aims to reconcile the apparent paradox between such robustness and the remarkable flexibility organisms display for coping with the ever-changing forces of the environment. A recent theme in evolutionary systems biology seeks to understand how this happens at the level of gene regulatory networks, namely how evolution has led to the creation, deletion, or readaptation of network parts to perform distinct tasks.

Today it is commonly accepted that gene regulatory networks display *modularity*, the fact that they are composed of multiple sub-networks—or modules—which function independently (or quasi-independently) of the rest of the network, therefore allowing the dissection of different parts as a way to reconstruct the whole system [Hartwell et al., 1999, Wagner et al., 2007]. The origin of modularity in gene regulatory networks is still debated. Some advocate for modularity being favoured by natural selection, as it endows the network the capacity to evolve [Espinosa-Soto and Wagner, 2010, Wagner and Zhang, 2011, Wagner and Altenberg, 1996], while others propose that it emerges as a side-effect of genome growth and change—as an evolutionary *spandrel*, a phenotypic trait which is a byproduct of a true adaptation [Solé and Valverde, 2006, Gould and Lewontin, 1979] (see also [Clune et al., 2013]).

The finding that gene regulatory networks display modularity has led researchers to delve into the details of how individual modules operate, and what is their role in the global behaviour of the whole network. Large-scale analyses of gene regulatory networks have shown that there are small sub-networks which

are statistically enriched, i.e., their presence in such networks is higher that one would expect were the network completely random. These circuits have been dubbed *network motifs*, and understanding their function has since been one of the main ambitions of systems biology research [Milo et al., 2002a]. Network motifs are sufficiently simple to study their dynamical behaviours mathematically, so that insight can be gained into the function of the whole network through a bottom-up approach. They come in different shapes and colors: feedback circuits such as positive or negative self-regulation, which can act as bistable switches or molecular clocks, respectively [Ferrell, 2014, Tsai et al., 2008]; integral feedbacks which adapt the system in the face of environmental perturbations [Briat et al., 2016, Aoki et al., 2019]; incoherent feed-forward circuits that can detect fold-changes in molecular activity [Goentoro et al., 2009] or accelerate response times [Mangan et al., 2006]; or coherent feed-forward loops that provide fast responses to step-like positive inputs, but induce delays to negative inputs [Mangan et al., 2003], to name a few.

Nonetheless, a network being modular does not imply its constituent modules have single specific functions. In fact, even the simplest genetic circuits are able to display a wide range of dynamical behaviours depending on the external environment or the strength of their intrinsic interactions [Ingram et al., 2006, Payne and Wagner, 2015]. The possibilities offered by synthetic biology to engineer biological circuits both at the level of single cells and multicellular tissues has motivated the study, both theoretical and experimental, of specific circuits displaying *multi-functionality*—the capacity to exhibit multiple dynamical behaviours without changing structure nor adding or removing any of the circuits' elements[1] [Jiménez et al., 2017, Mireles and Conrad, 2018]. These include, for example, circuits that can be bistable or oscillatory depending on the system's parameters [Purcell et al., 2011], or even for the same parameter values [Panovska-Griffiths et al., 2012, Perez-Carrasco et al., 2018], or systems where cellular pattern formation coexists with stable homogeneous states [Formosa-Jordan and Ibañes, 2014, Palau-Ortin et al., 2015]. This notion of multi-functionality challenges a prevalent view in systems biology regarding the relation between a circuits' structure and its presumed function [Ingram et al., 2006]. The correspondence blurs when functions are dependent on the environmental context, as often are in circuits operating at distinct developmental stages. In these situations, both the circuit's topology *and* the environment determine the function, and while a small, isolated circuit can be relatively easy to understand, accurate knowledge about the environment is seldom available.

Therefore, one needs to understand the entire repertoire of dynamical be-

[1] Here we define *function* in terms of the spatiotemporal repertoire of qualitatively different behaviours the system is able to exhibit, such as oscillations, bistability, pattern formation, excitability, etc., although the term has also been used in the same context to refer to the diverse ways a circuit behaves in response to external inputs, as is done, for example, in [Wall et al., 2005].

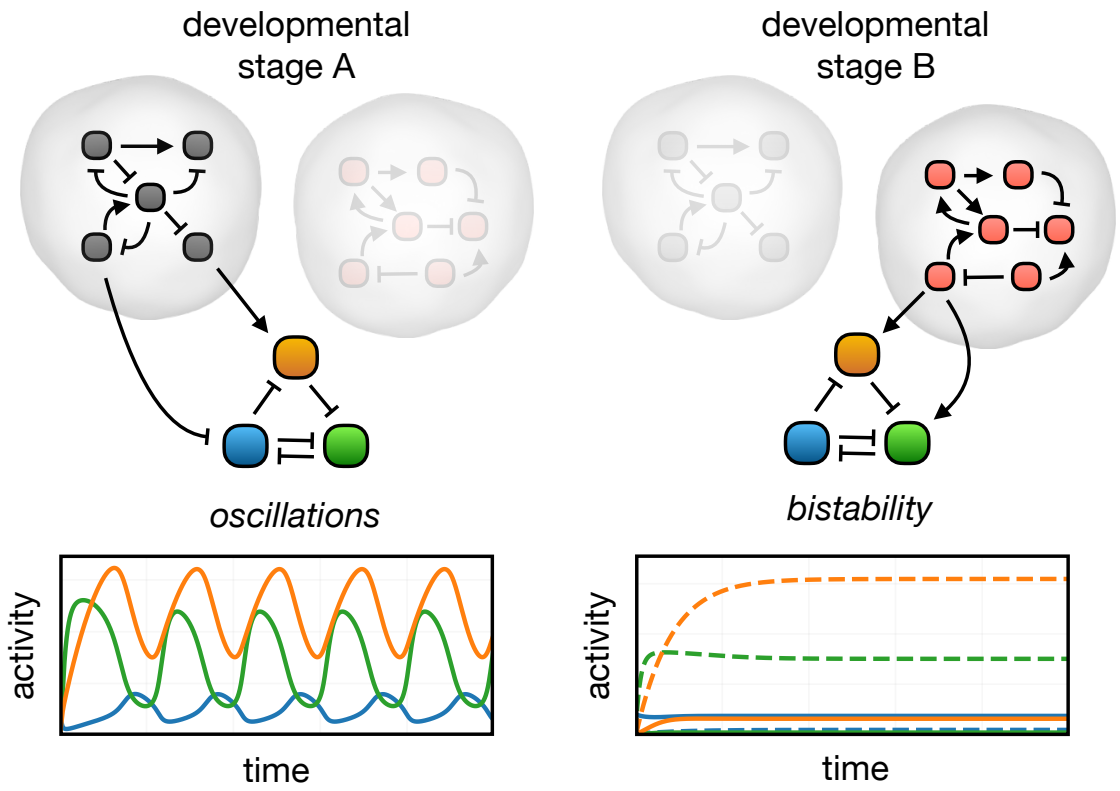



**Figure 7.1: The function of many genetic circuits are context-dependent.** Many circuits in developmental biology display multi-functionality, i.e. their topology allows for several, qualitatively different dynamical regimes. In this diagram, two qualitatively distinct functions—oscillations and bistability—are possible within the AC-DC circuit [Panovska-Griffiths et al., 2012, Perez-Carrasco et al., 2018]. The developmental stage, i.e. the cellular context within which the circuit is embedded, dictates its final function.

haviours to fully specify its role on the behaviour of full gene regulatory networks [Alexander et al., 2009]. Finding minimal motifs capable of exhibiting different functions is essential to understand how gene regulatory networks operate on the whole, as well as for engineering circuits which are efficiently build and easy to manipulate, a task which becomes difficult the larger the circuit, where unwanted and unpredictable interactions can appear [Borkowski et al., 2016].

Our goal in this next section is to introduce and study in detail one such minimal network motif, the reversible mixed feedback loop (RMFL), a representative example of a circuit which is itself not decomposable, as it cannot be subdivided without losing its functions, but is functionally modular, i.e. its repertoire of dynamical behaviours—monostabilty, bistability and oscillations—can be easily partitioned. Is based on the mixed feedback loop (MFL) proposed by François and Hakim [François and Hakim, 2005], a network motif found to be widespread in gene networks from bacteria, yeast and animals [Yeger-Lotem et al., 2004], consisting of the transcriptional regulation of a gene by another, together with the binding and subsequent inactivation of their corresponding proteins. The

dynamics of the MFL can be either bistable or oscillatory, depending on whether the transcriptional regulation is repressive of activating, respectively [François and Hakim, 2005]. As we will see, allowing for complex reversibility generates a much richer spectrum of behaviours, both at the single-cell level and when the system becomes coupled by diffusion. Since up to our knowledge these scenarios have not yet been explored, our goal in the next sections is to shed light on the dynamical repertoire the RMFL can exhibit. Moreover, we particularly stress the importance of explicitly consider the protein complex as a variable, which can have important consequences on the dynamics of the system.

## 7.2 The reversible mixed feedback loop

The interest in modularity and its implications for accurately mapping the structure of gene regulatory networks (genotypes) to specific traits (phenotypes), has motivated the search for dynamical modules, circuits characterized by the spectrum of dynamical behaviours they are able to exhibit [Jaeger and Monk, 2021a, Wagner and Zhang, 2011]. *In vivo* analyses of bacterial and yeast transcriptional and protein-protein interaction networks have identified recurrent circuits which have been subsequently found in *in silico* network explorations searching for specific functionalities, such as bistability or oscillations [Shen-Orr et al., 2002, François and Hakim, 2004, Yeger-Lotem et al., 2004]. One of these transcriptional/protein interaction circuits is the so called *mixed feedback loop* (MFL), which consists of the transcriptional regulation of one of the proteins by the other, and the formation of complex between the two proteins [François and Hakim, 2005]. Mathematical analysis of the MLF has revealed that when the transcriptional regulation is repressive, the MFL exhibits bistability, due to the effective positive feedback loop generated by transcriptional repression plus post-transcriptional repression due to complex formation [François and Hakim, 2005]. In contrast, for transcriptional activation, the resultant negative feedback loop leads to self-sustained oscillations (Figure 7.2) [François and Hakim, 2005].

Here we consider a modified version of the repressive MFL, where the formation of the complex between the two proteins is reversible, and capable of feeding back into the activity of the two proteins (from now on, reversible mixed feedback loop, RMFL). While the original circuit with transcriptional repression is only able to display monostability and bistability, here we will show that the reversible system can be both monostable, bistable *and* oscillatory, depending on the specific values of the parameters. Importantly, this happens without changing the qualitative nature of the interactions—i.e. without switching from transcriptional repression to transcriptional activation. This makes the RMFL truly multi-functional, contrasting with the original MFL where each instance—transcriptional activation and transcriptional repression—can be regarded as a different circuit.

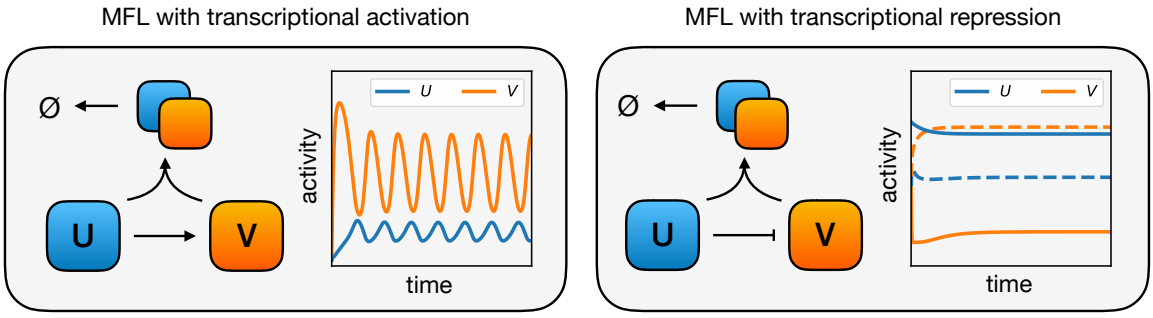



**Figure 7.2: Effective interactions and dynamics of the mixed feedback loop.** In the original mathematical analysis of the MFL [François and Hakim, 2005], one of the proteins ($U$) transcriptionally activates (Left panel) or represses (Right panel) the activity of the other ($V$), while both proteins are able to bind irreversibly into a complex which is either rapidly degraded or it cannot disassociate. The circuit is able to display oscillations or bistability depending on whether the transcriptional regulation activates or represses the activity of the other, respectively. Monostability (not shown) is possible in both cases. The dynamics of the complex are not shown, as it does not feed back on the activity of $U$ and $V$.

In the RMFL the mechanism for bistability is the same as in the original repressive MFL—a double negative feedback—while oscillations emerge as a consequence of complex reversibility, a situation that becomes favourable when the degradation of the complex is very small or zero. Thus, the seemingly inoffensive incorporation of complex reversibility introduces novel and non-intuitive behaviours, of which we are going to explore in detail. The particular choice of transcriptional repression over activation is deliberate. As we will see, in the case of transcriptional activation the system can only have a single fixed point, which can be stable or oscillatory—no bistability is possible. Thus, in our search for multi-functionality, the MRFL with transcriptional activation is uninteresting compared to its repressive version.

### 7.2.1 Dynamics and stability of fixed points

To formulate a single-celled version of the repressive RMFL, we consider, as in its original formulation, a protein $U$ which is able to repress the activity of another protein $V$, while the two are able to form a complex $C$. This complex is assumed to be reversible and can become degraded. In what follows, we will assume repression happens at the level of transcription, so that $U$ impairs the production of $V$ by binding to its promoter. Denoting the concentrations of each protein as $U, V$ and $C$, this situation is illustrated with the following

dynamical model:

$$\frac{dU}{dt} = \alpha - d_u U - k_c UV + \delta C \tag{7.1a}$$
$$\frac{dV}{dt} = \gamma \frac{k^n}{k^n + U^n} - d_v V - k_c UV + \delta C \tag{7.1b}$$
$$\frac{dC}{dt} = k_c UV - \delta C - d_c C \tag{7.1c}$$

Here proteins $U$ are produced with rate $\alpha$ and are degraded linearly with rate $d_u$. The formation of the complex $C$ happens with a binding rate $k_c$ and disassociates with rate $\delta$. The protein $V$ has a maximum production rate $\gamma$, is transcriptionally repressed by $U$ with a promoter dissociation constant $k$ and cooperativity $n$, and is degraded linearly with rate $d_v$. Finally, the complex can also be degraded with rate $d_c$. This formulation differs with respect to the original MFL in that we do not explicitly consider the dynamics of mRNA nor the binding of proteins to the promoter (see Section 3.1 for the details involved in such approximations). Moreover, as already stressed, in this case the complex is reversible, so $\delta \neq 0$. Therefore, contrary to [François and Hakim, 2005], the dynamics of the complex variable $C$ must be explicitly taken into account.

As a limit case, it is easy to see that for $d_c = 0$, i.e. if the complex is not degraded, the system has only one fixed point, with $U_s = \alpha/d_u$, $V_s = \frac{\gamma}{d_v}\frac{k^n}{k^n+(U_s)^n}$, $C_s = \frac{k_c}{\delta} U_s V_s$, where the subscript $s$ denotes the stationary state, i.e. the solutions of Equation 7.1 when the time-derivatives are set to zero. As we will see, this fixed point can be either stable or oscillatory. When $d_c \neq 0$ and for arbitrary $n$, however, finding analytical expressions for the steady states is not possible, and we must resort to numerical calculations. To visualize the possible behaviours of the full system, we first compute the nullclines Equation 7.1, by setting the third equation to zero and substituting on the first and second equations. In implicit form, these nullclines in the $(U, V)$ plane are:

$$F_U(U,V) = \alpha - d_u U - k_c UV\left(1 - \frac{\delta}{\delta + d_c}\right) = 0 \tag{7.2a}$$
$$F_V(U,V) = \gamma \frac{k^n}{k^n + U^n} - d_v V - k_c UV\left(1 - \frac{\delta}{\delta + d_c}\right) = 0 \tag{7.2b}$$

In Figure 7.3 we show the distinct dynamical regimes the RMFL is able to exhibit. By tuning parameters which might potentially change in different environmental and/or developmental contexts (in this case $\alpha$ and $d_c$), we see that the RMFL is able to display oscillations, monostability and bistability. This contrasts with the original MFL [François and Hakim, 2005], where oscillations and

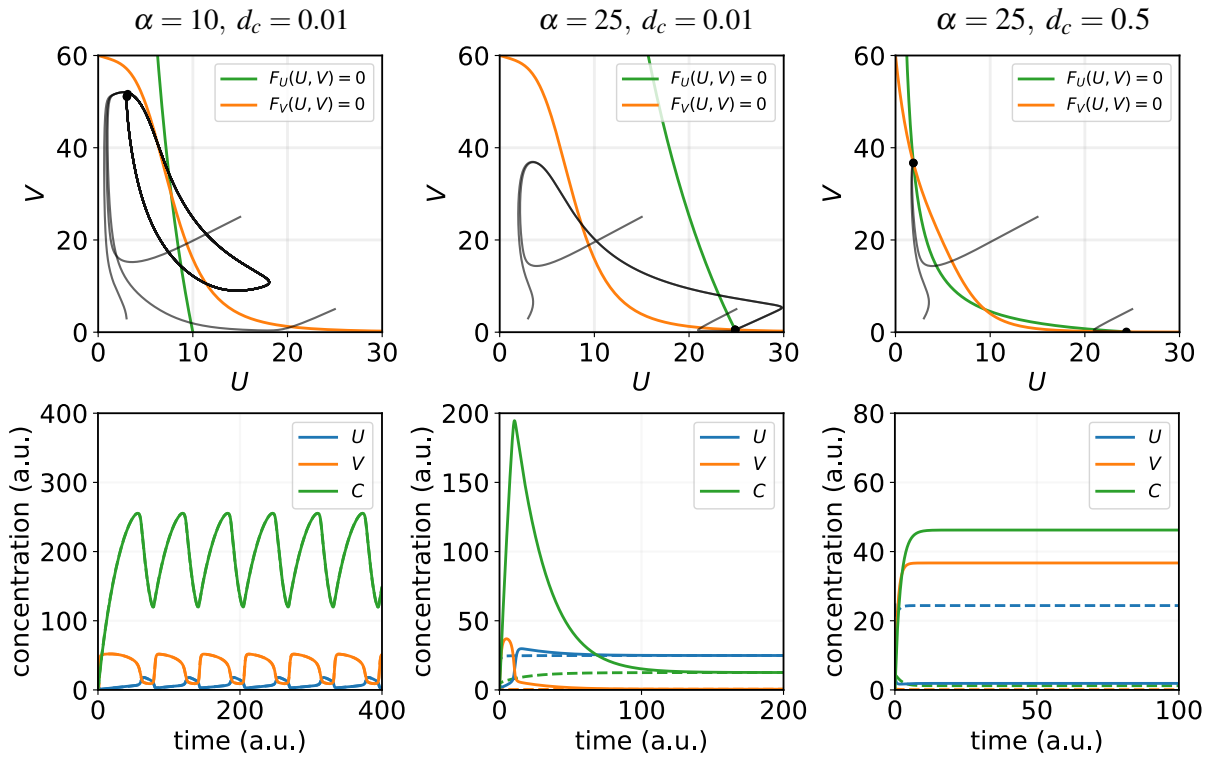



**Figure 7.3: Dynamical regimes of the RMFL with transcriptional repression. Top)** Nullclines $F_U(U,V)=0$ and $F_V(U,V)=0$ (Equation 7.2), with the fixed points of the system corresponding at their intersections (black circles). Black curves correspond to three different trajectories in the phase space $(U,V)$. Black dots denote the final time point of the simulations. **Bottom)** Time evolution of $U(t)$, $V(t)$ and $C(t)$ for two of the trajectories shown in the top images. The rest of the parameters are $\gamma=60$, $d_u=d_v=1$, $k_c=1$, $\delta=1$, $k=8$, $n=4$.

bistability stem from qualitatively different transcriptional interactions, namely activation and repression, respectively. The distinction is important. In real biological systems, it is hard to imagine a protein acting as a transcriptional activator to a particular gene, and suddenly swapping its role to a transcriptional repressor of the same gene, due to a change in environmental conditions or developmental context. On the other hand, parameters such as the rates of transcription, degradation or complex formation can easily be modified by other molecules such as transcription factors, enhancers, proteases, hormones, microRNAs, etc., the presence of which might depend on the tissue or organ the circuit is operating in, external conditions such as temperature of pH, or the developmental stage of the organism.

The bistable regime is relatively straightforward to understand. When the complex rapidly degrades after its formation (high $d_c$), feedback from $C$ to $U$ and $V$ is small, and thus complex formation effectively acts as a negative feedback. When coupled with the inhibition of $V$ by $U$, this generates a double inhibition similar to a toggle-switch, where high activity of $U$ is associated with

low activity of $V$, and vice-versa. At specific parameter values, this leads to a region where the two states, high $U$ low $V$, and low $U$ high $V$ coexist. We could model this bistable regime by setting $\delta = 0$, as when the complex degrades very fast the effect complex reversibility is small. This is the limit case studied in [François and Hakim, 2005]. Importantly, bistability can only appear when the complex can be degraded, i.e., when $d_c > 0$, as for $d_c = 0$ Equation 7.1 can only have a single fixed point.

The oscillatory regime is a little bit more intricate, and it can appear when the complex cannot be degraded (or it can but with a very slow rate) and complex reversibility is nonzero. When $V$ is present in high concentrations, it can rapidly capture $U$ proteins, preventing them from inhibiting its expression. This state with high $V$ and low $U$ is maintained in time as $U$ proteins are slowly produced and the complex builds up, until it reaches a point where $U$ reaches the repression threshold of $V$ (mediated by the parameter $k$), rapidly diminishing its concentration. During this decrease, $U$ increases as the complex begins to disassociate, until $V$ reaches a point where it can again capture $U$, starting the cycle again.

For completeness, we will now show that the RMFL with transcriptional activation is not able to display all the behaviours of its repressive counterpart. In particular, we will prove that bistability is impossible. To see this, notice that in the case of transcriptional activation, the nullclines are:

$$F_U(U,V) = \alpha - d_u U - k_c UV\left(1 - \frac{\delta}{\delta + d_c}\right) = 0 \tag{7.3a}$$

$$F_V(U,V) = \gamma \frac{U^n}{k^n + U^n} - d_v V - k_c UV\left(1 - \frac{\delta}{\delta + d_c}\right) = 0 \tag{7.3b}$$

By isolating $V$ from both equations and equating the resulting expressions, it's easy to see that the following identity is fulfilled:

$$\alpha - d_u U = \gamma \frac{U^n}{k^n + U^n} \frac{k_c U}{d_v + k_c U} \tag{7.4}$$

The left hand side of this equation is a decreasing straight line, while the right hand side is a product of two monotonically increasing functions (at least on the interval $(0, \infty)$), and therefore also a monotonically increasing function. Therefore, the two curves can only cross at one point, for all values of the parameters (as long as they do not change sign). From the analysis of the original MFL we know that this point can be either stable or oscillatory [François and Hakim, 2005], so here we are not going to study its stability.

Going back to the repressive RMFL, as we have seen that both monostabiliy, bistability and oscillations can appear, we are interested in studying how those depend on the parameters of the model. This can be done by studying the

stability of the fixed points through linear stability analysis (see Section 3.2). We first compute the Jacobian:

$$J = \begin{pmatrix} -d_u - k_c V_s - \lambda & -k_c U_s & \delta \\ -\mathcal{F} - k_c V_s & -d_v - k_c U_s - \lambda & \delta \\ k_c V_s & k_c U_s & -\delta - d_c - \lambda \end{pmatrix} \tag{7.5}$$

where $\lambda$ are its eigenvalues. Since we do not have an analytical solution for the steady states $U_s$, $V_s$, $C_s$, we first need to compute them numerically. The characteristic polynomial obtained by taking the determinant of $J$ has the form $\lambda^3 + a_2\lambda^2 + a_1\lambda + a_0 = 0$. By defining $b_1 \equiv d_u + k_c V_s$, $b_2 \equiv d_v + k_c U_s$, $b_3 \equiv \delta + d_c$ and $b_4 = \mathcal{F} + k_c V_s$, where $\mathcal{F} \equiv n\gamma \frac{k^n U_s^{n-1}}{(k^n + U_s^n)^2}$, we can write the $a_i$'s as:

$$\begin{aligned} a_2 &= b_1 + b_2 + b_2, \quad a_1 = b_1 b_2 + b_1 b_3 + b_2 b_3 - \delta k_c V_s - \delta k_c U_s - k_c U_s b_4 \\ a_0 &= b_1 b_2 b_3 + \delta k_c^2 U_s V_s + \delta k_c U_s b_4 - \delta k_c V_s b_2 - k_c U_s b_3 b_4 - \delta k_c U_s b_1 \end{aligned} \tag{7.6}$$

As detailed in Section 3.2, a sufficient condition for fixed points to be stable is that the real parts of all the eigenvalues are negative, i.e. $\mathrm{Re}(\lambda) < 0$ for all $\lambda$. Given the expressions for $a_0$, $a_1$ and $a_2$, this is equivalent to the Routh-Hurwitz conditions:

$$a_2 > 0, \quad a_0 > 0, \quad a_2 a_1 - a_0 > 0 \tag{7.7}$$

The bifurcation diagrams in Figure 7.4 show the fixed points of the system and their stability as the parameter $\alpha$ changes. In the top row, a single steady state with low $U$ and high $V$ gives way to a bistable region through a saddle-node bifurcation, where there is coexistence between two opposite stable states, high $V$ low $U$ and low $V$ high $U$. As $\alpha$ takes larger values, the bistable region disappears through yet another saddle-node bifurcation, leading to monostability again, with high $U$ and low $V$. In the bottom row of Figure 7.4, oscillations emerge through a supercritical Hopf bifurcation as $\alpha$ exceeds a certain critical value, only to disappear into monostability again through another supercritical Hopf bifurcation. In Figure 7.5 we show how the regions where bistability and oscillations appear in the $(\alpha, \gamma)$ plane. The oscillatory regime only appears for large enough values of $\gamma$, and for intermediate values of $\alpha$. This happens because for the system to oscillate, $V$ proteins must be at sufficiently high values to rapidly sequester $U$, and $U$ must reach sufficiently high levels so that it can exert its repressive action on $V$. For small $\alpha$, $U$ cannot reach sufficiently high values to repress $V$, while for large $\alpha$, $V$ is always repressed. Therefore, an intermediate regime is necessary for oscillations to occur.

In Figure 7.5 (Left), the continuous line (Hopf curve) enclosing the blue region corresponds to the Routh-Hurwitz conditions being exactly equal to zero, i.e. when the eigenvalues associated with the single fixed point have $\mathrm{Re}(\lambda) = 0$.

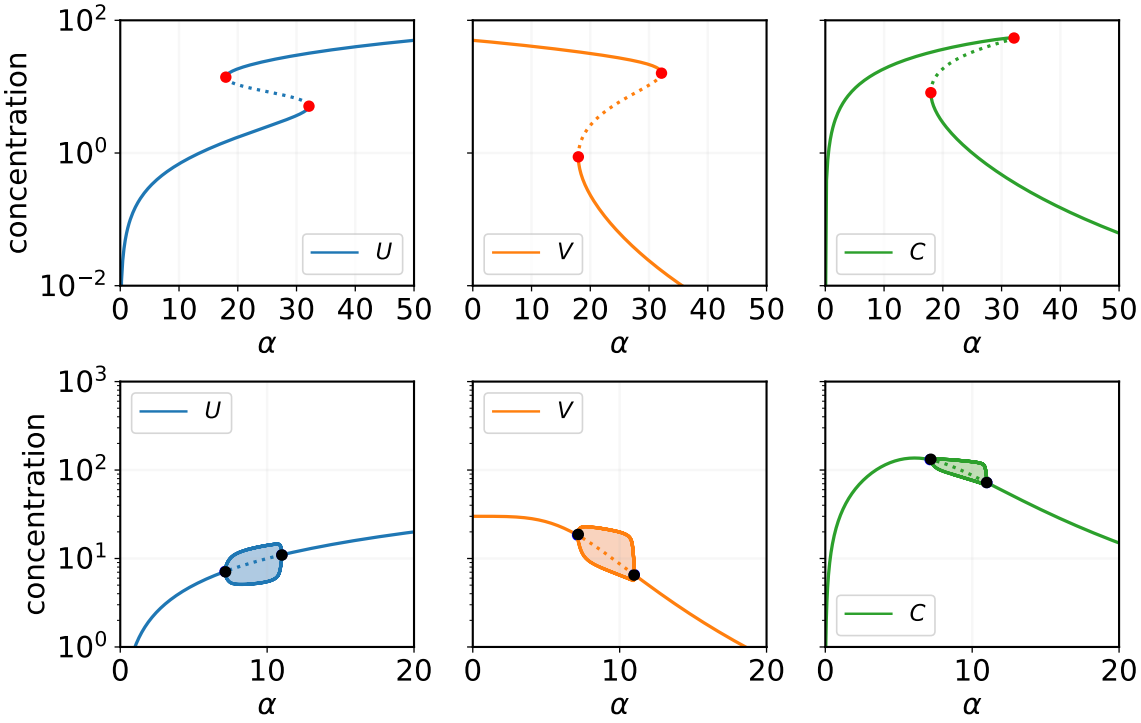



**Figure 7.4: Bifurcation diagrams showing bistability and oscillations in the RMFL. Top:** Fixed points $U_s$ (blue), $V_s$ (orange), $C_s$ (green) as a function of the control parameter $\alpha$, showing how as it takes larger values, the single fixed point of the system gives way to a region of bistability, which disappears at still higher values of $\alpha$. Dotted lines represent unstable fixed points. Red dots mark saddle-node bifurcations. Parameter values are $\gamma = 50$, $d_u = d_v = 1$, $k_c = 1$, $\delta = 1$, $k = 8$, $d_c = 0.5$, $n = 4$. **Bottom:** Fixed points $U_s$ (blue), $V_s$ (orange), $V_s$ (green) as a function of $\alpha$, showing how the stable fixed point loses stability through a supercritical Hopf bifurcation (black dots), from which oscillations with small amplitude rapidly emerge. The shaded regions enclosed by the lines represent the amplitude of the oscillations, while dotted lines represent the unstable fixed point associated with the limit cycle. Parameter values are the same as in the top panels, with the exception of $d_c = 0$ and $\gamma = 30$. Bifurcation diagrams for the Hopf bifurcations have been computed with the Python package PyDSTool [Clewley et al., 2007].

The dark-blue region corresponds to parameter values where $\mathrm{Im}(\lambda) \neq 0$. The dashed curve (Hopf curve) encloses the parameter region where $\mathrm{Im}(\lambda) = 0$. For the bistable regime, sufficiently high values of $\gamma$ and $\alpha$ are needed. As complex formation is a very strong interaction—the term $k_c UV$ can potentially be very large—, it needs to be compensated by sufficiently high production rates to prevent the system from remaining in a state with low $U$ and low $V$. When $\alpha \gg \gamma$, only the state with high $U$ and low $V$ is possible, as $U$ strongly inhibits $V$, at the same time as it sequesters it. When $\gamma \gg \alpha$, the opposite happens, as $V$ sequesters $U$ and prevents the transcriptional repression. For intermediate values, however, due to the mutual inhibition between $U$ and $V$—$U$ transcriptionally represses $V$ and $V$ sequesters $U$—the two states high $U$ low $V$ and low $U$ high $V$ are stable. In Figure 7.5 (Right), the continuous curve

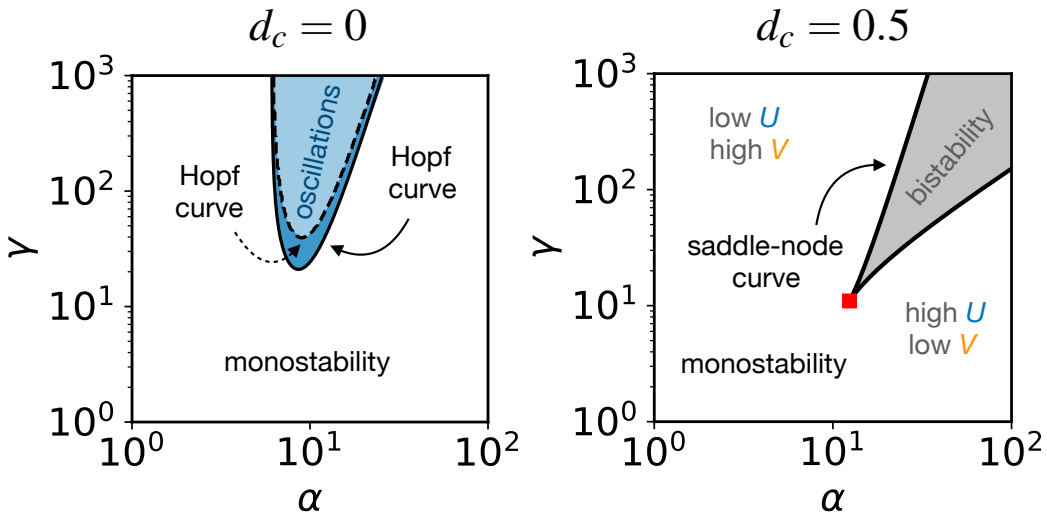



**Figure 7.5: Stability diagram for oscillatory and bistable regimes. Left:** Oscillatory regimes (blue region) enclosed by a curve of Hopf bifurcations (continuous line), where a pair of conjugate eigenvalues cross the imaginary line. The region enclosed by the dashed lines corresponds to oscillatory states where the imaginary part of the eigenvalues is exactly zero. **Right:** Bistable regime (grey region), enclosed by a curve of saddle-node bifurcations. The red square marks the cusp point when two saddle-node collide and annihilate each other. The values of the remaining parameters are $d_u = d_v = 1$, $k_c = 1$, $\delta = 1$, $k = 8$, $n = 4$.

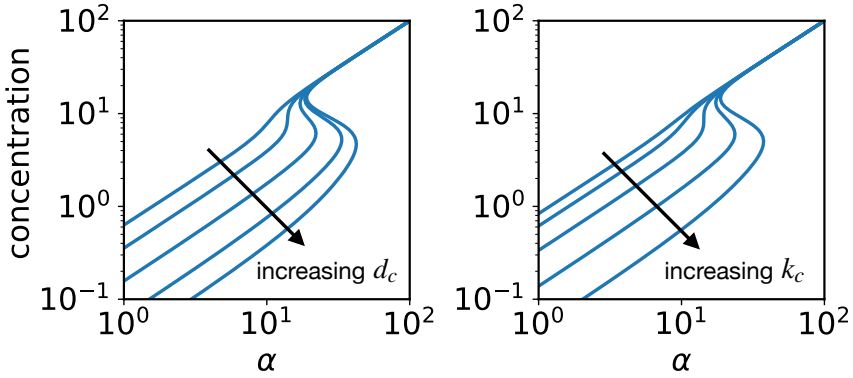



**Figure 7.6: Bistability is promoted by complex formation and degradation.** Steady states of $U$ as a function of the production rate $\alpha$, showing a bistable region that emerges as $d_c$ and $k_c$ take large enough values. In both panels, $d_c$ and $k_c$ go from 0.01 to 1. The rest of the parameters are $\gamma = 50$, $d_u = d_v = 1$, $\delta = 1$, $k = 8$, $n = 4$, $k_c = 1$ in the left panel and $d_c = 0.5$ in the right panel.

traces the position of the saddle-node bifurcations, which enclose the bistable region (grey area). These curves coalesce at a codimension 2 cusp bifurcation (red square), where bistability disappears.

As in the original formulation of the MFL, bistability emerges due to the double negative feedback induced by transcriptional repression plus dimerization. When the complex is rapidly degraded, the effect of complex dissociation and the subsequent feedback on the dynamics of $U$ and $V$ is small, and thus a high con-

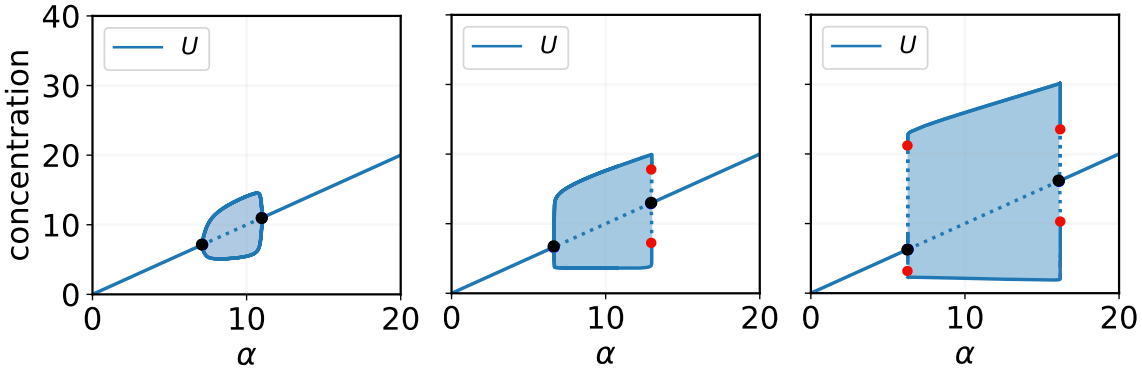



**Figure 7.7: Hopf bifurcations can be supercritical or subcritical.** As $\gamma$ takes larges values, the region where the circuit displays oscillations increases and the transition from monostability to oscillations becomes sharper, with finite-amplitude oscillations appearing right after the bifurcation point. Red dots denote saddle points separating unstable (dashed lines) and stable (continuous lines) branches of the limit cycle. The rest of the parameters are $d_u = d_v = 1$, $k_c = 1$, $k = 8$, $\delta = 1$, $n = 4$, $d_c = 0$. Simulations have been computed with the Python package PyDSTool [Clewley et al., 2007].

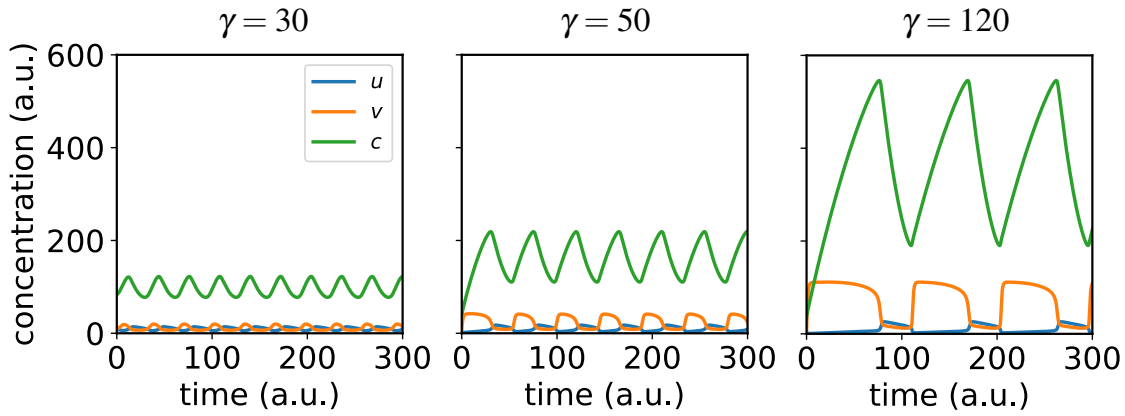



**Figure 7.8: The amplitude and period of the oscillations can increase indefinitely as $\gamma$ takes larger values.** In the oscillatory region, as $\gamma$ takes larger values the maximum value $V$ can take increases. The rest of the parameters are $d_u = d_v = 1$, $k_c = 1$, $k = 8$, $\delta = 1$, $n = 4$, $d_c = 0$.

centration of any of them reinforces itself by titrating the other. While molecular titration alone can already create a sharp switch between the two species as the concentration of one increases with respect to the other [Buchler and Louis, 2008], the additional negative regulation through transcriptional repression provides sufficient nonlinearity to generate a bistable region, where both high and low states coexist. Bistability in this case is not novel, for it emerges through the same mechanism as that of the original repressive MFL [François and Hakim, 2005]. In Figure 7.6 we show how this regime is promoted for high values of the complex formation rate $k_c$ and the degradation rate $d_c$. For small $d_c$ and $k_c$, complex formation and dissociation compensate, and the circuit ef-

fectively behaves as a monostable system. For high $d_c$, if $k_c$ is small the effect of complex formation will be insignificant, and thus the circuit will effectively consist of a negative regulation of $V$ by $U$, leading to monostability. However, for sufficiently large values of $k_c$, the effect of complex formation begins to be noticeable, leading to the circuit effectively behaving as a toggle-switch, with an intermediary bistable region.

The case of oscillations is novel, in the sense that it only emerges for nonzero dissociation rate ($\delta \neq 0$) and small complex degradation ($d_c \ll 1$), a regime which is not explored in the original MFL [François and Hakim, 2005]. In the limit where $d_c = 0$, the system has a single fixed-point, which as we have seen can be oscillatory for certain range of parameters. For $d_c = 0$, these oscillations can wither emerge through a supercritical or subcritical Hopf bifurcation. In the latter case, the transition from monostability to oscillations is abrupt, and finite-amplitude oscillations emerge. This behaviour is favoured as $\gamma$ takes larger values. In fact, notice that the oscillatory region keeps existing for arbitrarily large $\gamma$. This happens because when $\gamma$ has reached a certain value, the mechanism for generating oscillations does not depend how large is $\gamma$, but on the capability of $U$ to repress its activity. However, $\gamma$ does control both the amplitude and the period of the oscillations, as it dictates the time for the complex to build up and the time until $U$ reaches a value large enough to repress $V$. In the next section, we will explore which are the effects of introducing noise to this oscillatory regime.

### 7.2.2 The RMFL with intrinsic noise

For completeness, we also explored the behaviour of the system in the presence of intrinsic fluctuations in the molecular reactions of the RMFL. On the one hand, it is known that the presence of noise in the bistable regime of the repressive MFL can induce stochastic switching between the two stable states [Li and Li, 2008]. However, since stochastic switching is a common feature in systems displaying bistability, we will not explore it here. On the other hand, the MFL with transcriptional activation has been shown to display oscillations induced purely by noise, as long as the system remains close to the Hopf bifurcation [Li and Li, 2008]. This is a more interesting phenomenon, as it is less clear why noise must promote the onset of oscillations. To test whether the RMFL is able to display noise-induced oscillations, we simulated the system through the chemical Langevin equation [Gillespie, 2000] (see Chapter 3 for details). Close to the subcritical Hopf bifurcation, due to the proximity to a finite amplitude limit cycle, small fluctuations from the fixed point can lead the system to undergo a large excursion in phase space before relaxing back to the fixed point. This kind of behaviour is a hallmark of excitable systems [Rué and Garcia-Ojalvo, 2011]. As seen in Figure 7.9, in this regime the RMFL exhibits noise-induced pulses, the mean frequency—but not the amplitude—of which depends on the

noise strength, mediated by the parameter Ω. This is an example of *coherence resonance*, a phenomenon commonly present in systems displaying excitability [Pikovsky and Kurths, 1997, Lindner et al., 2004]. In our case, for small noise strengths, pulses happen only infrequently and the system mainly fluctuates around the stable steady state. As the noise strength increases, activity pulses become more and more frequent, until the system basically oscillates as if it was deterministic. This means that the excursion in phase-space induced by noise is itself not affected by it. Only if the noise strength increases further do fluctuations dominate the system, at which point the oscillatory regime is destroyed. This is in contrast with the noise-induced oscillations studied in the original MFL [Li and Li, 2008], where the amplitude of the oscillations changes with noise strength. It is important to stress that noise-induced oscillations emerge for parameters where the deterministic system does not oscillate. As pointed in [Li and Li, 2008], this phenomenon may confer robustness to perturbations, as the oscillatory regime comprises a much larger parameter region than the one expected in the deterministic system.

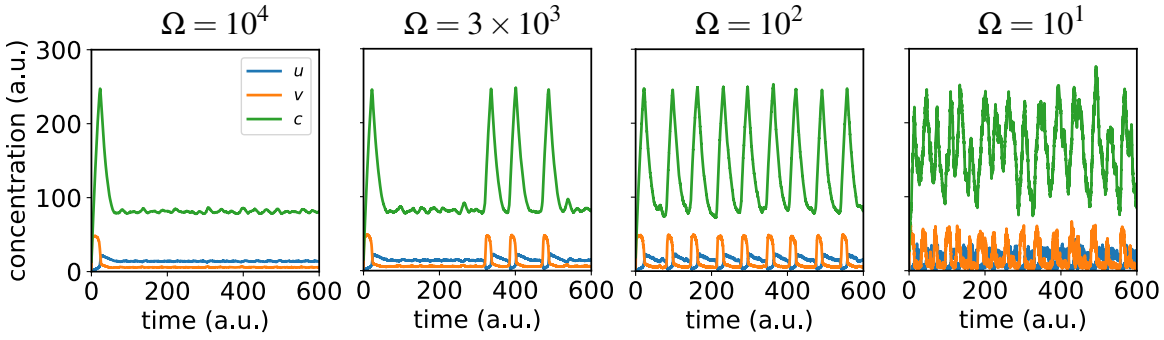



**Figure 7.9: Oscillations induced by noise close to a Hopf bifurcation.** Close to the Hopf bifurcation, fluctuations may lead an otherwise stable state to become oscillatory, depending on the noise strength, mediated by Ω. Parameters are $\alpha = 14$, $\gamma = 50$ $d_u = d_v = 1$, $k_c = 1$, $\delta = 1$, $k = 8$, $n = 4$, $d_c = 0$.

To further explore the multi-functional behaviours of the RMFL, in the next section we study how the circuit behaves when we allow diffusive coupling to occur, focusing on the case where the complex is the sole diffusing factor.

## 7.3 The diffusively coupled mixed feedback loop

While the single-cell version of the RMFL is interesting on its own—as a simple circuit that can behave as either a bistable switch or a clock—we want to know whether the introduction of spatial coupling leads to novel characteristics. The motivation behind studying the system with spatial coupling is twofold. First, in biologically inspired dynamical systems—specially those with high nonlinearities such as the RMFL—the introduction of a spatial component can lead to qualitatively new behaviours such as the appearance of inhomogeneous pat-

terns, propagation of waves or even irreversible state transitions, such as the disappearance of fixed points or limit cycles [Durrett and Levin, 1994]. Classic examples are the emergence of spatially periodic (Turing) patterns in activator-inhibitor reaction-diffusion systems, where diffusion destabilizes a previously stable homogeneous state, or the existence of travelling waves in the Fisher-KPP equation—a version of the logistic growth equation where diffusive coupling is added [Murray, 2002]. A particularly dramatic effect induced by spatial coupling is found in the ecological context of three-species competition, where the mobility rate of the species modulates the transition between extinction and survival [Reichenbach et al., 2007]. Second, when dealing with developmental processes it is important to know how to bridge scales between distinct levels of description. In the archetypal case, one needs to understand how the possible states of a gene regulatory circuit become translated to particular physical traits. Adding a spatial component to the dynamics of our genetic circuit is a first step in this direction.

As already mentioned, spatial coupling will be introduced via the diffusion of the complex, while neither $U$ nor $V$ will be able to move. Two main reasons are behind this choice: first, introducing spatial coupling via $U$, $V$ or both does not change the qualitative dynamics of the system. At most, in the oscillatory regime cells can become synchronized—which is expected for diffusive coupling—and the parameter regimes where bistability and oscillations appear can change[1]. Linear stability analysis further supports the view that no spatial instability can occur in these scenarios. Second, the introduction of spatial coupling via the diffusion of the complex conceals an interaction which at first glance may seem paradoxical, given the smoothing nature of diffusion: as the complex diffuses to neighbouring cells and disassociates, the resulting proteins $U$ are able to repress $V$ in those cells, in a mechanism akin to lateral inhibition, where two neighbouring cells repress each other's activity, only in this case cell-to-cell interactions are not juxtacrine, but diffusive. Thus, diffusion of the complex may in fact have the opposite effect one would expect for classical diffusion. As is well-known, cellular arrays coupled by lateral inhibition interactions can display salt-and-pepper patterns, the archetypical example of which are those between Delta and Notch [Collier et al., 1996]. Like the framework used to model *Marchantia* rhizoids in Chapter 6, in order to mimic the specific structure of cellular tissues here we treat space as a discrete array of cells. Our main aim is to explore the consequences of this lateral inhibition-like diffusive interaction, and whether the resulting spatial behaviours are of interest in developmental contexts.

[1]The results of these simulations are not shown here.

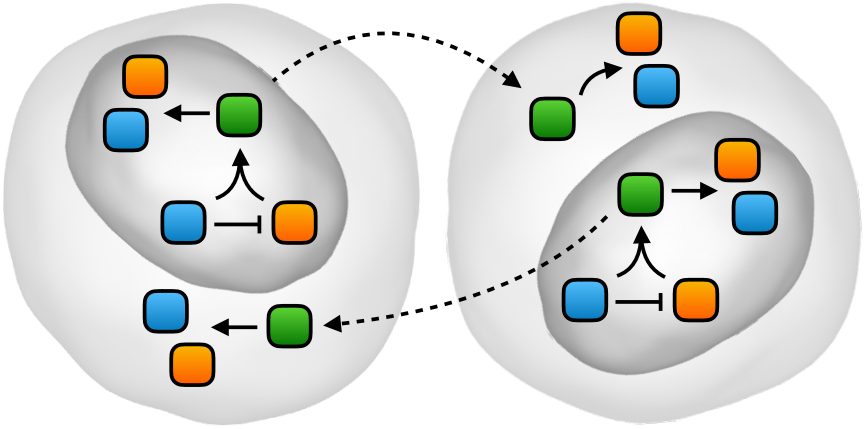


**Figure 7.10: Two cells with a RMFL coupled by diffusion of the complex.** In the diffusively coupled RMFL, $u$ and $v$ form a complex which is able to move from cell to cell (dashed lines) and disassociate therein. The resulting proteins $u$ and $v$ are then able to perform their role as part of the RMFL in that cell.

### 7.3.1 Two-cell system

To understand the possible consequences of diffusive coupling, we first study a system with two interacting cells, which are able to exchange complex proteins through diffusive transport. In the case where $d_c > 0$, since the system can be bistable, the introduction of spatial coupling may lead to non-linear instabilities which become hard to analyse mathematically. When $d_c = 0$, however, the system can only have a single fixed point, which can be either stable or oscillatory. For simplicity, we assume the complex cannot be degraded, and thus we set $d_c = 0$. In this case, upon introducing spatial coupling the stability of this fixed point can be easily studied through linear stability analysis.

To formulate the two-cell system, we label each cell by the index $i$—which can take the values $i = 1, 2$—and write the dynamics of the diffusively coupled two-cell RMFL as:

$$\frac{du_i}{dt} = \alpha - d_u u_i - k_c u_i v_i + \delta c_i \tag{7.8a}$$

$$\frac{dv_i}{dt} = \gamma \frac{k^n}{k^n + u_i^n} - d_v v_i - k_c u_i v_i + \delta c_i \tag{7.8b}$$

$$\frac{dc_i}{dt} = k_c u_i v_i - \delta c_i + D(c_j - c_i) \tag{7.8c}$$

where $j = 2, 1$. We write the variables in lower case (as opposed to the previous section) to emphasize that we deal with a system coupled by diffusion. Notice that the two-cell system has a trivial solution $(u_1, v_1, c_1) = (u_2, v_2, c_2) = (u_s, v_s, c_s)$, where $u_s$, $v_s$ and $c_s$ is the same fixed point as in the single-cell system.

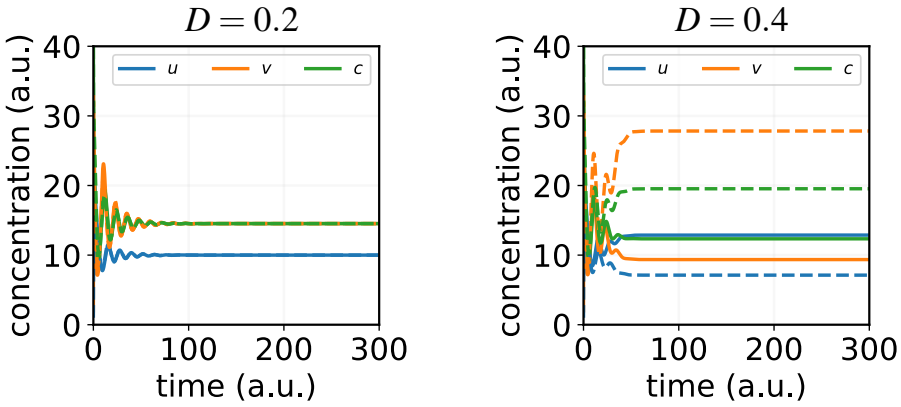



**Figure 7.11: Lateral inhibition due to diffusion in the two-cell system.** When two cells with the RMFL become coupled through the diffusion of $c$, cells can adopt opposite fates (cell 1: continuous lines; cell 2: dashed lines). For small $D$ (left, $D = 0.2$) the homogeneous state where the two cells have the same fixed point is stable. As $D$ takes larger values (right, $D = 0.4$), this homogeneous state loses stability, and the two cells adopt opposite fates. The remaining parameters are $\alpha = 10$, $\gamma = 50$, $d_u = d_v = 1$, $k_c = 1$, $k = 8$, $\delta = 10$, $n = 4$. In the simulation, the two cells begin with similar initial conditions.

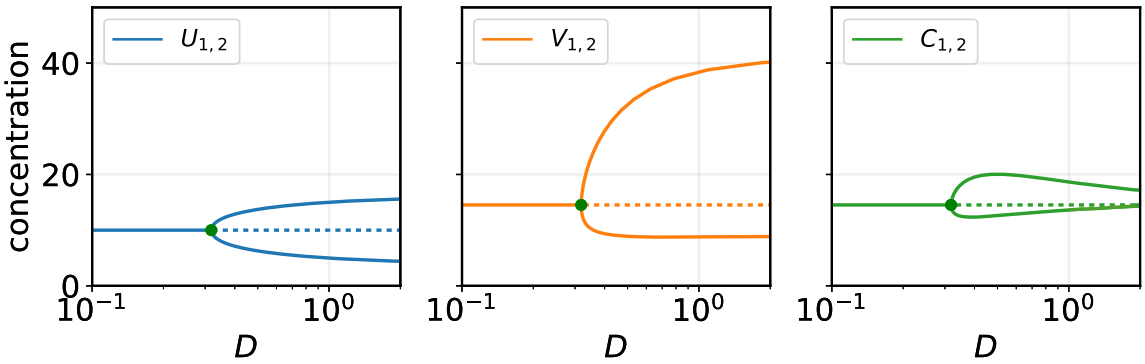



**Figure 7.12: Bifurcation diagram showing the splitting between cell states due to diffusive coupling.** In the two-cell system, for small values of the diffusion coefficient the only stable steady state corresponds to the two cells having the same $u, v, c$. As $D$ crosses a critical value, this homogeneous state loses stability through a pitchfork bifurcation (green circle), and two opposite stable states—one with high $u$ low $v$ and another with low $u$ high $v$—emerge. The remaining parameters are $\alpha = 10$, $\gamma = 50$, $d_u = d_v = 1$, $k_c = 1$, $k = 8$, $\delta = 10$, $n = 4$, corresponding to the uncoupled system in the monostable state. Continuous (dashed) lines denote stable (unstable) fixed points

This state corresponds to the two cells behaving in exactly the same manner.

To see if novel behaviours appear when diffusion is introduced, we simulate the dynamics of the two-cell system. In Figure 7.11 we show the dynamics of $u, v, c$ for cell 1 (continuous lines) and cell 2 (dashed lines). For the regime where each cell only has a stable fixed point, diffusive coupling can induce the splitting of the two cells into different, opposite states, with cell 1 having high $u$ and low $v$ and cell 2 low $u$ and high $v$ (Figure 7.11). Due to the symmetry of the

system—we can interchange the indexes 1 and 2 and the equations remain the same—the opposite state with cell 2 having high $u$ and low $v$ and cell 1 having low $u$ and high $v$ is equally likely. In Figure 7.12, the bifurcation diagram shows how as $D$ takes larger values, the homogeneous state loses stability through a pitchfork bifurcation, and two opposite states appear. Importantly, these states appear in a parameter regime where the single-cell system is monostable (recall that for $d_c = 0$ bistability at the single cell level is not possible). Therefore, the presence of diffusive coupling through the complex induces lateral inhibition between cells.

This splitting can also happen when the fixed point is oscillatory. In Figure 7.13 we see how this oscillatory state can be arrested when diffusion if present. When there is no diffusive coupling (Figure 7.13 A), the two cells oscillate out of synchrony, as for different initial conditions each cell will reach the limit cycle at a different time. For small values of $D$, the two cells synchronize their oscillations, as diffusion acts as a steadying mechanism, smoothing out any initial difference in activity (Figure 7.13 B). When $D$ takes larger values, the two cells can initially synchronize, only to split into opposite states after a certain time, with a cell having high $u$ and low $v$ (in this case cell 2, dashed line), and the other having low $u$ and high $v$ (in this case, cell 1, continuous line). The choice between one or the other will depend on the initial conditions of the system. Finally, when $D$ is large enough, oscillations are no longer stable and the two cells rapidly adopt opposite fates, with a cell with high $u$ and low $v$ and the other with low $u$ and high $v$ (o viceversa) (Figure 7.13 D). What will be the consequences of such dynamics when, instead of coupling two-cells, a whole array is able to interact via the diffusion of the complex? This will be explored in detail in the next section.

### 7.3.2 The RMFL in cellular lattices

As revealed by analysing the two-cell system, diffusive coupling can act as a destabilizing force, pushing neighbouring cells towards opposite states. It remains to be seen, however, how these behaviours translate to the full, coupled system of cells within a tissue. For simplicity, and without loss of generality, we will study the coupled system in one spatial dimension, where $N$ cells are arranged in a linear chain, and then extend the results to a two-dimensional square lattice. Again, for simplicity in the calculations we consider that the complex does not degrade, so $d_c = 0$. The diffusively coupled RMFL has the

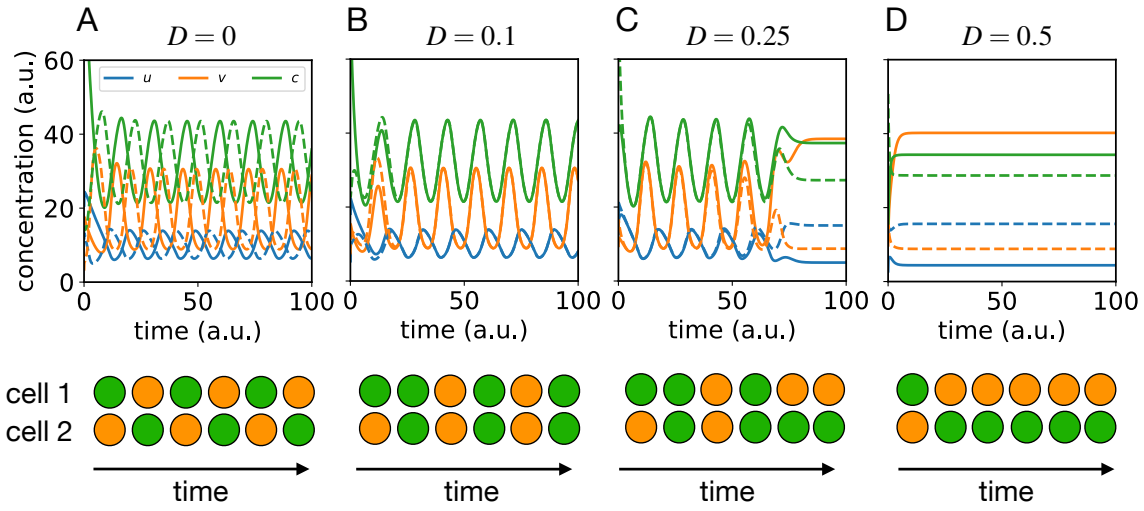



**Figure 7.13: Dynamical regimes of the two-cell system.** When two cells with the RMFL become coupled through the diffusion of $c$, cells can adopt opposite fates (cell 1: continuous lines; cell 2: dashed lines). This can happen either directly (D, $D = 0.5$) or after an oscillatory transient (C, $D = 0.25$). For small diffusion coefficient $D$ both cells oscillate in synchrony (B, $D = 0.1$), whereas when $D = 0$ cells oscillate our of synchrony, as they reach the limit cycle at different times, depending on initial conditions. The sketches below each panel graphically represent the corresponding cellular states over time. The remaining parameters are $\alpha = 10$, $\gamma = 50$, $d_u = d_v = 1$, $k_c = 1$, $k = 8$, $\delta = 5$, $n = 4$. The two cells have random initial conditions given by are $u_0 = \mathcal{U}[0, 10]$, $v_0 = \mathcal{U}[0, 10]$, $c_0 = \mathcal{U}[0, 100]$, where $\mathcal{U}$ is a random number taken from a uniform distribution.

form:

$$\frac{du_i}{dt} = \alpha - d_u u_i - k_c u_i v_i + \delta c_i \tag{7.9a}$$

$$\frac{dv_i}{dt} = \gamma \frac{k^n}{k^n + u_i^n} - k_c u_i v_i + \delta c_i - d_v v_i \tag{7.9b}$$

$$\frac{dc_i}{dt} = k_c u_i v_i - \delta c_i + D\nabla^2 c_i \tag{7.9c}$$

where $D$ is the diffusion coefficient and $\nabla^2$ denotes the discrete Laplacian operator, which in 1D has the form $\nabla^2 c_i = \frac{1}{\Delta x^2}(c_{i+1} + c_{i-1} - 2c_i)$. For simplicity, from now on we choose $\Delta x = 1$. When analysing the single-cell system (i.e., in the absence of diffusion), we have shown that the system has a single fixed point, which can either be stable or oscillatory. We now want to asses what is the effect of diffusion on the stability of such state. As explained in Part I, the stability of fixed points in spatially extended systems like this one can also be analysed through linear stability analysis. In this case, the Jacobian matrices $J_0$ and $J_1$ (see Part I) are:

$$J_0 = \begin{pmatrix} -d_u - k_c v_s & -k_c u_s & \delta \\ -\mathcal{F} - k_c v_s & -d_v - k_c u_s & \delta \\ k_c v_s & k_c u_s & -\delta \end{pmatrix}, \quad J_1 = \begin{pmatrix} 0 & 0 & 0 \\ 0 & 0 & 0 \\ 0 & 0 & 2D\Big[\cos(\frac{2\pi q}{N}) - 1\Big] \end{pmatrix} \tag{7.10}$$

where, as before, $\mathcal{F} \equiv n\gamma \frac{k^n u_s^{n-1}}{(k^n + u_s^n)^2}$. The additional term $2D\Big[\cos(\frac{2\pi q}{N}) - 1\Big]$ appears due to the Fourier decomposition of the perturbations around the homogeneous steady state (see Part I), and will be the one dictating the spatial modes that will become unstable if any instability occurs. The wavenumber $q \in [0, N]$ will tell us the specific spatial mode that dominates such instability. The characteristic polynomial of the Jacobian $J = J_0 + J_1$ can be written as $\lambda^3 + a_2\lambda^2 + a_1\lambda + a_0 = 0$, where $\lambda$ are the eigenvalues of the system, and again:

$$\begin{gathered} a_2 = b_1 + b_2 + b_2, \quad a_1 = b_1 b_2 + b_1 b_3 + b_2 b_3 - \delta k_c v_s - \delta k_c u_s - k_c u_s b_4 \\ a_0 = b_1 b_2 b_3 + \delta k_c^2 u_s v_s + \delta k_c u_s b_4 - \delta k_c v_s b_2 - k_c u_s b_3 b_4 - \delta k_c u_s b_1 \\ b_1 = d_u + k_c v_s, \quad b_2 = k_c u_s + d_v \\ b_3 = \delta + d_c + 2D - 2D\cos(2\pi q/N), \quad b_4 = \mathcal{F} + k_c v_s \end{gathered} \tag{7.11}$$

By numerically solving the characteristic polynomial, we can identify four distinct dynamical regimes depending on the real and complex parts of $\lambda$ (Figure 7.14). In the first of these scenarios, dubbed *homogeneous regime*, all the modes $q$ have $\mathrm{Re}(\lambda_q) < 0$, implying that there cannot be any spatial instability and the system ends up in a linearly stable homogeneous steady state, with the same stationary values of $(u_s, v_s, c_s)$ as in the uncoupled case. When there are modes fulfilling $\mathrm{Re}(\lambda_q) > 0$ and $\mathrm{Im}(\lambda_q) = 0$, the homogeneous steady state becomes linearly unstable, and pattern formation is possible. In this regime, hereafter dubbed *Turing regime*—in a nod to Turing patterns induced by diffusion —the fastest growing mode corresponds to the wavenumber $q = N/2$, suggesting that the emerging patterns will have periodicity $N/q = 2$, i.e. there will be a spatial alternation of cell states with high $u$ low $v$ and with low $u$ and high $v$. A third regime, the *Hopf regime*, corresponds to having modes fulfilling $\mathrm{Re}(\lambda_q) > 0$ and $\mathrm{Im}(\lambda_q) \neq 0$, which lead to the formation of bulk oscillations, where the whole system is expected to cycle homogeneously. Finally, a fourth *Turing-Hopf regime* is possible, where some modes have $\mathrm{Re}(\lambda_q) > 0$ and $\mathrm{Im}(\lambda_q) \neq 0$ and others have $\mathrm{Re}(\lambda_q) > 0$ and $\mathrm{Im}(\lambda_q) = 0$, i.e. there is coexistence between modes associated with bulk oscillations and stationary patterns.

In Figure 7.15 we show the different regimes obtained from linear stability analysis in the $(\alpha, \gamma)$ plane, and in Figure 7.16 their corresponding dynamical behaviours obtained by numerically integrating the dynamical equations. In the homogeneous regime, the system simply ends up in a homogeneous steady

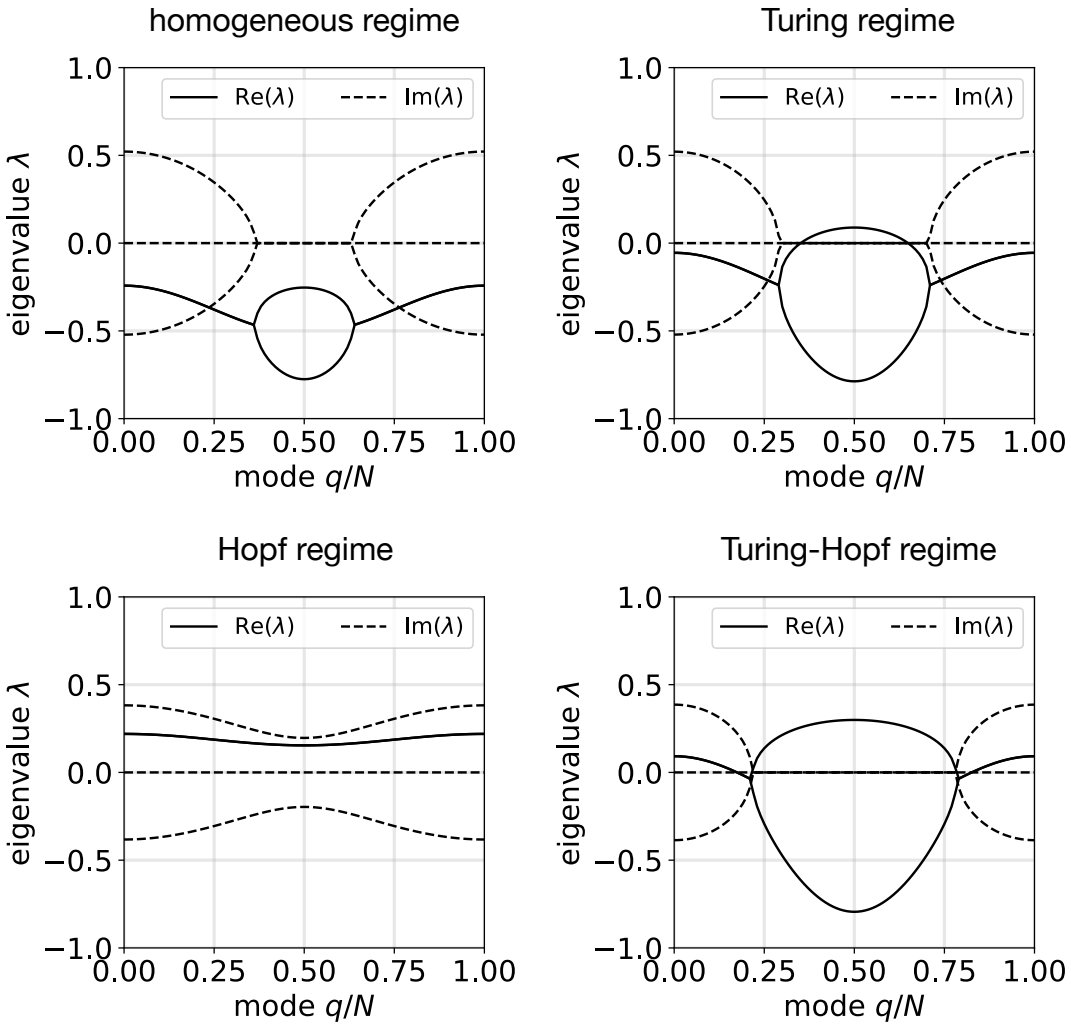



**Figure 7.14: Eigenvalues $\lambda$ of the spatially extended system as a function of Fourier modes $q/N$.** Depending on the nature of the eigenvalues of the system, distinct patterning regimes are possible. In the homogeneous regime, the homogeneous state is stable; in the Turing regime, the homogeneous state loses stability and patterns with periodicity $N/q_c = 2$ appear; in the Hopf regime, the system oscillates homogeneously; in the Turing-Hopf regime, modes associated with periodic patterns and homogeneous oscillations coexist. The common parameter values in all the panels are $\alpha = 10$, $d_u = d_v = 1$, $k = 8$, $k_c = 1$, $n = 4$. The remaining parameters are $D = 0.2$, $\gamma = 30$, $d = 10$ in the homogeneous regime, $D = 0.2$, $\gamma = 50$, $d = 10$ in the Turing regime, $D = 0.04$, $\gamma = 100$, $d = 10$ in the Hopf regime and $D = 0.2$, $\gamma = 50$, $d = 5$ in the Turing-Hopf regime. System size is $N = 100$.

state, as expected from linear stability analysis. The continuous curve enclosing the turquoise region corresponds to the Turing bifurcation, where the eigenvalue associated with the mode $q_c = N/2$ has $\mathrm{Re}(\lambda_q) = 0$ and $\mathrm{Im}(\lambda_q) = 0$. Inside the Turing region, salt-and-pepper patterns are possible, and emerge from an instability of the spatially homogeneous state (Figure 7.16 top right). In these patterns, states where cells alternate periodically in space appear, as expected from the periodicity of the largest growing mode $q = N/2$ predicted from linear

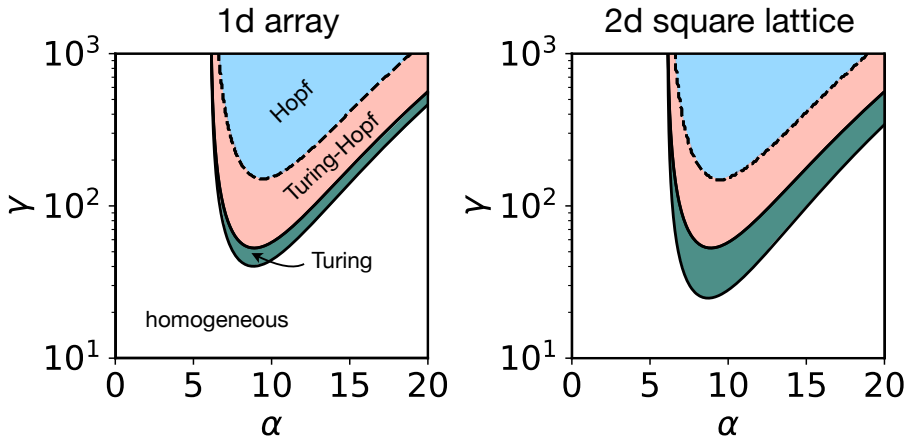



**Figure 7.15: Stability diagram of the spatial RMFL.** Regions in the $(\alpha, \gamma)$ space where distinct dynamical regimes appear. In the Turing region (turquoise), periodic pattern can emerge. In the Turing-Hopf region (light red), patterns and oscillations can coexist if the real part of the associated eigenvalues are similar. If not, the regime with the associated eigenvalues with largest real part will dominate over the other. In the Hopf regime (light blue), the system exhibits bulk oscillations. The rest of the parameters are $k = 8$, $n = 4$, $d_u = d_v = 1$, $k_c = 1$, $\delta = 10$, $D = 0.3$.

stability analysis. The continuous line enclosing the light red region corresponds to the transition from the Turing regime to the Turing-Hopf regime, where a pair of conjugate eigenvalues with positive real part associated with the homogeneous modes $q_c = 0, N$ appear. In the Truing-Hopf regime of coexistence, we observe that the dominating mode—the mode associated with the eigenvalue with largest real part—dictates the final state of the system. If these are oscillatory modes (i.e., $Im(\lambda_q) \neq 0$), then the system keeps oscillating. If instead the dominating modes are of the Turing type ($Im(\lambda_q) = 0$), cells can either rapidly form patterns, or oscillate during some time only to become arrested into the patterned state (Figure 7.16 bottom right). In this hybrid regime, the time of the oscillatory transient before a patterned state will depend on the initial conditions of the system.

Thus, we see that when the RMFL becomes coupled diffusively, novel types of spatiotemporal behaviours can appear. A particularly interesting feature revealed by linear stability analysis, consistent with the behaviours found in the two-cell system, is that periodic patterns can emerge either from a spatially homogeneous steady state or from uniform bulk oscillations. In the first case, the homogeneous state loses stability due to diffusion, similar to the instabilities observed in classic Turing systems. The resulting patterns consist of alternating cells with opposite fates, with periodicity dominated by the modes $q = N/2$. These patterns bear a striking similarity to the salt-and-pepper patterns displayed by Notch-Delta interactions (Figure 7.16 and Figure 7.17), even though the underlying mechanisms are very different—one via paracrine (diffusive) signalling, the other through juxtacrine (direct cell-to-cell contact) signalling.

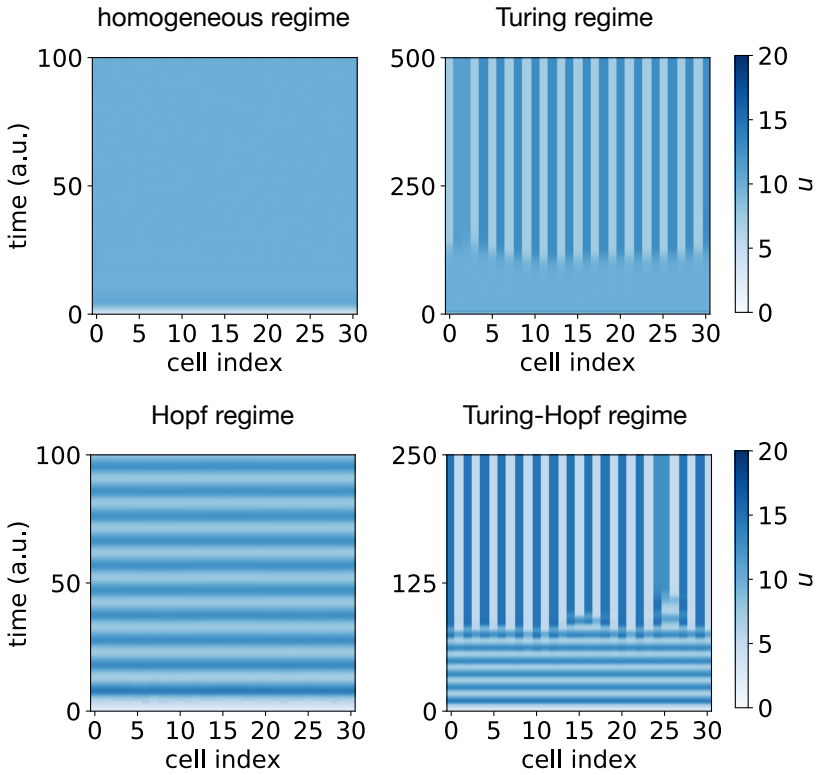



**Figure 7.16: Dynamics for 1D patterns in different regimes.** Cellular array of size $N = 30$ showing the activity of $u$. In the homogeneous regime, uniform patterns are stable. In the Turing regime, homogeneous patterns lose stability due to diffusion, leading to lateral inhibition patterns, where cells alternate their states between high and low $u$. In the Hopf regime, the system oscillates as a whole. In the Turing-Hopf regime, bulk oscillations become unstable, generating once more lateral inhibition patterns. Parameter values for each regime are the same as in Figure 7.14. Initial conditions for the simulations are $u_0 = \mathcal{U}_N[0, 10]$, $v_0 = \mathcal{U}_N[0, 10]$, $c_0 = \mathcal{U}_N[0, 100]$, where $\mathcal{U}_N$ is a random uniform distribution of length $N$, the number of cells.

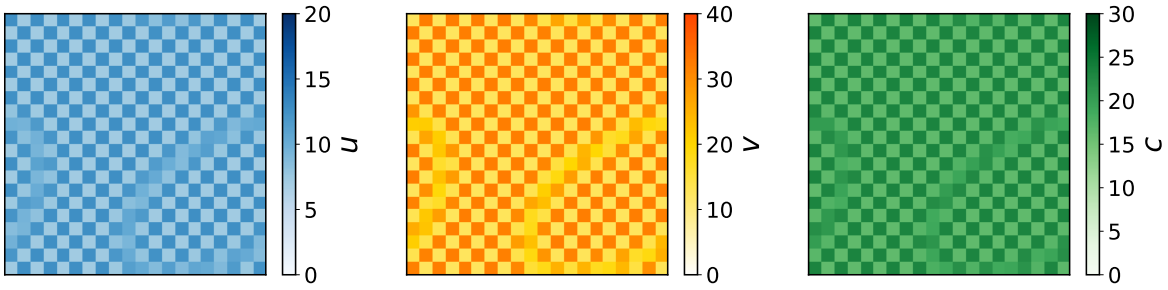



**Figure 7.17: Salt-and-pepper patterns in the two-dimensional RMFL.** Square cellular array of size $20 \times 20$ displaying salt-and-pepper patterns. The patterns emerge through a Turing instability of the homogeneous state. Parameters are $\alpha = 10$, $\gamma = 50$, $k = 8$, $n = 4$, $d_u = d_v = 1$, $k_c = 1$, $\delta = 10$, $d_c = 0$, $D = 0.1$.

When the system is in the Turing-Hopf regime and the Turing modes dominate, bulk oscillations are unstable, but can appear transiently if there is low

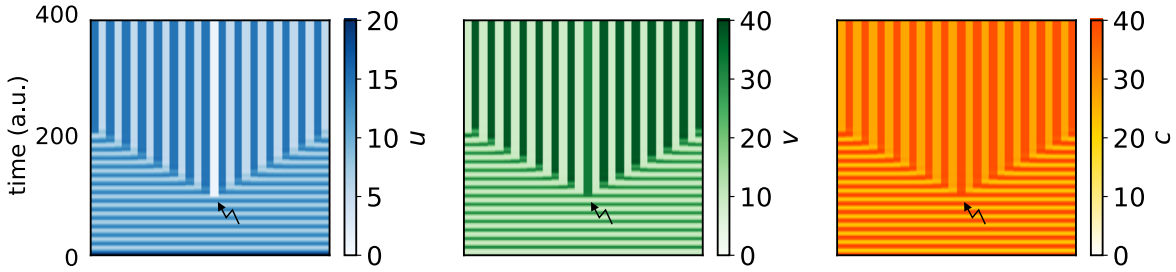



**Figure 7.18: Oscillations can be destabilized upon a perturbation.** In the Turing-Hopf regime, depending on the eigenvalue with largest real part, only one type of pattern will be stable. In this case, since the eigenvalue corresponding to the Turing modes has larger real part, oscillations can rapidly become arrested upon a perturbation (in this case, we impose $u_{15} = 1$ for $t > 100$, leading to a patterned state formed as a travelling wave propagates across the whole system. Initial conditions are $(u_0, v_0, c_0) = (0, 0, 0)$ for all cells, avoiding any variability. Parameters are $\alpha = 10$, $d_u = 1$, $k_c = 1$, $\delta = 5$, $d_v = 1$, $\gamma = 50$, $k = 8$, $n = 4$, $D = 0.2$.

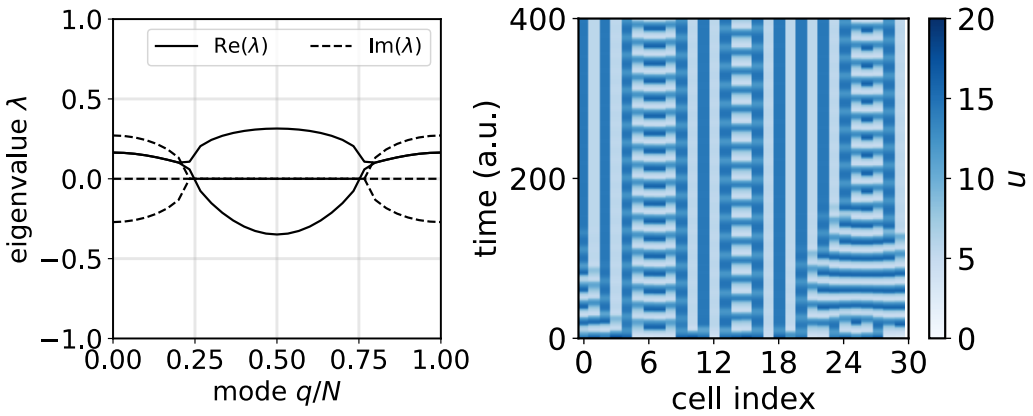



**Figure 7.19: Chimeras: coexistence between oscillations and pattern.s Left:** Oscillatory and Turing modes coexist, and the real part of the corresponding eigenvalues are similar. **Right:** Some cells keep oscillating while others remain in a patterned state. Initial conditions for the simulations are $u_0 = \mathcal{U}_N[0, 10]$, $v_0 = \mathcal{U}_N[0, 10]$, $c_0 = \mathcal{U}_N[0, 100]$, where $\mathcal{U}_N$ is a random uniform distribution of length $N$, the size of the domain. Parameters are $\alpha = 10$, $d_u = 1$, $k_c = 1$, $\delta = 3$, $d_v = 1$, $\gamma = 50$, $k = 8$, $n = 4$, $D = 0.1$.

variability in initial conditions, only to become arrested in a salt-and-pepper pattern (Figure 7.16). In this parameter space but without diffusion the system is oscillatory (as in Figure 7.7, Middle), meaning that salt-and-pepper patterns appear due to a diffusion induced instability of the oscillatory homogeneous state. If there is no variability in initial conditions, the system can remain in an oscillatory state indefinitely. In this regime, a perturbation in some of the cells can rapidly lead to pattern formation, which is progressively formed as a travelling wave induced by the perturbation propagates across the system (Figure 7.18).

In the Turing-Hopf regime, it is also possible that the real parts of the eigen-

values associated with oscillatory and Turing modes have similar values. In these special cases, oscillations and patterns can be both stable, and the system can be partitioned into regions with oscillatory activity and regions with patterns (Figure 7.19). We call these spatiotemporal states *chimeras* (or chimera states), in allusion to the chimeras observed in ensembles of coupled oscillators, spatiotemporal states characterized by the coexistence between synchronous and asynchronous oscillations [Panaggio and Abrams, 2015, Dudkowski et al., 2014]. In our case, however, coexistence happens between oscillations and patterns, not between synchronous and asynchronous oscillations, so the two definitions of chimera states differ.

### 7.3.3 Noise-induced phenomena

As in the spatially uncoupled case, we explored how the system behaves when intrinsic noise stemming from the molecular interactions is taken into account. By numerically exploring the system with the chemical Langevin equation (see Chapter 3), we found that the system can exhibit noise-induced patterns. In Figure 7.20, we show these patterns for the parameters $\alpha = 1, d_u = 0.6, k_c = 2, \delta = 0.2, D = 0.075 - 0.2, \gamma = 5, k = 1, m = 4$ and system size $\Omega = 10^6$ (Figure 7.20). These patterns are static and appear when some parts of the system reach stable equilibrium while others keep oscillating, until the whole system ends up in the steady state. More formally, this happens in the Turing-Hopf regime, when oscillatory and patterning modes coexist. If patterning modes dominate and there is no variability in initial conditions, the system may begin to oscillate in bulk, but due to a large enough fluctuation a cell may become arrested, generating a perturbation that progressively propagates across the whole system in an oscillatory manner (similar to what happens in Figure 7.18). As the bulk of the system keeps oscillating, the fronts reaching the stable regions become arrested, and the cycle repeats until the whole system reaches the patterned steady state Figure 7.21. The approximately circular nature of the patterns appears due the symmetry of the diffusive coupling, together with the progressive arrest of oscillations at single points in space. Importantly, these patterns can only be observed if there is low variability in initial conditions, as otherwise initial spatial differences in the variables would dominate over fluctuations, leading to patterns without apparent structure. When there is low variability, the occasional arrest of the oscillations in specific locations of the system is purely induced by noise. If noise strength is larger (smaller $\Omega$), the fluctuations arresting the oscillatory state in space become much more frequent, thus preventing the observation of well-defined patterns.

An additional source of variability can come from irregularities in cell shapes. We explore how these static perturbations affect the dynamics in the Turing-Hopf regime. In Figure 7.22 we show patterns obtained with same parameter set as in Figure 7.20, in the absence of noise. Just like dynamic fluctuations

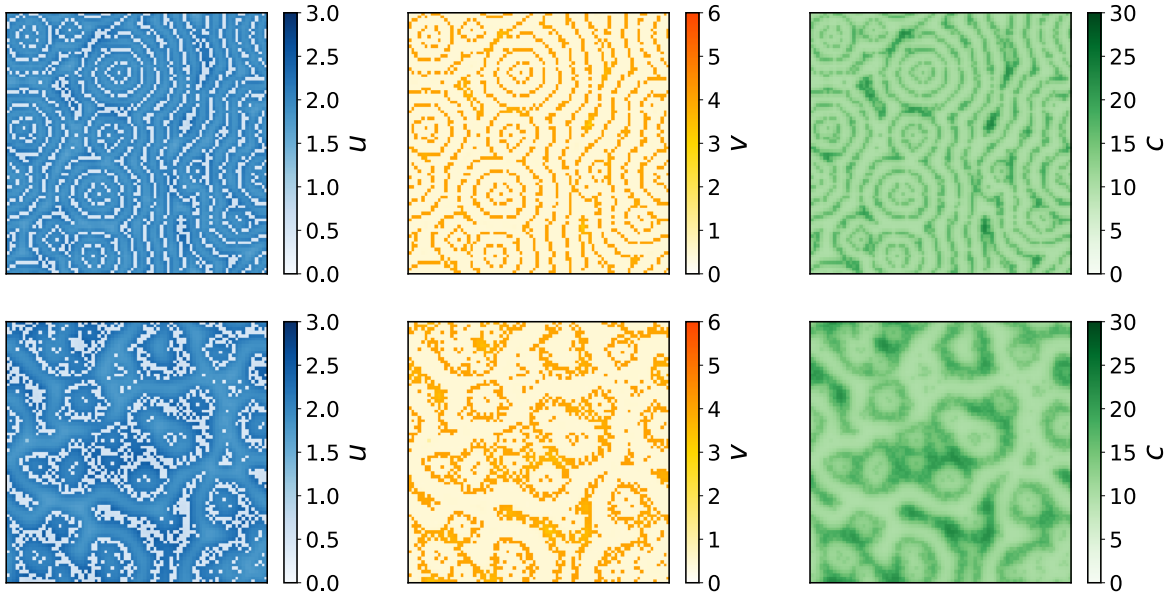



**Figure 7.20: Circular patterns emerging due to the arrest of oscillatory fronts.** Close to the Turing-Hopf instability, homogeneous oscillations can become arrested when they collide with stable regions which emerge due to noise. Simulations have been performed with a lattice size of $80 \times 80$ and $D = 0.075$ (Top panels), and $D = 0.2$ (Bottom panels). The rest of the parameters are $\alpha = 1$, $\gamma = 5$, $k = 1$, $n = 4$, $d_u = 0.6$, $d_v = 1$, $k_c = 2.1$, $\delta = 0.2$, $d_c = 0$. In both cases, the volume of the system is $\Omega = 10^6$. Initial conditions are set to $(u_0, v_0, c_0) = (0, 0, 0)$ for all cells.

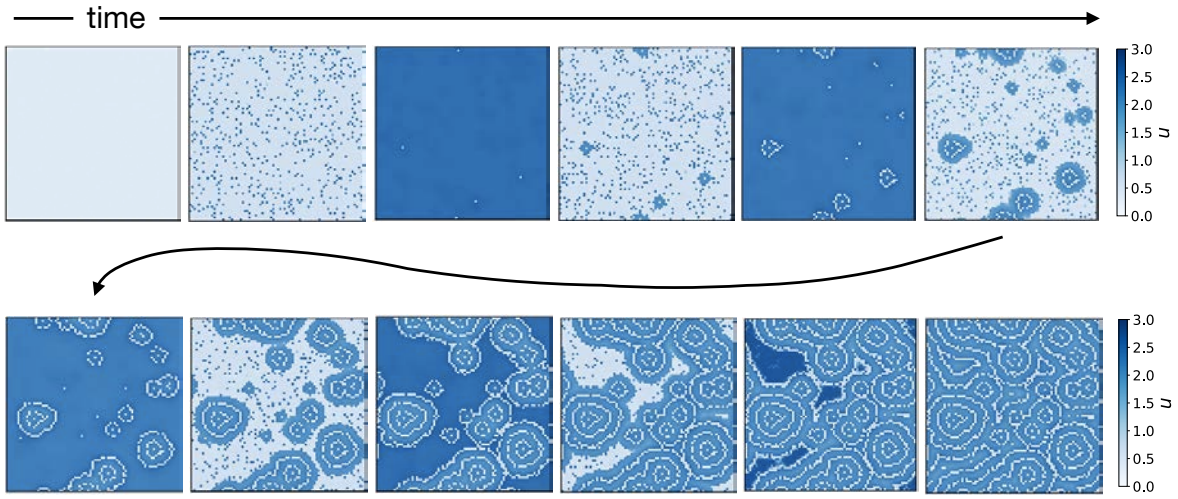



**Figure 7.21: Time evolution of circular patterns.** In the Turing-Hopf regime, when Turing modes dominate but the system begins with initial conditions with low variability, the system can oscillate for some time, until large enough fluctuations arrest some of the cells, which will subsequently arrest the oscillatory fronts, forming circular patterns. Parameters and initial conditions as in Figure 7.20 (Top).

can to induce spatial structures, the disorder provided by the irregular cellular layout can also drive the arrest of oscillations.

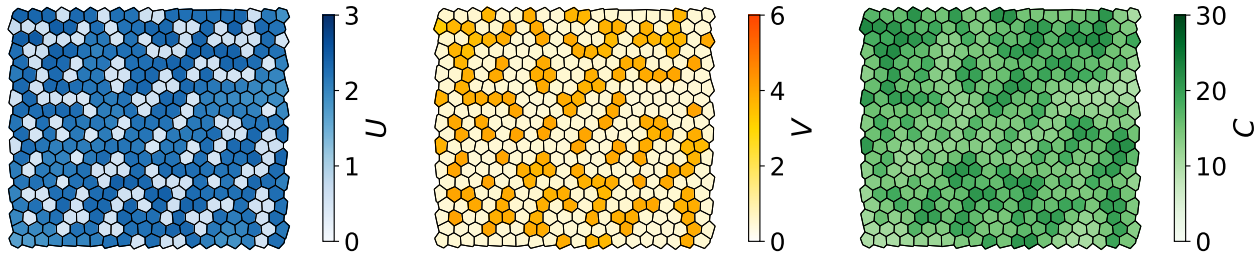



**Figure 7.22: Patterns in irregular lattices.** In the Turing-Hopf regime, oscillations can be arrested due to variability in the cellular structure of the tissue. The more variability, the faster the arrest will occur.

## 7.4 Discussion

In this chapter we have explored the dynamical behaviours of a reversible version of the mixed feedback loop (RMFL) genetic circuit, showing that, in the spatially uncoupled case, it can display both oscillatory and bistable activity without changing the qualitative nature of the interactions. Bistability appears through a saddle-node bifurcation due to the double negative feedback conferred by the negative regulation plus complex formation, and is promoted by high complex degradation. Oscillations, for their part, emerge through a Hopf bifurcation when the degradation of the complex is small. Due to their antagonistic dependence on complex degradation, the two regimes do not overlap, making the RMFL functionally modular.

The structural simplicity of the RMFL, together with its functional diversity, points to a widespread role in the functioning of gene regulatory networks. Indeed, the MFL has been found to be involved in the regulation of many cellular processes in eukaryotes, including the NF-$\kappa$B signalling pathway in mammalian cells [Krishna et al., 2006], in the pathway of the p53 tumor suppressor protein [Bar-Or et al., 2000], or in the circadian clock of the fungus *Neurospora crassa* [Loros and Dunlap, 2001, François, 2005] (see [François and Hakim, 2005] for a more exhaustive list). In most of these cases, the system displays oscillatory behaviour, whereas bistability is rarely observed. Up to our knowledge, in any of these studies the specific role of the complex has been assessed. Given its strong effect on the dynamical repertoire of the MFL, it would be interesting to consider whether complex reversibility is possible in such systems.

More broadly, the RMFL may have a wide range of applicability in the context of developmental biology. Switching from one type of behaviour to another in response to different environmental cues is a hallmark of developmental processes. The dynamical modularity exhibited by the RMFL may constitute one such a way to achieve this multi-functionality without compromising the circuit's structure. It's important to stress that the RMFL, while functionally modular—as distinct dynamical behaviours such as bistability and oscillations

do not generally overlap in phase space—, it is *not* structurally decomposable: take out any of its constituent interactions and multi-functionality disappears. In this sense, the RMFL is an instance of circuit displaying complete *emergent* modularity, i.e. it is not decomposable into its simpler building blocks, but all their activities are carried out by the same set of components [Jaeger and Monk, 2021b]. This contrasts with hybrid multi-functional networks, where there is no structural overlap between components that carry out different functions. In general, multi-functional networks are neither completely hybrid nor purely emergent, but fall somewhere in between. For example, the AC-DC circuit, consisting of a three-gene repressilator coupled with a toggle switch between two of them [Panovska-Griffiths et al., 2012, Perez-Carrasco et al., 2018] (see Figure 7.1) is one of such circuits. While both the repressilator and the toggle-switch have distinct functions—oscillations and bistability, respectively—eliminating one of these interactions within the circuit—for instance, removing the toggle-switch but keeping the structure of the repressilator—does not impair the circuit's ability to oscillate. However, eliminating the interaction of the toggle-switch that interferes with the mutually inhibitory nature of the repressilator may completely destroy the ability of the circuit to display multi-functionality.

This might have important implications for evolution. More often than not phenotypic traits evolve independently from other traits, suggesting that functional modularity is present in their underlying generative processes [Hansen, 2003, Wagner, 2008]. As has been pointed out, functional dissociability is a prerequisite for evolvability, while structural modularity is not [Wagner and Altenberg, 1996]. Evolvability can be thought of as the propensity of a particular trait to vary, given the constraints imposed by the underlying genetic architecture [Wagner and Altenberg, 1996, Pigliucci, 2008]. For instance, the lack of structural modularity of the RMFL circuit implies that mutations in any of its constituent parts (say, in the structure of one of its proteins which prevents subsequent binding) will simultaneously interfere with its ability to display both oscillations and bistability. In this sense, strong mutations affecting the very structure of the system completely destroy its multi-functional nature. If these functions have important roles in the workings of gene regulatory networks, then these kind of mutations can be detrimental, and the circuit might solidify into a configuration with low evolvability [Jiménez et al., 2017]. However, progressive changes that allow the circuit to explore the space of multi-functionality—for example, via small variations in the parameters controlling the molecular reactions—, but that are not strong enough to completely destroy it, might constitute a route for phenotypic variability, and therefore a substrate for evolutionary change to take place.

Introducing spatial coupling to the RMFL via the diffusion of the complex leads to a rich repertoire of spatiotemporal behaviours, such as salt-and-pepper patterns, chimera states where oscillations and stable patterns coexist, or static

concentric circles induced by noise, further highlighting the multi-functional nature of the circuit. We see most of these spatiotemporal structures as being relevant in the context of developmental biology. The ability of the RMFL to generate periodic patterns is perhaps the most direct, as it provides an alternative mechanism to standard lateral inhibition. While the formation of salt-and-pepper patterns is usually mediated juxtacrine signalling (as in the case of Notch and Delta), those observed in the RMFL rely instead on paracrine signalling, which is mediated by the diffusion and subsequent dissociation of the complex. This has important implications, as depending on the specific values of the parameters, these patters can emerge either from a spatially homogeneous state or from bulk oscillations.

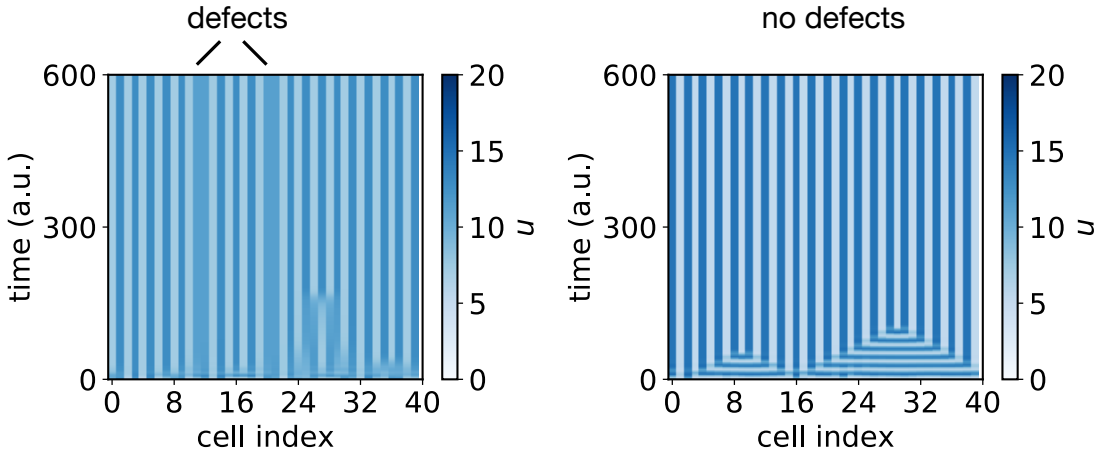



**Figure 7.23: Oscillatory transients prevent the appearance of pattern defects.** Simulations where there is cell to cell variability in initial conditions, in this case with $u_0 = \mathcal{U}_N[0, 10]$, $v_0 = \mathcal{U}_N[0, 10]$, $c_0 = \mathcal{U}_N[0, 30]$, where $\mathcal{U}_N$ is a random uniform distribution of length $N$, the size of the domain. **Left:** In the Turing regime, variability in initial conditions leads to patterning defects. **Right:** Cellular synchronization due to bulk oscillations allows the system to avoid patterning defects. Common parameters are $\alpha = 10$, $\gamma = 50$, $k = 1$, $n = 4$, $d_u = 1$, $d_v = 1$, $k_c = 1$, $D = 0.2$. In the left panel $\delta = 10$ (Turing regime), while in the right panel $\delta = 5$ (Turing-Hopf regime).

This latter situation is quite interesting, as the synchronized oscillations preceding the formation of the patterns might constitute a mechanism for avoiding patterning defects. In standard lateral inhibition, cell to cell variability in initial conditions might lead to imperfect periodicity, a situation which would be mitigated if cellular states previously synchronize in an oscillatory fashion, as any initial variability would smooth out (Figure 7.23). In the RMFL, the synchronization of oscillations between cells is a direct consequence of diffusive coupling. Remarkably, it is the same diffusive coupling that destabilizes the oscillations and leads to pattern formation. Recent results suggest that signalling delays in a simplified model of lateral inhibition—which generate an oscillatory transient before pattern formation—may constitute a mechanism to avoid patterning defects [Glass et al., 2016]. A next step on this line is to quantify

how these defects explicitly depend on this transient, and which are the critical parameters controlling such process.

Oscillations and periodic patterns pervade developmental processes, and rapidly switching between the two may constitute a suitable mechanism for interpreting external signals. The segmentation clock is an archetypical example where oscillatory activity (periodicity in time) is translated into patterns (periodicity in space). During vertebrate embryogenesis, synchronized oscillations in the posterior cells of the body become arrested as the embryo grows, partitioning the trunk into well-spaced segments [Hubaud and Pourquié, 2014]. How this happens has been traditionally explained through the clock-and-wavefront model, where oscillatory activity becomes frustrated due to a signalling gradient which forms as the body grows [Cooke and Zeeman, 1976]. However, since the nature of oscillations in posterior cells still remains poorly understood, recent studies have challenged this view. For example, [Cotterell et al., 2015] have proposed an alternative version for somitogenesis though a reaction-diffusion mechanism, which solely involves short-range interactions, without the need of an external signalling gradient. This model has been mathematically studied in detail in [Pantoja-Hernández et al., 2021]. The mechanisms by which the RMFL leads to patterning from an oscillatory transient might be of interest in this context. In the Turing-Hopf regime, if patterning modes dominate, oscillations can be arrested either due to variability in initial conditions (the time of arrest depending on the specific form of such variability), through an external perturbation (Figure 7.18) or through noise (Figure 7.20 and Figure 7.21). Thus there are at least three ways of controlling the time of arrest which can be exploited by the organism to generate periodic patterns. While true coexistence between patterns and oscillations only exists when the two corresponding modes dominate (i.e. when the real part of their associated eigenvalues is similar), there is another way to induce such behaviours without the need of overlapping modes: by introducing signalling gradients. In this way, stable oscillations and patterns can coexist because their associated modes are dominant in different regions of space, but without true local coexistence. How signalling gradients affect the spatiotemporal behaviours of the RMFL remains to be explored, but in light of its already diverse dynamical repertoire, novel outcomes are to be expected.

Biological development involves a very tight coordination between gene expression in time and space. The processes involved in such an unfolding do not solely depend on the interactions between genes, but also on its dialectical association with the environment, partly random and unpredictable, partly constructed by the organism itself [Levins and Lewontin, 1985]. Indeed, no embryo grows without a warm womb or a protected egg. Understanding development is understanding how diverse functions or phenotypic traits arise from these relationships. The study of simple gene regulatory circuits such as the reversible mixed feedback loop, which are capable of performing multiple functions depending on different environmental cues, is thus of utmost importance for un-

derstanding how gene regulatory networks reliably specify functional traits, how they endow traits the capacity to evolve, and how this ultimately leads to the extraordinary complexity of living systems.

# Part IV

# Conclusions

# Chapter 8

# Conclusions and perspectives

The ideas put forward in this thesis can be broadly framed within the context of developmental biology. Our approach has mainly relied on developing theoretical models to understand genetic circuits underlying cellular decision-making, be it in stem cells (as in the BRAVO and WOX5 circuit of Chapter 4 and Chapter 5), epidermal cells (rhizoid precursors in the *Marchantia* gemmae of Chapter 6) or in more generic contexts (as in Chapter 7). In this last chapter we outline the main conclusions of each chapter, as well as the perspectives we can envisage for future research.

In Part II, we focused on the regulatory interactions between BRAVO and WOX5, two transcription factors involved in the regulation of quiescent center cells in the *Arabidopsis* root stem cell niche.

- In Chapter 4, these interactions have been studied by considering the stem cell niche as a whole, without taking into account spatial effects. The main findings of this work can be summarized as follows:
  - BRAVO and WOX5 interact in a feedback circuit whose effective regulations include the activation of BRAVO by WOX5, the activation of WOX5 by BRAVO and the negative feedbacks of BRAVO and WOX5. With these regulations we are able to explain the behaviour of all loss of function and overexpressor mutants.
  - The effective activation of WOX5 by BRAVO can be understood as a double repression, where BRAVO alleviates the negative feedback of WOX5. Parameter exploration and comparison with experimental data favours this regulation, as opposed to an actual activation of WOX5 by BRAVO.
  - The alleviation of the WOX5 self-repression by BRAVO can be molecularly realized by the formation of a complex between BRAVO and WOX5, an interaction observed experimentally.

  - The interactions between BRAVO and WOX5 suggest a mechanism for the regulation of stem cell quiescence, where the complex is expected to play a fundamental role.

  An immediate line for further research would be to confirm (or disprove) that the complex is indeed the factor controlling stem cell quiescence. Studying the protein structure of BRAVO and WOX5, how do they bind and how the complex may regulate cell cycle genes would shed light on this process.

  The fate of cells in the *Arabidopsis* root stem cell niche is tightly regulated by multiple signals, including transcription factors, hormones or reactive oxygen species. A natural question is thus to understand the role of these other signals in the behaviour of the BRAVO-WOX5 circuit. Brassinosteroids have already been shown to affect both the activity of BRAVO and WOX5, but other hormones such as auxins and cytokinins may also play a part yet to be uncovered. WOX5 has also been shown to interact with other factors such as PLTs, as well as with the peptide CLE40. Disclosing how is BRAVO affected by these molecules would add further insight into the structure and behaviour of the intricate networks regulating stem cell maintenance.

  On a broader scale, understanding the general mechanisms by which quiescent cells remain in an undifferentiated state and only occasionally undergo division, will elucidate the role they play in maintaining stem cell niche homeostasis, and how this contributes to the proper functioning of the plant.

- Chapter 5 is a follow-up of Chapter 4, where the BRAVO-WOX5 interactions are evaluated in a spatial context. To model this situation, we include the diffusion of WOX5, which can move outside the quiescent center and is able to activate BRAVO therein. With this approach, we found that:

  - The formation of a complex, together with the activation of BRAVO by WOX5 is enough to explain the spatial behaviour of BRAVO expression, including the expansion of the activity domain of the BRAVO promoter in *bravo* loss of function mutants.
  - In WT plants, BRAVO, by interacting with WOX5 both transcriptionally and through the formation of a complex, actively confines its own expression domain the stem cell niche. Incidentally, these interactions also confine the domain of WOX5 activity to the quiescent center.
  - A mechanism involving the repression of an intermediary activator by BRAVO can also participate in the process to confine BRAVO expression.

  - Modelling the system in a realistic root layout accurately recapitulates the expression patterns of both BRAVO and WOX5 both in the WT and in loss of function mutants.
  - We propose a mechanism of self-confinement which involves the attenuation of a mobile activator. This mechanism can take place in two different ways: by immobilization of the mobile activator, or by reducing the production of the activator.

What is the role of BRAVO self-confinement in the *Arabidopsis* stem cell niche? One possibility would be that, like *Dpp* in *Drosophila* or *Shh* in mice, BRAVO is needed to maintain a proper pool of stem cells in an undifferentiated state. Finding whether BRAVO affects VI cell homeostasis would shed light on the problem.

As modelling becomes more and more common in plant biology, having a diverse spectrum of mathematical and computational approaches will provide the necessary toolkit to tackle biological question from diverse points of view. The framework we use in this chapter, consisting of the modelling of several molecular species in a realistic root layout via heterogeneous reaction-diffusion equations, constitutes a novel approach which can be exploited to study not only roots, but shoots, leaves or any spatially extended system where distinct diffusion coefficient might be at play.

It has been proposed that non-linear degradation, and in particular processes involving sequestration of morphogens by receptors, might confer robustness of signalling gradients upon changes in the production rate of such molecules at their source [Eldar et al., 2003, Shilo and Barkai, 2016]. Making the analogy of WOX5 acting as a morphogen, then its interaction with BRAVO may constitute a way to maintain a "robust" activity profile in the face of fluctuations or external disturbances affecting the state of QC cells. It would be interesting to test this hypothesis by perturbing such states with the exogenous induction of hormones such as brassinosteroids or auxin, or by subjecting plants to stresses such as drought or cold.

Part III has focused on the role of gene circuits operating in cellular layouts coupled by the diffusion of one of the molecules, and how such interactions are able to generate patterned structures of different cell types. We develop models based on reaction-diffusion equations, but the peculiarity that diffusive interactions are not implemented in a continuum but in a discrete lattice, where each node represents a cell. We apply this approach to the formation of rhizoid precursor patterns in the *Marchantia* epidermis (Chapter 6) and in a generic circuit (Chapter 7)

- In Chapter 6 we proposed a reaction-diffusion model for the formation and maintenance of rhizoid precursor patterns in the epidermis of *Marchantia*

*polymorpha* gemmae. Rhizoid specification is dependent on the interactions between RSL1 – which induces rhizoid formation – and the microRNA FRH1, which is able to repress the activity of RSL1 [Honkanen et al., 2018, Proust et al., 2016, Thamm et al., 2020]. These factors have been shown to interact as an activator-inhibitor system [Thamm et al., 2020], but the consequences of such interactions had not been previously explored. The conclusions of our work are:

- A null model where the distribution of rhizoid precursors is completely random and rhizoid precursors emerge through cell-autonomous choices is not able to recapitulate experimental observations. This supports the view that lateral inhibition interactions between cells are needed, as previously proposed [Thamm et al., 2020].
- Bistability in the activity of RSL1 provides a natural way for the binary nature of cells in the gemma epidermis, namely rhizoid or epidermal cell. For instance, this bistability can be achieved through the self-activation of RSL1.
- The activator-inhibitor structure of the RSL1-FRH1 system provides a natural way to generate the patterns observed experimentally. In particular, diffusion of FRH1 to neighbouring cells acts as a lateral inhibition mechanism, leading to the formation of mainly filamentous clusters of rhizoid precursors.
- To generate the characteristic patterns observed experimentally, lateral inhibition must act hand-in-hand with a random component stemming from variability in the initial states of the cells.
- With the introduction of two new measures, namely 1) the fraction of clusters of a certain size and type among the totality of clusters and 2) the fraction of cells with a certain number of neighbours for a cluster of a certain size, we are able to compare experimental measurements of cluster structure with the predictions of the model, finding excellent agreement.

Rhizoids mainly function as anchors to the soil and as nutrient-absorbing devices. But both rhizoids and epidermal cells must coexist in gemma epidermis, as each type has its specific functions. One thus may ponder on the origins of the specific fraction of rhizoids to epidermal cells, and on the structure and distribution of rhizoid clusters. Is there any adaptive explanation for such patterns? In particular, what is the role of lateral inhibition in such a process? Exploring how rhizoid specification happens in other species of the genus *Marchantia*, or even in other evolutionarily more distant liverworts, might shed some light on these questions.

On this line, experiments such as growing plants under water or nutrient deficiency and observing the changes (or lack of) in the distribution of

rhizoids changes might also illuminate the specific functions of rhizoids and their distribution across the gemma epidermis.

More specific to the particular regulations between RSL1 and FRH1, another interesting problem would be to find other factors affecting the distribution of rhizoids and how these can be understood within the context of the RSL1-FRH1 circuit. Among these factors auxin has been shown to promote the activity of RSL1, so it would be interesting to test its effect on rhizoid formation in *Marchantia*.

Activator-inhibitor systems such as the RSL1-FRH1 are known to be able to display Turing patterns. The prospect of having distinct kinds of rhizoid patterns is appealing to a modeller, as it would provide direct evidence that the regulatory interactions between RSL1-FRH1 and indeed at work. Perturbing *Marchantia* gemmae with exogenous factors or growing them in distinct conditions might be an approach to test this hypothesis.

Finally, although is not shown in this thesis, exploring the dynamics of the RSL1-FRH1 circuit reveals distinct dynamical regimes such as oscillatory states and excitability. Whether such behaviours are possible *in planta*, and whether they have a functional role in the developmental processes of *Marchantia* gemmae are other interesting ideas worth testing.

- In Chapter 7 we studied a small regulatory circuit—the reversible mixed feedback loop (RMFL)—, consisting of a trascriptional repression and the formation of a protein complex. The system is multi-functional, i.e., it can exhibit a wide spectrum of dynamical regimes, including monostability, bistability and oscillations. When spatial coupling is introduced via diffusion of the protein complex, additional spatiotemporal structures can emerge, including salt-and-pepper patterns, chimera states or concentric circles induced by noise.

  - In contrast to the original mixed feedback loop proposed by [François and Hakim, 2005], the bistable and oscillatory regimes in the RMFL emerge without changing the nature of the transcriptional regulations. Notably, this multi-functionality only happens when complex formation is reversible.
  - While bistability is expected in the RMFL with transcriptional repression, oscillations are novel, and can emerge sharply and with a large amplitude. Close to the subcritical Hopf bifurcation, the system can be excitable, a property that can be exploited by introducing fluctuations, leading to noise-induced oscillations in a parameter regime where the deterministic counterpart does not oscillate.
  - Introducing spatial coupling between cells through the diffusion of the complex generates additional spatiotemporal structures, including salt-

and-pepper patterns, bulk oscillations, oscillatory transients which become arrested to form salt-and-pepper patterns, or chimeras, states where oscillatory and patterned regions coexist.

- Diffusion of the reversible complex in the RMFL constitutes a novel mechanism to drive lateral inhibition.
- Pattern states can emerge either through the destabilization of a linearly homogeneous steady state, or through the arrest of bulk oscillations due to initial inhomogeneities. In this last case, by synchronizing the oscillations between cells, the presence of oscillatory transients before pattern formation may constitute a mechanism to avoid patterning defects.
- In parameter regimes where oscillations and patterns coexist, introducing spatiotemporal intrinsic noise can lead to the emergence of circular patterns formed as oscillations become arrested.

This work is an archetypal example of a recently emerging theme in developmental systems biology, namely that a circuit's topology does not unequivocally determine function, but that function may depend on external conditions. Finding small, modular circuits such as this one, and understanding their dynamic possibilities is of essential for understanding the evolution of functional traits in living systems.

The recurrent presence of the mixed feedback loop in gene regulatory networks is suggestive of its functionality. While the single-cell version of the mixed feedback loop has been found to be present in many real biological systems, to our knowledge, there has not been any study where spatial coupling is taken into account. It would be exciting to find a real-life example of such circuit and see whether it displays the diversity of patterns we see theoretically.

The ultimate aim of systems biology is to understand life at its most fundamental level. As quintessential complex systems, living organisms display characteristics that cannot be reduced to the behaviours of their parts alone. Instead, it is their systems nature that characterizes their most iconic idiosyncrasies, from the inner workings of a cell to the convoluted structure of the nervous system. Mathematical models allow us to study living systems at distinct levels of organization, be it gene regulatory networks, cells, tissues, or whole organs, as well as equipping us with tools needed to bridge between these different biological scales, whether they can be isolated and studied independently, or instead they need to be treated as a whole. Crucially, theoretical models provide much-needed frameworks for understanding experimental observations, without which our inquiries would be, in Darwin's words, no more than "*go into a gravel-pit and count the pebbles and describe the colours*[1]". The

[1]See the quote at the beginning of this document.

work presented in this thesis exemplifies how mathematical and computational models are able to shed light on many of these aspects, specifically in the context of cellular decision-making. These approaches are fundamental in our quest to understand life and will surely become increasingly common in the years to come.

# Resum en català

En aquest capítol intentaré resumir breument els principals temes en els quals he estat treballant durant aquests anys. Aquesta tesi es pot incloure dins el marc de física no lineal, aplicada a la biologia del desenvolupament, la branca de la biologia que estudia els canvis—tan genètics, morfològics o de comportament—produïts en els organismes des del seu naixement fins a la seva mort. En particular, hem estudiat aquests processos biològics en plantes, encara que en algunes seccions tractem temes més genèrics. L'enfocament amb el qual afrontem aquests problemes és el de la biologia de sistemes, el marc teòric que estudia les interaccions entre les parts constituents dels organismes, siguin molècules, gens o cèl·lules. En aquest camp, els models matemàtics són el pa de cada dia, i les simulacions numèriques un companatge indispensable. Amb aquestes eines, el comportament dinàmic dels sistemes biològics es pot estudiar i comparar amb les observacions experimentals, que a la vegada formen la base per construir els models matemàtics, en una constant retroalimentació entre teoria i pràctica.

L'objectiu principal de la tesi és entendre, mitjançant aquest enfocament teòric, els processos biològics involucrats en la presa de decisions cel·lulars, ja estiguin relacionades amb la divisió, la diferenciació, o la generació de senyals moleculars. La tesi s'estructura en 7 capítols englobats en tres parts principals, la primera de les quals és introductòria (capítols 1, 2 i 3). Aquesta serveix per contextualitzar la tesi, donant una visió global sobre els temes que es tractaran més tard.

El principal cos de la tesi el componen les parts II i III, on la majoria de les contribucions queda reflectida. En el Capítol 4 (primer capítol de la Part II), s'han estudiat les regulacions genètiques entre dos factors de transcripció—anomenats BRAVO i WOX5—involucrats en la divisió d'un grup de cèl·lules mare en l'arrel de la planta model *Arabidopsis thaliana*. A la punta de l'arrel d'*Arabidopsis*, un petit grup de cèl·lules anomenat *nínxol de cèl·lules mare* (traducció literal de l'anglès *stem cell niche*) destaquen per la seva capacitat de renovar-se contínuament, dividint-se i produint cèl·lules que acaben formant part de diferents teixits de l'arrel. Dins aquest nínxol de cèl·lules mare, un petit grup de cèl·lules que es divideixen infreqüentment anomenat centre quiescent (quiescent center en anglès, QC per abreviar), ajuda a preservar la identitat

de les cèl·lules mare mitjançant senyals moleculars que avui dia encara estan per descobrir. Mitjançant models matemàtics, i amb dades experimentals dels nostres col·laboradors, establim interaccions genètiques entre els dos factors BRAVO i WOX5, trobant que es regulen mútuament i que les seves corresponents proteïnes poden interactuar físicament formant un complex proteic. Amb aquestes regulacions proposem un mecanisme senzill per a la regulació de la divisió cel·lular del QC, i proposem que el complex entre les dues proteïnes podria ser rellevant. La feina realitzada en aquest capítol contribueix en la comprensió dels mecanismes genètics mitjançant els quals les cèl·lules quiescents romanen sense dividir-se durant llargs períodes de temps, ens ajuda a entendre el paper que tenen en la regulació de cèl·lules mare i com aquest contribueix al funcionament normal de la planta.

En el Capítol 5 (segon capítol de la Part II) ampliem el model matemàtic de les interaccions entre BRAVO i WOX5 per incloure explícitament l'estructura cel·lular de l'arrel. Mitjançant un model de reacció-difusió, demostrem que la formació del complex, juntament amb la difusió de WOX5, és capaç d'explicar qualitativament els patrons d'expressió observats experimentalment en arrels de plantes silvestres (WT) i en arrels on aquests factors de transcripció han perdut la seva funció (mutants). En particular, veiem que BRAVO, mitjançant la unió i posterior inactivació de WOX5, confina la seva activitat genètica al nínxol de cèl·lules mare. Això suggereix que BRAVO pot ser un factor important en el manteniment de les cèl·lules mare al nínxol de l'arrel.

En la Part III de la tesi estudiem els circuits genètics que operen en dissenys cel·lulars acoblats per la difusió d'una de les molècules, i com aquestes interaccions són capaços de generar estructures modelades de diferents tipus cel·lulars. Desenvolupem models basats en equacions de reacció-difusió, però la particularitat que les interaccions difusives no s'implementen en un continu sinó en una xarxa discreta, on cada node representa una cèl·lula. Apliquem aquest enfocament a la formació de patrons de precursors rizoides a l'epidermis de *Marchantia polymorpha* ( Capítol 6) i en un circuit genèric ( Capítol 7)

En el primer capítol d'aquesta part (Capítol 6) hem estudiat la formació de rizoides en la planta *Marchantia polymorpha*. Els rizoides són estructures filamentoses d'algunes plantes sense arrel que tenen la funció de fixar la planta al substrat i absorbir nutrients i aigua. A l'epidermis dels embrions de *Marchantia*, cèl·lules precursores de rizoides s'especifiquen a partir d'un camp de cèl·lules inicialment equivalents durant el primer dia després de la germinació l'embrió. A partir d'experiments d'altres grups i dels nostres col·laboradors, proposem un mecanisme per a que els patrons de rizoides sorgeixin de les interaccions entre dos elements, el micro ARN FRH1 i el factor de transcripció RSL1, coneguts per promoure la formació de rizoides. El nostre enfocament es basa en equacions diferencials acoblades en una xarxa de cèl·lules que imiten l'epidermis de *Marchantia*, i té en compte les regulacions genètiques ja conegudes entre RSL1

i FRH1. Veiem que aquests dos elements constitueixen un sistema d'activador-inhibidor, on RSL1 activa FRH1 i FRH1 inhibeix RSL1. Com que FRH1 és suposadament mòbil, aquesta inhibició no es produeix únicament a una mateixa cèl·lula, sinó també a cèl·lules veïnes. El nostre model és capaç de predir quantitativament tots els resultats experimentals amb alta precisió, tant en condicions de tipus silvestre com en mutants. Aquest estudi constitueix un clar exemple on la modelització matemàtica i computacional il·lumina les interaccions darrere de la presa de decisions cel·lulars i la formació de patrons.

Finalment, en el Capítol 7 (el segon capítol de la Part III) explorem matemàticament un circuit genètic les interaccions del qual són capaces de generar un ampli repertori de comportaments dinàmics, incloent-hi biestabilitat, oscil·lacions, i la formació de patrons quan el circuit s'acobla mitjançant difusió. El model es basa en el *mixed feedback loop* (en català *bucle de retroalimentació mixte*), un circuit que apareix de manera recurrent en anàlisis estadístiques de bases de dades d'interacció entre gens i proteïnes. El circuit involucra un bucle de retroalimentació negativa entre dos gens i la formació d'un complex reversible entre les proteïnes corresponents. Analitzant exhaustivament els comportaments dinàmics del sistema, trobem les condicions per les quals cada règim és possible. Estudiem també les conseqüències d'introduir l'acoblament entre cèl·lules mitjançant la difusió del complex, i mostrem com els estats homogenis en l'espai—siguin estables o oscil·latoris—, poden perdre estabilitat per culpa d'aquest acoblament difusiu, donant lloc a patrons periòdics. L'exploració de les dinàmiques del sistema acoblat revela l'existència de comportaments híbrids com les quimeres—estats on conviuen regions oscil·lants amb regions on els patrons són estables—o l'aparició de patrons circulars degut a de la presència de fluctuacions intrínseques de les reaccions moleculars. Aquest treball proporciona un mecanisme novedós per generar patrons periòdics, i demostra l'efecte poc intuïtiu de la difusió ja anticipat per Turing, és a dir, com a agent desestabilitzador d'un estat inicialment homogeni en l'espai, donant lloc a estructures periòdiques estables. També personifica un tema cada cop més comú en la biologia evolutiva de sistemes: la importància de petits circuits genètics capaços de realitzar múltiples funcions sense la necessitat de modificar-ne l'estructura. A més, posa èmfasi en el fet que la topologia d'un circuit no determina inequívocament la seva funció, sinó que aquesta pot dependre de les condicions externes a les quals el circuit hi està integrat. Desxifrar l'estructura i les functions d'aquests tipus de circuits és per tant de gran importància per entendre com regulacions genètiques i moleculars acaben esdevenint en trets fenotípics, propietats que formaran el substrat en el qual l'evolució podrà actuar.

# List of Figures


1.1 Quaking aspens from Utah, posidonia from Menorca and duckweeds from the Lake of Banyoles. . . . 4
1.2 The biomass distribution on Earth . . . 5
1.3 Morphological differences between teosinte and maize . . . 6
1.4 Plant illustrations by Joseph D. Hooker . . . 8
1.5 Illustrations from Charles Darwin's books on plants . . . 10

2.1 Fauna of the Cambrian . . . 17
2.2 Early evolution of land plants. . . . 18
2.3 Roots, root hairs and rhizoids . . . 19
2.4 Initial stages of *Arabidopsis* development and root structure . . . 21
2.5 Gemma development in *Marchantia* . . . 22
2.6 Patterns in biology across scales . . . 24
2.7 Reaction-diffusion Turing patterns. . . . 26
2.8 Pattern formation through positional information. . . . 27
2.9 Pattern formation through lateral inhibition. . . . 28

3.1 Gene regulation from mRNA to protein . . . 34
3.2 Transcriptional activation and repression for distinct dissociation constants . . . 37
3.3 The genetic toggle-switch . . . 39
3.4 Bifurcation diagram of the toggle-switch . . . 41
3.5 Labelling schemes for the square, regular hexagonal, and irregular lattices. . . . 44
3.6 The effect of variability in irregular lattices. . . . 45
3.7 Types of stability of a fixed point. . . . 47
3.8 Diffusion induced instability in a discrete lattice. . . . 54

4.1 Classic picture of SCN maintenance in the *Arabidopsis* root apical meristem . . . 61
4.2 BRAVO and WOX5 are required for the QC identity and stem cell maintenance. . . . 63
4.3 GFP expression of *pBRAVO* and *pWOX5* in WT and mutants. 64
4.4 Generic interactions between BRAVO and WOX5. . . . 66

4.5 Behaviour of $P_B$ and $P_W$ in the alleviation and activation models. 69
4.6 Model results of $pB$ and $pW$ in WT and mutants. . . . . 73
4.7 Effect of brassinosteroids on promoter fold-changes. . . . . 76
4.8 Promoter fold-changes in the alleviation and activation models. 77
4.9 Complex formation model. . . . . 78
4.10 Protein fold-changes in the complex formation model. . . . . 80
4.11 Promoter fold-changes in the complex formation model. . . . . 81
4.12 Promoter fold-changes without complex formation. . . . . 82
4.13 Complex formation model in the presence of an additional sequestrator. . . . . 83
4.14 Promoter fold-changes in the complex formation model with an additional sequestrator. . . . . 85
4.15 The effect of sequestrator binding strengths on protein fold changes. 85
4.16 BRAVO and WOX5 have a joint role in repressing QC divisions. 88
4.17 Regulation of QC division by BRAVO and WOX5. . . . . 90
4.18 BRAVO and WOX5 promote primary root growth and lateral root development. . . . . 95
4.19 BRAVO and WOX5 expression patterns in overexpressing lines. 96
4.20 BRAVO expression in the *bravo wox5* mutant background. . . . 97
4.21 BRAVO and WOX5 expression is BL regulated. . . . . 98
4.22 BRAVO physically interacts with WOX5. . . . . 99
4.23 Promoter fold-changes in the alleviation and activation models for higher parameter variability. . . . . 100
4.24 Promoter fold-changes in the complex formation model with an additional sequestrator with high activity. . . . . 101
4.25 Higher $N$ reduces the error of QC division contributions. . . . . 101

5.1 *pBRAVO* activity in WT and in loss of function mutants. . . . . 105
5.2 Immobilization by sequestration model. . . . . 110
5.3 Parameter dependence of $pB(x)$ in the immobilization by sequestration model. . . . . 112
5.4 Expansion and expression ratios in the immobilization by sequestration model. . . . . 113
5.5 The presence of an additional sequestrator impairs BRAVO self-confinement. . . . . 114
5.6 Attenuation by sequestration model. . . . . 116
5.7 Expansion and expression ratios in the attenuation by sequestration model. . . . . 117
5.8 Parameter dependence of $pB(X)$ in the attenuation by sequestration model. . . . . 118
5.9 Repression model. . . . . 120
5.10 Expansion and expression ratios in the repression model. . . . . 121
5.11 Parameter dependence of $pB(X)$ in the repression model. . . . . 122

5.12 Diagram of the mixed model. . . . . 123
5.13 Construction of a realistic root layout. . . . . 124
5.14 Pixel type assignment in the segmented root layout. . . . . 125
5.15 Cellular domains where production of BRAVO and WOX5 is enabled in the simulations. . . . . 126
5.16 *pBRAVO:GFP* simulated in realistic root layouts . . . . . 129
5.17 *pBRAVO:GFP* simulated in variants of the mixed model . . . . 130
5.18 Immobilization by sequestration model for different parameter values. . . . . 137
5.19 Immobilization by sequestration model with an additional sequestrator. . . . . 138
5.20 Attenuation by sequestration model for different parameter values. 139
5.21 Repression model for different parameter values. . . . . 140
5.22 Activity of *pWOX5:GFP* and *WOX5* in the absence of other regulatory factors. . . . . 140
5.23 Stationary profiles of all proteins and GFP reporters of promoters corresponding to Figure 5.16 (Mixed Model). . . . . 141

6.1 Developmental stages of *Marchantia polymorpha* . . . . . 147
6.2 Distribution of rhizoid precursors in WT (Tak-2) and mutants. . 148
6.3 Distribution of cluster sizes and average neighbour density of rhizoid precursors in experimental data from WT (Tak-1 and Tak-2) plants. . . . . 149
6.4 Distribution of cluster sizes and average neighbour density of rhizoid precursors in $RSL1^{GOF}$ and $frh1^{lof}$ plants. . . . . 149
6.5 Distributions of ON cells predicted by the null model and their statistics. . . . . 151
6.6 Distinct configurations of clusters of 2, 3 and 4. . . . . 152
6.7 Mean neighbour density and fraction $F_r^k$ of cluster types for the null model. . . . . 154
6.8 Comparison between the null model and experimental WT distributions. . . . . 155
6.9 Comparison between the null model and experimental mutant distributions. . . . . 155
6.10 Interactions between RSL1 and FRH1 considered in the model. . 157
6.11 Steady states of the model for a single cell. . . . . 160
6.12 Three examples of WT patterns obtained with the simulations. . 161
6.13 Comparison of $f_k$ and $n_k$ between the model and experiments in [Thamm et al., 2020] in the WT. . . . . 161
6.14 Patterns in WT and mutant phenotypes obtained with the model. 162
6.15 Comparison of $f_k$ and $n_k$ between the model and experiments in [Thamm et al., 2020] in mutants. . . . . 163
6.16 Time evolution of rhizoid precursor patterns. . . . . 164

6.17 Rhizoid precursor patterns for different values of $R_0$. . . . . 164
6.18 Distinct patterns emerge as the coupling strength changes. . . . 165
6.19 The uncoupled system behaves as the null model. . . . . 166
6.20 Fraction of cluster types $F_r^k$ for 3, 4 and 5-clusters. . . . . 167
6.21 Fraction of cells with $l$ neighbours $g_l^k$ for 3, 4 and 5-clusters. . . 167
6.22 Large compact clusters are not stable. . . . . 168
6.23 Three examples of Tak-1 gemmae from our collaborators. . . . . 169
6.24 Comparison between data from [Thamm et al., 2020] and data from our collaborators. . . . . 169
6.25 Simulated cluster-size distribution and average neighbour density. 170
6.26 Fraction of cluster types $F_r^k$ for 3, 4 and 5-clusters. . . . . 171
6.27 Fraction of rhizoid precursors with $l$ rhizoid precursor neighbours $g_l^k$ for 3,4 and 5-clusters. . . . . 171
6.28 Stability of clusters. . . . . 172

7.1 The functions of many genetic circuits are context-dependent. . 184
7.2 Effective interactions and dynamics of the mixed feedback loop. 186
7.3 Dynamical regimes of the RMFL with transcriptional repression 188
7.4 Bifurcation diagrams showing bistability and oscillations in the RMFL. . . . . 191
7.5 Stability diagram for oscillatory and bistable regimes . . . . . 192
7.6 Bistability is promoted by complex formation and degradation. . 192
7.7 Hopf bifurcations can be supercritical or subcritical. . . . . 193
7.8 The amplitude and period of the oscillations can increase indefinitely as $\gamma$ increases. . . . . 193
7.9 Oscillations induced by noise close to a Hopf bifurcation. . . . . 195
7.10 Two cells with a RMFL coupled by diffusion of the complex. . . 197
7.11 Lateral inhibition due to diffusion in the two-cell system. . . . . 198
7.12 Bifurcation diagram showing the splitting between cell states due to diffusive coupling. . . . . 198
7.13 Dynamical regimes of the two-cell system. . . . . 200
7.14 Eigenvalues $\lambda$ of the 1-dimensional spatially extended system as a function of Fourier modes $q/N$. . . . . 202
7.15 Stability diagram of the spatial RMFL. . . . . 203
7.16 Time-evolution of the system in the four distinct regimes . . . . 204
7.17 Salt-and-pepper patterns in the two-dimensional RMFL. . . . . 204
7.18 Oscillations can be destabilized upon a perturbation . . . . . 205
7.19 Chimeras: coexistence between oscillations and patterns . . . . 205
7.20 Circular patterns emerging due to the arrest of oscillatory fronts 207
7.21 Time evolution of circular patterns . . . . . 207
7.22 Patterns in irregular lattices. . . . . 208
7.23 Oscillatory transients prevent the appearance of pattern defects. 210

# List of Tables


4.1 Table summarizing the experimental observations of *pBRAVO:GFP* and *pWOX5:GFP* in WT plants, in *bravo*, *wox5* and *bravo wox5* mutants, and in the overexpression lines *35S:WOX5-GR* and *35S:BRAVO-Ei:pWOX5:GFP*. From these observations we can infer the possible interactions between the two transcription factors. . . . . 65
4.2 Default parameters of the alleviation model. . . . . 71
4.3 Default parameters of the activation model. . . . . 72
4.4 Non-dimensional parameters of the alleviation (Left) and activation (Right) models. . . . . 74
4.5 Parameters of the complex formation model. . . . . 82

5.1 Additional parameters for the immobilization by sequestration model with an additional sequestrator (ISAS). . . . . 115
5.2 Default parameters of the *immobilization by sequestration* (IS), *attenuation by sequestration* (AS) and *repression* (R) models. . . 121
5.3 Default parameters of the mixed model in the realistic root layout. 131

6.1 Parameters of the simplified adimensional model. . . . . 159

# Contributions and publications

The work presented throughout this thesis has been published as the following articles:

- I. Betegón-Putze*, J. Mercadal*, N. Bosch, A. Planas-Riverola, M. Marquès-Bueno, J. Vilarrasa-Blasi, D. Frigola, R. Corinna Burkart, C. Martínez, A. Conesa, R. Sozzani, Y. Stahl, S. Prat, M. Ibañes, A. I. Caño-Delgado. *Precise transcriptional control of cellular quiescence by BRAVO/WOX5 complex in Arabidopsis roots.* Molecular Systems Biology **17**(6) e9864 (2021) — Chapter 4

- J. Mercadal*, I. Betegón-Putze, N. Bosch, A. I. Caño-Delgado, M. Ibañes. *Self-confined expression in the Arabidopsis root stem cell niche.* bioR$\chi$iv (2021) https://doi.org/10.1101/2021.12.02.468941 — Chapter 5 (submitted)

  *Equal contributions

As of the submission of this thesis (February 2022), two more papers are in preparation, each corresponding to the results presented in Chapter 6 and Chapter 7.

# Bibliography


[Aichinger et al., 2012] Aichinger, E., Kornet, N., Friedrich, T., and Laux, T. (2012). Plant Stem Cell Niches. *Annu. Rev. Plant Biol.*, 63:615–636.

[Aida et al., 2004] Aida, M., Beis, D., Heidstra, R., Willemsen, V., Blilou, I., Galinha, C., Nussaume, L., Noh, Y.-S., Amasino, R., and Scheres, B. (2004). The PLETHORA genes mediate patterning of the Arabidopsis root stem cell niche. *Cell*, 119(1):109–120.

[Alberts et al., 2014] Alberts, B., Johnson, A., Lewis, J., Raff, M., Roberts, K., and Walter, P. (2014). *Molecular Biology of the Cell*. W. W. Norton & Company.

[Alexander et al., 2009] Alexander, R. P., Kim, P. M., Emonet, T., and Gerstein, M. B. (2009). Understanding modularity in molecular networks requires dynamics. *Science Signaling*, 2(81):pe44.

[Alon, 2007] Alon, U. (2007). Network motifs: theory and experimental approaches. *Nature Reviews Genetics*, 6:450–461.

[Alon, 2019] Alon, U. (2019). *An Introduction to Systems Biology: Design Principles of Biological Circuits*. Chapman and Hall/CRC.

[Antebi et al., 2020] Antebi, Y. E., Linton, J. M., Klumpe, H., Bintu, B., Gong, M., Su, C., McCardell, R., and Elowitz, M. B. (2020). Combinatorial Signal Perception in the BMP Pathway. *https://www.biorxiv.org/content/10.1101/2020.12.08.412643v1*.

[Aoki et al., 2019] Aoki, S. K., Lillacci, G., Gupta, A., Baumschlager, A., Schweingruber, D., and Khammash, M. (2019). A universal biomolecular integral feedback controller for robust perfect adaptation. *Nature*, 570:533–537.

[Arnaud-Haond et al., 2012] Arnaud-Haond, S., Duarte, C. M., Diaz-Almela, E., Marbà, N., Sintes, T., and Serrão, E. A. (2012). Implications of extreme life span in clonal organisms: millenary clones in meadows of the threatened seagrass *Posidonia oceanica*. *PLoS One*, 7(2):e30454.

[Ball, 2009] Ball, P. (2009). *Nature's Patterns: a tapestry in three parts. 1: Shapes*. Oxford University Press.

[Ball, 2013] Ball, P. (2013). In retrospect: On Growth and Form. *Nature*, 494:32–33.

[Bar-On et al., 2018] Bar-On, Y. M., Phillips, R., and Milo, R. (2018). The biomass distribution on Earth. *Proceedings of the National Academy of Sciences*, 115(25):6506–6511.

[Bar-Or et al., 2000] Bar-Or, R. L., Maya, R., Segel, L. A., Alon, U., and A J Levine, M. O. (2000). Generation of oscillations by the p53-Mdm2 feedback loop: a theoretical and experimental study. *Proceedings of the National Academy of Sciences*, 97(21):11250–11255.

[Barlow et al., 2016] Barlow, J., Lennox, G. D., Joice Ferreira, E. B., Lees, A. C., Nally, R. M., Thomson, J. R., de Barros Ferraz, S. F., Louzada, J., Oliveira, V. H. F., Parry, L., de Castro Solar, R. R., Vieira, I. C. G., Aragão, L. E. O. C., Begotti, R. A., Braga, R. F., Cardoso, T. M., de Oliveira Jr, R. C., Jr, C. M. S., Moura, N. G., Nunes, S. S., Siqueira, J. V., Pardini, R., Silveira, J. M., de Mello, F. Z. V., Veiga, R. C. S., Venturieri, A., and Gardner, T. A. (2016). Anthropogenic disturbance in tropical forests can double biodiversity loss from deforestation. *Nature*, 535(7610):144–147.

[Barnosky et al., 2012] Barnosky, A. D., Hadly, E. A., Bascompte, J., Berlow, E. L., Brown, J. H., Fortelius, M., Getz, W. M., Harte, J., Hastings, A., Marquet, P. A., Martinez, N. D., Mooers, A., Roopnarine, P., Vermeij, G., Williams, J. W., Gillespie, R., Kitzes, J., Marshall, C., Matzke, N., Mindell, D. P., Revilla, E., and Smith, A. B. (2012). Approaching a state shift in Earth's biosphere. *Nature*, 486(7401):52–58.

[Bartel, 2009] Bartel, D. P. (2009). MicroRNAs: Target Recognition and Regulatory Functions. *Cell*, 136(2):215–233.

[Bateman et al., 1992] Bateman, R. M., Crane, P. R., DiMichele, W. A., Kenrick, P. R., Rowe, N. P., Speck, T., and Stein, W. E. (1992). Early Evolution of Land Plants: Phylogeny, Physiology, and Ecology of the Primary Terrestrial Radiation. *Annu. Rev. Ecol. Syst.*, 29:263–292.

[Becker and Marin, 2009] Becker, B. and Marin, B. (2009). Streptophyte algae and the origin of embryophytes. *Annals of Botany*, 103(7):999–1004.

[Becskei et al., 2001] Becskei, A., Séraphin, B., and Serrano, L. (2001). Positive feedback in eukaryotic gene networks: cell differentiation by graded to binary response conversion. *EMBO Journal*, 20(10):2528–2535.

[Bejarano et al., 2007] Bejarano, F., Pérez, L., Apidianakis, Y., Delidakis, C., and Milán, M. (2007). Hedgehog restricts its expression domain in the *Drosophila* wing. *EMBO Reports*, 8(8):778–783.

[Bengtson et al., 2017] Bengtson, S., Sallstedt, T., Belivanova, V., and Whitehouse, M. (2017). Three-dimensional preservation of cellular and subcellular structures suggests 1.6 billion year-old crown-group red algae. *PLoS Biology*, 15(3):e2000735.

[Berckmans et al., 2020] Berckmans, B., Kirschner, G., Gerlitz, N., Stadler, R., and Simon, R. (2020). CLE40 Signaling Regulates Root Stem Cell Fate. *Plant Physiology*, 182(4):1776–1792.

[Betegón-Putze et al., 2021] Betegón-Putze, I., Mercadal, J., Bosch, N., Planas-Riverola, A., Marquès-Bueno, M., Vilarrasa-Blasi, J., Frigola, D., Burkart, R. C., Martínez, C., Conesa, A., Sozzani, R., Stahl, Y., Prat, S., Ibañes, M., and Caño-Delgado, A. I. (2021). Precise transcriptional control of cellular quiescence by BRAVO/WOX5 complex in Arabidopsis roots. *Molecular Systems Biology*, 17(6):e9864.

[Borkowski et al., 2016] Borkowski, O., Ceroni, F., Stan, G.-B., and Ellis, T. (2016). Overloaded and stressed: whole-cell considerations for bacterial synthetic biology. *Current Opinion in Microbiology*, 33:123–130.

[Bowman, 2017] Bowman, J. L. (2017). Insights into Land Plant Evolution Garnered from the *Marchantia polymorpha* Genome. *Cell*, 171(2):287–304.

[Bray, 2016] Bray, S. J. (2016). Notch signalling in context. *Nature Reviews Molecular Cell Biology*, 17:722–735.

[Briat et al., 2016] Briat, C., Gupta, A., and Khammash, M. (2016). Antithetic Integral Feedback Ensures Robust Perfect Adaptation in Noisy Biomolecular Networks. *Cell Systems*, 2(1):15–26.

[Britannica, 2019] Britannica, T. E. o. E. (2019). Gene. *Encyclopedia Britannica*, page `https://www.britannica.com/science/gene`.

[Buchler et al., 2005] Buchler, N. E., Gerland, U., and Hwa, T. (2005). Nonlinear protein degradation and the function of genetic circuits. *Proceedings of the National Academy of Sciences*, 102(27):9559–9564.

[Buchler and Louis, 2008] Buchler, N. E. and Louis, M. (2008). Molecular Titration and Ultrasensitivity in Regulatory Networks. *Journal of Molecular Biology*, 384(5):1106–1119.

[Burkart et al., 2019] Burkart, R. C., Strotmann, V. I., Kirschner, G. K., Akinci, A., Czempik, L., Maizel, A., Weidtkamp-Peters, S., and Stahl, Y.

(2019). PLETHORA and WOX5 interaction and subnuclear localisation regulates Arabidopsis root stem cell maintenance. *https://www.biorxiv.org/content/10.1101/818187v1*.

[Cannataro et al., 2017] Cannataro, V. L., McKinley, S. A., and Mary, C. M. S. (2017). The evolutionary trade-off between stem cell niche size, aging, and tumorigenesis. *Evolutionary Applications*, 10(6):590–602.

[Cao et al., 2014] Cao, J.-G., Dai, X.-L., Zou, H.-M., and Wang, Q.-X. (2014). Formation and development of rhizoids of the liverwort Marchantia polymorpha. *Journal of the Torrey Botanical Society*, 141(2):126–134.

[Carlsbecker et al., 2010] Carlsbecker, A., Lee, J.-Y., Roberts, C. J., Dettmer, J., Lehesranta, S., Zhou, J., Lindgren, O., Moreno-Risueno, M. A., Vatén, A., Thitamadee, S., Campilho, A., Sebastian, J., Bowman, J. L., Helariutta, Y., and Benfey, P. N. (2010). Cell signalling by microRNA165/6 directs gene dose-dependent root cell fate. *Nature*, 465(7296):316–321.

[Chang et al., 2016] Chang, C., Bowman, J. L., and Meyerowitz, E. M. (2016). Field Guide to Plant Model Systems. *Cell*, 167(2):325–339.

[Chen and McKearin, 2003] Chen, D. and McKearin, D. (2003). Dpp Signaling Silences *bam* Transcription Directly to Establish Asymmetric Divisions of Germline Stem Cells. *Current Biology*, 13(20):1786–1791.

[Chitwood et al., 2009] Chitwood, D. H., Nogueira, F. T., Howell, M. D., Montgomery, T. A., Carrington, J. C., and Timmermans, M. C. (2009). Pattern formation via small RNA mobility. *Development*, 23:549–554.

[Chitwood and Timmermans, 2010] Chitwood, D. H. and Timmermans, M. C. P. (2010). Small RNAs are on the move. *Nature*, 467:415–419.

[Clark et al., 2019] Clark, N. M., Buckner, E., Fisher, A. P., Nelson, E. C., Nguyen, T. T., Simmons, A. R., de Luis Balaguer, M. A., Butler-Smith, T., Sheldon, P. J., Bergmann, D. C., Williams, C. M., and Sozzani, R. (2019). Stem-cell-ubiquitous genes spatiotemporally coordinate division through regulation of stem-cell-specific gene networks. *Nature Communications*, 10(5574).

[Clark et al., 2020] Clark, N. M., Fisher, A. P., Berckmans, B., den Broeck, L. V., Nelson, E. C., Nguyen, T. T., Bustillo-Avendaño, E., Zebell, S. G., Moreno-Risueño, M. A., Simon, R., Gallagher, K. L., and Sozzani, R. (2020). Protein complex stoichiometry and expression dynamics of transcription factors modulate stem cell division. *Proceedings of the National Academy of Sciences*, 117(26):15332–15342.

[Classen et al., 2005] Classen, A.-K., Anderson, K. I., Marois, E., and Eaton, S. (2005). Hexagonal packing of *Drosophila* wing epithelial cells by the planar cell polarity pathway. *Developmental Cell*, 9(6):805–817.

[Clewley et al., 2007] Clewley, R., Sherwood, W., LaMar, M., and Guckenheimer, J. (2007). PyDSTool, a software environment for dynamical systems modeling. *http://pydstool.sourceforge.net*.

[Clune et al., 2013] Clune, J., Mouret, J.-B., and Lipson, H. (2013). The evolutionary origins of modularity. *Proceedings of the Royal Society B*, 280(1755):20122863.

[Cobb, 2017] Cobb, M. (2017). 60 years ago, Francis Crick changed the logic of biology. *PLoS Biology*, 15(9):e2003243.

[Cohen, 1991] Cohen, B. M. (1991). Nikolai Ivanovich Vavilov: The Explorer and Plant Collector. *Economic Botany*, 45(1):38–46.

[Collier et al., 1996] Collier, J. R., Monk, N. A. M., Maini, P. K., and Lewis, J. H. (1996). Pattern Formation by Lateral Inhibition with Feedback: a Mathematical Model of Delta-Notch Intercellular Signalling. *J. Theor. Biol.*, 183:429–446.

[Cooke and Zeeman, 1976] Cooke, J. and Zeeman, E. C. (1976). A Clock and Wavefront Model for Control of the Number of Repeated Structures during Animal Morphogenesis. *Journal of Theoretical Biology*, 58(2):455–476.

[Corson et al., 2017] Corson, F., Couturier, L., Rouault, H., Mazouni, K., and Schweisguth, F. (2017). Self-organized Notch dynamics generate stereotyped sensory organ patterns in *Drosophila*. *Science*, 356(6337):eaai7407.

[Cotterell et al., 2015] Cotterell, J., Robert-Moreno, A., and Sharpe, J. (2015). A Local, Self-Organizing Reaction-Diffusion Model Can Explain Somite Patterning in Embryos. *Cell Systems*, 1(4):257–269.

[Crick, 1958] Crick, F. (1958). On protein synthesis. *Symposia of the Society for Experimental Biology*, 12:138–163.

[Crick, 1970] Crick, F. (1970). Central Dogma of Molecular Biology. *Nature*, 227:561–563.

[Cross and Greenside, 2009] Cross, M. C. and Greenside, H. (2009). *Pattern Formation and Dynamics in Nonequilibrium Systems*. Cambridge University Press.

[Cross and Hohenberg, 2010] Cross, M. C. and Hohenberg, P. C. (2010). Pattern formation outside of equilibrium. *Rev Mod Phys*, 64(3):851.

[Cruz-Ramírez et al., 2012] Cruz-Ramírez, A., Díaz-Triviño, S., Blilou, I., Grieneisen, V. A., Sozzani, R., Zamioudis, C., Miskolczi, P., Nieuwland, J., Benjamins, R., Dhonukshe, P., Caballero-Pérez, J., Horvath, B., Long, Y., Mähönen, A. P., Zhang, H., Xu, J., Murray, J. A., Benfey, P. N., Bako, L., Marée, A. F., and Scheres, B. (2012). A Bistable Circuit Involving SCARECROW-RETINOBLASTOMA Integrates Cues to Inform Asymmetric Stem Cell Division. *Cell*, 150(5):1002–1015.

[Cruz-Ramírez et al., 2013] Cruz-Ramírez, A., Díaz-Triviño, S., Wachsman, G., Du, Y., Arteága-Vázquez, M., Zhang, H., Benjamins, R., Blilou, I., Neef, A. B., Chandler, V., and Scheres, B. (2013). A SCARECROW-RETINOBLASTOMA Protein Network Controls Protective Quiescence in the Arabidopsis Root Stem Cell Organizer. *PLoS Biology*, 11(11):e1001724.

[Day, 2013] Day, J. (2013). Botany meets archaeology: people and plants in the past. *Journal of Experimental Botany*, 64(18):5805–5816.

[de Vries and Archibald, 2018] de Vries, J. and Archibald, J. M. (2018). Plant evolution: landmarks on the path to terrestrial life. *New Phytologist*, 217(4):1428–1434.

[Desmond and Moore, 1992] Desmond, A. and Moore, J. R. (1992). *Darwin*. Penguin.

[Digiuni et al., 2008] Digiuni, S., Schellmann, S., Geier, F., Greese, B., Pesch, M., Wester, K., Dartan, B., Mach, V., Srinivas, B. P., Timmer, J., Fleck, C., and Hülskamp, M. (2008). A competitive complex formation mechanism underlies trichome patterning on *Arabidopsis* leaves. *Molecular Systems Biology*, 4(217).

[Ding et al., 2020] Ding, B., Patterson, E. L., Holalu, S. V., Li, J., Johnson, G. A., Stanley, L. E., Greenlee, A. B., Peng, F., Jr, H. D. B., Blinov, M. L., Blackman, B. K., and Yuan, Y.-W. (2020). Two MYB Proteins in a Self-Organizing Activator-Inhibitor System Produce Spotted Pigmentation Patterns. *Current Biology*, 30(5):802–814.

[Ding et al., 2017] Ding, C., Schreiber, S. G., Roberts, D. R., Hamann, A., and Brouard, J. S. (2017). Post-glacial biogeography of trembling aspen inferred from habitat models and genetic variance in quantitative traits. *Scientific Reports*, 7(1):4672.

[Dinneny and Benfey, 2008] Dinneny, J. R. and Benfey, P. N. (2008). Plant Stem Cell Niches: Standing the Test of Time. *Cell*, 132(4):553–557.

[Dolan et al., 1993] Dolan, L., Janmaat, K., Willemsen, V., Linstead, P., Poethig, S., Roberts, K., and Scheres, B. (1993). Cellular organisation of the Arabidopsis thaliana root. *Development*, 119:71–84.

[Dudkowski et al., 2014] Dudkowski, D., Maistrenko, Y., and Kapitaniak, T. (2014). Different types of chimera states: An interplay between spatial and dynamical chaos. *Physical Review E*, 90(032920).

[Durrett and Levin, 1994] Durrett, R. and Levin, S. (1994). The Importance of Being Discrete (and Spatial). *Theoretical Population Biology*, 46:363–394.

[Eddison et al., 2000] Eddison, M., Roux, I. L., and Lewis, J. (2000). Notch signaling in the development of the inner ear: Lessons from Drosophila. *Proceedings of the National Academy of Sciences*, 97(22):11692–11699.

[Eldar et al., 2003] Eldar, A., Rosin, D., Shilo, B.-Z., and Barkai, N. (2003). Self-Enhanced Ligand Degradation Underlies Robustness of Morphogen Gradients. *Developmental Cell*, 5:635–646.

[Elowitz et al., 2002] Elowitz, M. B., Levine, A. J., Siggia, E. D., and Swain, P. S. (2002). Stochastic gene expression in a single cell. *Science*, 297(5584):1183–1186.

[Endersby, 2001] Endersby, J. (2001). Joseph Hooker: the making of a botanist. *Endeavour*, 25(1):3–7.

[Espinosa-Soto and Wagner, 2010] Espinosa-Soto, C. and Wagner, A. (2010). Specialization can drive the evolution of modularity. *PLoS Computational Biology*, 6(3):e1000719.

[Fabian et al., 2010] Fabian, M. R., Sonenberg, N., and Filipowicz, W. (2010). Regulation of mRNA Translation and Stability by microRNAs. *Annual Review of Biochemistry*, 79:351–379.

[Fagotto and Gumbiner, 1996] Fagotto, F. and Gumbiner, B. M. (1996). Cell contact-dependent signaling. *Developmental Biology*, 180(2):445–454.

[Fahd, 1996] Fahd, T. (1996). *Botany and agriculture, in Encyclopedia of the History of Arabic Science*. London: Routledge.

[FAO et al., 2020] FAO, IFAD, UNICEF, WFP, and WHO (2020). The State of Food Security and Nutrition in the World 2020. Transforming food systems for affordable healthy diets.

[Farhadifar et al., 2007] Farhadifar, R., Röper, J.-C., Aigouy, B., Eaton, S., and Jülicher, F. (2007). The influence of cell mechanics, cell-cell interactions, and proliferation on epithelial packing. *Current Biology*, 17(24):2095–2104.

[Farin et al., 2016] Farin, H. F., Jordens, I., Mosa, M. H., Basak, O., Korving, J., Tauriello, D. V. F., de Punder, K., Angers, S., Peters, P. J., Maurice, M. M., and Clevers, H. (2016). Visualization of a short-range Wnt gradient in the intestinal stem-cell niche. *Nature*, 530(7590):340–343.

[Ferrell, 2014] Ferrell, J. E. (2014). Self-perpetuating states in signal transduction: positive feedback, double-negative feedback and bistability. *Current Opinion in Cell Biology*, 14(2):140–148.

[Ferrell and Ha, 2014] Ferrell, J. E. and Ha, S. H. (2014). Ultrasensitivity part I: Michaelian responses and zero-order ultrasensitivity. *Trends in Biochemical Sciences*, 39(10):496–503.

[Flannery, 1973] Flannery, K. V. (1973). The Origins of Agriculture. *Annual Review of Anthropology*, 2:271–310.

[Fleming et al., 2008] Fleming, H. E., Janzen, V., Celso, C. L., Guo, J., Leahy, K. M., Kronenberg, H. M., and Scadden, D. T. (2008). Wnt Signaling in the Niche Enforces Hematopoietic Stem Cell Quiescence and Is Necessary to Preserve Self-Renewal In Vivo. *Cell Stem Cell*, 2(3):274–283.

[Flores-Sandoval et al., 2018] Flores-Sandoval, E., Eklund, D. M., Hong, S.-F., Alvarez, J. P., Fisher, T. J., Lampugnani, E. R., Golz, J. F., Vázquez-Lobo, A., Dierschke, T., Lin, S.-S., and Bowman, J. L. (2018). Class C ARFs evolved before the origin of land plants and antagonize differentiation and developmental transitions in *Marchantia polymorpha*. *New Phytologist*, 218(4):1612–1630.

[Formosa-Jordan and Ibañes, 2014] Formosa-Jordan, P. and Ibañes, M. (2014). Competition in Notch signaling with cis enriches cell fate decisions. *PLoS One*, 9(4):e95744.

[Forzani et al., 2014] Forzani, C., Aichinger, E., Sornay, E., Willemsen, V., Laux, T., Dewitte, W., and Murray, J. A. H. (2014). WOX5 Suppresses CYCLIN D Activity to Establish Quiescence at the Center of the Root Stem Cell Niche. *Current Biology*, 24:1939–1944.

[Frangedakis et al., 2021] Frangedakis, E., Shimamura, M., Villarreal, J. C., Li, F.-W., Tomaselli, M., Waller, M., Sakakibara, K., Renzaglia, K. S., and Szövényi, P. (2021). The hornworts: morphology, evolution and development. *New Phytologist*, 229:735–754.

[François, 2005] François, P. (2005). A model for the *Neurospora* circadian clock. *Biophysical Journal*, 88(4):2369–2383.

[François and Hakim, 2004] François, P. and Hakim, V. (2004). Design of genetic networks with specified functions by evolution in silico. *Proceedings of the National Academy of Sciences*, 101(2):580–585.

[François and Hakim, 2005] François, P. and Hakim, V. (2005). Core genetic module: The mixed feedback loop. *Physical Review E*, 72(031908).

[Freeman, 2000] Freeman, M. (2000). Feedback control of intercellular signalling in development. *Nature*, 408(6810):313–319.

[Fürst-Jansen et al., 2020] Fürst-Jansen, J. M. R., de Vries, S., and de Vries, J. (2020). Evo-physio: on stress responses and the earliest land plants. *Journal of Experimental Botany*, 71(11):3254–3269.

[Gardner et al., 2000] Gardner, T. S., Cantor, C. R., and Collins, J. J. (2000). Construction of a genetic toggle switch in Escherichia coli. *Nature*, 403:339–342.

[Gascoigne, 2011] Gascoigne, J. (2011). *Science In The Service Of Empire: Joseph Banks, the British State and the Uses of Science in the Age of Revolution*. Cambridge University Press.

[Gayon, 2016] Gayon, J. (2016). From Mendel to epigenetics: History of genetics. *Comptes Rendus Biologies*, 339(7-8):225–230.

[Gerland et al., 2002] Gerland, U., Moroz, J. D., and Hwa, T. (2002). Physical constraints and functional characteristics of transcription factor-DNA interaction. *Proceedings of the National Academy of Sciences*, 99(19):12015–12020.

[Giam, 2017] Giam, X. (2017). Global biodiversity loss from tropical deforestation. *Proceedings of the National Academy of Sciences*, 114(23):5775–5777.

[Gillespie, 2000] Gillespie, D. T. (2000). The chemical Langevin equation. *Journal of Chemical Physics*, 114(1):297–306.

[Glass et al., 2016] Glass, D. S., Jin, X., and Riedel-Kruse, I. H. (2016). Signaling Delays Preclude Defects in Lateral Inhibition Patterning. *Physical Review Letters*, 116(12):128102.

[Godfray et al., 2018] Godfray, H. C. J., Aveyard, P., Garnett, T., Hall, J. W., Key, T. J., Lorimer, J., Pierrehumbert, R. T., Scarborough, P., Springmann, M., and Jebb, S. A. (2018). Meat consumption, health, and the environment. *Science*, 361(6399):eaam5324.

[Goentoro et al., 2009] Goentoro, L., Shoval, O., Kirschner, M. W., and Alon, U. (2009). The Incoherent Feedforward Loop Can Provide Fold-Change Detection in Gene Regulation. *Molecular Cell*, 36:894–899.

[González-García et al., 2011] González-García, M.-P., Vilarrasa-Blasi, J., Zhiponova, M., Divol, F., Mora-García, S., Russinova, E., and Caño-Delgado, A. I. (2011). Brassinosteroids control meristem size by promoting cell cycle progression in Arabidopsis roots. *Development*, 138:849–859.

[Gooley, 2012] Gooley, T. (2012). *The Natural Explorer*. London: Sceptre.

[Gould, 1978] Gould, S. J. (1978). Sociobiology: the art of storytelling. *New Scientist*, 80:530–533.

[Gould, 1989] Gould, S. J. (1989). *Wonderful Life: the Burgess Shale and the nature of history*. W. W. Norton & Company.

[Gould, 1994] Gould, S. J. (1994). The evolution of life on earth. *Scientific American*, 271(4):84–91.

[Gould and Lewontin, 1979] Gould, S. J. and Lewontin, R. C. (1979). The Spandrels of San Marco and the Panglossian paradigm: a critique of the adaptationist programme. *Proc. R. Soc. Lond. B*, 205:581–598.

[Green and Sharpe, 2015] Green, J. B. A. and Sharpe, J. (2015). Positional information and reaction-diffusion: two big ideas in developmental biology combine. *Development*, 142:1203–1211.

[Grieneisen et al., 2007] Grieneisen, V. A., Xu, J., Marée, A. F. M., Hogeweg, P., and Scheres, B. (2007). Auxin transport is sufficient to generate a maximum and gradient guiding root growth. *Nature*, 449(25):1008–1013.

[Grierson et al., 2014] Grierson, C., Nielsen, E., Ketelaarc, T., and Schiefelbein, J. (2014). Root Hairs. *Arabidopsis Book*, 12(e0172).

[Griscom et al., 2017] Griscom, B. W., Adams, J., Ellis, P. W., Houghton, R. A., Lomax, G., Miteva, D. A., Schlesinger, W. H., Shoch, D., Siikamäki, J. V., Smith, P., Woodbury, P., Zganjar, C., Blackman, A., Campari, J., Conant, R. T., Delgado, C., Elias, P., Gopalakrishna, T., Hamsik, M. R., Herrero, M., Kiesecker, J., Landis, E., Laestadius, L., Leavitt, S. M., Minnemeyer, S., Polasky, S., Potapov, P., Putz, F. E., Sanderman, J., Silvius, M., Wollenberg, E., and Fargione, J. (2017). Natural climate solutions. *Proceedings of the National Academy of Sciences*, 114(44):11645–11650.

[Grosberg and Strathmann, 2007] Grosberg, R. K. and Strathmann, R. R. (2007). The Evolution of Multicellularity: A Minor Major Transition? *Annual Review of Ecology, Evolution, and Systematics*, 38:621–654.

[Guantes and Poyatos, 2006] Guantes, R. and Poyatos, J. F. (2006). Dynamical principles of two-component genetic oscillators. *PLoS Computational Biology*, 2(3):e30.

[Gupta et al., 2020] Gupta, A., Rico-Medina, A., and Caño-Delgado, A. I. (2020). The physiology of plant responses to drought. *Science*, 368(6488):266–269.

[Halatek et al., 2018] Halatek, J., Brauns, F., and Frey, E. (2018). Self-organization principles of intracellular pattern formation. *Phil. Trans. R. Soc. B*, 373(1747):20170107.

[Han et al., 2008] Han, Y.-G., Spassky, N., Romaguera-Ros, M., Garcia-Verdugo, J.-M., Aguilar, A., Schneider-Maunoury, S., and Alvarez-Buylla, A. (2008). Hedgehog signaling and primary cilia are required for the formation of adult neural stem cells. *Nature Neuroscience*, 11(3):277–284.

[Hansen, 2003] Hansen, T. F. (2003). Is modularity necessary for evolvability? Remarks on the relationship between pleiotropy and evolvability. *Biosystems*, 69(2-3):83–94.

[Harris et al., 2005] Harris, M. P., Williamson, S., Fallon, J. F., Meinhardt, H., and Prum, R. O. (2005). Molecular evidence for an activator-inhibitor mechanism in development of embryonic feather branching. *Proceedings of the National Academy of Sciences*, 102(33):11734–11739.

[Hartwell et al., 1999] Hartwell, L. H., Hopfield, J. J., Leibler, S., and Murray, A. W. (1999). From molecular to modular cell biology. *Nature*, 402:C47–C52.

[Haughn and Somerville, 1988] Haughn, G. W. and Somerville, C. R. (1988). Genetic control of morphogenesis in *Arabidopsis*. *Developmental Genetics*, 9:73–89.

[Henig, 2001] Henig, R. M. (2001). *The Monk in the Garden: The Lost and Found Genius of Gregor Mendel, the Father of Genetics*. Houghton Mifflin.

[Hetherington and Dolan, 2018a] Hetherington, A. J. and Dolan, L. (2018a). Bilaterally symmetric axes with rhizoids composed the rooting structure of the common ancestor of vascular plants. *Phil. Trans. R. Soc. B*, 373(1739):20170042.

[Hetherington and Dolan, 2018b] Hetherington, A. J. and Dolan, L. (2018b). Stepwise and independent origins of roots among land plants. *Nature*, 561(7722):235–238.

[Hickey et al., 2019] Hickey, L. T., Hafeez, A. N., Robinson, H., Jackson, S. A., Leal-Bertioli, S. C. M., Tester, M., Gao, C., Godwin, I. D., Hayes, B. J., and Wulff, B. B. H. (2019). Breeding crops to feed 10 billion. *Nature Biotechnology*, 37:744–754.

[Hogeweg, 2011] Hogeweg, P. (2011). The roots of bioinformatics in theoretical biology. *PLoS Computational Biology*, 7(3):e1002021.

[Hohmann-Marriott and Blankenship, 2011] Hohmann-Marriott, M. F. and Blankenship, R. E. (2011). Evolution of Photosynthesis. *Annual Review of Plant Biology*, 62(4):515–548.

[Honkanen et al., 2016] Honkanen, S., Jones, V. A. S., Morieri, G., Champion, C., Hetherington, A. J., Kelly, S., Proust, H., Saint-Marcoux, D., Prescott,

H., and Dolan, L. (2016). The Mechanism Forming the Cell Surface of Tip-Growing Rooting Cells Is Conserved among Land Plants. *Current Biology*, 26:3238–3244.

[Honkanen et al., 2018] Honkanen, S., Thamm, A., Arteaga-Vazquez, M. A., and Dolan, L. (2018). Negative regulation of conserved RSL class I bHLH transcription factors evolved independently among land plants. *eLife*, 7:e38529.

[Horst et al., 2015] Horst, R. J., Fujita, H., Lee, J. S., Rychel, A. L., Garrick, J. M., Kawaguchi, M., Peterson, K. M., and Torii, K. U. (2015). Molecular Framework of a Regulatory Circuit Initiating Two-Dimensional Spatial Patterning of Stomatal Lineage. *PLoS Genetics*, 11(7):e1005374.

[Hu and Ma, 2021] Hu, X. and Ma, J. (2021). The Founder of Plant Taxonomy in China: HU Hsen-Hsu. *Protein Cell*, doi:10.1007/s13238-021-00877-0.

[Huang et al., 2019] Huang, H., Ullah, F., Zhou, D.-X., Yi, M., and Zhao, Y. (2019). Mechanisms of ROS Regulation of Plant Development and Stress Responses. *Frontiers in Plant Science*, 10(800).

[Hubaud and Pourquié, 2014] Hubaud, A. and Pourquié, O. (2014). Signalling dynamics in vertebrate segmentation. *Nature Reviews Molecular Cell Biology*, 15:709–721.

[Ingram et al., 2006] Ingram, P. J., Stumpf, M. P., and Stark, J. (2006). Network motifs: structure does not determine function. *BMC Genomics*, 7(108).

[Ishizaki et al., 2016] Ishizaki, K., Nishihama, R., Yamato, K. T., and Kohchi, T. (2016). Molecular Genetic Tools and Techniques for *Marchantia polymorpha* Research. *Plant and Cell Physiology*, 57(2):262–270.

[Jacob, 1977] Jacob, F. (1977). Evolution and tinkering. *Science*, 196(4295):1161–1166.

[Jaeger and Monk, 2021a] Jaeger, J. and Monk, N. (2021a). Dynamical Modularity of the Genotype-Phenotype Map. *In: Evolutionary Systems Biology: Advances, Questions, and Opportunities*, Editor: Anton Crombach(Springer).

[Jaeger and Monk, 2021b] Jaeger, J. and Monk, N. (2021b). Dynamical modules in metabolism, cell and developmental biology. *Interface Focus*, 11(3):20210011.

[Jaeger et al., 2004] Jaeger, J., Surkova, S., Blagov, M., Janssens, H., Kosman, D., Kozlov, K. N., Manu, Myasnikova, E., Vanario-Alonso, C. E., Samsonova, M., Sharp, D. H., and Reinitz, J. (2004). Dynamic control of positional information in the early *Drosophila embryo*. *Nature*, 430(6997):368–371.

[Jang et al., 2011] Jang, G., Yi, K., Pires, N. D., Menand, B., and Dolan, L. (2011). RSL genes are sufficient for rhizoid system development in early diverging land plants. *Development*, 138:2273–2281.

[Jiménez et al., 2017] Jiménez, A., Cotterell, J., Munteanu, A., and Sharpe, J. (2017). A spectrum of modularity in multi-functional gene circuits. *Molecular Systems Biology*, 13(4):925.

[Jones and Dolan, 2012] Jones, V. A. and Dolan, L. (2012). The evolution of root hairs and rhizoids. *Annals of Botany*, 110:205–212.

[Joravsky, 1986] Joravsky, D. (1986). *The Lysenko Affair*. University of Chicago Press.

[Jung et al., 2018] Jung, C., Bandilla, P., von Reutern, M., Schnepf, M., Rieder, S., Unnerstall, U., and Gaul, U. (2018). True equilibrium measurement of transcription factor-DNA binding affinities using automated polarization microscopy. *Nature Communications*, 9(1):1605.

[Jönsson et al., 2005] Jönsson, H., Heisler, M., Reddy, G. V., Agrawal, V., Gor, V., Shapiro, B. E., Mjolsness, E., and Meyerowitz, E. M. (2005). Modeling the organization of the WUSCHEL expression domain in the shoot apical meristem. *Bioinformatics*, 21(1):i232–i240.

[Kaern et al., 2005] Kaern, M., Elston, T. C., Blake, W. J., and Collins, J. J. (2005). Stochasticity in gene expression: from theories to phenotypes. *Nature Reviews Genetics*, 6:451–464.

[Kato et al., 2020] Kato, H., Yasui, Y., and Ishizaki, K. (2020). Gemma cup and gemma development in *Marchantia polymorpha*. *New Phytologist*, 228(2):459–465.

[Keller and McClintock, 1983] Keller, E. F. and McClintock, B. (1983). *Feeling for the Organism*. Freeman San Francisco.

[Kenrick, 2017] Kenrick, P. (2017). How land plant life cycles first evolved. *Science*, 358(6370):1538–1539.

[Kenrick and Crane, 1997] Kenrick, P. and Crane, P. R. (1997). The origin and early evolution of plants on land. *Nature*, 389:33–39.

[Kenrick and Strullu-Derrien, 2014] Kenrick, P. and Strullu-Derrien, C. (2014). The Origin and Early Evolution of Roots. *Plant Physiology*, 166(2):570–580.

[Kidner et al., 2000] Kidner, C., Sundaresan, V., Roberts, K., and Dolan, L. (2000). Clonal analysis of the Arabidopsis root confirms that position, not lineage, determines cell fate. *Planta*, 211:191–199.

[Knauer et al., 2013] Knauer, S., Holt, A., Rubio-Somoza, I., Tucker, E. J., Hinze, A., Pisch, M., Javelle, M., Timmermans, M. C., Tucker, M. R., and Laux, T. (2013). A protodermal miR394 signal defines a region of stem cell competence in the *Arabidopsis* shoot meristem. *Developmental Cell*, 24(2):125–132.

[Knoll, 2011] Knoll, A. H. (2011). The Multiple Origins of Complex Multicellularity. *Annual Review of Earth and Planetary Sciences*, 39:217–239.

[Kohchi et al., 2021] Kohchi, T., Yamato, K. T., Ishizaki, K., Yamaoka, S., and Nishihama, R. (2021). Development and Molecular Genetics of *Marchantia polymorpha*. *Annu. Rev. Plant Biol.*, 72:19.1–19.26.

[Kondo and Miura, 2010] Kondo, S. and Miura, T. (2010). Reaction-Diffusion Model as a Framework for Understanding Biological Pattern Formation. *Science*, 329(5999):1616–1620.

[Kong et al., 2018] Kong, X., Tian, H., Yu, Q., Zhang, F., Wang, R., Gao, S., Xu, W., Liu, J., Shani, E., Fu, C., Zhou, G., Zhang, L., Zhang, X., and Ding, Z. (2018). PHB3 Maintains Root Stem Cell Niche Identity through ROS-Responsive AP2/ERF Transcription Factors in Arabidopsis. *Cell Reports*, 22(5):1350–1363.

[Krishna et al., 2006] Krishna, S., Jensen, M. H., and Sneppen, K. (2006). Minimal model of spiky oscillations in NF-$\kappa$B signaling. *Proceedings of the National Academy of Sciences*, 103(29):10840–10845.

[Laxton, 1998] Laxton, E. (1998). *The Famine Ships: The Irish Exodus to America*. Holt Paperbacks.

[Lee, 2017] Lee, J. (2017). Stability of Finite Difference Schemes on the Diffusion Equation with Discontinuous Coefficients. *https://math.mit.edu/research/highschool/rsi/documents/2017Lee.pdf*.

[Lee and Schiefelbein, 2002] Lee, M. M. and Schiefelbein, J. (2002). Cell pattern in the *Arabidopsis* root epidermis determined by lateral inhibition with feedback. *The Plant Cell*, 14(3):611–618.

[Lenton, 2011] Lenton, T. M. (2011). Early warning of climate tipping points. *Nature Climate Change*, 1(4):201–209.

[Leone, 1952] Leone, C. A. (1952). Genetics: Lysenko versus Mendel. *Transactions of the Kansas Academy of Science*, 55(4):369–380.

[Levins and Lewontin, 1985] Levins, R. and Lewontin, R. (1985). *The Dialectical Biologist*. Harvard University Press.

[Li and Li, 2008] Li, D. and Li, C. (2008). Noise-induced dynamics in the mixed-feedback-loop network motif. *Physical Review E*, 77(011903).

[Lin et al., 2016] Lin, P.-C., Lu, C.-W., Shen, B.-N., Lee, G.-Z., Bowman, J. L., Arteaga-Vazquez, M. A., Liu, L.-Y. D., Hong, S.-F., Lo, C.-F., Su, G.-M., Kohchi, T., Ishizaki, K., Zachgo, S., Althoff, F., Takenaka, M., Yamato, K. T., and Lin, S.-S. (2016). Identification of miRNAs and Their Targets in the Liverwort Marchantia polymorpha by Integrating RNA-Seq and Degradome Analyses. *Plant and Cell Physiology*, 57(2):339–358.

[Lin and Bowman, 2018] Lin, S.-S. and Bowman, J. L. (2018). MicroRNAs in *Marchantia polymorpha*. *New Phytologist*, 220(2):409–416.

[Lindner et al., 2004] Lindner, B., García-Ojalvo, J., Neimand, A., and Schimansky-Geier, L. (2004). Effects of noise in excitable systems. *Physics Reports*, 392:321–424.

[Liu and Chen, 2018] Liu, L. and Chen, X. (2018). Intercellular and systemic trafficking of RNAs in plants. *Nature Plants*, 4:869–878.

[Liu et al., 2017] Liu, Y., Xu, M., Liang, N., Zheng, Y., Yu, Q., and Wu, S. (2017). Symplastic communication spatially directs local auxin biosynthesis to maintain root stem cell niche in Arabidopsis. *Proceedings of the National Academy of Sciences*, 114(15):4005–4010.

[Livio, 2003] Livio, M. (2003). *The Golden Ratio: The Story of Phi, the World's Most Astonishing Number*. New York: Broadway Books.

[Long et al., 2017] Long, Y., Stahl, Y., Weidtkamp-Peters, S., Postma, M., Zhou, W., Goedhart, J., Sánchez-Pérez, M.-I., Gadella, T. W. J., Simon, R., Scheres, B., and Blilou, I. (2017). In vivo FRET-FLIM reveals cell-type-specific protein interactions in Arabidopsis roots. *Nature*, 548:97–101.

[Loose et al., 2008] Loose, M., Fischer-Friedrich, E., Ries, J., Kruse, K., and Schwille, P. (2008). Spatial regulators for bacterial cell division self-organize into surface waves in vitro. *Science*, 320(5877):789–792.

[Loros and Dunlap, 2001] Loros, J. J. and Dunlap, J. C. (2001). Genetic and molecular analysis of circadian rhythms in *Neurospora*. *Annual Review of Physiology*, 63:757–794.

[Lv et al., 2018] Lv, B., Tian, H., Zhang, F., Liu, J., Lu, S., Bai, M., Li, C., and Ding, Z. (2018). Brassinosteroids regulate root growth by controlling reactive oxygen species homeostasis and dual effect on ethylene synthesis in Arabidopsis. *PLoS Genetics*, 14(1):e1007144.

[Machold et al., 2003] Machold, R., Hayashi, S., Rutlin, M., Muzumdar, M. D., Nery, S., Corbin, J. G., Gritli-Linde, A., Dellovade, T., Porter, J. A., Rubin, L. L., Dudek, H., McMahon, A. P., and Fishell, G. (2003). Sonic hedgehog is required for progenitor cell maintenance in telencephalic stem cell niches. *Neuron*, 39(6):937–950.

[Maloof et al., 2010] Maloof, A. C., Rose, C. V., Beach, R., Samuels, B. M., Calmet, C. C., Erwin, D. H., Poirier, G. R., Yao4, N., and Simons, F. J. (2010). Possible animal-body fossils in pre-Marinoan limestones from South Australia. *Nature Geoscience*, 3:653–659.

[Mangan et al., 2006] Mangan, S., Itzkovitz, S., Zaslaver, A., and Alon, U. (2006). The incoherent feed-forward loop accelerates the response-time of the gal system of *Escherichia coli*. *Journal of Molecular Biology*, 356(5):1073–1081.

[Mangan et al., 2003] Mangan, S., Zaslaver, A., and Alon, U. (2003). The coherent feedforward loop serves as a sign-sensitive delay element in transcription networks. *Journal of Molecular Biology*, 334(2):197–204.

[Matosevich and Efroni, 2021] Matosevich, R. and Efroni, I. (2021). The Quiescent Center and Root Regeneration. *Journal of Experimental Botany*, 72(19):6739–6745.

[McCalman, 2009] McCalman, I. (2009). *Darwin's Armada: Four Voyages and the Battle for the Theory of Evolution*. W. W. Norton & Company.

[Meinhardt, 1982] Meinhardt, H. (1982). *Models of Biological Pattern Formation*. Academic Press.

[Meinhardt, 1983] Meinhardt, H. (1983). A model for the prestalk/prespore patterning in the slug of the slime mold Dictyostelium discoideum. *Differentiation*, 24(3):191–202.

[Meinhardt and de Boer, 2001] Meinhardt, H. and de Boer, P. A. (2001). Pattern formation in *Escherichia coli*: a model for the pole-to-pole oscillations of Min proteins and the localization of the division site. *Proceedings of the National Academy of Sciences*, 98(25):14202–14207.

[Meinhardt and Gierer, 1972] Meinhardt, H. and Gierer, A. (1972). A theory of biological pattern formation. *Kybernetic*, 12(1):30–39.

[Meinhardt and Gierer, 2000] Meinhardt, H. and Gierer, A. (2000). Pattern formation by local self-activation and lateral inhibition. *BioEssays*, 22:753–760.

[Menand et al., 2007] Menand, B., Yi, K., Jouannic, S., Hoffmann, L., Ryan, E., Linstead, P., Schaefer, D. G., and Dolan, L. (2007). An Ancient Mechanism Controls the Development of Cells with a Rooting Function in Land Plants. *Science*, 316:1477–1480.

[Mercadal et al., 2021] Mercadal, J., Betegón-Putze, I., Bosch, N., Caño-Delgado, A. I., and Ibañes, M. (2021). Self-confined expression in the *Arabidopsis* root stem cell niche. *https://www.biorxiv.org/content/10.1101/2021.12.02.468941*.

[Milo and Phillips, 2016] Milo, R. and Phillips, R. (2016). *Cell biology by the numbers*. Garland Science, New York.

[Milo et al., 2002a] Milo, R., Shen-Orr, S., Itzkovitz, S., Kashtan, N., and an U. Alon, D. C. (2002a). Network Motifs: Simple Building Blocks of Complex Networks. *Science*, 298(5594):824–827.

[Milo et al., 2002b] Milo, R., Shen-Orr, S. S., Itzkovitz, S., Kashtan, N., Chklovskii, D. B., and Alon, U. (2002b). Network Motifs: Simple Building Blocks of Complex Networks. *Nature*, 298(5594):824–827.

[Mireles and Conrad, 2018] Mireles, V. and Conrad, T. O. F. (2018). Reusable building blocks in biological systems. *Journal of the Royal Society Interface*, 15(149):20180595.

[Miyashima et al., 2011] Miyashima, S., Koi, S., Hashimoto, T., and Nakajima, K. (2011). Non-cell-autonomous microRNA165 acts in a dose-dependent manner to regulate multiple differentiation status in the *Arabidopsis* root. *Development*, 138(11):2303–2313.

[Molina et al., 2011] Molina, J., Sikora, M., Garud, N., Flowers, J. M., Rubinstein, S., Reynolds, A., Huang, P., Jackson, S., Schaal, B. A., Bustamante, C. D., Boyko, A. R., and Purugganan, M. D. (2011). Molecular evidence for a single evolutionary origin of domesticated rice. *Proceedings of the National Academy of Sciences*, 108(20):8351–8356.

[Mori et al., 2008] Mori, Y., Jilkine, A., and Edelstein-Keshet, L. (2008). Wave-pinning and cell polarity from a bistable reaction-diffusion system. *Biophysical Journal*, 94(9):3684–3697.

[Morris et al., 2018] Morris, J. L., Puttick, M. N., Clark, J. W., Edwards, D., Kenrick, P., Pressel, S., Wellman, C. H., Yang, Z., Schneider, H., and Donoghue, P. C. J. (2018). The timescale of early land plant evolution. *Proceedings of the National Academy of Sciences*, 115(10):E2274–E2283.

[Mortality and of Death Collaborators, 2016] Mortality, G. . and of Death Collaborators, C. (2016). Global, regional, and national life expectancy, all-cause

mortality, and cause-specifi c mortality for 249 causes of death, 1980–2015: a systematic analysis for the Global Burden of Disease Study 2015. *The Lancet*, 388(10053):1459–1544.

[Morton, 1981] Morton, A. G. (1981). *History of Botanical Science: An Account of the Development of Botany from Ancient Times to the Present Day*. Academic Press.

[Murray, 1988] Murray, J. D. (1988). How the Leopard Gets Its Spots. *Scientific American*, 258(3):80–87.

[Murray, 2002] Murray, J. D. (2002). *Mathematical Biology*. Springer-Verlag.

[Mutte et al., 2018] Mutte, S. K., Kato, H., Rothfels, C., Melkonian, M., Wong, G. K.-S., and Weijers, D. (2018). Origin and evolution of the nuclear auxin response system. *eLife*, 7:e33399.

[Mähönen et al., 2014] Mähönen, A. P., Tusscher, K. T., Siligato, R., Smetana, O., Díaz-Triviño, S., Salojärvi, J., Wachsman, G., Prasad, K., Heidstra, R., and Scheres, B. (2014). PLETHORA gradient formation mechanism separates auxin responses. *Nature*, 515(7525):125–129.

[Nanjundiah, 2003] Nanjundiah, V. (2003). Alan Turing and "The Chemical Basis of Morphogenesis". *In: Sekimura T., Noji S., Ueno N., Maini P.K. (eds) Morphogenesis and Pattern Formation in Biological Systems. Springer, Tokyo*, doi.org/10.1007/978-4-431-65958-7_3.

[Nemeth and Bodine, 2007] Nemeth, M. J. and Bodine, D. M. (2007). Regulation of hematopoiesis and the hematopoietic stem cell niche by Wnt signaling pathways. *Cell Research*, 17(9):746–758.

[Nusse et al., 2008] Nusse, R., Fuerer, C., Ching, W., Harnish, K., Logan, C., Zeng, A., ten Berge, D., and Kalani, Y. (2008). Wnt signaling and stem cell control. *Cold Spring Harbor Symposia on Quantitative Biology*, 73:59–66.

[Ootani et al., 2009] Ootani, A., Li, X., Sangiorgi, E., Ho, Q. T., Ueno, H., Toda, S., Sugihara, H., Fujimoto, K., Weissman, I. L., Capecchi, M. R., and Kuo, C. J. (2009). Sustained in vitro intestinal epithelial culture within a Wnt-dependent stem cell niche. *Nature Medicine*, 15(6):701–706.

[Palau-Ortin et al., 2015] Palau-Ortin, D., Formosa-Jordan, P., Sancho, J. M., and Ibañes, M. (2015). Pattern selection by dynamical biochemical signals. *Biophysical Journal*, 108(6):1555–1565.

[Palma et al., 2005] Palma, V., Lim, D. A., Dahmane, N., Sánchez, P., Brionne, T. C., Herzberg, C. D., Gitton, Y., Carleton, A., Alvarez-Buylla, A., and i Altaba, A. R. (2005). Sonic hedgehog controls stem cell behavior in the postnatal and adult brain. *Development*, 132(2):335–344.

[Pan et al., 2011] Pan, Y., Birdsey, R. A., Fang, J., Houghton, R., Kauppi, P. E., Kurz, W. A., Phillips, O. L., Shvidenko, A., Lewis, S. L., Canadell, J. G., Ciais, P., Jackson, R. B., Pacala, S. W., McGuire, A. D., Piao, S., Rautiainen, A., Sitch, S., and Hayes, D. (2011). A large and persistent carbon sink in the world's forests. *Science*, 333(6045):988–993.

[Panaggio and Abrams, 2015] Panaggio, M. J. and Abrams, D. M. (2015). Chimera states: coexistence of coherence and incoherence in networks of coupled oscillators. *Nonlinearity*, 28:R67–R87.

[Panovska-Griffiths et al., 2012] Panovska-Griffiths, J., Page, K. M., and Briscoe, J. (2012). A gene regulatory motif that generates oscillatory or multiway switch outputs. *Journal of the Royal Society Interface*, 10(79):20120826.

[Pantoja-Hernández et al., 2021] Pantoja-Hernández, J., Breña-Medina, V. F., and Santillán, M. (2021). Hybrid reaction-diffusion and clock-and-wavefront model for the arrest of oscillations in the somitogenesis segmentation clock. *https://doi.org/10.1101/2020.09.04.283515*.

[Paulsson, 2005] Paulsson, J. (2005). Models of stochastic gene expression. *Physics of Life Reviews*, 2(2):157–175.

[Payne and Wagner, 2015] Payne, J. L. and Wagner, A. (2015). Function does not follow form in gene regulatory circuits. *Scientific Reports*, 5(13015):1–10.

[Perez-Carrasco et al., 2018] Perez-Carrasco, R., Barnes, C. P., Schaerli, Y., Isalan, M., Briscoe, J., and Page, K. M. (2018). Combining a Toggle Switch and a Repressilator within the AC-DC Circuit Generates Distinct Dynamical Behaviors. *Cell Systems*, 6(4):521–530.

[Perilli et al., 2012] Perilli, S., Mambro, R. D., and Sabatini, S. (2012). Growth and development of the root apical meristem. *Current Opinion in Plant Biology*, 15(1):17–23.

[Petricka et al., 2012] Petricka, J. J., Winter, C. M., and Benfey, P. N. (2012). Control of Arabidopsis Root Development. *Annu. Rev. Plant Biol.*, 63:563–590.

[Petrovic et al., 2014] Petrovic, J., Formosa-Jordan, P., Luna-Escalante, J. C., Abelló, G., Ibañes, M., Neves, J., and Giraldez, F. (2014). Ligand-dependent Notch signaling strength orchestrates lateral induction and lateral inhibition in the developing inner ear. *Development*, 141(11):2313–2324.

[Phillips et al., 2012] Phillips, R., Kondev, J., Theriot, J., Garcia, H. G., and Orme, N. (2012). *Physical Biology of the Cell*. Garland Science, New York.

[Pi et al., 2015] Pi, L., Aichinger, E., van der Graaff, E., Llavata-Peris, C. I., Weijers, D., Hennig, L., Groot, E., and Laux, T. (2015). Organizer-Derived WOX5 Signal Maintains Root Columella Stem Cells through Chromatin-Mediated Repression of CDF4 Expression. *Developmental Cell*, 33:576–588.

[Pigliucci, 2008] Pigliucci, M. (2008). Is evolvability evolvable? *Nature Reviews Genetics*, 9(1):75–82.

[Pikovsky and Kurths, 1997] Pikovsky, A. S. and Kurths, J. (1997). Coherence Resonance in a Noise-Driven Excitable System. *Physical Review Letters*, 78(5):775–778.

[Poore and Nemecek, 2018] Poore, J. and Nemecek, T. (2018). Reducing food's environmental impacts through producers and consumers. *Science*, 360(6392):987–992.

[Popkin, 2019] Popkin, G. (2019). How much can forests fight climate change? *Nature*, 565(7739):280–282.

[Pourquié, 2001] Pourquié, O. (2001). Vertebrate Somitogenesis. *Annu. Rev. Cell Dev. Biol.*, 17:311–350.

[Proust et al., 2016] Proust, H., Honkanen, S., Jones, V. A., Morieri, G., Prescott, H., Kelly, S., Ishizaki, K., Kohchi, T., and Dolan, L. (2016). RSL Class I Genes Controlled the Development of Epidermal Structures in the Common Ancestor of Land Plants. *Current Biology*, 26:93–99.

[Purcell et al., 2011] Purcell, O., di Bernardo, M., Grierson, C. S., and Savery, N. J. (2011). A Multi-Functional Synthetic Gene Network: A Frequency Multiplier, Oscillator and Switch. *PLoS ONE*, 6(2):e16140.

[Rahni et al., 2016] Rahni, R., Efroni, I., and Birnbaum, K. D. (2016). A Case for Distributed Control of Local Stem Cell Behavior in Plants. *Developmental Cell*, 38(6):635–642.

[Raspopovic et al., 2014] Raspopovic, J., Marcon, L., Russo, L., and Sharpe, J. (2014). Digit patterning is controlled by a Bmp-Sox9-Wnt Turing network modulated by morphogen gradients. *Science*, 345(6196):566–570.

[Rattis et al., 2004] Rattis, F. M., Voermans, C., and Reya, T. (2004). Wnt signaling in the stem cell niche. *Current Opinion in Hematology*, 11(2):88–94.

[Reed, 1942] Reed, H. S. (1942). *A Short History of the Plant Sciences*. New York: Ronald Press.

[Reichenbach et al., 2007] Reichenbach, T., Mobilia, M., and Frey, E. (2007). Mobility promotes and jeopardizes biodiversity in rock-paper-scissors games. *Nature*, 448(7157):1046–1049.

[Rietkerk et al., 2004] Rietkerk, M., Dekker, S. C., de Ruiter, P. C., and van de Koppel, J. (2004). Self-Organized Patchiness and Catastrophic Shifts in Ecosystems. *Science*, 305(5692):1926–1929.

[Rim et al., 2011] Rim, Y., Huang, L., Chu, H., Han, X., Cho, W. K., Jeon, C. O., Kim, H. J., Hong, J.-C., Lucas, W. J., and Kim, J.-Y. (2011). Analysis of Arabidopsis Transcription Factor Families Revealed Extensive Capacity for Cell-to-Cell Movement as Well as Discrete Trafficking Patterns. *Molecules and Cells*, 32(6):519–526.

[Rosenfeld et al., 2002] Rosenfeld, N., Elowitz, M. B., and Alon, U. (2002). Negative autoregulation speeds the response times of transcription networks. *Journal of Molecular Biology*, 323(5):785–793.

[Rué and Garcia-Ojalvo, 2011] Rué, P. and Garcia-Ojalvo, J. (2011). Gene circuit designs for noisy excitable dynamics. *Mathematical Biosciences*, 231:90–97.

[Sabatini et al., 2003] Sabatini, S., Renze Heidstra, M. W., and Scheres, B. (2003). SCARECROW is involved in positioning the stem cell niche in the Arabidopsis root meristem. *Genes & Development*, 17:354–358.

[Sablowski, 2004] Sablowski, R. (2004). Plant and animal stem cells: conceptually similar, molecularly distinct? *Trends in Cell Biology*, 14(11).

[Sablowski, 2007] Sablowski, R. (2007). The dynamic plant stem cell niches. *Current Opinion in Plant Biology*, 10:639–644.

[Saiz et al., 2020] Saiz, N., Mora-Bitria, L., Rahman, S., George, H., Herder, J. P., Garcia-Ojalvo, J., and Hadjantonakis, A.-K. (2020). Growth-factor-mediated coupling between lineage size and cell fate choice underlies robustness of mammalian development. *eLife*, 9:e56079.

[Sakakibara et al., 2003] Sakakibara, K., Nishiyama, T., Sumikawa, N., Kofuji, R., Murata, T., and Hasebe, M. (2003). Involvement of auxin and a homeodomain-leucine zipper I gene in rhizoid development of the moss *Physcomitrella patens*. *Development*, 130(20):4835–4486.

[Sarkar et al., 2007] Sarkar, A. K., Luijten, M., Miyashima, S., Lenhard, M., Hashimoto, T., Nakajima, K., Scheres, B., Heidstra, R., and Laux, T. (2007). Conserved factors regulate signalling in Arabidopsis thaliana shoot and root stem cell organizers. *Nature*, 446:811–814.

[Saunders, 1993] Saunders, P. T. (1993). Alan Turing and Biology. *IEEE Annals of the History of Computing*, 15(3):33–36.

[Savas et al., 2012] Savas, J. N., Toyama, B. H., Xu, T., 3rd, J. R. Y., and Hetzer, M. W. (2012). Extremely long-lived nuclear pore proteins in the rat brain. *Science*, 335(6071):942.

[Scadden, 2006] Scadden, D. T. (2006). The stem-cell niche as an entity of action. *Nature*, 441(7097):1075–1079.

[Scheffer et al., 2009] Scheffer, M., Bascompte, J., Brock, W. A., Brovkin, V., Carpenter, S. R., Dakos, V., Held, H., van Nes, E. H., Rietkerk, M., and Sugihara, G. (2009). Early-warning signals for critical transitions. *Nature*, 461(7260):53–59.

[Schellmann et al., 2002] Schellmann, S., Schnittger, A., Kirik, V., Wada, T., Okada, K., Beermann, A., Thumfahrt, J., Jürgens, G., and Hülskamp, M. (2002). TRIPTYCHON and CAPRICE mediate lateral inhibition during trichome and root hair patterning in *Arabidopsis*. *The EMBO Journal*, 21(19):5036–5046.

[Scheres, 2007] Scheres, B. (2007). Stem-cell niches: nursery rhymes across kingdoms. *Nature Reviews Molecular Cell Biology*, 8:345–354.

[Schmitt, 1971] Schmitt, C. B. (1971). Theophrastus in the Middle Ages. *Viator*, 2:257–270.

[Schreiber et al., 2009] Schreiber, G., Haran, G., and Zhou, H. X. (2009). Fundamental Aspects of Protein-Protein Association Kinetics. *Chemical Reviews*, 109(3):839–860.

[Schwanhäusser et al., 2013] Schwanhäusser, B., Busse, D., Li, N., Dittmar, G., Schuchhardt, J., Wolf, J., Chen, W., and Selbach, M. (2013). Global quantification of mammalian gene expression control. *Nature*, 495(7439):126–127.

[Sena et al., 2009] Sena, G., Wang, X., Liu, H.-Y., Hofhuis, H., and Birnbaum, K. D. (2009). Organ regeneration does not require a functional stem cell niche in plants. *Nature*, 457:1150–1153.

[Shaal, 2019] Shaal, B. (2019). Plants and people: Our shared history and future. *Plants, People, Planet*, 1:14–19.

[Shen-Orr et al., 2002] Shen-Orr, S. S., Milo, R., Mangan, S., and Alon, U. (2002). Network motifs in the transcriptional regulation network of *Escherichia coli*. *Nature Genetics*, 31(1):64–68.

[Shibata and Sugimoto, 2019] Shibata, M. and Sugimoto, K. (2019). A gene regulatory network for root hair development. *Journal of Plant Research*, 132(3):301–309.

[Shilo and Barkai, 2016] Shilo, B.-Z. and Barkai, N. (2016). Buffering Global Variability of Morphogen Gradients. *Developmental Cell*, 40:429–438.

[Shimamura, 2016] Shimamura, M. (2016). Marchantia polymorpha: Taxonomy, Phylogeny and Morphology of a Model System. *Plant and Cell Physiology*, 57(2):230–256.

[Shimotohno et al., 2018] Shimotohno, A., Heidstra, R., Blilou, I., and Scheres, B. (2018). Root stem cell niche organizer specification by molecular convergence of PLETHORA and SCARECROW transcription factor modules. *Genes & Development*, 32:1085–1100.

[Sick et al., 2006] Sick, S., Reinker, S., Timmer, J., and Schlake, T. (2006). WNT and DKK determine hair follicle spacing through a reaction-diffusion mechanism. *Science*, 314(5804):1447–1450.

[Singh and Harris, 2005] Singh, A. B. and Harris, R. C. (2005). Autocrine, paracrine and juxtacrine signaling by EGFR ligands. *Cellular Signalling*, 17(10):1183–1193.

[Skopelitis et al., 2017] Skopelitis, D. S., Benkovics, A. H., Husbands, A. Y., and Timmermans, M. C. P. (2017). Boundary Formation through a Direct Threshold-Based Readout of Mobile Small RNA Gradients. *Developmental Cell*, 43:265–273.

[Skopelitis et al., 2018] Skopelitis, D. S., Hill, K., Klesen, S., Marco, C. F., von Born, P., Chitwood, D. H., and Timmermans, M. C. P. (2018). Gating of miRNA movement at defined cell-cell interfaces governs their impact as positional signals. *Nature Communications*, 9(3107).

[Solly et al., 2017] Solly, J. E., Cunniffe, N. J., and Harrison, C. J. (2017). Regional Growth Rate Differences Specified by Apical Notch Activities Regulate Liverwort Thallus Shape. *Current Biology*, 27(1):16–26.

[Solomon et al., 2009] Solomon, S., Plattner, G.-K., Knutti, R., and Friedlingstein, P. (2009). Irreversible climate change due to carbon dioxide emissions. *Proceedings of the National Academy of Sciences*, 106(6):1704–1709.

[Solé and Valverde, 2006] Solé, R. V. and Valverde, S. (2006). Are network motifs the spandrels of cellular complexity? *Trends in Ecology and Evolution*, 21(9):419–422.

[Soyfer, 2001] Soyfer, V. N. (2001). The consequences of political dictatorship for Russian science. *Nature Reviews Genetics*, 2(9):723–729.

[Spooner et al., 2005] Spooner, D. M., McLean, K., Ramsay, G., Waugh, R., and Bryan, G. J. (2005). A single domestication for potato based on multilocus amplified fragment length polymorphism genotyping. *Proceedings of the National Academy of Sciences*, 102(41):14694–14699.

[Spradling et al., 2001] Spradling, A. C., Drummond-Barbosa, D., and Kai, T. (2001). Stem cells find their niche. *Nature*, 414:98–104.

[Stehfest et al., 2009] Stehfest, E., Bouwman, L., van Vuuren, D. P., den Elzen, M. G. J., Eickhout, B., and Kabat, P. (2009). Climate benefits of changing diet. *Climatic Change*, 95(1):83–102.

[Strager, 2016] Strager, H. (2016). *A Modest Genius: The story of Darwin's Life and how his ideas changed everything*. CreateSpace Independent Publishing Platform.

[Strogatz, 2014] Strogatz, S. H. (2014). *Nonlinear Dynamics and Chaos*. CRC Press.

[Su et al., 2020] Su, C. J., Murugan, A., Linton, J. M., Yeluri, A., Bois, J., Klumpe, H., Antebi, Y. E., and Elowitz, M. B. (2020). Ligand-receptor promiscuity enables cellular addressing. *https://www.biorxiv.org/content/10.1101/2020.12.08.412643v1*.

[Swain et al., 2002] Swain, P. S., Elowitz, M. B., and Siggia, E. D. (2002). Intrinsic and extrinsic contributions to stochasticity in gene expression. *Proceedings of the National Academy of Sciences*, 99(20):12795–12800.

[Swarup et al., 2005] Swarup, R., Kramer, E. M., Perry, P., Knox, K., Leyser, H. M. O., Haseloff, J., Beemster, G. T. S., Bhalerao, R., and Bennett, M. J. (2005). Root gravitropism requires lateral root cap and epidermal cells for transport and response to a mobile auxin signal. *Nature Cell Biology*, 7(11):1057–1065.

[Süel et al., 2006] Süel, G. M., Garcia-Ojalvo, J., Liberman, L. M., and Elowitz, M. B. (2006). An excitable gene regulatory circuit induces transient cellular differentiation. *Nature*, 440(23):545–550.

[TAIR, 2017] TAIR, T. A. I. R. (2017). `https://www.arabidopsis.org/servlets/TairObject?type=aa_sequence&id=1009128733`.

[Tam et al., 2015] Tam, T. H. Y., Catarino, B., and Dolan, L. (2015). Conserved regulatory mechanism controls the development of cells with rooting functions in land plants. *Proceedings of the National Academy of Sciences*, 112(29):E3959–E3968.

[Tang et al., 2020] Tang, Q., Pang, K., Yuan, X., and Xiao, S. (2020). A one-billion-year-old multicellular chlorophyte. *Nature Ecology and Evolution*, 4(4):543–549.

[ten Hove et al., 2015] ten Hove, C. A., Lu, K.-J., and Weijers, D. (2015). Building a plant: cell fate specification in the early Arabidopsis embryo. *Development*, 142(3):420–430.

[Thamm, 2019] Thamm, A. (2019). The microRNA FEW RHIZOIDS1 controls rhizoid patterning in the liverwort *Marchantia polymorpha*. *PhD Thesis*, https://ora.ox.ac.uk/objects/uuid:5720a6a9-1640-484b-9709-ba56fc77f4b4.

[Thamm et al., 2020] Thamm, A., Saunders, T. E., and Dolan, L. (2020). MpFEW RHIZOIDS1 miRNA-Mediated Lateral Inhibition Controls Rhizoid Cell Patterning in Marchantia polymorpha. *Current Biology*, 30:1905–1915.

[Thimann, 1974] Thimann, K. V. (1974). Fifty Years of Plant Hormone Research. *Plant Physiology*, 54(4):450–453.

[Thompson, 1992] Thompson, D. W. (1992). *On Growth and Form*. Dover.

[Tian et al., 2014a] Tian, H., Jia, Y., Niu, T., Yu, Q., and Ding, Z. (2014a). The key players of the primary root growth and development also function in lateral roots in Arabidopsis. *Plant Cell Reports*, 33(5):745–753.

[Tian et al., 2014b] Tian, H., Wabnik, K., Niu, T., Li, H., Yu, Q., Pollmann, S., Vanneste, S., Govaerts, W., Rolcík, J., Geisler, M., Friml, J., and Ding, Z. (2014b). WOX5-IAA17 feedback circuit-mediated cellular auxin response is crucial for the patterning of root stem cell niches in Arabidopsis. *Molecular Plant*, 7(2):277–289.

[Tian et al., 2018] Tian, Y., Fan, M., Qin, Z., Lv, H., Wang, M., Zhang, Z., Zhou, W., Zhao, N., Li, X., Han, C., Ding, Z., Wang, W., Wang, Z.-Y., and Bai, M.-Y. (2018). Hydrogen peroxide positively regulates brassinosteroid signaling through oxidation of the BRASSINAZOLE-RESISTANT1 transcription factor. *Nature Communications*, 9(1063).

[Torii, 2012] Torii, K. U. (2012). Two-dimensional spatial patterning in developmental systems. *Trends in Cell Biology*, 22(8):438–446.

[Tsai et al., 2008] Tsai, T. Y.-C., Choi, Y. S., Ma, W., Pomerening, J. R., Tang, C., and Ferrell, J. E. (2008). Robust, tunable biological oscillations from interlinked positive and negative feedback loops. *Science*, 321(5885):126–129.

[Tsimring, 2014] Tsimring, L. S. (2014). Noise in biology. *Reports on Progress in Physics*, 77(2):026601.

[Tsuzuki et al., 2019] Tsuzuki, M., Futagami, K., Shimamura, M., Inoue, C., Kunimoto, K., Oogami, T., Tomita, Y., Inoue, K., Kohchi, T., Yamaoka, S., Araki, T., Hamada, T., and Watanabe, Y. (2019). An Early Arising Role of the MicroRNA156/529-SPL Module in Reproductive Development Revealed by the Liverwort *Marchantia polymorpha*. *Current Biology*, 29(19):3307–3314.e5.

[Turing, 1952] Turing, A. M. (1952). The chemical basis of morphogenesis. *Phil. Trans. R. Soc. B*, 237:37–72.

[van Berkel et al., 2013] van Berkel, K., de Boer, R. J., Scheres, B., and ten Tusscher, K. (2013). Polar auxin transport: models and mechanisms. *Development*, 140(11):2253–2268.

[van den Berg et al., 1995] van den Berg, C., Willemsen, V., Hage, W., Weisbeek, P., and Scheres, B. (1995). Cell fate in the Arabidopsis root meristem determined by directional signalling. *Nature*, 378:62–65.

[van den Berg et al., 1997] van den Berg, C., Willemsen, V., Hendriks, G., Weisbeek, P., and Scheres, B. (1997). Short-range control of cell differentiation in the Arabidopsis root meristem. *Nature*, 390:287–289.

[van der Walt et al., 2014] van der Walt, S., Schönberger, J. L., Nunez-Iglesias, J., Boulogne, F., Warner, J. D., Yager, N., Gouillart, E., Yu, T., and the *scikit-image* contributors (2014). *scikit-image*: Image processing in Python. *PeerJ*, 2(e453):`https://doi.org/10.7717/peerj.453`.

[van Wyhe, 2007] van Wyhe, J. (2007). Mind the gap: did Darwin avoid publishing his theory for many years? *Notes and Records of The Royal Society*, 61(2):177–205.

[Vilarrasa-Blasi et al., 2014] Vilarrasa-Blasi, J., González-García, M.-P., Frigola, D., Fàbregas, N., Alexiou, K. G., López-Bigas, N., Rivas, S., Jauneau, A., Lohmann, J. U., Benfey, P. N., Ibañes, M., and Caño-Delgado, A. I. (2014). Regulation of Plant Stem Cell Quiescence by a Brassinosteroid Signaling Module. *Developmental Cell*, 30:36–47.

[Virtanen and SciPy 1.0 Contributors, 2020] Virtanen, P. and SciPy 1.0 Contributors (2020). SciPy 1.0: fundamental algorithms for scientific computing in Python. *Nature Methods*, 17(13):261–272.

[Voß et al., 2014] Voß, U., Bishopp, A., Farcot, E., and Bennett, M. J. (2014). Modelling hormonal response and development. *Trends in Plant Science*, 19(5):311–319.

[Wagner, 2008] Wagner, A. (2008). Robustness and evolvability: a paradox resolved. *Proceedings of the Royal Society B*, 275(1630):91–100.

[Wagner and Altenberg, 1996] Wagner, G. P. and Altenberg, L. (1996). Complex adaptations and the evolution of evolvability. *Evolution*, 50(3):967–976.

[Wagner et al., 2007] Wagner, G. P., Pavlicev, M., and Cheverud, J. M. (2007). The road to modularity. *Nature Reviews Genetics*, 8(12):921–931.

[Wagner and Zhang, 2011] Wagner, G. P. and Zhang, J. (2011). The pleiotropic structure of the genotype–phenotype map: the evolvability of complex organisms. *Nature Reviews Genetics*, 12(3):204–213.

[Wall et al., 2005] Wall, M. E., Dunlop, M. J., and Hlavacek, W. S. (2005). Multiple functions of a feed-forward-loop gene circuit. *Journal of Molecular Biology*, 349(3):501–514.

[Watson and Crick, 1953] Watson, J. D. and Crick, F. H. C. (1953). Molecular Structure of Nucleic Acids: A Structure for Deoxyribose Nucleic Acid. *Nature*, 171:737–738.

[Wellman et al., 2003] Wellman, C. H., Osterloff, P. L., and Mohiuddin, U. (2003). Fragments of the earliest land plants. *Nature*, 425(6955):282–285.

[Weyers and Paterson, 2001] Weyers, J. D. B. and Paterson, N. W. (2001). Plant hormones and the control of physiological processes. *New Phytologist*, 152(3):375–407.

[Wolpert, 1969] Wolpert, L. (1969). Positional Information and the Spatial Pattern of Cellular Differentiation. *J. Theoret. Biol.*, 25:1–47.

[Wolpert, 1971] Wolpert, L. (1971). Positional Information and Pattern Formation. *Current topics in developmental biology*, 6:183–224.

[Xie and Spradling, 1998] Xie, T. and Spradling, A. C. (1998). *decapentaplegic* Is Essential for the Maintenance and Division of Germline Stem Cells in the *Drosophila* Ovary. *Cell*, 94(2):251–260.

[Yadav et al., 2011] Yadav, R. K., Perales, M., Gruel, J., Girke, T., Jösson, H., and Reddy, G. V. (2011). WUSCHEL protein movement mediates stem cell homeostasis in the Arabidopsis shoot apex. *Genes & Development*, 25:2025–2030.

[Yadav et al., 2014] Yadav, S. R., Yan, D., Sevilem, I., and Helariutta, Y. (2014). Plasmodesmata-mediated intercellular signaling during plant growth and development. *Frontiers in Plant Science*, 5(44).

[Yang et al., 2019] Yang, C. J., Samayoa, L. F., Bradbury, P. J., Olukolu, B. A., Xue, W., York, A. M., Tuholski, M. R., Wang, W., amd Michael A Neumeyer, L. L. D., de Jesus Sanchez-Gonzalez, J., Romay, M. C., Glaubitz, J. C., Sun,

Q., Buckler, E. S., Holland, J. B., and Doebley, J. F. (2019). The genetic architecture of teosinte catalyzed and constrained maize domestication. *Proceedings of the National Academy of Sciences*, 116(12):5643–5652.

[Yeger-Lotem et al., 2004] Yeger-Lotem, E., Sattath, S., Kashtan, N., Itzkovitz, S., Milo, R., Pinter, R. Y., Alon, U., and Margalit, H. (2004). Network motifs in integrated cellular networks of transcription–regulation and protein–protein interaction. *Proceedings of the National Academy of Sciences*, 101(16):5934–5939.

[Yoshiyamaa et al., 2009] Yoshiyamaa, K., Conklina, P. A., Huefner, N. D., and Britt, A. B. (2009). Suppressor of gamma response 1 (SOG1) encodes a putative transcription factor governing multiple responses to DNA damage. *Proceedings of the National Academy of Sciences*, 106(31):12843–12848.

[Yu et al., 2016] Yu, Q., Tian, H., Yue, K., Liu, J., Zhang, B., Li, X., and Ding, Z. (2016). A P-Loop NTPase Regulates Quiescent Center Cell Division and Distal Stem Cell Identity through the Regulation of ROS Homeostasis in Arabidopsis Root. *PLoS Genetics*, 12(9):e1006175.

[Zeder, 2008] Zeder, M. A. (2008). Domestication and early agriculture in the Mediterranean Basin: Origins, diffusion, and impact. *Proceedings of the National Academy of Sciences*, 105(33):11597–11604.

[Zeder, 2011] Zeder, M. A. (2011). The Origins of Agriculture in the Near East. *Current Anthropology*, 52(S4):S221–S235.

[Zhang and Kalderon, 2001] Zhang, Y. and Kalderon, D. (2001). Hedgehog acts as a somatic stem cell factor in the *Drosophila* ovary. *Nature*, 410(6828):599–604.

[Zhou et al., 2018] Zhou, Y., Yan, A., Han, H., Li, T., Geng, Y., Liu, X., and Meyerowitz, E. M. (2018). HAIRY MERISTEM with WUSCHEL confines CLAVATA3 expression to the outer apical meristem layers. *Science*, 361(6401):502–506.